People's Democratic Republic of Algeria

Ministry of Higher Education and Scientific Research

University of El Oued

Faculty of Exact Sciences

Laboratory of Valorization and Technology of Sahara Resources

A Doctoral Thesis

Submitted in Fulfillment of the Requirements for Degree of Doctor (LMD)

Field: Chemistry

Specialization: Organic Chemistry

Title:

Anti-inflammatory, antidiabetic and antibacterial activities, ADMET analysis, in silico toxicity prediction, and molecular docking study of N-ferrocenylmethyl-nitroaniline and N-ferrocenylmethyl-N-nitrophenyl- 4-nitrobenzamide

Presented by: Bekkar Yahia

Defended on 05/11/2025, in the presence of the Examination Committee:

Name	Rank	Affiliation	Role
Rebiai Abdelkrim	**Professor**	University of El-Oued	**Chair**
Lanez Elhafnaoui	**MCA**	University of El-Oued	**Supervisor**
Lanez Touhami	**Professor**	University of El-Oued	**Co-Supervisor**
Tlili Mohammed Laid	**MCA**	University of El-Oued	**Examiner**
Baira Fayçal	**MCA**	University of Batna 2	**Examiner**
Benyza Nabil	**MCA**	University of Khenchela	**Examiner**

Academic Year: 2025-2026 / 1447-1448 AH

Abstract:

This thesis presents a comprehensive evaluation of several ferrocenyl derivatives, including Ferrocenylmethyl-aniline (FMA), Ferrocenylmethyl-m-toluidine (3FMT), and their acylated derivatives synthesized in VTRS laboratory. The study investigates their potential as therapeutic agents through both *in vitro* and *in silico* approaches, focusing on their antidiabetic, anti-inflammatory, and antibacterial activities.

The new synthesized compounds, 3FMT and its acylated derivatives, were characterized using UV-Vis spectroscopy, electrochemistry, IR, and NMR techniques, which confirmed their proposed structures. Antidiabetic activity was evaluated through interactions with α-amylase, revealing significant inhibitory effects of the ferrocenyl derivatives, with binding energy (ΔG) values ranging from -24.1 to -34.78 kJ/mol and IC_{50} values between 0.69 and 64.5 µM. For anti-inflammatory activity was assessed through interactions with bovine serum albumin (BSA), showing that all compounds except FMA and 3FMT, effectively inhibited BSA denaturation, with IC_{50} values ranging from 1.72 to 7.26 µM and ΔG between -33.36 and -31.06 kJ/mol. These results indicate that all acylated compounds exhibit a stronger antidiabetic and anti-inflammatory compared the standard drug acarbose (IC_{50} of 259 µM) and diclofenac (IC_{50} of 15.81 µM). The antibacterial activity of these compounds was assessed against *E. coli*, *S. aureus*, *K. pneumoniae*, and *P. aeruginosa*, revealing moderate to strong antibacterial effects. However, their effectiveness was generally lower than that of amoxicillin, which demonstrated superior inhibition across all strains.

Molecular docking studies also corroborated these findings, demonstrating strong binding affinities of the compounds to α-amylase (ΔG between -5.85 and -7.84 kcal/mol), BSA (ΔG between -8.04 and -10.49 kcal/mol), and COX-2 (ΔG between -8.17 and -11.97 kcal/mol). For the antibacterial. Regarding antibacterial mechanisms, the ferrocenyl derivatives primarily targeted Peptidoglycan D,D-transpeptidase in *P. aeruginosa* and Penicillin-binding protein 2a in *S. aureus*. Additionally, some compounds interacted with Dihydrofolate reductase and DNA gyrase subunit B in *S. aureus*, Anthranilate-CoA ligase and Peptide deformylase in both *P. aeruginosa* and *E. coli*, and DNA topoisomerase IV in *K. pneumoniae*.

These results suggest that the ferrocenyl derivatives, particularly the acylated ones, have significant potential as inhibitors in antidiabetic, anti-inflammatory, and antibacterial pathways. Furthermore, quantum chemical calculations supported their stability and interactions within the active sites of these proteins, reinforcing their potential as promising therapeutic agents.

Keywords: Ferrocenyl derivatives; Antidiabetic activity; Anti-inflammatory activity; antibacterial activities; BSA; α-Amylase; Molecular docking; DFT.

Résumé :

Cette thèse présente une évaluation approfondie de plusieurs dérivés ferrocenylés, notamment la ferrocenylméthylaniline (FMA), la ferrocenylméthyl-m-toluidine (3FMT) et leurs dérivés acylés synthétisés en laboratoire VTRS. L'étude explore leur potentiel en tant qu'agents thérapeutiques à travers des approches *in vitro* et *in silico*, en mettant l'accent sur leurs activités antidiabétiques, anti-inflammatoires et antibactériennes.

Les nouveaux composés synthétisés, 3FMT et ses dérivés acylés, ont été caractérisés par spectroscopie UV-Vis, électrochimie, IR et RMN, confirmant ainsi leurs structures proposées. L'activité antidiabétique a été évaluée à travers leurs interactions avec l'α-amylase, révélant des effets inhibiteurs significatifs des dérivés ferrocenylés, avec des énergies de liaison (ΔG) comprises entre -24,1 et -34,78 kJ/mol et des valeurs d'IC_{50} variant de 0,69 à 64,5 µM. L'activité anti-inflammatoire a été étudiée à travers les interactions avec l'albumine sérique bovine (BSA), montrant que tous les composés, à l'exception de FMA et 3FMT, inhibent efficacement la dénaturation de la BSA, avec des IC_{50} comprises entre 1,72 et 7,26 µM et des ΔG allant de -33,36 à -31,06 kJ/mol. Ces résultats indiquent que tous les composés acylés présentent une activité antidiabétique et anti-inflammatoire plus forte que les médicaments standards, l'acarbose (IC_{50} de 259 µM) et le diclofénac (IC_{50} de 15,81 µM). L'activité antibactérienne de ces composés a été évaluée contre *E. coli*, *S. aureus*, *K. pneumoniae* et *P. aeruginosa*, révélant des effets antibactériens modérés à forts. Cependant, leur efficacité s'est avérée généralement inférieure à celle de l'amoxicilline, qui a montré une inhibition supérieure sur toutes les souches.

Les études de docking moléculaire ont corroboré ces résultats, mettant en évidence de fortes affinités de liaison des composés avec l'α-amylase (ΔG entre -5,85 et -7,84 kcal/mol), la BSA (ΔG entre -8,04 et -10,49 kcal/mol) et la COX-2 (ΔG entre -8,17 et -11,97 kcal/mol). Concernant les mécanismes antibactériens, les dérivés ferrocenylés ont principalement ciblé la Peptidoglycan D,D-transpeptidase chez *P. aeruginosa* et la protéine de liaison à la pénicilline 2a chez *S. aureus*. De plus, certains composés ont interagi avec la dihydrofolate réductase et la sous-unité B de la gyrase ADN chez *S. aureus*, l'Anthranilate-CoA ligase et la peptide déformylase chez *P. aeruginosa* et *E. coli*, ainsi que la topoisomérase IV de l'ADN chez *K. pneumoniae*.

Ces résultats suggèrent que les dérivés ferrocenylés, en particulier les formes acylées, possèdent un fort potentiel en tant qu'inhibiteurs des voies antidiabétiques, anti-inflammatoires et antibactériennes. De plus, les calculs chimiques quantiques ont confirmé leur stabilité et leurs

interactions avec les sites actifs de ces protéines, renforçant leur potentiel en tant qu'agents thérapeutiques prometteurs.

Mots-clés : Dérivés ferrocenylés; Activité antidiabétique; Activité anti-inflammatoire; Activité antibactérienne; BSA; α-Amylase; Docking moléculaire; DFT.

الملخص:

تقدم هذه الأطروحة تقييماً شاملاً لعدة مشتقات فيروسينيلية، بما في ذلك فيروسينيل ميثيل أنيلين (FMA)، فيروسينيل ميثيل-3-تولويدين (3FMT) و مشتقاتها الأسيلية التي تم تصنيعها في المختبر. تستكشف الدراسة إمكاناتها كعوامل علاجية من خلال نهج مزدوج يشمل الاختبارات داخل المختبر (*in vitro*) والمحاكاة الحاسوبية (*in silico*)، مع التركيز على أنشطتها المضادة لمرض السكري، والمضادة للالتهابات، والمضادة للبكتيريا.

تمت دراسة المركبات الجديدة، 3FMT ومشتقاتها الأسيلية، باستخدام تقنيات التحليل الطيفي بالأشعة فوق البنفسجية-المرئية (UV-Vis)، والكهروكيمياء، والأشعة تحت الحمراء (IR)، والرنين المغناطيسي النووي (NMR)، مما أكد البنية المقترحة لهذه المركبات. تم تقييم النشاط المضاد لمرض السكري من خلال دراسة تفاعلات المركبات مع إنزيم ألفا أميلاز، حيث أظهرت المشتقات الفيروسينيلية تأثيرات تثبيطية قوية، إذ تراوحت طاقة الارتباط (ΔG) بين 24.1- و34.78- كيلوجول/مول، وسُجلت قيم IC_{50} بين 0.69 و64.5 ميكرومول. كما تم تقييم النشاط المضاد للالتهابات عبر دراسة التفاعلات مع ألبومين مصل الأبقار(BSA) ، حيث لوحظ أن جميع المركبات، باستثناء FMA و3FMT، تثبط بشكل فعال عملية تفكك البروتيني (Dénaturation) لـBSA ، مع قيم IC_{50} تراوحت بين 1.72 و7.26 ميكرومول وطاقة ارتباط ΔG بين 33.36- و31.06- كيلوجول/مول. تشير هذه النتائج إلى أن جميع المركبات الأسيلية تتمتع بفعالية مضادة لمرض السكري ومضادة للالتهابات تفوق العقاقير المرجعية، مثل الأكاربوز (IC_{50} =259 ميكرومول) والديكلوفيناك (IC_{50} =15.81 ميكرومول).

تم تقييم النشاط المضاد للبكتيريا لهذه المركبات ضد سلالات بكتيرية شملت القولونيات المعوية (*E. coli*)، العنقوديات الذهبية (*S. aureus*)، و الكلبسيلا الرئوية (*K. pneumoniae*)، والزائفة الزرقاء (*P. aeruginosa*)، حيث أظهرت المركبات تأثيرات مضادة للبكتيريا تراوحت بين المتوسطة والقوية. ومع ذلك، كانت فعاليتها عمومًا أقل من الأموكسيسيلين، الذي أظهر تثبيطًا أقوى ضد جميع السلالات.

أكدت دراسات الإرساء الجزيئي (Molecular Docking) هذه النتائج، حيث أظهرت المركبات مستويات عالية من الارتباط مع ألفا أميلاز (ΔG بين 5.85- و7.84- كيلوكالوري/مول)، BSA (ΔG بين 8.04- و10.49- كيلوكالوري/مول)، وCOX-2 (ΔG بين 8.17- و11.97- كيلوكالوري/مول). فيما يتعلق بالآليات المضادة للبكتيريا، استهدفت المشتقات الفيروسينيلية بشكل رئيسي إنزيم ناقلة الببتيدوغليكان (D,D-transpeptidase) في الزائفة الزنجارية، وبروتين ارتباط البنسلين 2أ في المكورات العنقودية الذهبية. كما أظهرت بعض المركبات تفاعلات مع إنزيم مختزل ثنائي هيدروفولات والوحدة الفرعية ب لأنزيم التفاف الحمض النووي (DNAgyrase) في المكورات العنقودية الذهبية، بالإضافة إلى إنزيم ليغاز أنثرانيلات-مرافق الإنزيم A (Anthranilate-CoA ligase) وإنزيم إزالة الفورميل من الببتيد (Peptide deformylase) في كلٍّ من الزائفة الزنجارية والإشريكية القولونية. أما في الكلبسيلة الرئوية، فقد استهدفت المركبات إنزيم توبويزوميراز (DNA topoisomerase IV)، مما يشير إلى آليات متعددة لمكافحة العدوى البكتيرية.

تشير هذه النتائج إلى أن المشتقات الفيروسينيلية، لا سيما الأشكال الأسيلية منها، تمتلك إمكانات قوية كمثبطات في المسارات المضادة لمرض السكري، والمضادة للالتهابات، والمضادة للبكتيريا. علاوة على ذلك، أكدت الحسابات الكيميائية الكمومية ثبات هذه المركبات وقدرتها على التفاعل داخل المواقع النشطة لهذه البروتينات، مما يعزز إمكاناتها كعوامل علاجية واعدة.

الكلمات المفتاحية: مشتقات الفيروسين؛ النشاط المضاد لمرض السكري؛ النشاط المضاد للالتهابات؛ النشاط المضاد للبكتيريا؛ BSA؛ ألفا أميلاز؛ الإرساء الجزيئي؛ DFT.

LIST OF FIGURES

LIST OF TABLES

LIST OF ABBREVIATIONS

Abbreviation	Definition
3FMT	Ferrocenylmethyl-m-toluidine
3FMAT	N-Ferrocenylmethyl-N-acetyl-m-toluidine
3FMPT	N-Ferrocenylmethyl-N-propionyl-m-toluidine
3FMClAT	N-Ferrocenylmethyl-N-chloroacetyl-m-toluidine
3FMBT	N-Ferrocenylmethyl-N-benzoyl-m-toluidine
3FMPHT	N-Ferrocenylmethyl-N-phthaloyl-m-toluidine
3FM4NBT	N-Ferrocenylmethyl-N-(4-nitrobenzoyl)-m-toluidine
FMBA	N-Ferrocenylmethyl-N-benzoylaniline
FMAA	N-Ferrocenylmethyl-N-acetylaniline
FMA	N-Ferrocenylmethylaniline
ADMET	Absorption, distribution, metabolism, excretion, and toxicity
ARE	Acarbose
AXL	Amoxicillin
BSA	Bovine serum albumin
Bu_4NBF_4	Tetrabutylammonium tetrafluoroborate
$CDCl_3$	Chloroform-d
C_H	Heat capacity
CLtot	Total clearance
CNS	Central nervous system
CV	Cyclic voltammograms
DCM	Dichloromethane
DDIs	Drug-drug interactions
DI	Inhibition diameters
DIF	Diclofenac
DMF	Dimethylformamide
DMSO	Dimethyl sulfoxide
E. coli	*Escherichia coli*
EA	Electron affinity
E_{HOMO}	Highest occupied molecular orbital energy
E_{LUMO}	Lowest unoccupied molecular orbital energy
FT-IR	Fourier Transform Infrared spectroscopy
GI	Gastrointestinal
HBA	Hydrogen bond acceptors
HBD	Hydrogen bond donors
HSA	Human serum albumin
Hz	Hertz
IC_{50}	Half-maximal inhibitory concentration
IP	Ionization potential
J	Coupling constants
K	Binding constant
K. pneumoniae	*Klebsiella pneumoniae*
M	Molarity
MEP	Molecular electrostatic potential

mm	Millimeters
mV	Millivolts
MW	Molecular weight
NMR	Nuclear magnetic resonance
NSAIDs	Nonsteroidal anti-inflammatory drugs
OCT2	Renal organic cation transporter 2
P. aeruginosa	*Pseudomonas aeruginosa*
PBS	Phosphate buffer saline
P-gp	P-glycoprotein
Q	Thermal energy
Quaternary salt	N,N,N-trimethylammoniomethylferrocene iodide
RMSD	Root mean square deviation
S	Entropy
S. aureus	*Staphylococcus aureus*
SAIDs	Steroidal anti-inflammatory drugs
T1D	Type 1 diabetes
T2D	Type 2 diabetes
T2DM	Type 2 diabetes mellitus
TLC	Thin-layer chromatography
TPSA	Total polar surface area
UV-Vis	Ultraviolet-Visible spectroscopy
VDss	Steady-state volume of distribution
Å	Angström
ΔG	Binding free energy
ΔE_{L-H}	Energy gap
χ	Electronegativity
η	Global hardness
σ	Global softness
ω	Electrophilicity index
α	Polarizability
μ	Dipole moment

Table of Contents

General Introduction

Over the past few years, the development of novel ferrocene derivatives has sparked significant interest across various research domains, notably in organic synthesis [1], medicinal chemistry [2], and electrochemical investigations [3]. This interest arises primarily from the versatility and unique chemical properties of ferrocene, which make it a valuable scaffold for the design of biologically active compounds [4]. The incorporation of the ferrocene moiety into bioactive molecules often enhances their stability, lipophilicity, and bioavailability, making them more effective as therapeutic agents [5–7].

Ferrocene and its derivatives have attracted significant attention in medicinal chemistry due to their diverse pharmacological properties, including antidiabetic, anti-inflammatory, and anti-bacterial activities [4,7–15]. These properties have been extensively studied through both *in vitro* and in silico approaches, aiming to explore their potential therapeutic applications [8,11,14]. Specifically, researchers have focused on their efficacy in cellular models and their predicted interactions with biological targets, using techniques such as molecular docking and computational simulations [16–19].

In vitro studies have shown promising results, demonstrating the ability of certain ferrocene derivatives to modulate key cellular pathways involved in metabolic disorders like diabetes, inflammation, and bacterial infections [8–13]. Some of these compounds have exhibit antidiabetic effects by enhancing insulin sensitivity and promoting glucose uptake in cells, providing a potential mechanism for managing hyperglycemia in diabetic patients [9,13,20]. Moreover, their anti-inflammatory properties are linked to the inhibition of pro-inflammatory cytokines and signaling pathways that drive chronic inflammation [8,11]. Additionally, ferrocene derivatives have also shown antibacterial activity against a wide range of pathogenic bacteria, highlighting their potential as antimicrobial agents in treating bacterial infections [10,12].

In silico studies, which involve molecular docking and computational modeling, have been instrumental in understanding the pharmacological activities of ferrocene derivatives at the molecular level [19,21,22]. These computational approaches allow researchers to predict the binding affinity and interaction modes of ferrocene derivatives with specific biological targets, aiding in the rational design of more potent and selective drug candidates [18,19,23].

Moreover, the assessment of pharmacokinetic properties such as absorption, distribution, metabolism, excretion, and toxicity (ADMET) is essential for predicting the potential of ferrocene-

based compounds as therapeutic agents [19,24]. Understanding these properties can guide the optimization of ferrocene derivatives to enhance their pharmacological properties and improve their clinical success [19,24].

In this doctoral thesis, we examined the anti-diabetes, anti-inflammatory, and antibacterial activities of newly synthesized ferrocene derivatives, using both *in vitro* and *in silico* approaches. These derivatives were synthesized at the Saharan Resource Valorization and Technology Laboratory (VTRS), and their biological activities were experimentally assessed using UV-Vis spectroscopic techniques. Half-maximal inhibitory concentration (IC_{50}), binding free energy and binding constants for these activities were determined, followed by validation through molecular docking analysis using AutoDock Tools.

The manuscript is structured in two main sections:

- **The first section** comprises two chapters:

Chapter one provides a historical overview of the discovery of ferrocene, along with a discussion of its physicochemical and thermodynamic properties. It also describes various synthesis approaches for preparing ferrocene molecules , with particular emphasis on the diazonium reaction, which was a focal point of this study. Finally, it explores selected medical applications of ferrocene.

Chapter two presents an overview of the biological activities examined in this research, including antidiabetic, anti-inflammatory, and antibacterial activities.

- **The second section** focuses on the results and discussion, divided into two chapters:

Chapter three outlines the synthesis procedures for all ferrocene derivatives and the experimental methods used to assess their antidiabetic, anti-inflammatory, and antibacterial activities.

Chapter Four delve into the detailed investigation of these biological activities, combining spectroscopic data with molecular docking techniques to provide a comprehensive understanding of their mechanism of action.

The work concludes with a summary of the findings and their potential implications, emphasizing the value and significance of the synthesized ferrocene derivatives in medicinal chemistry.

Reference

[1] M.J.L. Tendero, A. Benito, J. Cano, J.M. Lloris, R. Martínez-Máñez, J. Soto, A.J. Edwards, P.R. Raithby, M.A. Rennie, Host molecules containing electroactive cavities obtained by the molecular assembly of redox-active ligands and metal ions, J. Chem. Soc., Chem. Commun. (1995) 1643–1644. https://doi.org/10.1039/C39950001643.

[2] N. Argyropoulos, E. Coutouli-Argyropoulou, Synthesis of unsymmetrical 1,1′-disubstituted ferrocenes. Formation of ferrocenophanes via intramolecular cycloaddition, J Organomet Chem 654 (2002) 117–122. https://doi.org/10.1016/S0022-328X(02)01394-3.

[3] B. Shaabani, Z. Shaghaghi, Synthesis, characterization and electrochemical properties of two new calix[4]arene derivatives bearing two ferrocene imine or ferrocene amine units at the upper rim, Tetrahedron 66 (2010) 3259–3264. https://doi.org/10.1016/j.tet.2010.02.056.

[4] S. Peter, B.A. Aderibigbe, Ferrocene-Based Compounds with Antimalaria/Anticancer Activity, Molecules 24 (2019) 3604. https://doi.org/10.3390/molecules24193604.

[5] M. Patra, G. Gasser, The medicinal chemistry of ferrocene and its derivatives, Nat Rev Chem 1 (2017) 0066. https://doi.org/10.1038/s41570-017-0066.

[6] B.S. Ludwig, J.D.G. Correia, F.E. Kühn, Ferrocene derivatives as anti-infective agents, Coord Chem Rev 396 (2019) 22–48. https://doi.org/10.1016/j.ccr.2019.06.004.

[7] B. Sharma, V. Kumar, Has Ferrocene Really Delivered Its Role in Accentuating the Bioactivity of Organic Scaffolds?, J Med Chem 64 (2021) 16865–16921. https://doi.org/10.1021/acs.jmedchem.1c00390.

[8] B. Ruan, J. Li, Q. Guo, M. Zhang, Z. Pei, Y. Hu, Synthesis, Characterization, and in vitro Anti-Inflammatory Activity of Novel Ferrocenyl(Piperazine-1-Yl)Methanone-based Derivatives, Med Chem (Los Angeles) 19 (2023) 915–924. https://doi.org/10.2174/1573406419666230214112800.

[9] S.-Z. Ren, Z.-C. Wang, D. Zhu, X.-H. Zhu, F.-Q. Shen, S.-Y. Wu, J.-J. Chen, C. Xu, H.-L. Zhu, Design, synthesis and biological evaluation of novel ferrocene-pyrazole derivatives containing nitric oxide donors as COX-2 inhibitors for cancer therapy, Eur J Med Chem 157 (2018) 909–924. https://doi.org/10.1016/j.ejmech.2018.08.048.

[10] N. Ahmed, N.K. Konduru, M. Owais, Design, synthesis and antimicrobial activities of novel ferrocenyl and organic chalcone based sulfones and bis-sulfones, Arabian Journal of Chemistry 12 (2019) 1879–1894. https://doi.org/10.1016/j.arabjc.2014.12.008.

[11] W.-Y. Guo, L.-Z. Chen, B.-N. Shen, X.-H. Liu, G.-P. Tai, Q.-S. Li, L. Gao, B.-F. Ruan, Synthesis and in vitro and in vivo anti-inflammatory activity of novel 4-ferrocenylchroman-2-one derivatives, J Enzyme Inhib Med Chem 34 (2019) 1678–1689. https://doi.org/10.1080/14756366.2019.1664499.

[12] Y. Swetha, E.R. Reddy, J.R. Kumar, R. Trivedi, L. Giribabu, B. Sridhar, B. Rathod, R.S. Prakasham, Synthesis, characterization and antimicrobial evaluation of ferrocene–oxime ether benzyl 1 H -1,2,3-triazole hybrids, New Journal of Chemistry 43 (2019) 8341–8351. https://doi.org/10.1039/C9NJ00660E.

[13] F. Asghar, S. Munir, S. Fatima, B. Murtaza, J. Patujo, A. Badshah, I.S. Butler, M.B. Taj, M.N. Tahir, Ferrocene-functionalized anilines as potent anticancer and antidiabetic agents: Synthesis, spectroscopic elucidation, and DFT calculations, J Mol Struct 1249 (2022) 131632. https://doi.org/10.1016/j.molstruc.2021.131632.

[14] R. Gul, W. Munir, E.A.M. Saleh, S. Shujah, M. Sirajuddin, S. Tabassum, K. ur Rehman, D. Khan, S.I. Al-Saeedi, E.A. Abdelrahman, Ferrocene based Schiff bases and their complexes: Synthesis, characterization and biological evaluation, J Organomet Chem 1003 (2024) 122944. https://doi.org/10.1016/j.jorganchem.2023.122944.

[15] J. Patujo, M. Azeem, M. khan, H. Muhammad, A. Raheel, S. Fatima, B. Mirza, Z. Hussain, A. Badshah, Assessing the biological potential of new symmetrical ferrocene based bisthiourea analogues, Bioorg Chem 106 (2021) 104180. https://doi.org/10.1016/j.bioorg.2020.104180.

[16] M.M. Hammoud, M. Khattab, M. Abdel-Motaal, J. Van der Eycken, R. Alnajjar, H.S. Abulkhair, A.A. Al-Karmalawy, Synthesis, structural characterization, DFT calculations, molecular docking, and molecular dynamics simulations of a novel ferrocene derivative to unravel its potential antitumor activity, J Biomol Struct Dyn 0 (2022) 1–18. https://doi.org/10.1080/07391102.2022.2082533.

[17] E. Lanez, T. Lanez, Molecular Docking Study of the Interaction of N- Ferrocenylmethyl-N-Phenylacetamide with DNA, (2018).

[18] E. Lanez, L. Bechki, T. Lanez, Synthesis, characterization and in vitro and in silico study of biological activities of some ferrocenylmethyl-nucleic bases derivatives, 2019. https://doi.org/10.13140/RG.2.2.22090.80320.

[19] S. Bano, A. Khan, F. Asghar, M. Usman, A. Badshah, S. Ali, Computational and Pharmacological Evaluation of Ferrocene-Based Acyl Ureas and Homoleptic Cadmium

Carboxylate Derivatives for Anti-diabetic Potential, Front Pharmacol 8 (2018) 1–16. https://doi.org/10.3389/fphar.2017.01001.

[20] P. Yao, J. Zhang, S. You, W. Qi, R. Su, Z. He, Ferrocene-modified peptides as inhibitors against insulin amyloid aggregation based on molecular simulation, J Mater Chem B 8 (2020) 3076–3086. https://doi.org/10.1039/d0tb00144a.

[21] A. Ahmad, K. Mahal, S. Padhye, F.H. Sarkar, R. Schobert, B. Biersack, New ferrocene modified lawsone Mannich bases with anti-proliferative activity against tumor cells, Journal of Saudi Chemical Society 21 (2017) 105–110. https://doi.org/10.1016/j.jscs.2016.03.005.

[22] L. El Hafnaoui, Etude in silico et in vitro de l ' interaction de quelques amides ferrocéniques avec l ' ADN Présenté par : LANEZ El Hafnaoui, (2017). https://doi.org/10.13140/RG.2.2.23802.90561.

[23] A. Ghiami-Shomami, B. Ghalami-Choobar, Y. Shigeta, Computational electrochemistry of a novel ferrocene derivative, J Mol Graph Model 85 (2018) 84–90. https://doi.org/10.1016/j.jmgm.2018.08.004.

[24] G. Sliwoski, S. Kothiwale, J. Meiler, E.W. Lowe, Computational Methods in Drug Discovery, Pharmacol Rev 66 (2014) 334–395. https://doi.org/10.1124/pr.112.007336.

Part 1: Bibliographic Overview

Chapter I: Chemistry of Ferrocene

Background:

1.1. Ferrocene Structure:

The discovery of bis-cyclopentadienyl iron, commonly known as ferrocene, marked a pivotal moment in organometallic chemistry. This compound, first identified in 1951 by Kealy and Pauson, sparked significant scientific interest. Their research, which involved the reaction of cyclopentadienyl magnesium bromide with iron chloride (Scheme I.1), was originally intended to couple the diene and synthesize fulvalene. However, instead of the expected product, they isolated a slightly orange powder with remarkable stability [1].

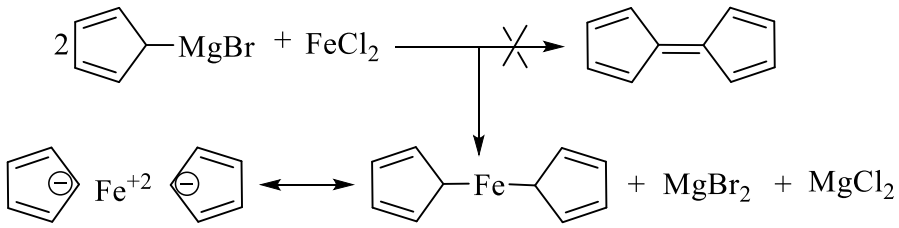

Scheme I.1. Pauson and Kealy's synthetic approach to ferrocene.

The stability of this newly discovered organometallic compound was attributed to the aromatic nature of the negatively charged cyclopentadienide anions. However, they were not the first to identify the η^5 "sandwich structure", The notation η^5 denotes that the iron cation is coordinated by all five atoms of the C_5H_5 rings.

The following year, Woodward and Wilkinson established the correct molecular structure of ferrocene, deducing its formula by observing that it exhibited reactivity characteristic of aromatic compounds, such as benzene [2]. Separately, Ernst Otto Fischer in Munich reached the same conclusion and expanded the study by synthesizing other metallocenes, including nickelocene and cobaltocene [3,4]. Another research group, led by Eiland and his team, confirmed the structure of ferrocene using X-ray crystallography, which was later validated through NMR spectroscopy [5].

Ferrocene's two cyclopentadienyl rings can adopt either an eclipsed (D_5h symmetry) or staggered (D_5d symmetry) conformations (Figure I.1). In condensed-phase experiments, the staggered conformation predominates [5–8], while in the gas phase, the eclipsed conformation is observed [9–11]. The eclipsed conformation has also been detected in solid-state experiments at 90 K and in solution at room temperature [12]. Most theoretical studies of ferrocene focus on the

gas phase or solutions, leading to a greater emphasis on the eclipsed (D_5h) structure over the D_5d conformer. This preference arises from the small energy difference between the two conformations and the low energy barrier for rotation about the Fe-C_5H_5 axis, which is approximately 4 kJ/mol [12].

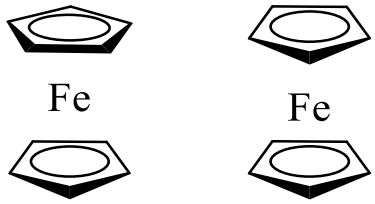

Figure I.1. Representation of ferrocene's conformations: the staggered form (left) and the eclipsed form (right).

1.2. Proprieties:

Ferrocene is an orange crystalline solid with a molecular weight of 186.04 g/mol, exhibiting high stability in air with a boiling point of 249°C and a melting point of 173-174°C [13]. Ferrocene is readily soluble in most organic solvents [14], with a solubility of about 0.1 mg/mL in water at 21°C and 100 mg/mL in dimethyl sulfoxide (DMSO) at 19.5°C [15]. It is also characterized by low toxicity [16].

Ferrocene remains thermally stable at high temperatures, retaining its structure up to 400°C [13]. Upon oxidation, ferrocene undergoes a color change from orange to deep blue due to the loss of one electron at +0.4 V, as measured with a saturated calomel electrode during cyclic voltammetry [17].

1.3. Reactivity:

The shared properties between benzene and ferrocene have significantly advanced the study of this organometallic compound, enabling a wide range of substitution reactions. Substitutions on the cyclopentadienyl ring occur through the direct formation of a sigma complex without direct involvement of the metal center. Two primary mechanisms have been proposed for this process [18]:

As depicted in Scheme I.2, Mechanism I involves a two-step pathway. Initially, the electrophile (E) undergoes a rapid SE2 reaction, temporarily breaking the iron–carbon bond while retaining the configuration. This step is followed by a rate-limiting process, which involves the

removal of a proton from outside the molecule. Finally, the process concludes with an SE2 inversion reaction.

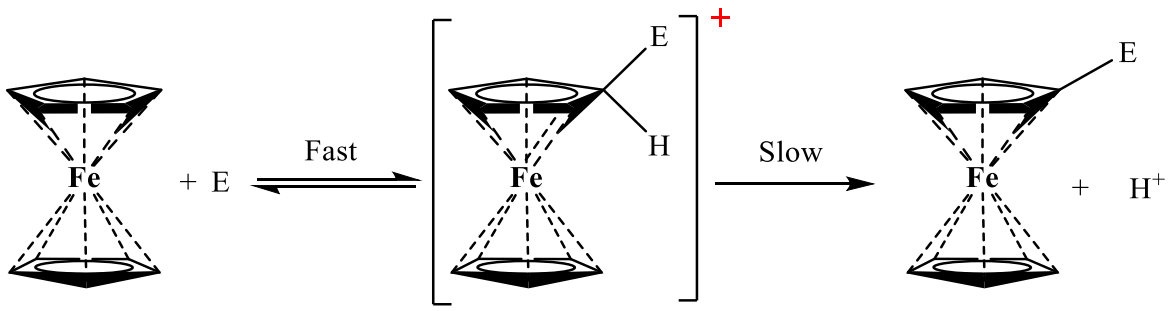

Scheme I.2. Mechanism I of substitution reactions on the cyclopentadienyl ring.

In contrast, Mechanism II (Scheme I.3) is initiated by an electrophilic attack through a rate- limiting SE2 reaction, leading to configuration reversal. Subsequently, rapidly departs from the inside while conserving the configuration.

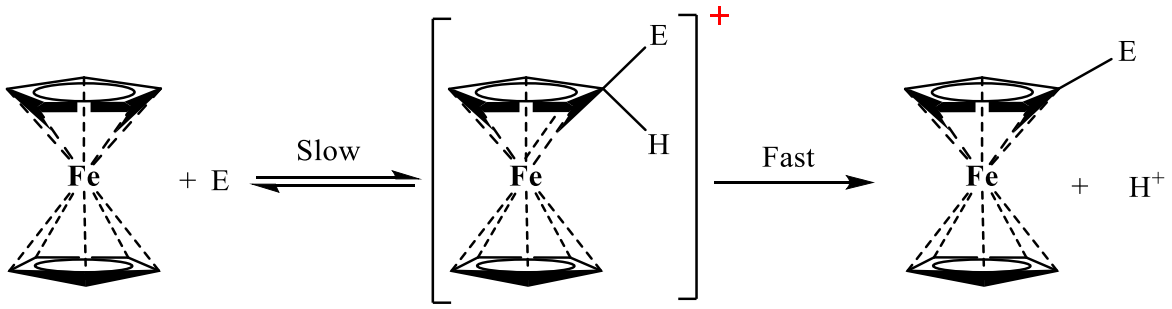

Scheme I.3. Mechanism II of substitution reactions on the cyclopentadienyl ring.

The removal of one electron from ferrocene results in the oxidation of the iron center to Fe^{3+}, forming salts that contain the blue ferricenium cation $(C_5H_5)_2Fe^+$. Ferrocene can be oxidized to the ferrocenium cation by various agents, and even when exposed to air in a low pH solution. The positively charged ferrocenium cation facilitates electrophilic substitution on ferrocene in the presence of mineral acids. Consequently, ferrocene carries a positive charge and exhibits resistance to electrophilic attacks [19,20].

The aromatic nature and high reactivity of ferrocene enable the synthesis of a wide range of derivatives, which serve as key intermediates in organic synthesis [18,21]. These derivatives are easily prepared and exhibit enough reactivity to facilitate the synthesis of novel organic compounds , often inaccessible through conventional methods.

The widely recognized ferrocene-based intermediate is ferrocenylmethyltrimethyl-ammonium iodide, a quaternary ammonium salt frequently used as a starting material for

synthesizing a variety of mono-substituted ferrocene derivatives. This salt is prepared through the aminomethylation of ferrocene [22], as shown in Scheme I.4.

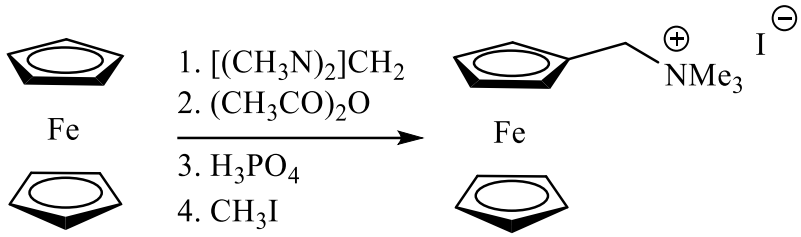

Scheme I.4. Synthetic pathway for quaternary salt formation.

The trimethylamine moiety in the quaternary salt can be readily substituted by various nucleophiles (Scheme I.5), including alkoxide [23], nucleobase [24], hydrazide reagents [25], carbanionic reagents [26], and amines [27]. In this study, we synthesized the quaternary salt and utilized it to prepare N-ferrocenylmethyl toluidine and its derivatives.

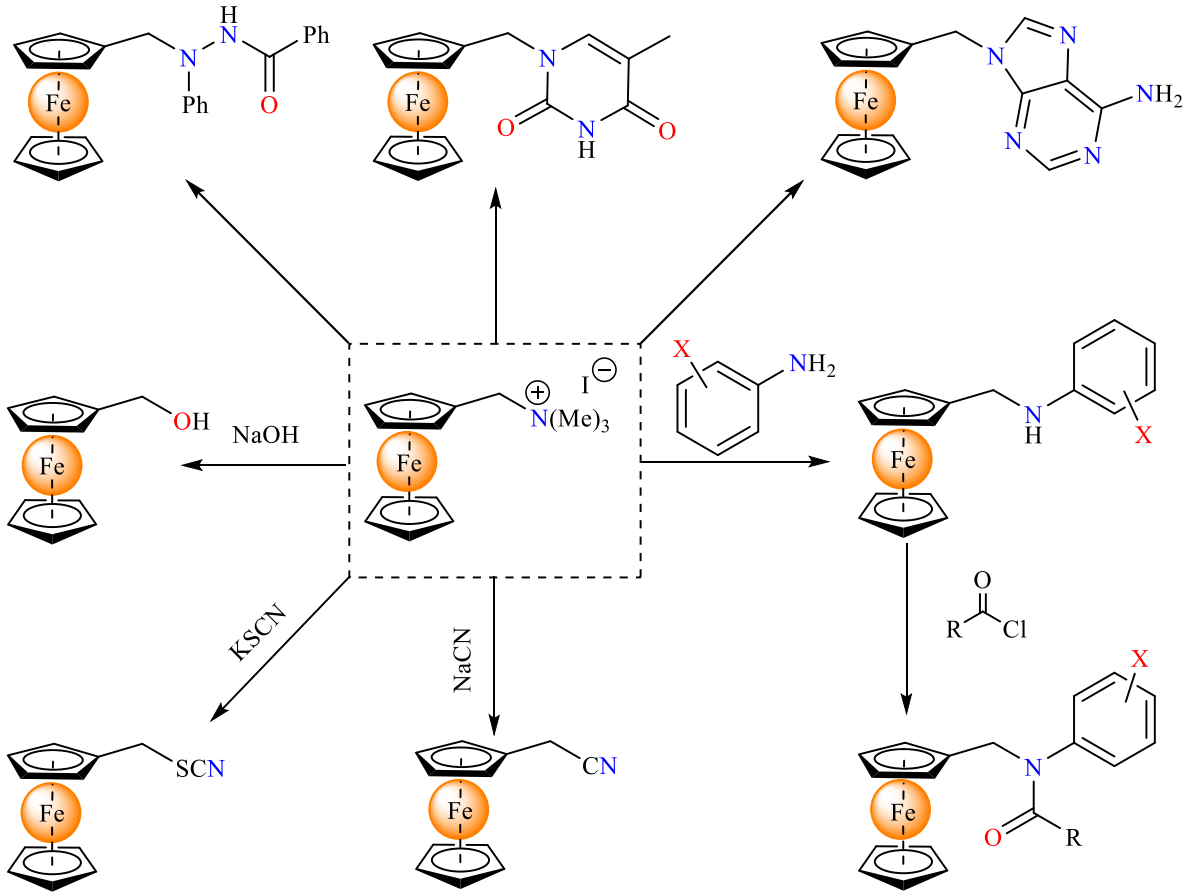

Scheme I.5. Reactivity of quaternary salt.

1.4. Practical Applications in Medicine:

Initially, the medicinal potential of ferrocene was not recognized upon its discovery. However, in recent years, both ferrocene and its derivatives have gained significant attention in medicinal chemistry. Their role as bioorganometallic compounds has also paved the way for the development of bioorganometallic chemistry [28]. The increasing interest in ferrocene-based compounds stems from their remarkable stability, non-toxic nature, and favorable redox properties [16].

This section focuses on ferrocenylmethyl derivatives that have been evaluated for biological activity evaluated through various techniques. The promising pharmacological effects observed in certain ferrocenylmethyl compounds have attracted considerable attention from researchers in drug discovery.

Several studies have demonstrated that certain ferrocene derivatives exhibit high biological activity both *in vitro* and *in vivo* against various diseases, including: malaria [29,30], cancer [31–35] fungal and bacterial infections [36–40], inflammation [41,42], and diabetes [43,44].

Chapter II: Biological Activities Overview

Introduction:

Inflammation, diabetes, and bacterial infections are interconnected health challenges, each exerting profound effects on the body's physiological processes. Chronic low-grade inflammation, often referred to as "metaflammation", plays a crucial role in the pathogenesis of both diabetes mellitus and susceptibility to bacterial infections [45]. Understanding the complex interactions between these conditions provides valuable insights into disease mechanisms and therapeutic strategies to mitigate their adverse effects.

Inflammation, characterized by the activation of immune cells and the release of pro-inflammatory cytokines, plays a dual role in diabetes mellitus. While acute inflammation is essential for infection defense and tissue repair, chronic inflammation contributes to insulin resistance, pancreatic beta-cell dysfunction, and endothelial dysfunction [46–48].

Diabetes mellitus, particularly type 2 diabetes mellitus (T2DM), significantly increases the risk of bacterial infections due to its multifaceted effects on the immune system and tissue integrity [49]. Hyperglycemia provides a favorable environment for bacterial growth, impairs immune responses, and compromises the skin and mucosal barriers, increasing vulnerability to infections. Common bacterial infections in diabetic patients include skin and soft tissue infections, urinary tract infections, respiratory tract infections, and diabetic foot infections, all of which are associated with prolonged hospitalizations and increased mortality rates [50,51].

Conversely, bacterial infections can worsen inflammation and disrupt glycemic control in diabetic patients, creating a vicious cycle of immune dysfunction and metabolic imbalance [52]. Bacterial pathogens activate innate immune responses, leading to the release of pro-inflammatory cytokines and chemokines that further amplify the inflammatory process. Moreover, bacterial toxins and virulence factors can directly impair insulin signaling pathways, worsening insulin resistance and contributing to hyperglycemia [53,54].

Understanding the dynamic relationship between inflammation, diabetes, and bacterial infections is essential for developing effective preventive and therapeutic strategies to reduce their negative impact on human health. Targeting inflammation through lifestyle modifications, pharmacotherapy, and immunomodulatory interventions represents a promising approach to improving outcomes for people with diabetes and reducing the burden of bacterial infections risks. Additionally, optimizing glycemic control and implementing infection prevention measures are

critical for minimizing the complications and improving overall health outcomes in this vulnerable population.

1. Inflammation Overview:

Inflammation is a vital immune response that protects to protect living organisms from harmful stimuli. It plays a crucial role in eliminating pathogens, repairing tissue damage, and maintaining homeostasis. Various factors can trigger inflammation, including [55,56]:

- Mechanical or physical factors: Such as radiation, electrical shock, extreme temperatures, and physical injury (e.g., puncture wounds or incisions).
- Chemical agents: Including corrosive substances like acids, bases, and other toxic mineral.
- Invasive microorganisms: Such as viruses, bacteria, parasites, fungi, and antigens.
- Vascular insufficiency: Ischemic tissue damage due to conditions like peripheral arterial disease (PAD), where narrowed arteries reduce blood flow to the legs, causing tissue damage and triggering an inflammatory response as the body attempts to heal the affected tissues [57].
- Dysregulated immune responses: Autoimmune diseases and allergic reactions. For example, in rheumatoid arthritis, the immune system mistakenly attacks joint tissues, leading to chronic inflammation, pain, and joint destruction over time [58].

This complex biological process (Figure II.1) involves the activation of immune cells and the release of inflammatory mediators, resulting in characteristic symptoms such as redness, swelling, heat, and pain [59]. Understanding the multifaceted nature of inflammation is essential for exploring its role in both normal physiology and various pathological conditions.

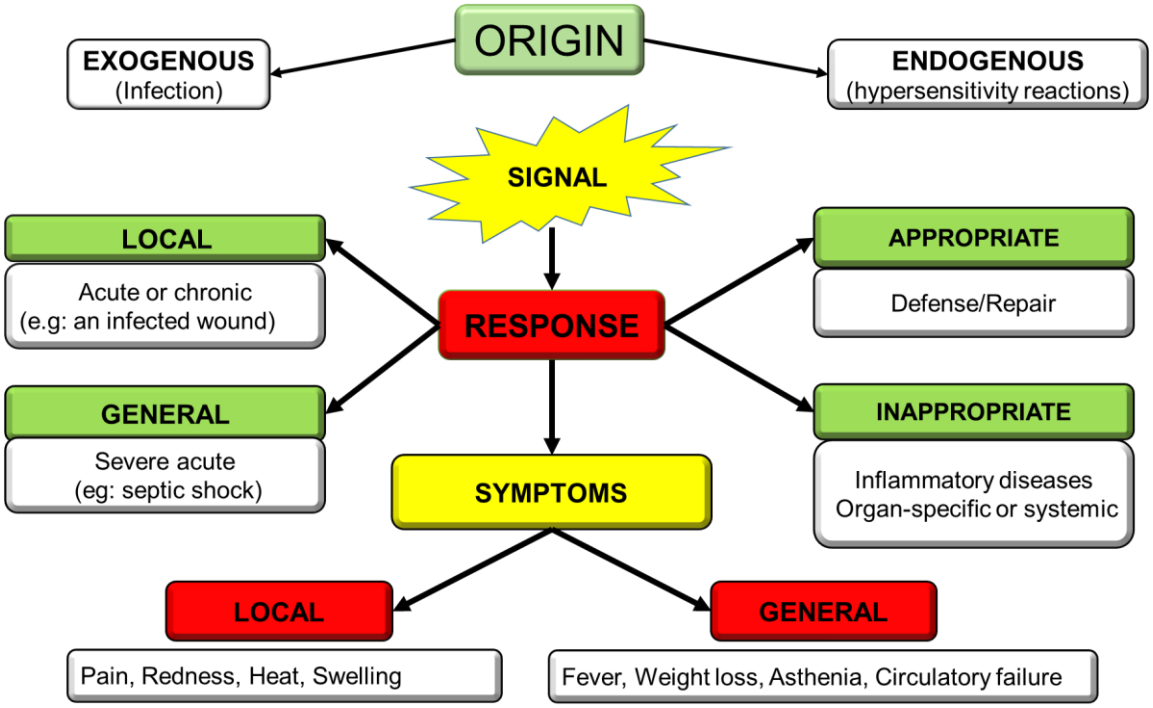

Figure II.1. Schematic representation of the inflammatory response.

1.1. Key Immune Cells Involved in Inflammation:

Resident sentinel cells are immune cells that remain in tissues, serving as the first line of defense by detecting and responding to pathogens or tissue damage. These include mast cells, dendritic cells, and macrophages, which are strategically located throughout various tissues to rapidly recognize potential threats and initiate immune responses. Additionally, platelets and lymphocytes also play crucial roles in the inflammatory process [60–62].

- Mast Cells are white blood cells found in connective tissues throughout the body. They play a key role in allergic reactions and help defend against pathogens by releasing histamine and other inflammatory substances [63].
- Dendritic Cells are antigen-presenting cells that specialize in capturing and processing antigens before presenting them to T cells. Found in the skin, mucosal tissues, and lymphoid organs, where they act as sentinels that detect pathogens and activate immune responses [64].
- Macrophages are large phagocytic cells distributed throughout body tissues. As part of the innate immune system, they engulf and digest pathogens, dead cells, and other debris while regulating inflammation and tissue repair [65].

- Platelets (Thrombocytes), are small cell fragments found in the blood that play a vital role in hemostasis. When blood vessels are damaged, platelets aggregate at the injury site, forming a clot to prevent further blood loss. Beyond clotting, they also contribute to immune responses by interacting with leukocytes and releasing inflammatory mediators [66].
- Lymphocytes are a type of white blood cell involved in the adaptive immune response, with two main types: B cells and T cells. B cells are responsible for producing antibodies that recognize and neutralize pathogens, while T cells perform various functions like directly killing infected cells, immune regulation, and activation of other immune cells [67].

1.2. Main Mediators of Inflammation:

1.1.1. Chemical mediators:

A wide range of endogenous chemical mediators, such as vasoactive amines (e.g., histamine and serotonin), peptides (e.g., bradykinin), and eicosanoids (e.g., leukotriene, thromboxane, prostacyclin, and prostaglandin), play a significant role in mediating the inflammatory process [68]. These mediators are released by various cells in response to infection, injury, or other inflammatory stimuli.

Among these, lipid mediators such as prostaglandins and leukotrienes, are derived from arachidonic acid, a polyunsaturated fatty acid present in membrane phospholipids. The release of arachidonic acid is catalyzed primarily by phospholipase A_2 type IV, an enzyme that facilitates the release of arachidonic acid from membrane lipids [69].

Following its release, arachidonic acid undergoes enzymatic metabolism via two major pathways (Figure II.2) [70]:

- The cyclooxygenase (COX) pathway, which generates prostaglandins and thromboxanes, key mediators involved in vasodilation, platelet aggregation, and the amplification of inflammatory signaling.
- The lipoxygenase (LOX) pathway, which produces leukotrienes and other bioactive lipids that contribute to immune cell chemotaxis, bronchoconstriction, and prolonged inflammatory responses.

These pathways are critical in modulating the intensity, duration, and resolution of inflammation, influencing both physiological and pathological immune responses.

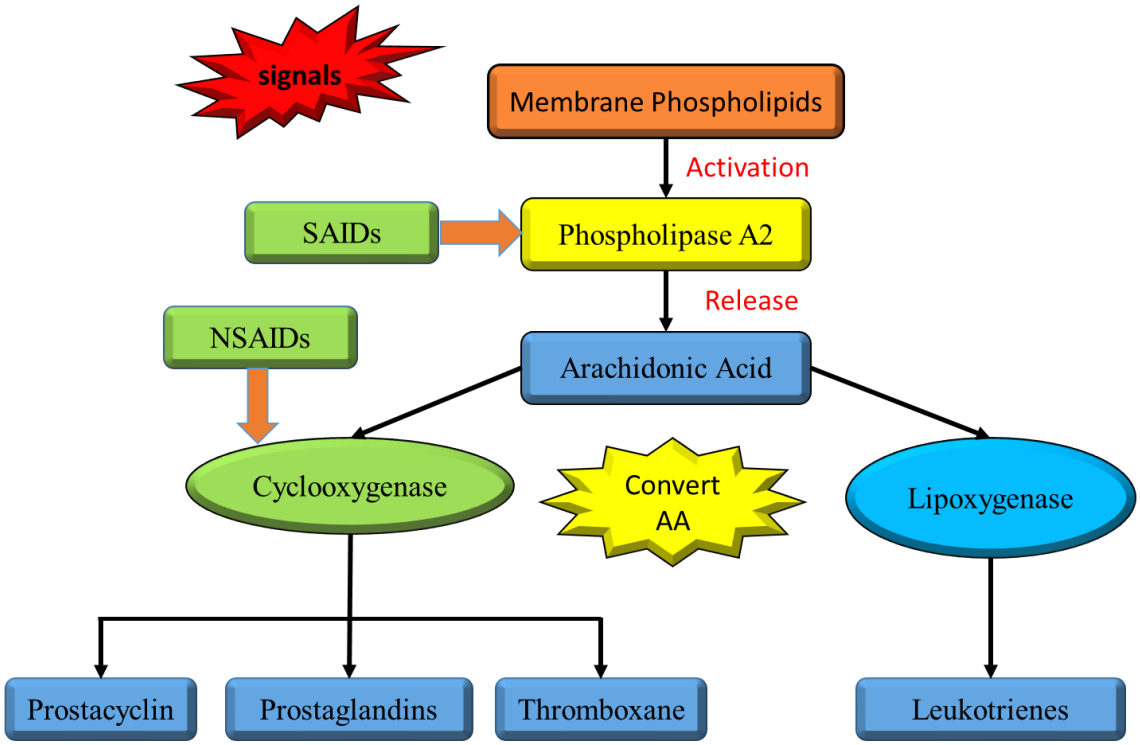

Figure II.2. Lipid mediators of inflammation and active site of anti-inflammatory agents.

1.1.2. Cytokines:

Cytokines are low molecular weight protein molecules that serve as soluble messengers within the immune system. They are produced by several cells of the immune system (Figure II.3), primarily by macrophages and mast cells, in response to various stimuli [71]. These molecules play crucial roles in regulating immune responses and inflammation by modulating the activities of immune cells and coordinating the body's defense mechanisms [72]. Cytokines include pro-inflammatory types such as tumor necrosis factor-alpha (TNF-α), interleukin-1 (IL-1), and interleukin-6 (IL-6), as well as anti-inflammatory cytokines like interleukin-10 (IL-10) [73,74]. The balance between these cytokines is crucial for maintaining homeostasis during inflammatory processes and ensuring an effective immune response.

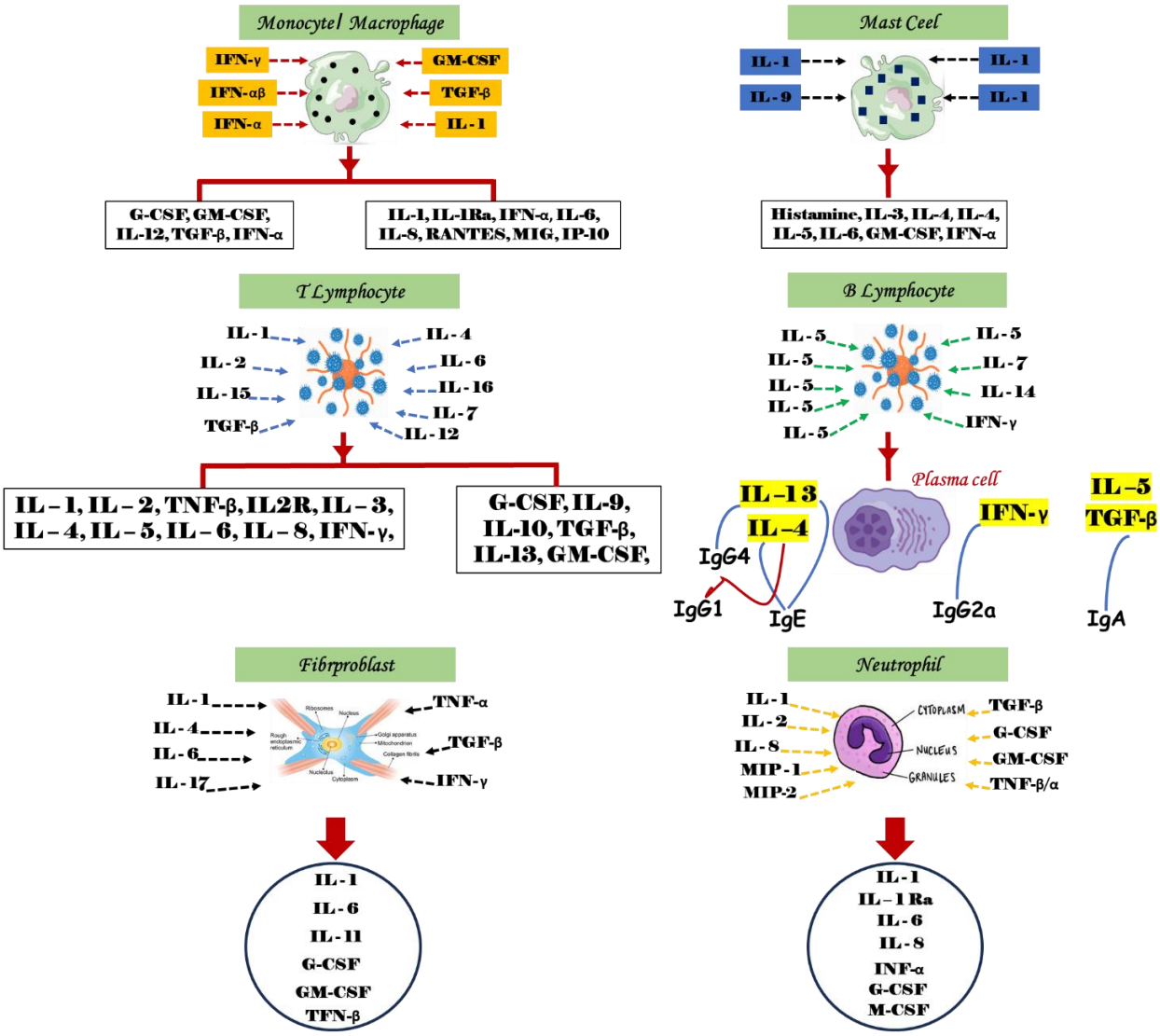

Figure II.3. Inflammatory cytokines, their main sources, and target cells.

1.3. Anti-Inflammatory:

1.1.3. Nonsteroidal anti-inflammatory drugs:

Nonsteroidal anti-inflammatory drugs (NSAIDs) are the primary medications utilized to reduce the harmful effects of inflammation. They inhibit the biosynthesis of prostaglandins from arachidonic acid by blocking COX enzymes. Common NSAIDs include diclofenac, ibuprofen, aspirin, and indomethacin [75].

1.1.4. Steroidal anti-inflammatory drugs:

Steroidal anti-inflammatory (SAIDs), also known as Corticosteroids, are synthetic derivatives of cortisol [76], They represent one of the most effective treatment for chronic inflammatory diseases such as asthma and rheumatoid arthritis. among them, we can mention: methylprednisolone, betamethasone, prednisone, and prednisolone [77,78].

These drugs exert their effects by acting like endogenous glucocorticoids, inhibiting phospholipase A_2 activity, and thereby preventing the release of arachidonic acid. This inhibition subsequently reduces the biosynthesis of prostaglandins and leukotrienes [79].

1.4. BSA and Inflammation Modulation:

Albumin, a vital globular protein, plays a fundamental role in regulating plasma pressure and maintaining nutritional balance by transporting a variety of endogenous and exogenous compounds within the bloodstream. The concentration of serum albumin in bodily fluids is closely linked to human health, serving as an indicator of nutritional status [80].

Bovine serum albumin (BSA), structurally similar to human serum albumin (HSA), is widely utilized as a model protein in various scientific researched. Due to its availability and comparable properties make BSA a practical substitute for HSA in experiments, offering valuable insights into albumin's biological functions and contributing to a deeper understanding of physiological processes and therapeutic applications [81,82]. Beyond its role in maintaining plasma colloid osmotic pressure, HSA has been found to possess crucial anti-inflammatory effects essential for vascular homeostasis [83,84]. Recent studies have identified novel anti-inflammatory properties of HSA, particularly in its interaction with vascular endothelial cells, further highlighting its significance in regulating vascular health [85].

Since HSA plays a crucial role in modulating immune responses and inflammation, its endogenous anti-inflammatory properties contribute significantly to vascular stability. Reduced HSA levels have been associated with increased inflammation in pathological conditions such as chronic liver disease and sepsis. Alterations in HSA function or availability, whether due to disease or certain medications, may disrupt immune homeostasis and compromise inflammatory control. However, the direct impact of pharmacological inhibition of HSA on immune regulation and inflammation remains incompletely understood and warrants further investigation [86–90].

2. Diabetes Mellitus Overview:

Diabetes mellitus is a chronic metabolic disorder with a multifactorial etiology, characterized by chronic hyperglycemia resulting from defect in insulin secretion and/or action. This deficiency leads to increased blood glucose levels, which in turn cause damage to carbohydrate, lipid, and protein metabolism [49]. The diagnosis of diabetes is typically involves measuring blood glucose levels in a fasting state. A diagnosis is confirmed when fasting blood glucose levels reach or exceed 1.26 g/L (7 mmol/L) and should be confirmed with repeated measurements [91].

Diabetes mellitus is classified into various types based its etiology and pathophysiology, with the two main types being type 1 and type 2 diabetes being the most prevalent forms [49].

2.1. Classification of Diabetes:

- **Type 1 diabetes (T1D)**, accounts for 5 to 10% of all diabetes cases, manifests when the immune system targets pancreatic β-cells (an autoimmune condition). This onset is often sudden and may be influenced by genetics and other unidentified factors. Individuals with T1D require daily insulin injections to manage their blood glucose levels [49].
- **Type 2 diabetes (T2D)**, comprising 90 to 95% of total diabetes cases. It happens when the body produces insulin but the cells demonstrate decreased sensitivity to it, a condition known as insulin resistance. Initially, the pancreas typically increases insulin secretion, but over time, beta-cell dysfunction impairs insulin production, resulting in chronic hyperglycemia. The combined effects of insulin resistance and insufficient insulin secretion lead to insufficient insulin activity, preventing the transfer of glucose from the bloodstream into the cells [49].

2.2. Pathophysiology:

Under normal physiological conditions, insulin regulates glucose metabolism by inhibiting hepatic glucose production, enhancing glucose uptake in skeletal muscle, and suppressing lipolysis (fatty acid) in adipose tissue. In T2D, various factors contribute to insulin resistance and beta-cell dysfunction, as shown in Figure II.4. Decreased insulin secretion also reduces the biological effect of insulin on target tissues. Impaired insulin signaling disrupts glucose uptake, and leads to elevated

free fatty acid levels which further exacerbate insulin resistance and beta-cell dysfunction. The resultant hyperglycemia creates a vicious cycle where chronic exposure to high glucose and fatty acid concentrations impact insulin secretion and action [92].

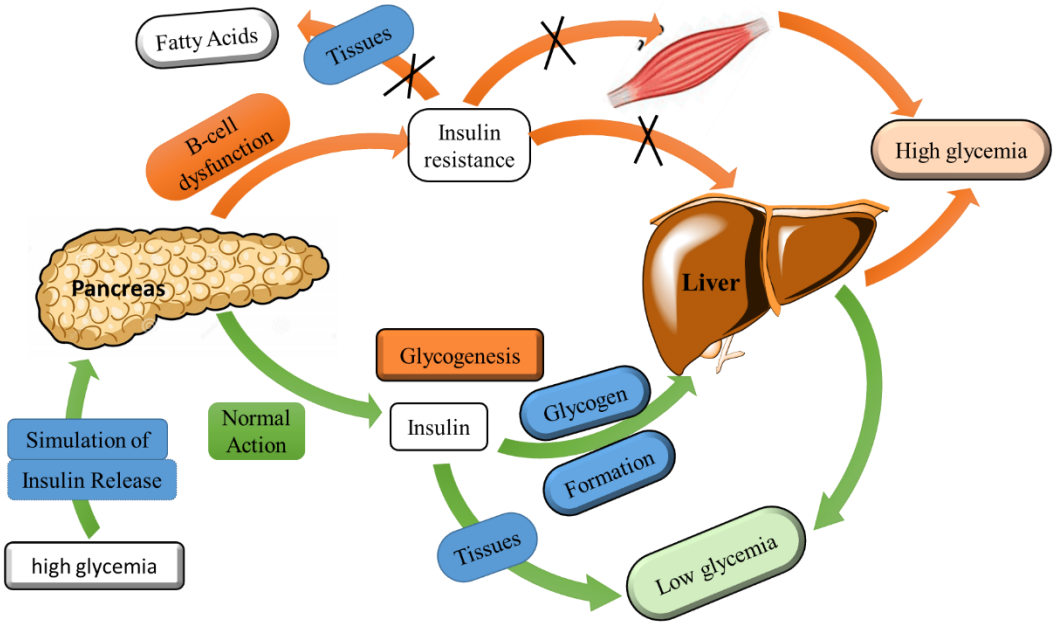

Figure II.4. Pathophysiology of hyperglycemia.

2.3. Diabetes Complications:

Irrespective of its type, diabetes can lead to serious complications that affect various organ systems and increasing the risk of morbidity and premature mortality. These complications include [93]:

- **Cardiovascular issues:** Individuals with diabetes have an elevated risk of developing cardiovascular diseases, including myocardial infarction (heart attack) and stroke due to the detrimental effects of hyperglycemia on blood vessels and overall cardiovascular health.
- **Kidney failure:** Diabetic nephropathy is a significant concern, where high blood sugar levels damage the kidneys over time, potentially leading to kidney failure.
- **Lower limb issues:** Peripheral neuropathy and poor circulation can result in leg amputations, as even minor injuries can become serious due to inadequate blood flow and nerve damage.

- **Vision loss:** Diabetic retinopathy is a leading cause of vision impairment and blindness, resulting from damage to the blood vessels in the retina.
- **Nerve damage:** Diabetic neuropathy affects various nerves throughout the body, leading to pain, tingling, and loss of sensation, particularly in peripheral nerves of the hands and feet.
- **Pregnancy complications:** poorly controlled diabetes during pregnancy can raise the risk of miscarriage, intrauterine fetal demise, and other complications, impacting both maternal and fetal health.

2.4. Diabetes Treatment:

Hyperglycemia in diabetes mellitus arises from an imbalance between the amount of insulin required to regulate metabolic processes and the amount of insulin secreted by β-cells. While insulin therapy is essential for T1D, dietary and lifestyle adjustments are the primary for managing T2D in its initial stages. However, when blood glucose levels remain uncontrolled despite diet, weight loss, exercise, and oral medications, insulin therapy may also become necessary for patients with T2D [94].

2.4.1. Non-pharmacological treatments:

The initial treatment for T2D focuses on lifestyle modifications, particularly a balanced diet and regular physical activity. Exercise plays a crucial role in improving muscle and joint functions, reducing fat deposits, especially in the abdominal region and can lead to weight loss. These physiological changes help combat insulin resistance and its associated complications [95].

2.4.2. Pharmacological treatments:

In the treatment of T1D, insulin therapy remains the most effective and available method to achieve glycemic control. Administered insulin acts as a substitute for endogenous insulin. Its primary effects on metabolic balance include stimulating uptake by peripheral tissues and activating metabolic pathways such as glycogen synthesis, glycolysis, lipogenesis, and protein synthesis. Furthermore, insulin aims to inhibit gluconeogenesis and lipolysis [96].

In the treatment of T2D, various oral pharmacological agents are available, classified into five major drug classes, these include sulfonylureas and benzoic acid derivatives (hypoglycemic agents), biguanides, α-glucosidase inhibitors, and thiazolidinediones (antihyperglycemic agents)

[97]. The primary differences among these drug classes lie in their mechanism of action, toxicity, and side effects [97].

- **Sulfonylureas**: These agents stimulate insulin secretion from pancreatic β-cells without affecting insulin synthesis, such as Glibenclamide (Figure II.5).

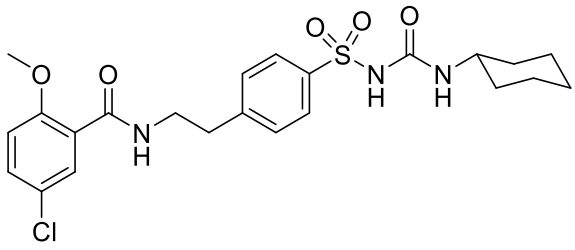

Figure II.5. Chemical structure of Glibenclamide.

- **Biguanides**: These drugs inhibit hepatic glucose production, reduces intestinal glucose absorption, and may affect lipid metabolism, such as Metformin (Figure II.6).

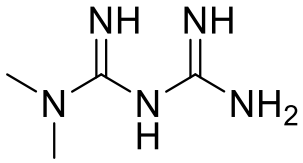

Figure II.6. Chemical structure of Metformin.

- **α-amylase and α-glucosidase inhibitors**: These drugs slow down the digestive absorption of complex carbohydrates by inhibiting key intestinal enzymes, improving postprandial glycemic control. Acarbose (Figure II.7) and Miglitol are well-known inhibitors acting on both α-amylase and α-glucosidase.

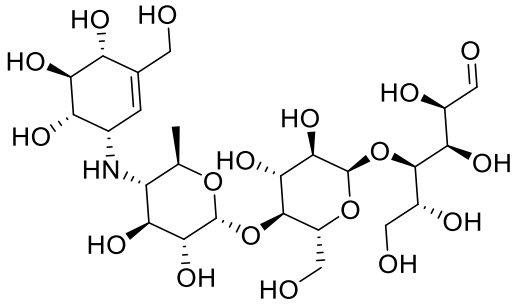

Figure II.7. Chemical structure of Acarbose.

- **Thiazolidinediones** (**Glitazones**): These molecules increase insulin sensitivity and improve β-cell function. like Rosiglitazone (Figure II.8).

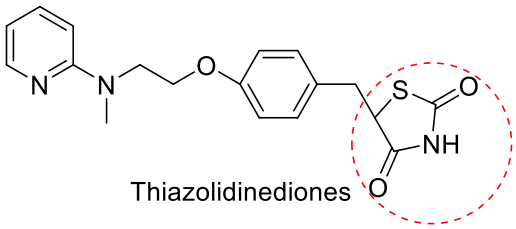

Figure II.8. Chemical structure of Rosiglitazone.

- **Glinides**: Similar sulfonylureas, these drugs stimulate rapid but short-lived insulin release from pancreatic β-cells, lasting for only one or two hours, such as Repaglinide (Figure II.9).

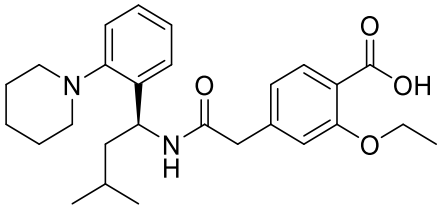

Figure II.9. Chemical structure of Repaglinide.

2.5. Mechanism of Action of α-Amylase and α-Glucosidase Inhibitors:

The digestion of complex carbohydrates involves α-amylase and α-glucosidase two essential enzymes responsible for breaking down polysaccharides into simpler sugars. Amylases, belong to the broader class of hydrolytic enzymes known as glycosidases, which break down the glycosidic bonds in starch into disaccharides that are subsequently converted into glucose (Figure II.10). Inhibiting these enzymes can delay the digestion of oligosaccharides and disaccharides, thereby slowing glucose absorption and reducing plasma glucose levels. This mechanism plays a crucial role in managing postprandial hyperglycemia [98,99].

Acarbose is a pseudo-tetrasaccharide of bacterial origin that acts as a competitive and reversible inhibitor of intestinal α-glucosidases and pancreatic α-amylase. It acts as a false substrate, delaying the hydrolysis of complex carbohydrates. This r prolongs the time glucose remains in the bloodstream, leading to a reduction in postprandial hyperglycemia without causing hyperinsulinemia [100–102].

However, these medications can cause liver disorders and other gastrointestinal symptoms such as diarrhea. Additionally, some of them may increase the incidence of kidney tumors, liver damage, and acute hepatitis [103].

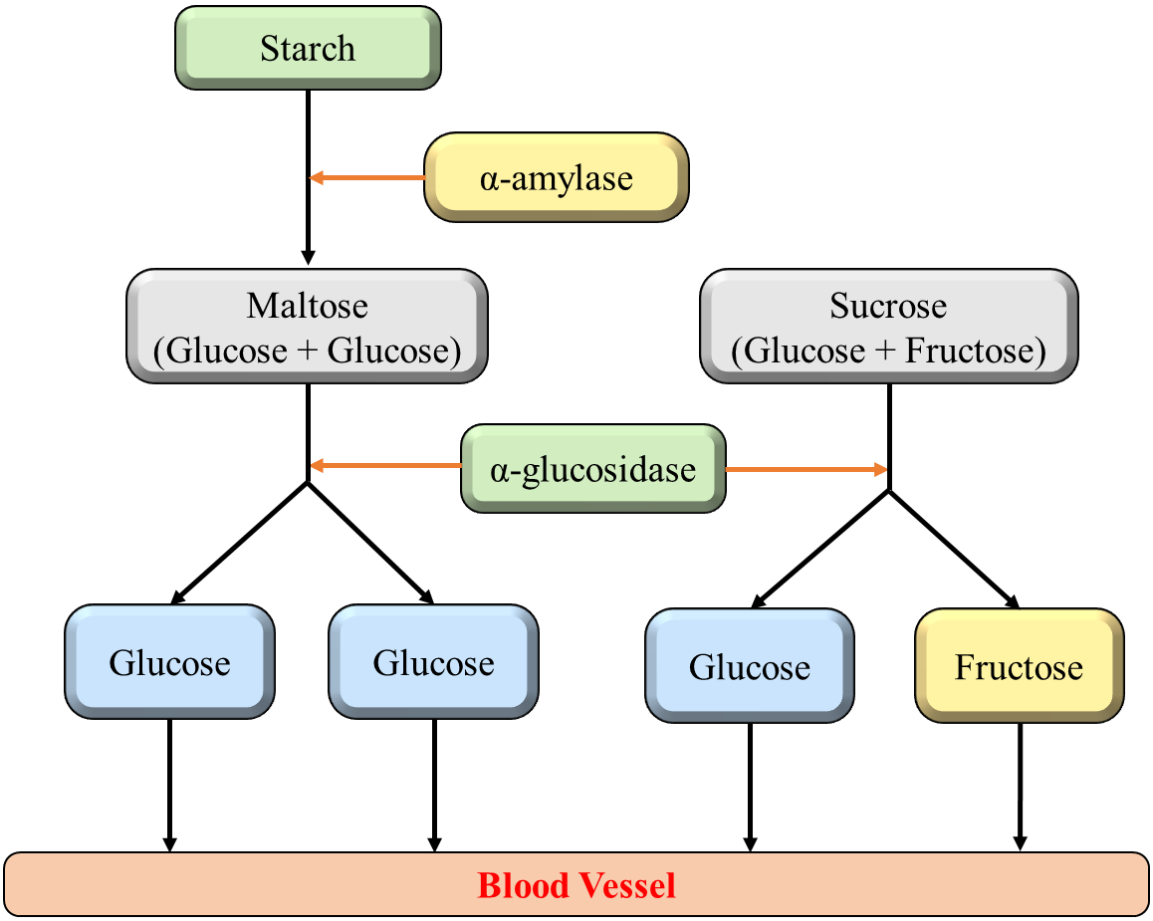

Figure II.10. Key stages in sugar digestion.

3. Bacteria Overview:

Bacteria are unicellular microorganisms classified as prokaryotes due to their lack of a nuclear membrane. They live in symbiosis with all living organisms, significantly influencing biological functions such as development, metabolism, reproduction, and especially immunity. In humans, commensal bacteria form the microbiota and are necessary and beneficial to our organism [104].

Bacteria are classified into Gram-positive and Gram-negative species, characterized by fundamental differences in their cell envelopes [105]. Morphologically, bacteria exhibit different shapes, including [106]:

- **Cocci**: Spherical-shaped bacteria.
- **Bacilli**: Rod-shaped bacteria.
- **Vibrios**: Curved-shaped bacteria.
- **Spirochetes**: Spiral-shaped bacteria.

Their cellular structures can be studied in detail under electron microscopy, which reveals significant differences between these bacterial types [106]. Despite having a similar internal cytoplasmic membrane, their external envelopes are significantly different. A key structural component common to all bacteria is peptidoglycan (PG), a critical polymer that provides structural strength. However, Gram-positive bacteria are monodermic, meaning they have a single membrane surrounded by a thick peptidoglycan layer, which is enriched with lipoteichoic acid (LTA) and wall teichoic acid (WTA), contributing to cell wall stability and interactions with the environment (Figure II.11). In contrast, Gram-negative bacteria are didermic, with a thin peptidoglycan layer sandwiched between an inner cytoplasmic membrane and an outer membrane. This outer membrane contains lipopolysaccharide (LPS), a crucial component that plays a key role in bacterial pathogenicity and immune system interactions (Figure II.11) [105,107,108].

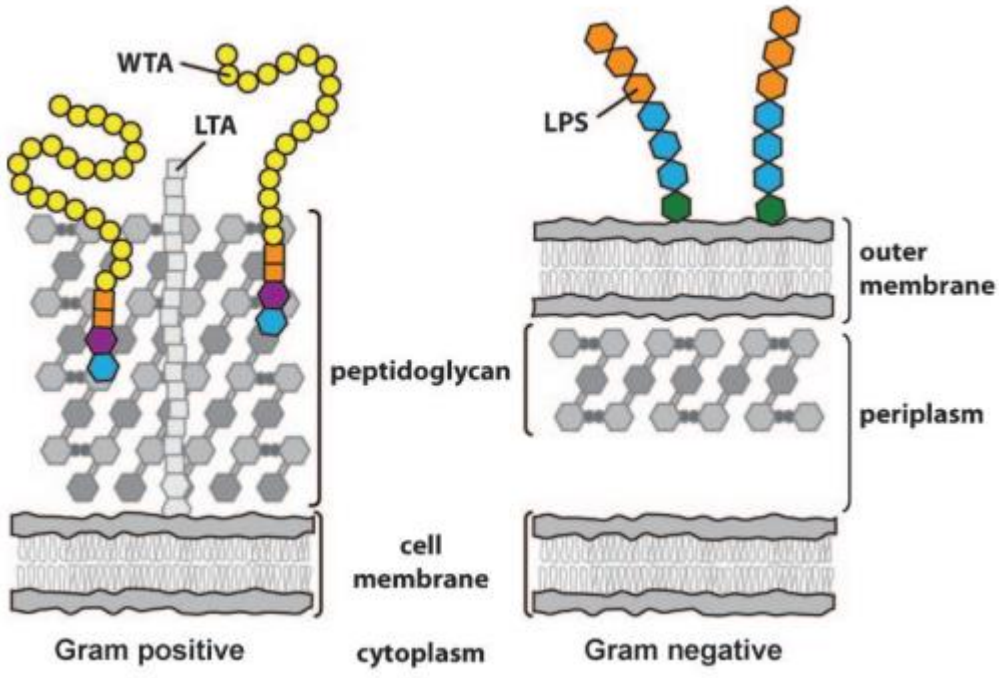

Figure II.11. Simplified representation of cell envelopes in Gram-positive and Gram-negative bacteria [109].

Peptidoglycan: Structure and Function

Peptidoglycan serves as a rigid exoskeleton, determining bacterial shape and provides essential mechanical protection against osmotic pressure. This structure is indispensable for bacterial survival, especially in various environmental conditions that could otherwise cause cellular lysis. Structurally, peptidoglycan is a heteropolymer made of disaccharide chains linked

together by oligopeptide side chains [105]. These disaccharides consist of alternating residues of N-acetylmuramic acid and N-acetylglucosamine linked by glycosidic bonds [110].

While many bacterial species contribute positively to host health, certain pathogenic bacteria are responsible for serious infectious diseases, some of which can be life-threatening to the host. The virulence of pathogenic bacteria is determined by several factors, including:

- **Invasive potential**, the bacterium's ability to penetrate and spread within host tissues.
- **Toxin production**, the secretion of harmful molecules that damage host cells and disrupt physiological processes.
- **Reproductive capacity**, which dictates how rapidly a bacterium can multiply within the host.

These traits are influenced by both bacterial and the host genetic composition. Over time, evolutionary pressures can favor certain bacterial strains, allowing them to survive, reproduce, and potentially become more virulent [111,112]. Antibiotics remain an effective treatment for most bacterial infections, targeting essential processes like cell wall synthesis, protein production, or DNA replication to neutralize pathogens. However, the rise of antibiotic resistance underscores the urgent need for responsible antibiotic use and the development of novel antimicrobial strategies [111,112].

3.1. Antibiotics and Their Modes of Action:

Antibiotics are active substances produced by microorganisms or derived through semi-synthetic or synthetic derivatives. They function by either destroying bacteria or inhibiting their growth [113]. Due to their high specificity, they are effective even at low concentrations [114–117]. Based on their mode of action, antibiotics are classified as either:

- Bacteriostatic: which inhibit the growth and replication of bacteria (e.g., tetracyclines, phenicols, macrolides) [118].
- Bactericidal: which actively destroy bacterial cells (e.g., beta-lactams, aminoglycosides, polypeptides) [118].

Each antibiotic has a specific spectrum of activity, determining the bacterial species it affects. A broad-spectrum antibiotic is effective against a wide range of bacterial species, whereas a narrow-spectrum antibiotic targets specific microbe. The spectrum and mode of action of antibiotics vary widely, contributing to their therapeutic uses [119–121].

The various families of antibiotics are classified based on their primary mechanism of action (Figure II.12) [119–121]:

- **Inhibitors of bacterial cell wall synthesis:** Antibiotics like beta-lactams (e.g., penicillin) prevent the formation of peptidoglycan, weakening the bacterial cell wall and causing cell lysis.
- **Inhibitors of protein synthesis:** Some antibiotics, such as tetracyclines and macrolides, bind to bacterial ribosomes, inhibiting protein production, which is vital for bacterial growth.
- **Inhibition of nucleic acid (RNA/DNA) synthesis:** Quinolones and rifamycins block bacterial DNA replication or RNA transcription, preventing cell proliferation.
- **Inhibitors of Peptidoglycan Synthesis:** Glycopeptide (e.g., vancomycin) disrupt peptidoglycan cross-linking, weakening the bacterial cell wall.
- **Complex or unknown mechanisms:** Some antibiotics exhibit unique or incompletely elucidated mechanisms of action.

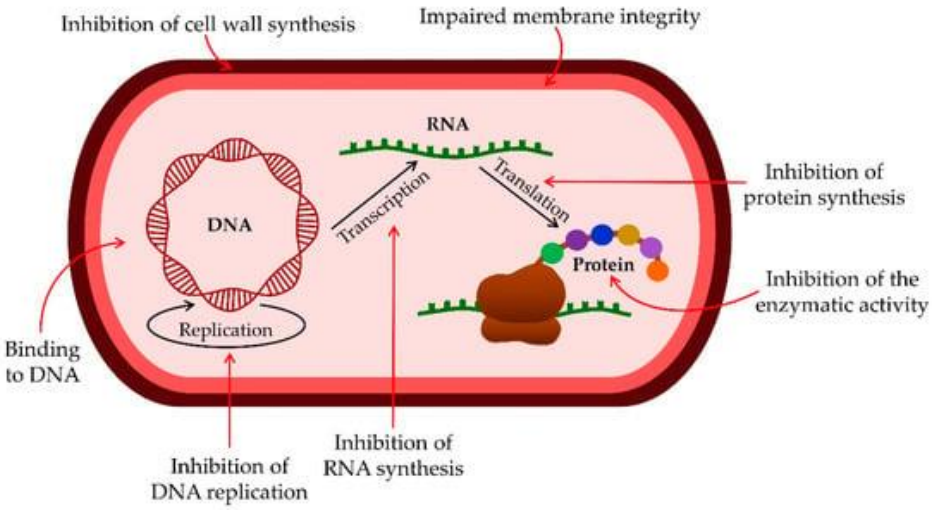

Figure II.12. Antibiotics' modes of action [120].

The excessive and inappropriate use of antibiotics has led to two major concerns: side effects associated with their use and the development of antibiotic resistance in certain microbial populations.

Like any medication, antibiotics carry the risk of drug interactions, which can either decrease or amplify the effects of other treatments, along with the risk of unwanted side effects. These risks depend on the chemical family (e.g., penicillins, cephalosporins, fluoroquinolones, and

macrolides) or the molecule itself (e.g., moxifloxacin, erythromycin, amoxicillin, and vancomycin) [122,123].

The side effects can affect multiple systems in the body, particularly on the digestive and renal systems, leading to conditions such as diarrhea, nausea, or kidney impairment. In some cases, these side effects may be reversible, while in others, they could have long-term consequences. Additionally, antibiotic resistance complicates treatment strategies, making previously manageable infections harder to control and leading to the search for alternative therapies [122,123].

3.2. Antibiotic Resistance:

Bacterial resistance refers to the ability of bacteria to prevent an antibiotic from acting against them. As a result, standard treatments become ineffective, which allows infections to persist and potentially spread [124]. The use of antibiotics to treat an actual or suspected infection applies selective pressure on bacteria, forcing them to either adapt or die [125,126]. The surviving bacteria may carry drug resistance genes, which they can transfer to other strains within their genus and species or even to unrelated species, leading to the widespread development of resistance [125,126].

Types of Bacterial Resistance:

- **Natural resistance:** Occurs when all strains of a particular species are inherently resistant to a specific antibiotic. For example, Gram-negative bacteria are naturally resistant to hydrophobic antibiotics because these molecules struggle to penetrate their outer membrane. Similarly, mycoplasmas, which lack a cell wall, are resistant to β-lactam, as this class of drugs targets peptidoglycan synthesis [127].
- **Acquired resistance:** Acquired bacterial resistance develops in strains of a species that were previously susceptible to an antibiotic. It involves the acquisition of a genetic factor, either by chromosomal mutations or the horizontal transfer of resistance genes from other microorganisms. As a result, bacteria that were once easily controlled by antibiotics become resistant, posing significant challenges to treatment [128].

3.3. Mechanisms of Bacterial Resistance to Antibiotics:

Beyond natural resistances, bacteria develop additional resistance mechanisms in response to the selection pressure exerted by antibiotic use. These resistances involve biochemical

mechanisms with genetic modifications and can be transmitted to other bacteria, accelerating the spread of resistance [129].

Major Mechanisms of Resistance (Figure II.13):

- **Enzymatic inactivation:** This is the most common mechanism and affects all major antibiotic classes. Bacteria produce enzymes that either modify or hydrolyze the antibiotic, rendering them inactive before they reach their target [130].

  Example: β-lactamases, which break down β-lactam antibiotics (e.g., penicillins, cephalosporins).

- **Modification of Antibiotic Penetration:** Common in Gram-negative bacteria, this resistance mechanism results from structural changes in the bacterial cell wall or membrane, which reduce antibiotic entry. This effectively reduces the drug's concentration at its target, diminishing its effectiveness [131].

  Example: Alterations in porins (membrane proteins) limit the penetration of β-lactams, aminoglycosides, and fluoroquinolones.

- **Active efflux pumps:** Bacteria equipped with efflux pumps can actively expel antibiotics from their cells as soon as they enter. These pumps are specific proteins that transport harmful molecules out of the bacterial cell, leading to reduced intracellular concentrations of the antibiotic and decreased effectiveness [132].

  Example: Multidrug efflux pumps in *Pseudomonas aeruginosa* and *Escherichia coli* can expel multiple antibiotic classes.

- **Target Modification or Substitution:** Antibiotic generally needs to bind to its target to exert its effect. If the bacterium modifies the target structure or substitutes it with a resistant form, the antibiotic can no longer recognize or bind effectively. This resistance mechanism often extends to an entire family of antibiotics, affecting multiple drugs that target the same pathway.[133].

  Example: Methicillin-resistant Staphylococcus aureus modifies penicillin-binding proteins, reducing β-lactam efficacy.

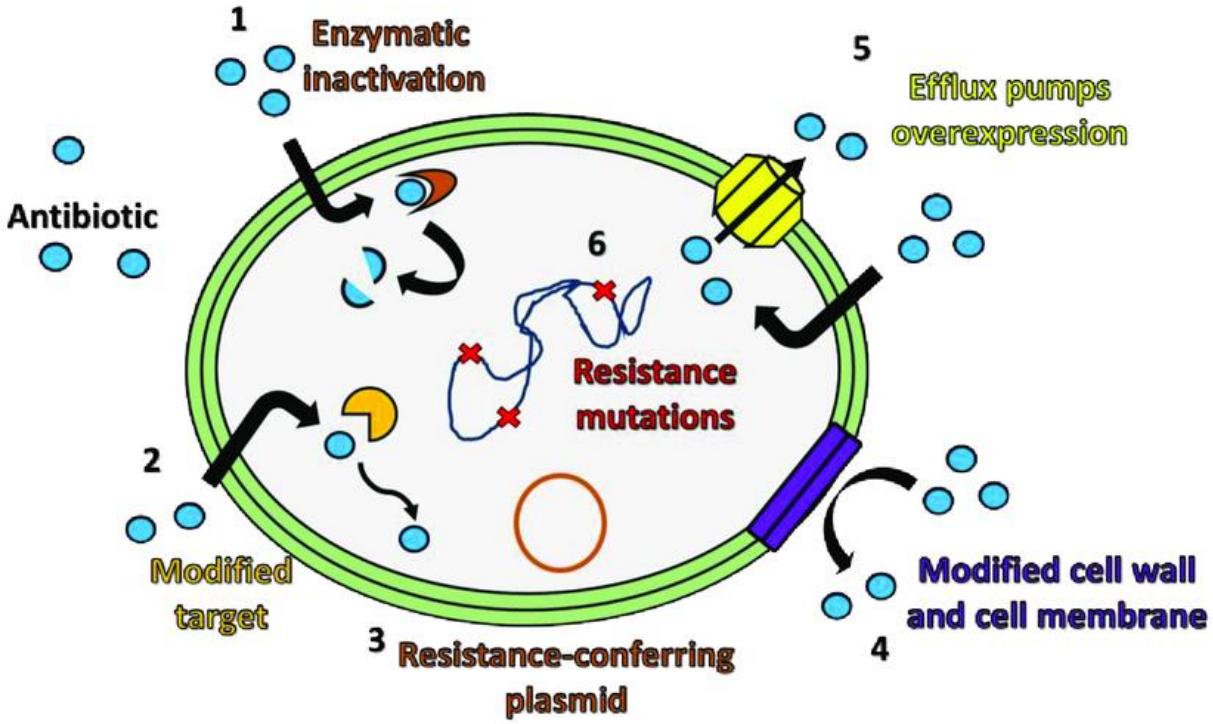

Figure II.13. Mechanisms of bacterial resistance [134].

3.4. Description of the Studied Bacteria:

- **Escherichia coli:**

Escherichia coli (E. coli) is Gram-negative, facultative anaerobic coccobacillus, generally motile due to the presence of flagella. commonly found in the intestines of humans and animals, where most strains play an essential role in the digestion. *E. coli* ferments glucose and lactose with gas production and can be transmitted through contaminated food or water, causing mild gastroenteritis or more severe symptoms like abdominal cramps, diarrhea, and vomiting [135].

- **Pseudomonas aeruginosa:**

Pseudomonas aeruginosa (*P. aeruginosa*) is a Gram-negative, obligate aerobic rod-shaped bacterium, mobile due to a mono polar flagellum. It is commonly found in soil, water, and the digestive tracts, where it exists as a commensal organism. However, it is an opportunistic pathogen, causing infections mainly in immunocompromised individuals or those with underlying health conditions. *P. aeruginosa* can cause a wide range of infections, including respiratory infections, urinary tract infections, bloodstream infections, and wound infections [136].

- **Staphylococcus aureus:**

Staphylococcus aureus (*S. aureus*) is a Gram-positive non-motile, facultative anaerobic coccus, typically spherical in shape, commonly found on the skin and mucous membranes of humans and animals. While it is part of the normal microbiota, it is also a major opportunistic pathogen, responsible for a wide range of infections including, osteomyelitis (bone infection, particularly in children), arthritis (joint infection), septicemia (life-threatening bloodstream infections), and pneumonia (often involving multiple small abscesses in both lungs) [137].

- **Klebsiella pneumoniae:**

Klebsiella pneumoniae (*K. pneumoniae*) is a Gram-negative, non-motile, facultative anaerobic bacterium, commonly found in the environment (soil and water) and in the gastrointestinal tract of humans and animals. It is an important nosocomial pathogen, frequently associated with hospital-acquired infections, such as pneumonia, urinary tract infections, bloodstream infections, and wound infections [138].

The selected bacterial strains (*E. coli*, *P. aeruginosa*, *S. aureus*, and *K. pneumoniae*) were chosen because they represent clinically relevant and diverse pathogenic species that are frequently implicated in human infections and exhibit different resistance profiles.

- *E. coli* and *K. pneumoniae* are Enterobacteriaceae commonly involved in gastrointestinal and urinary tract infections.
- *P. aeruginosa* is an opportunistic pathogen known for its intrinsic resistance and relevance in hospital-acquired infections.
- *S. aureus* represents Gram-positive pathogens, allowing comparison with the Gram-negative group.

This selection ensures a broad-spectrum evaluation of antibacterial activity against both Gram-positive and Gram-negative bacteria, covering clinical diversity and resistance potential.

Reference

[1] T.J. KEALY, P.L. PAUSON, A New Type of Organo-Iron Compound, Nature 168 (1951) 1039–1040. https://doi.org/10.1038/1681039b0.

[2] G. Wilkinson, M. Rosenblum, M.C. Whiting, R.B. Woodward, THE STRUCTURE OF IRON BIS-CYCLOPENTADIENYL, J Am Chem Soc 74 (1952) 2125–2126. https://doi.org/10.1021/ja01128a527.

[3] E.O. Fischer, W. Pfab, Cyclopentadien-Metallkomplexe, ein neuer Typ metallorganischer Verbindungen, Zeitschrift Für Naturforschung B 7 (1952) 377–379. https://doi.org/10.1515/znb-1952-0701.

[4] W. Pfab, E.O. Fischer, Zur Kristallstruktur der Di-cyclopentadienyl-verbindungen des zweiwertigen Eisens, Kobalts und Nickels, Z Anorg Allg Chem 274 (1953) 316–322. https://doi.org/10.1002/zaac.19532740603.

[5] P.F. Eiland, R. Pepinsky, X-RAY EXAMINATION OF IRON BISCYCLOPENTADIENYL, J Am Chem Soc 74 (1952) 4971–4971. https://doi.org/10.1021/ja01139a527.

[6] T.P. Gryaznova, S.A. Katsyuba, V.A. Milyukov, O.G. Sinyashin, DFT study of substitution effect on the geometry, IR spectra, spin state and energetic stability of the ferrocenes and their pentaphospholyl analogues, J Organomet Chem 695 (2010) 2586–2595. https://doi.org/10.1016/j.jorganchem.2010.08.031.

[7] J.D. DUNITZ, L.E. ORGEL, Bis-cyclopentadienyl Iron: a Molecular Sandwich, Nature 171 (1953) 121–122. https://doi.org/10.1038/171121a0.

[8] J.D. Dunitz, L.E. Orgel, A. Rich, The crystal structure of ferrocene, Acta Crystallogr 9 (1956) 373–375. https://doi.org/10.1107/S0365110X56001091.

[9] A. Haaland, J. Lusztyk, D.P. Novak, J. Brunvoll, K.B. Starowieyski, Molecular structures of dicyclopentadienylmagnesium and dicyclopentadienylchromium by gas-phase electron diffraction, J Chem Soc Chem Commun (1974) 54. https://doi.org/10.1039/c39740000054.

[10] A. Haaland, J.E. Nilsson, T. Olson, T. Norin, The Determination of Barriers to Internal Rotation by Means of Electron Diffraction. Ferrocene and Ruthenocene., Acta Chem Scand 22 (1968) 2653–2670. https://doi.org/10.3891/acta.chem.scand.22-2653.

[11] R.K. Bohn, A. Haaland, On the molecular structure of ferrocene, Fe(C5H5)2, J Organomet Chem 5 (1966) 470–476. https://doi.org/10.1016/S0022-328X(00)82382-7.

[12] N. Mohammadi, A. Ganesan, C.T. Chantler, F. Wang, Differentiation of ferrocene D5d and D5h conformers using IR spectroscopy, J Organomet Chem 713 (2012) 51–59. https://doi.org/10.1016/j.jorganchem.2012.04.009.

[13] A. Bhattacharjee, A. Rooj, D. Roy, M. Roy, Thermal Decomposition Study of Ferrocene [(C5H5)2Fe], Journal of Experimental Physics 2014 (2014) 1–8. https://doi.org/10.1155/2014/513268.

[14] M. Dąbrowski, B. Misterkiewicz, A. Sporzyński, Solubilities of Substituted Ferrocenes in Organic Solvents, J Chem Eng Data 46 (2001) 1627–1631. https://doi.org/10.1021/je010197q.

[15] T. Okabe, K. Nakazaki, T. Igaue, N. Nakamura, B. Donnio, D. Guillon, J.-L. Gallani, Synthesis and physical properties of ferrocene derivatives. XXI. Crystal structure of a liquid crystalline ferrocene derivative, 1,1'-bis[3-[4-(4-methoxyphenoxycarbonyl)phenoxy]propyloxycarbonyl]ferrocene, J Appl Crystallogr 42 (2009) 63–68. https://doi.org/10.1107/S0021889808042039.

[16] M.F.R. Fouda, M.M. Abd-Elzaher, R.A. Abdelsamaia, A.A. Labib, On the medicinal chemistry of ferrocene, Appl Organomet Chem 21 (2007) 613–625. https://doi.org/10.1002/aoc.1202.

[17] N.G. Connelly, W.E. Geiger, Chemical Redox Agents for Organometallic Chemistry, Chem Rev 96 (1996) 877–910. https://doi.org/10.1021/cr940053x.

[18] G.D. Broadhead, J.M. Osgerby, P.L. Pauson, 127. Ferrocene derivatives. Part V. Ferrocenealdehyde, Journal of the Chemical Society (Resumed) (1958) 650. https://doi.org/10.1039/jr9580000650.

[19] D.M. Knight, R.C. Schlitt, Assay of Alkyl and Hydroxyalkyl Ferrocenes by Potentiometric Titration., Anal Chem 37 (1965) 470–471. https://doi.org/10.1021/ac60223a008.

[20] G.L.K. Hoh, W.E. McEwen, J. Kleinberg, Substituent Effects in the Chronopotentiometric Oxidation of Ferrocenes, J Am Chem Soc 83 (1961) 3949–3953. https://doi.org/10.1021/ja01480a005.

[21] A.N. Nesmeyanov, V.A. Sazonova, V.N. Drozd, Hydroxyferrocene, Tetrahedron Lett 1 (1959) 13–15. https://doi.org/10.1016/S0040-4039(00)91032-3.

[22] J.M. Osgerby, P.L. Pauson, 128. Ferrocene derivatives. Part VI. DL-ferrocenylalanine, Journal of the Chemical Society (Resumed) (1958) 656. https://doi.org/10.1039/jr9580000656.

[23] G. Gasser, A.J. Fischmann, C.M. Forsyth, L. Spiccia, Products of hydrolysis of (ferrocenylmethyl)trimethylammonium iodide: Synthesis of hydroxymethylferrocene and bis(ferrocenylmethyl) ether, J Organomet Chem 692 (2007) 3835–3840. https://doi.org/10.1016/j.jorganchem.2007.05.020.

[24] E. Lanez, L. Bechki, T. Lanez, Ferrocenylmethylnucleobases: Synthesis, dft calculations, electrochemical and spectroscopic characterisation, Chemistry and Chemical Technology 14 (2020) 146–153. https://doi.org/10.23939/chcht14.02.146.

[25] S.R. Gupta, P. Mourya, M.M. Singh, V.P. Singh, Synthesis, structural, electrochemical and corrosion inhibition properties of two new ferrocene Schiff bases derived from hydrazides, J Organomet Chem 767 (2014) 136–143. https://doi.org/10.1016/j.jorganchem.2014.05.038.

[26] P.N. Kelly, A. Prêtre, S. Devoy, I. O'Rielly, R. Devery, A. Goel, J.F. Gallagher, A.J. Lough, P.T.M. Kenny, Synthesis, structural characterisation and biological activity of novel N-(ferrocenylmethyl)benzene-carboxamide derivatives, J Organomet Chem 692 (2007) 1327–1331. https://doi.org/10.1016/j.jorganchem.2006.11.012.

[27] A. Kedadra, T. Lanez, E. Lanez, H. Hemmami, M. Henni, Synthesis and antioxidant activity of six novel N-ferrocenylmethyl-N-(nitrophenyl)- and -N-(cyanophenyl)-acetamides: Cyclic voltammetry and molecular docking studies, Journal of Electrochemical Science and Engineering 12 (2022) 293–304. https://doi.org/10.5599/jese.1162.

[28] M. Patra, G. Gasser, The medicinal chemistry of ferrocene and its derivatives, Nat Rev Chem 1 (2017) 0066. https://doi.org/10.1038/s41570-017-0066.

[29] W.A. Wani, E. Jameel, U. Baig, S. Mumtazuddin, L.T. Hun, Ferroquine and its derivatives: New generation of antimalarial agents, Eur J Med Chem 101 (2015) 534–551. https://doi.org/10.1016/j.ejmech.2015.07.009.

[30] T. Itoh, S. Shirakami, N. Ishida, Y. Yamashita, T. Yoshida, H.S. Kim, Y. Wataya, Synthesis of novel ferrocenyl sugars and their antimalarial activities., Bioorg Med Chem Lett 10 (2000) 1657–9. https://doi.org/10.1016/s0960-894x(00)00313-9.

[31] C. Ornelas, Application of ferrocene and its derivatives in cancer research, New Journal of Chemistry 35 (2011) 1973. https://doi.org/10.1039/c1nj20172g.

[32] B. Lal, A. Badshah, A.A. Altaf, M.N. Tahir, S. Ullah, F. Huq, Synthesis, characterization and antitumor activity of new ferrocene incorporated N,N′-disubstituted thioureas, Dalton Transactions 41 (2012) 14643–14650. https://doi.org/10.1039/c2dt31570j.

[33] X.-F. Huang, L.-Z. Wang, L. Tang, Y.-X. Lu, F. Wang, G.-Q. Song, B.-F. Ruan, Synthesis, characterization and antitumor activity of novel ferrocene derivatives containing pyrazolyl-moiety, J Organomet Chem 749 (2014) 157–162. https://doi.org/10.1016/j.jorganchem.2013.08.043.

[34] J.-N. Wei, Z.-D. Jia, Y.-Q. Zhou, P.-H. Chen, B. Li, N. Zhang, X.-Q. Hao, Y. Xu, B. Zhang, Synthesis, characterization and antitumor activity of novel ferrocene-coumarin conjugates, J Organomet Chem 902 (2019) 120968. https://doi.org/10.1016/j.jorganchem.2019.120968.

[35] A. Adaika, T. Lanez, E. Lanez, in Vitro and in Silico Evaluation of Anticancer Activity of N,N-Dimethylaminomethylferrocene, Journal of Fundamental and Applied Sciences 11 (2019) 748–768. https://jfas.info/index.php/JFAS/article/view/289.

[36] S. Benabdesselam, H. Izza, T. Lanez, E.K. Guechi, Synthesis, antioxidant and antibacterial activities of 3-nitrophenyl ferrocene, IOP Conf Ser Mater Sci Eng 323 (2018) 012007. https://doi.org/10.1088/1757-899X/323/1/012007.

[37] C. Biot, N. François, L. Maciejewski, J. Brocard, D. Poulain, Synthesis and antifungal activity of a ferrocene-fluconazole analogue., Bioorg Med Chem Lett 10 (2000) 839–41. https://doi.org/10.1016/s0960-894x(00)00120-7.

[38] B. Long, C. He, Y. Yang, J. Xiang, Synthesis, characterization and antibacterial activities of some new ferrocene-containing penems, Eur J Med Chem 45 (2010) 1181–1188. https://doi.org/10.1016/j.ejmech.2009.12.045.

[39] S. Ali, A.A. Altaf, A. Badshah, Imtiaz-Ud-Din, B. Lal, S. Kamal, S. Ullah, DNA interaction, antibacterial and antifungal studies of 3-nitrophenylferrocene, Journal of the Chemical Society of Pakistan 35 (2013) 922–928.

[40] E.M. Njogu, B. Omondi, V.O. Nyamori, Synthesis, physical and antimicrobial studies of ferrocenyl-N-(pyridinylmethylene)anilines and ferrocenyl-N-(pyridinylmethyl)anilines, South African Journal of Chemistry 69 (2016) 51–66. https://doi.org/10.17159/0379-4350/2016/v69a7.

[41] W.-Y. Guo, L.-Z. Chen, B.-N. Shen, X.-H. Liu, G.-P. Tai, Q.-S. Li, L. Gao, B.-F. Ruan, Synthesis and in vitro and in vivo anti-inflammatory activity of novel 4-ferrocenylchroman-2-one derivatives, J Enzyme Inhib Med Chem 34 (2019) 1678–1689. https://doi.org/10.1080/14756366.2019.1664499.

[42] B. Ruan, J. Li, Q. Guo, M. Zhang, Z. Pei, Y. Hu, Synthesis, Characterization, and in vitro Anti-Inflammatory Activity of Novel Ferrocenyl(Piperazine-1-Yl)Methanone-based

Derivatives, Med Chem (Los Angeles) 19 (2023) 915–924. https://doi.org/10.2174/1573406419666230214112800.

[43] S. Bano, A. Khan, F. Asghar, M. Usman, A. Badshah, S. Ali, Computational and Pharmacological Evaluation of Ferrocene-Based Acyl Ureas and Homoleptic Cadmium Carboxylate Derivatives for Anti-diabetic Potential, Front Pharmacol 8 (2018) 1–16. https://doi.org/10.3389/fphar.2017.01001.

[44] A. Adaika, Y. Bekkar, S. Youmbai, L. Bourougaa, E. Lanez, M.L. Ben Amor, K. Nesba, T. Lanez, L. Bechki, Synthesis, Antioxidant, and Antidiabetic Potential of Ferrocenylmethylnucleobase Compounds: In Vitro, In Silico Molecular Docking, DFT Calculation, and Molecular Dynamic Simulations, Appl Organomet Chem 39 (2025). https://doi.org/10.1002/aoc.7988.

[45] G.S. Hotamisligil, Inflammation and metabolic disorders, Nature 444 (2006) 860–867. https://doi.org/10.1038/nature05485.

[46] T. V. Rohm, D.T. Meier, J.M. Olefsky, M.Y. Donath, Inflammation in obesity, diabetes, and related disorders, Immunity 55 (2022) 31–55. https://doi.org/10.1016/j.immuni.2021.12.013.

[47] A. Jurjus, A. Eid, S. Al Kattar, M.N. Zeenny, A. Gerges-Geagea, H. Haydar, A. Hilal, D. Oueidat, M. Matar, J. Tawilah, I.H. Hussein, P. Schembri-Wismayer, F. Cappello, G. Tomasello, A. Leone, R.A. Jurjus, Inflammatory bowel disease, colorectal cancer and type 2 diabetes mellitus: The links, BBA Clin 5 (2016) 16–24. https://doi.org/10.1016/j.bbacli.2015.11.002.

[48] G. Daryabor, M.R. Atashzar, D. Kabelitz, S. Meri, K. Kalantar, The Effects of Type 2 Diabetes Mellitus on Organ Metabolism and the Immune System, Front Immunol 11 (2020). https://doi.org/10.3389/fimmu.2020.01582.

[49] Diagnosis and Classification of Diabetes Mellitus, Diabetes Care 33 (2010) S62–S69. https://doi.org/10.2337/dc10-S062.

[50] C.E. Butrico, N. Klopfenstein, E.R. Green, J.R. Johnson, S.H. Peck, C.B. Ibberson, C.H. Serezani, J.E. Cassat, Hyperglycemia Increases Severity of Staphylococcus aureus Osteomyelitis and Influences Bacterial Genes Required for Survival in Bone, Infect Immun 91 (2023). https://doi.org/10.1128/iai.00529-22.

[51] J. Chávez-Reyes, C.E. Escárcega-González, E. Chavira-Suárez, A. León-Buitimea, P. Vázquez-León, J.R. Morones-Ramírez, C.M. Villalón, A. Quintanar-Stephano, B.A.

Marichal-Cancino, Susceptibility for Some Infectious Diseases in Patients With Diabetes: The Key Role of Glycemia, Front Public Health 9 (2021). https://doi.org/10.3389/fpubh.2021.559595.

[52] L.M.A.J. Muller, K.J. Gorter, E. Hak, W.L. Goudzwaard, F.G. Schellevis, A.I.M. Hoepelman, G.E.H.M. Rutten, Increased Risk of Common Infections in Patients with Type 1 and Type 2 Diabetes Mellitus, Clinical Infectious Diseases 41 (2005) 281–288. https://doi.org/10.1086/431587.

[53] J.L.M. Carrillo, F.P.C. Rodríguez, O.G. Coronado, M.A.M. García, J.F.C. Cordero, Physiology and Pathology of Innate Immune Response Against Pathogens, in: Physiology and Pathology of Immunology, InTech, 2017. https://doi.org/10.5772/intechopen.70556.

[54] C.-S. Chen, A. Bellier, C.-Y. Kao, Y.-L. Yang, H.-D. Chen, F.C.O. Los, R. V. Aroian, WWP-1 Is a Novel Modulator of the DAF-2 Insulin-Like Signaling Network Involved in Pore-Forming Toxin Cellular Defenses in Caenorhabditis elegans, PLoS One 5 (2010) e9494. https://doi.org/10.1371/journal.pone.0009494.

[55] J.-Y. Sun, C.-Y. You, K. Dong, H.-S. You, J.-F. Xing, Anti-inflammatory, analgesic and antioxidant activities of 3,4-oxo-isopropylidene-shikimic acid, Pharm Biol 54 (2016) 2282–2287. https://doi.org/10.3109/13880209.2016.1153663.

[56] Vanlalhruaii, C. Malsawmtluangi, H. Lalhlenmawia, Evaluation of in vitro anti-inflammatory activity of the spadix of Colocasia affinis, Sci Vis 19 (2019) 30–34. https://doi.org/10.33493/scivis.19.02.06.

[57] T.L. Haas, P.G. Lloyd, H. Yang, R.L. Terjung, Exercise Training and Peripheral Arterial Disease, in: Compr Physiol, Wiley, 2012: pp. 2933–3017. https://doi.org/10.1002/cphy.c110065.

[58] H.-Y. Yap, S. Tee, M. Wong, S.-K. Chow, S.-C. Peh, S.-Y. Teow, Pathogenic Role of Immune Cells in Rheumatoid Arthritis: Implications in Clinical Treatment and Biomarker Development, Cells 7 (2018) 161. https://doi.org/10.3390/cells7100161.

[59] Y. Geng, S. Zhu, Z. Lu, H. Xu, J.-S. Shi, Z.-H. Xu, Anti-inflammatory Activity of Mycelial Extracts from Medicinal Mushrooms, Int J Med Mushrooms 16 (2014) 319–325. https://doi.org/10.1615/IntJMedMushrooms.v16.i4.20.

[60] F. Crea, L.M. Biasucci, Innate immune inflammatory response to danger: when, how, and why does a friend become a foe?, Eur Heart J 33 (2012) 1434–1437. https://doi.org/10.1093/eurheartj/ehs033.

[61] K. Newton, V.M. Dixit, Signaling in Innate Immunity and Inflammation, Cold Spring Harb Perspect Biol 4 (2012) a006049–a006049. https://doi.org/10.1101/cshperspect.a006049.

[62] D. Hirayama, T. Iida, H. Nakase, The Phagocytic Function of Macrophage-Enforcing Innate Immunity and Tissue Homeostasis, Int J Mol Sci 19 (2017) 92. https://doi.org/10.3390/ijms19010092.

[63] M. Krystel-Whittemore, K.N. Dileepan, J.G. Wood, Mast Cell: A Multi-Functional Master Cell, Front Immunol 6 (2016). https://doi.org/10.3389/fimmu.2015.00620.

[64] K. Liu, Dendritic Cells, in: Encyclopedia of Cell Biology, Elsevier, 2016: pp. 741–749. https://doi.org/10.1016/B978-0-12-394447-4.30111-0.

[65] U. Lendeckel, S. Venz, C. Wolke, Macrophages: shapes and functions, ChemTexts 8 (2022) 12. https://doi.org/10.1007/s40828-022-00163-4.

[66] T. Przygodzki, B. Luzak, H. Kassassir, E. Mnich, M. Boncler, K. Siewiera, M. Kosmalski, J. Szymanski, C. Watala, Diabetes and Hyperglycemia Affect Platelet GPIIIa Expression: Effects on Adhesion Potential of Blood Platelets from Diabetic Patients under In Vitro Flow Conditions, Int J Mol Sci 21 (2020) 3222. https://doi.org/10.3390/ijms21093222.

[67] A. Izcue, J.L. Coombes, F. Powrie, Regulatory Lymphocytes and Intestinal Inflammation, Annu Rev Immunol 27 (2009) 313–338. https://doi.org/10.1146/annurev.immunol.021908.132657.

[68] L.A. Abdulkhaleq, M.A. Assi, R. Abdullah, M. Zamri-Saad, Y.H. Taufiq-Yap, M.N.M. Hezmee, The crucial roles of inflammatory mediators in inflammation: A review, Vet World 11 (2018) 627–635. https://doi.org/10.14202/vetworld.2018.627-635.

[69] M. Jöhr, T.-M. Berger, S. Ruesch, Choix de l'analgésie systémique selon le terrain, Ann Fr Anesth Reanim 26 (2007) 546–553. https://doi.org/10.1016/j.annfar.2007.03.022.

[70] M. Bennett, D.W. Gilroy, Lipid Mediators in Inflammation, Microbiol Spectr 4 (2016). https://doi.org/10.1128/microbiolspec.MCHD-0035-2016.

[71] T.M. Wright, Cytokines in acute and chronic inflammation, Frontiers in Bioscience 2 (1997) A171. https://doi.org/10.2741/A171.

[72] T. Liu, L. Zhang, D. Joo, S.-C. Sun, NF-κB signaling in inflammation, Signal Transduct Target Ther 2 (2017) 17023. https://doi.org/10.1038/sigtrans.2017.23.

[73] C.D. Buckley, D.W. Gilroy, C.N. Serhan, Proresolving Lipid Mediators and Mechanisms in the Resolution of Acute Inflammation, Immunity 40 (2014) 315–327. https://doi.org/10.1016/j.immuni.2014.02.009.

[74] H. Matsumoto, H. Ogura, K. Shimizu, M. Ikeda, T. Hirose, H. Matsuura, S. Kang, K. Takahashi, T. Tanaka, T. Shimazu, The clinical importance of a cytokine network in the acute phase of sepsis, Sci Rep 8 (2018) 13995. https://doi.org/10.1038/s41598-018-32275-8.

[75] B. Erdogan, M. Is, F. V. Aker, S.T. Emon, T. Engin, E.A. Akar, E. Sayman, H. Somay, Preventative effect of diclofenac sodium and/or diltiazem in rats with epidural fibrosis, Bratislava Medical Journal 120 (2019) 813–818. https://doi.org/10.4149/BLL_2019_135.

[76] A.E. Coutinho, K.E. Chapman, The anti-inflammatory and immunosuppressive effects of glucocorticoids, recent developments and mechanistic insights, Mol Cell Endocrinol 335 (2011) 2–13. https://doi.org/10.1016/j.mce.2010.04.005.

[77] D.E. Becker, Basic and Clinical Pharmacology of Glucocorticosteroids, Anesth Prog 60 (2013) 25–32. https://doi.org/10.2344/0003-3006-60.1.25.

[78] L. Kessel, B. Tendal, K.J. Jørgensen, D. Erngaard, P. Flesner, J.L. Andresen, J. Hjortdal, Post-cataract Prevention of Inflammation and Macular Edema by Steroid and Nonsteroidal Anti-inflammatory Eye Drops, Ophthalmology 121 (2014) 1915–1924. https://doi.org/10.1016/j.ophtha.2014.04.035.

[79] S. Ramamoorthy, J.A. Cidlowski, Corticosteroids. Mechanisms of Action in Health and Disease, Rheumatic Disease Clinics of North America 42 (2016) 15–31. https://doi.org/10.1016/j.rdc.2015.08.002.

[80] M. Visser, S.B. Kritchevsky, A.B. Newman, B.H. Goodpaster, F.A. Tylavsky, M.C. Nevitt, T.B. Harris, Lower serum albumin concentration and change in muscle mass: the Health, Aging and Body Composition Study, Am J Clin Nutr 82 (2005) 531–537. https://doi.org/10.1093/ajcn.82.3.531.

[81] G. Fanali, A. di Masi, V. Trezza, M. Marino, M. Fasano, P. Ascenzi, Human serum albumin: From bench to bedside, Mol Aspects Med 33 (2012) 209–290. https://doi.org/10.1016/j.mam.2011.12.002.

[82] A. Jahanban-Esfahlan, A. Ostadrahimi, R. Jahanban-Esfahlan, L. Roufegarinejad, M. Tabibiazar, R. Amarowicz, Recent developments in the detection of bovine serum albumin, Int J Biol Macromol 138 (2019) 602–617. https://doi.org/10.1016/j.ijbiomac.2019.07.096.

[83] G. Rabbani, S.N. Ahn, Structure, enzymatic activities, glycation and therapeutic potential of human serum albumin: A natural cargo, Int J Biol Macromol 123 (2019) 979–990. https://doi.org/10.1016/j.ijbiomac.2018.11.053.

[84] S. Arques, Human serum albumin in cardiovascular diseases, Eur J Intern Med 52 (2018) 8–12. https://doi.org/10.1016/j.ejim.2018.04.014.

[85] C.-Y. Shen, K.-J. Li, C.-H. Wu, C.-H. Lu, Y.-M. Kuo, S.-C. Hsieh, C.-L. Yu, Unveiling the molecular basis of inflamm-aging induced by advanced glycation end products (AGEs)-modified human serum albumin (AGE-HSA) in patients with different immune-mediated diseases, Clinical Immunology 252 (2023) 109655. https://doi.org/10.1016/j.clim.2023.109655.

[86] K. Watanabe, H. Kinoshita, T. Okamoto, K. Sugiura, S. Kawashima, T. Kimura, Antioxidant Properties of Albumin and Diseases Related to Obstetrics and Gynecology, Antioxidants 14 (2025) 55. https://doi.org/10.3390/antiox14010055.

[87] X. Zheng, Z. Bai, T. Wang, F.G. Romeiro, A. Mancuso, C.A. Philips, Y.J. Wong, F.G. Nery, X. Qi, Human Albumin Infusion for the Management of Liver Cirrhosis and Its Complications: An Overview of Major Findings from Meta-analyses, Adv Ther 40 (2023) 1494–1529. https://doi.org/10.1007/s12325-023-02430-3.

[88] J.P. Doweiko, D.J. Nompleggi, Reviews: The Role of Albumin in Human Physiology and Pathophysiology, Part III: Albumin and Disease States, Journal of Parenteral and Enteral Nutrition 15 (1991) 476–483. https://doi.org/10.1177/0148607191015004476.

[89] C.J. Wiedermann, Anti-inflammatory activity of albumin, Crit Care Med 35 (2007) 981–982. https://doi.org/10.1097/01.CCM.0000257234.87784.91.

[90] B.R. Don, G. Kaysen, POOR NUTRITIONAL STATUS AND INFLAMMATION: Serum Albumin: Relationship to Inflammation and Nutrition, Semin Dial 17 (2004) 432–437. https://doi.org/10.1111/j.0894-0959.2004.17603.x.

[91] J. El Ouazzani, A. Ghalem, G. El Ouazzani, N. Ismaili, N. El Ouafi, Management of hyperglycemia during and in the immediate follow-up of acute coronary syndrome, J Saudi Heart Assoc 30 (2018) 113–121. https://doi.org/10.1016/j.jsha.2017.08.003.

[92] M. Stumvoll, B.J. Goldstein, T.W. van Haeften, Type 2 diabetes: principles of pathogenesis and therapy, The Lancet 365 (2005) 1333–1346. https://doi.org/10.1016/S0140-6736(05)61032-X.

[93] P. Prabhakar Reddy, A.K. Tiwari, R. Ranga Rao, K. Madhusudhana, V. Rama Subba Rao, A.Z. Ali, K. Suresh Babu, J. Madhusudana Rao, New Labdane diterpenes as intestinal α-glucosidase inhibitor from antihyperglycemic extract of Hedychium spicatum (Ham. Ex

Smith) rhizomes, Bioorg Med Chem Lett 19 (2009) 2562–2565. https://doi.org/10.1016/j.bmcl.2009.03.045.

[94] B.K. Tripathi, A.K. Srivastava, Diabetes mellitus: complications and therapeutics., Med Sci Monit 12 (2006) RA130-47. http://www.ncbi.nlm.nih.gov/pubmed/16810145.

[95] A. V Raveendran, Non-pharmacological Treatment Options in the Management of Diabetes Mellitus, Eur Endocrinol 14 (2018) 31. https://doi.org/10.17925/EE.2018.14.2.31.

[96] D.E. Kelley, J.P. Reilly, T. Veneman, L.J. Mandarino, Effects of insulin on skeletal muscle glucose storage, oxidation, and glycolysis in humans, American Journal of Physiology-Endocrinology and Metabolism 258 (1990) E923–E929. https://doi.org/10.1152/ajpendo.1990.258.6.E923.

[97] R.A. Harrigan, M.S. Nathan, P. Beattie, Oral agents for the treatment of type 2 diabetes mellitus: Pharmacology, toxicity, and treatment, Ann Emerg Med 38 (2001) 68–78. https://doi.org/10.1067/mem.2001.114314.

[98] H. Mechchate, I. Es-safi, A. Louba, A.S. Alqahtani, F.A. Nasr, O.M. Noman, M. Farooq, M.S. Alharbi, A. Alqahtani, A. Bari, H. Bekkari, D. Bousta, In Vitro Alpha-Amylase and Alpha-Glucosidase Inhibitory Activity and In Vivo Antidiabetic Activity of Withania frutescens L. Foliar Extract, Molecules 26 (2021) 293. https://doi.org/10.3390/molecules26020293.

[99] B. Amiri, N.S. Hosseini, F. Taktaz, K. Amini, M. Rahmani, M. Amiri, K. Sadrjavadi, A. Jangholi, S. Esmaeili, Inhibitory effects of selected antibiotics on the activities of α-amylase and α-glucosidase: In-vitro, in-vivo and theoretical studies, European Journal of Pharmaceutical Sciences 138 (2019) 105040. https://doi.org/10.1016/j.ejps.2019.105040.

[100] C. Shibao, Acarbose, in: Primer on the Autonomic Nervous System, Elsevier, 2012: pp. 639–641. https://doi.org/10.1016/B978-0-12-386525-0.00134-7.

[101] E. Gil, E. Guardiola, [Effect of acarbose on glycemia and pancreatic hormone secretion induced by usual meals in Spain]., Rev Clin Esp 191 (1992) 416–21. http://www.ncbi.nlm.nih.gov/pubmed/1488514.

[102] M. Malaguarnera, I. Giugno, P. Ruello, D. Maugeri, G. Pistone, Treatment of familial hypertriglyceridaemia with acarbose, Diabetes Obes Metab 2 (2000) 33–38. https://doi.org/10.1046/j.1463-1326.2000.00065.x.

[103] S. Shobana, Y.N. Sreerama, N.G. Malleshi, Composition and enzyme inhibitory properties of finger millet (Eleusine coracana L.) seed coat phenolics: Mode of inhibition of α-

glucosidase and pancreatic amylase, Food Chem 115 (2009) 1268–1273. https://doi.org/10.1016/j.foodchem.2009.01.042.

[104] M.C. Abt, E.G. Pamer, Commensal bacteria mediated defenses against pathogens, Curr Opin Immunol 29 (2014) 16–22. https://doi.org/10.1016/j.coi.2014.03.003.

[105] T.J. Silhavy, D. Kahne, S. Walker, The Bacterial Cell Envelope, Cold Spring Harb Perspect Biol 2 (2010) a000414–a000414. https://doi.org/10.1101/cshperspect.a000414.

[106] K.D. Young, Bacterial morphology: why have different shapes?, Curr Opin Microbiol 10 (2007) 596–600. https://doi.org/10.1016/j.mib.2007.09.009.

[107] M.R. Yeaman, N.Y. Yount, Mechanisms of Antimicrobial Peptide Action and Resistance, Pharmacol Rev 55 (2003) 27–55. https://doi.org/10.1124/pr.55.1.2.

[108] J. Li, J.-J. Koh, S. Liu, R. Lakshminarayanan, C.S. Verma, R.W. Beuerman, Membrane Active Antimicrobial Peptides: Translating Mechanistic Insights to Design, Front Neurosci 11 (2017). https://doi.org/10.3389/fnins.2017.00073.

[109] J.G. Swoboda, J. Campbell, T.C. Meredith, S. Walker, Wall Teichoic Acid Function, Biosynthesis, and Inhibition, ChemBioChem 11 (2010) 35–45. https://doi.org/10.1002/cbic.200900557.

[110] W. Vollmer, D. Blanot, M.A. De Pedro, Peptidoglycan structure and architecture, FEMS Microbiol Rev 32 (2008) 149–167. https://doi.org/10.1111/j.1574-6976.2007.00094.x.

[111] H.D. Isenberg, Pathogenicity and virulence: another view, Clin Microbiol Rev 1 (1988) 40–53. https://doi.org/10.1128/CMR.1.1.40.

[112] A.K. Sharma, N. Dhasmana, N. Dubey, N. Kumar, A. Gangwal, M. Gupta, Y. Singh, Bacterial Virulence Factors: Secreted for Survival, Indian J Microbiol 57 (2017) 1–10. https://doi.org/10.1007/s12088-016-0625-1.

[113] N. Kasanah, M.T. Hamann, Development of antibiotics and the future of marine microorganisms to stem the tide of antibiotic resistance, Current Opinion in Investigational Drugs 5 (2004) 827–837. http://www.ncbi.nlm.nih.gov/pubmed/15600239.

[114] S.P. Bernier, M.G. Surette, Concentration-dependent activity in natural environments, Front Microbiol 4 (2013). https://doi.org/10.3389/fmicb.2013.00020.

[115] L. Sandegren, Selection of antibiotic resistance at very low antibiotic concentrations, Ups J Med Sci 119 (2014) 103–107. https://doi.org/10.3109/03009734.2014.904457.

[116] G. Kapoor, S. Saigal, A. Elongavan, Action and resistance mechanisms of antibiotics: A guide for clinicians, J Anaesthesiol Clin Pharmacol 33 (2017) 300. https://doi.org/10.4103/joacp.JOACP_349_15.

[117] L. Tian, H. Fang, Q. Mao, Y. Bai, Z. Ye, D. Hu, X. Wang, Y. Hou, N. Ye, S. Zhang, Y. Ma, Low Concentrations of Antibiotics Alter Microbial Communities and Induce High Abundances of Antibiotic-Resistant Genes in Ornamental Water, Water (Basel) 15 (2023) 3047. https://doi.org/10.3390/w15173047.

[118] S. Bernatová, O. Samek, Z. Pilát, M. Šerý, J. Ježek, P. Jákl, M. Šiler, V. Krzyžánek, P. Zemánek, V. Holá, M. Dvořáčková, F. Růžička, Following the Mechanisms of Bacteriostatic versus Bactericidal Action Using Raman Spectroscopy, Molecules 18 (2013) 13188–13199. https://doi.org/10.3390/molecules181113188.

[119] G.M.S. Soares, L.C. Figueiredo, M. Faveri, S.C. Cortelli, P.M. Duarte, M. Feres, Mechanisms of action of systemic antibiotics used in periodontal treatment and mechanisms of bacterial resistance to these drugs, Journal of Applied Oral Science 20 (2012) 295–309. https://doi.org/10.1590/S1678-77572012000300002.

[120] J. Talapko, T. Meštrović, M. Juzbašić, M. Tomas, S. Erić, L. Horvat Aleksijević, S. Bekić, D. Schwarz, S. Matić, M. Neuberg, I. Škrlec, Antimicrobial Peptides—Mechanisms of Action, Antimicrobial Effects and Clinical Applications, Antibiotics 11 (2022) 1417. https://doi.org/10.3390/antibiotics11101417.

[121] G.M. Matos, B. Garcia-Teodoro, C.P. Martins, P. Schmitt, F. Guzmán, A.C.O. de Freitas, P.H. Stoco, F.A. Ferreira, M.J. Stadnik, D. Robl, L.M. Perazzolo, R.D. Rosa, Antimicrobial Spectrum of Activity and Mechanism of Action of Linear Alpha-Helical Peptides Inspired by Shrimp Anti-Lipopolysaccharide Factors, Biomolecules 13 (2023) 150. https://doi.org/10.3390/biom13010150.

[122] X. Lu, G. Zhen, Y. Liu, T. Hojo, A.L. Estrada, Y.-Y. Li, Long-term effect of the antibiotic cefalexin on methane production during waste activated sludge anaerobic digestion, Bioresour Technol 169 (2014) 644–651. https://doi.org/10.1016/j.biortech.2014.07.056.

[123] F.R. Bruniera, F.M. Ferreira, L.R.M. Saviolli, M.R. Bacci, D. Feder, M. da Luz Gonçalves Pedreira, M.A. Sorgini Peterlini, L.A. Azzalis, V.B. Campos Junqueira, F.L.A. Fonseca, The use of vancomycin with its therapeutic and adverse effects: a review., Eur Rev Med Pharmacol Sci 19 (2015) 694–700. http://www.ncbi.nlm.nih.gov/pubmed/25753888.

[124] G. Mancuso, A. Midiri, E. Gerace, C. Biondo, Bacterial Antibiotic Resistance: The Most Critical Pathogens, Pathogens 10 (2021) 1310. https://doi.org/10.3390/pathogens10101310.

[125] C.M. Hasan, D. Dutta, A.N.T. Nguyen, Revisiting Antibiotic Resistance: Mechanistic Foundations to Evolutionary Outlook, Antibiotics 11 (2021) 40. https://doi.org/10.3390/antibiotics11010040.

[126] Md.A. Salam, Md.Y. Al-Amin, M.T. Salam, J.S. Pawar, N. Akhter, A.A. Rabaan, M.A.A. Alqumber, Antimicrobial Resistance: A Growing Serious Threat for Global Public Health, Healthcare 11 (2023) 1946. https://doi.org/10.3390/healthcare11131946.

[127] E.M. Wellington, A.B. Boxall, P. Cross, E.J. Feil, W.H. Gaze, P.M. Hawkey, A.S. Johnson-Rollings, D.L. Jones, N.M. Lee, W. Otten, C.M. Thomas, A.P. Williams, The role of the natural environment in the emergence of antibiotic resistance in Gram-negative bacteria, Lancet Infect Dis 13 (2013) 155–165. https://doi.org/10.1016/S1473-3099(12)70317-1.

[128] R. Hershberg, Antibiotic-Independent Adaptive Effects of Antibiotic Resistance Mutations, Trends in Genetics 33 (2017) 521–528. https://doi.org/10.1016/j.tig.2017.05.003.

[129] J.M.A. Blair, M.A. Webber, A.J. Baylay, D.O. Ogbolu, L.J. V. Piddock, Molecular mechanisms of antibiotic resistance, Nat Rev Microbiol 13 (2015) 42–51. https://doi.org/10.1038/nrmicro3380.

[130] N.M. Vega, J. Gore, Collective antibiotic resistance: mechanisms and implications, Curr Opin Microbiol 21 (2014) 28–34. https://doi.org/10.1016/j.mib.2014.09.003.

[131] R. Singh, S. Sahore, P. Kaur, A. Rani, P. Ray, Penetration barrier contributes to bacterial biofilm-associated resistance against only select antibiotics, and exhibits genus-, strain- and antibiotic-specific differences, Pathog Dis 74 (2016) ftw056. https://doi.org/10.1093/femspd/ftw056.

[132] V. Cattoir, Pompes d'efflux et résistance aux antibiotiques chez les bactéries, Pathologie Biologie 52 (2004) 607–616. https://doi.org/10.1016/j.patbio.2004.09.001.

[133] D. Hughes, D.I. Andersson, Evolutionary Trajectories to Antibiotic Resistance, Annu Rev Microbiol 71 (2017) 579–596. https://doi.org/10.1146/annurev-micro-090816-093813.

[134] G.V. De Gaetano, G. Lentini, A. Famà, F. Coppolino, C. Beninati, Antimicrobial Resistance: Two-Component Regulatory Systems and Multidrug Efflux Pumps, Antibiotics 12 (2023) 965. https://doi.org/10.3390/antibiotics12060965.

[135] J.Y. Lim, J. Yoon, C.J. Hovde, A brief overview of Escherichia coli O157:H7 and its plasmid O157., J Microbiol Biotechnol 20 (2010) 5–14.

[136] S.P. Diggle, M. Whiteley, Microbe Profile: Pseudomonas aeruginosa: opportunistic pathogen and lab rat, Microbiology (N Y) 166 (2020) 30–33. https://doi.org/10.1099/mic.0.000860.

[137] D. Liu, Enterotoxin-Producing Staphylococcus aureus, in: Molecular Medical Microbiology, Elsevier, 2015: pp. 979–995. https://doi.org/10.1016/B978-0-12-397169-2.00055-X.

[138] R. Abbas, M. Chakkour, H. Zein El Dine, E.F. Obaseki, S.T. Obeid, A. Jezzini, G. Ghssein, Z. Ezzeddine, General Overview of Klebsiella pneumonia: Epidemiology and the Role of Siderophores in Its Pathogenicity, Biology (Basel) 13 (2024) 78. https://doi.org/10.3390/biology13020078.

Part 2: Experimental and Theoretical Investigations

Chapter III: Experimental and Theoretical Procedures

2. Experimental Procedures:

2.1. Materials and Methods:

2.1.1. Chemicals and reagents:

dimethylformamide (DMF) (analytical grade, from PROLABO) was used as solvent without further purification for cyclic voltammetry assays, tetrabutylammonium tetrafluoroborate (Bu_4NBF_4) (electrochemical grade, 99 %, Sigma-Aldrich) was used as supporting electrolyte and its concentration was kept 0.1 M. All chemical reagents and solvents were obtained from commercial sources unless otherwise specified and were used without further purification. All synthesis procedures were conducted under an inert nitrogen atmosphere.

2.1.2. Analytical techniques and instrumentation:

- **Chromatography:**

Thin-layer chromatography (TLC) was performed on aluminum plates coated with silica gel. The developed plates were exposed to iodine vapor for visualization and dried using a dryer.

- **Melting Point:**

Melting temperatures were measured using a GallenKamp melting point with capillary tubes.

- **Cyclic Voltammetry (CV):**

Cyclic voltammograms were obtained using a PGZ301 potentiostat/galvanostat (Radiometer Analytical, SAS, France). Experiments were performed in a three-electrode system. The reference electrode was Hg/Hg_2Cl_2, the auxiliary electrode was a platinum wire, and the working electrode was platinum. The experiments were conducted in DMF with 0.1 M Bu_4NBF_4 as the supporting electrolyte.

For the characterization of synthesized ferrocene derivatives, cyclic voltammograms were recorded for 10 mM solutions in DMF. The potential range was 0 to 800 mV, and measurements were performed at different scanning rates (50, 100, 150, 200, 300, 400, 500 mV. s^{-1}) at 298 K. The potentials were reported in millivolts (mV) relative to using the Fe^{+2}/Fe^{+3} couple as reference.

➢ **UV-Vis Spectroscopy:**

Electronic absorption spectra were recorded using a Shimadzu UV-1800 spectrophotometer at room temperature in a 5 mL quartz voltammetric cell. Data were acquired using UV probe software version 2.34 (Shimadzu), and analysis was carried out using OriginLab software version 2.0 (Integral Software, France).

UV-Vis spectra of the synthesized ferrocene derivatives were obtained for 1 mM solutions in DMF at room temperature.

➢ **Infrared Spectroscopy:**

Infrared spectra were recorded using a Shimadzu IRAffinity-1 FT-IR spectrometer, with samples prepared as KBr pellets. The data were reported as percentage transmittances at given wave numbers.

➢ **NMR Spectroscopy:**

^{1}H, ^{13}C and DEPT 135 NMR spectra were recorded on a Bruker 600 MHz spectrometer at ambient temperature. Samples were prepared in $CDCl_3$ or DMSO-d_6, with chemical shifts (δ) were reported in parts per million (ppm) relative to tetramethylsilane (TMS) as an internal standard.

For chemical shift referencing, $CDCl_3$ was set at 7.26 ppm for ^{1}H NMR and 77.16 ppm for ^{13}C NMR. Coupling constants were reported in Hertz (Hz). The spectral interpretation followed standard notations, where (s) denotes a singlet, (d) a doublet, (t) a triplet, and (m) a multiplet.

2.2. Synthesis:

2.2.1. Synthesis of quaternary salt:

The preparation of ferrocene derivatives requires the initial synthesis of a quaternary salt. This is achieved through a multi-step process, starting with the reaction of ferrocene and a Mannich reagent, catalyzed by phosphoric acid and using acetic acid as a solvent [1]. The overall reaction pathway is shown in Scheme III.1.

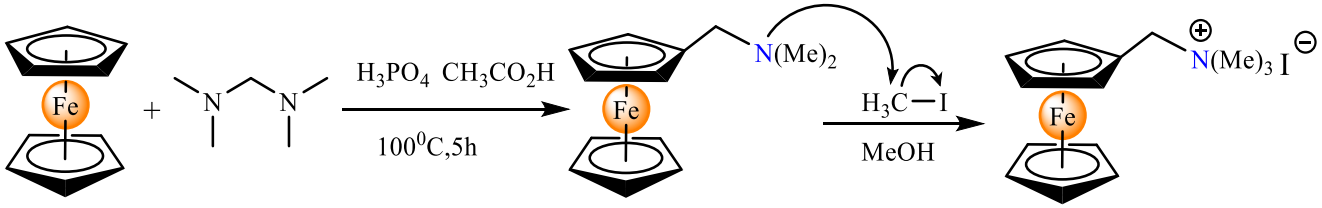

Scheme III.1. Synthesis pathway of quaternary salt.

In the first step, the Mannich reagent selectively reacts with one of the ferrocene rings to form the monosubstituted compound N,N-dimethylaminomethylferrocene, which is easily separated and obtained with a significant. In the second step, N,N-dimethylaminomethylferrocene is treated with iodomethane to produce the thermodynamically stable ferrocenylmethyltrimethyl-ammonium iodide (quaternary salt**)** in high purity [2]. This compound is then used in further synthetic reactions. The preparation of quaternary salt involves a three-step process:

A) Synthesis of Methylene-bis-dimethylamine (Mannich reagent):

The Mannich reagent was synthesized through the condensation of dimethylamine with formaldehyde [3], as shown in Scheme III.2. To initiate the reaction, 34.68 g (1.16 mol) of 34% aqueous formaldehyde was placed in a 500 mL flask equipped with a magnetic stirrer and thermometer, then cooled in an ice bath. A 40% aqueous solution of dimethylamine (104.8 g, 2.3 mole) was slowly added drop by drop using a separatory funnel, ensuring that the temperature remained below 15°C due to exothermic nature of the reaction.

Following the complete addition of dimethylamine and one hour of stirring, potassium hydroxide was introduced to neutralize the reaction, resulting in the formation of two distinct layers. The organic layer was dried using an additional quantity of potassium hydroxide pellets (approximately 10 g) and left to stand overnight. After filtration, the product is distilled, yielding 190.7 g (81.3 %) of methylene-bis-dimethylamine, with a boiling point ranging between 83-84°C, closely matching the literature yield of 83% [2].

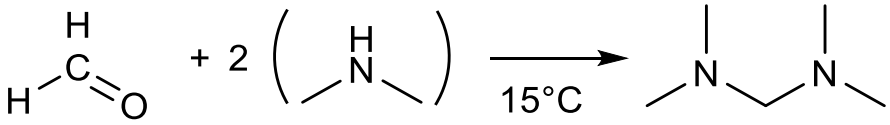

Scheme III.2. Synthesis pathway of Mannich reagent.

B) Synthesis of N,N-dimethylaminomethylferrocene:

In a 1-liter three-neck flask equipped with a condenser, magnetic stirrer, and a continuous nitrogen flow setup, 42.5 g (0.23 mol) of ferrocene, 39 g (0.38 mol) of methylene-bis-dimethylamine, 41 g (0.42 mol) of orthophosphoric acid, and 350 mL of acetic acid were combined. The mixture was heated in a boiling water bath at 100°C for 5 hours with vigorous stirring under a nitrogen atmosphere.

After cooling to room temperature, the dark brown solution was diluted with 500 ml of distilled water. Unreacted ferrocene was removed by extraction with ether three times (3 x 175

mL). The aqueous layer was cooled in an ice bath and made strongly alkaline by adding potassium hydroxide pellets. A black oily layer of tertiary ferrocene amine appears on the surface of the alkaline solution, which was dissolved by adding more water. The resulting mixture was extracted with ether three times (3 x 250 mL), and the organic layer was washed with water and dried over sodium sulfate. After evaporating the solvent, 42 g of dark red viscous liquid of N,N-dimethylaminomethylferrocene (Figure III.1) was obtained with a yield of 76% (Literature yield: 80%) [3].

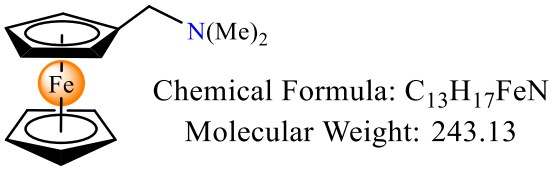

Figure III.1. Chemical structure of N,N-dimethylaminomethylferrocene.

C) Synthesis of Quaternary salt:

A quantity of 50 g (0.21 mol) of N,N-dimethylaminomethylferrocene was dissolved in 57 ml of methanol and heated on a boiling water bath at 100°C for 5 minutes. Then, 57 mL (1.06 mol) of iodomethane was added dropwise to the solution. As the reaction is exothermic, rapid addition could lead to vigorous boiling.

Upon cooling to room temperature, the product solidifies after the addition of ether. The solid was filtered, washed with ether, and dried at room temperature to give 65 g of yellow precipitate of N,N,N-trimethylammoniummethylferrocene iodide (Figure III.2) with a yield of 82% (Literature: 89%) [4].

FTIR (KCl) ν (cm^{-1}): 1238.2; 1473.5; 2399.3; 3012.6 and 3618.2

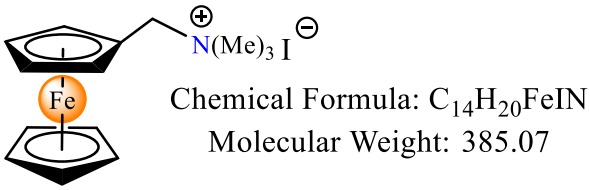

Figure III.2. Chemical structure of quaternary salt.

2.2.2. Synthesis of N-Ferrocenylmethylaniline and its derivatives:

N-Ferrocenylmethylaniline (FMA) was synthesized following established literature protocols [5]. The reaction was carried out by treating the quaternary salt with an excess of aniline in distilled water at a temperature between 100 and 110°C (Scheme III.3).

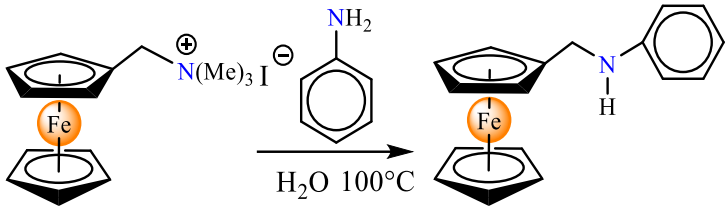

Scheme III.3. Synthesis pathway of FMA.

After the initial synthesis, acylation of the product was carried out in toluene using acyl chloride reagents, as shown in Scheme III.4. All reaction were conducted in a three-neck flask equipped with a condenser, a magnetic stirrer, and a continuous nitrogen flow setup.

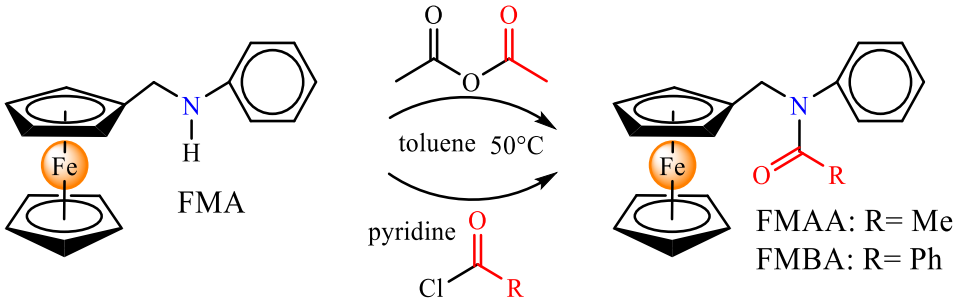

Scheme III. 4. Acylation pathway of FMA.

➢ **Synthesis of N-Ferrocenylmethyl aniline (FMA):**

FMA (6.6 mmol, 66%) was obtained by reacting 3.84 g (0.01 mol) of the quaternary salt with 5.58 g (0.06 mol) of aniline in 600 mL of distilled water. The mixture was stirred for 4 to 5 hours at a temperature between 100 and 110°C. The product was then extracted with toluene, and the organic phase was evaporated, yielding in a brown-orange residue.

This residue was recrystallized from an ethanol-water mixture, yielding 1.91 g of yellow FMA crystals (Figure III.3) with an overall yield of 66% (Literature yield: 70%) [1]. The boiling point was 85-86°C (Literature: 85-85.5°C) [1].

FTIR (KCl) ν (cm^{-1}): 3398 (NH), 3095-3035 (CH SP^2), 2843 (CH_2), 1604-1425 (C=C), 1310 (C-N), 491 (Cp-Fe-Cp).

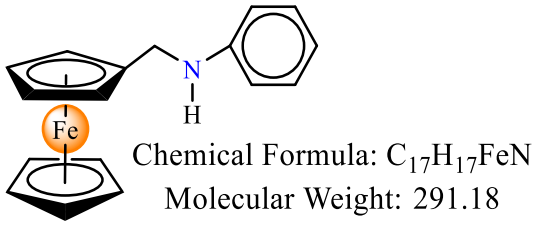

Figure III.3. Chemical structure of FMA.

➢ **Synthesis of N-Ferrocenylmethyl-N-acetylaniline (FMAA):**

FMAA (1.95 mmol; 89%) (Figure III.4) was obtained as described in previously published work [6], by reacting 635.4 mg of FMA (2.18 mmol) with 5.5 mL acetic anhydride at 50-55°C under vigorous stirring for 20 minutes. After solvent evaporation, an orange solid was obtained, which was recrystallized from an ethanol/water mixture, yielding 647.4 mg of orange needle-shaped crystals with a melting point of 116-117°C.

FTIR (KCl) ν (cm^{-1}): 3088-3039 (C-H, SP^2), 2980 (C-H, CH_2), 1652 (C=O), 1595-1390 (C=C), 1281 (C-N), 476 (Cp-Fe-Cp).

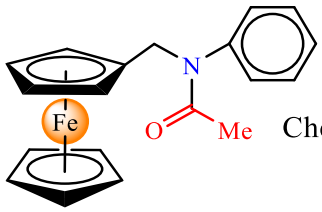

Chemical Formula: $C_{19}H_{19}FeNO$
Molecular Weight: 333.21

Figure III.4. Chemical structure of FMAA.

➢ **Synthesis of N-Ferrocenylmethyl-N-benzoylaniline (FMBA):**

FMBA (Figure III.5) was synthesized by reacting 500 mg of FMA (1.72 mmol) with 368.2 mg of benzoyl chloride (2.63 mmol) in the presence 1.72 mmol of pyridine, following literature procedures [6,7]. The mixture was stirred for 25 minutes at 45-50°C. The organic phase was then washed with a 6 M solution of hydrochloric acid, and the solvent was evaporated. The obtained solid was recrystallized from a 1:2 water/ethanol mixture, yielding 509.6 mg of golden needle-shaped crystals with a crystallization yield of 75%, and melting point of 126-127°C.

FTIR (KCl) ν (cm^{-1}): 3097-3030 (C-H, SP^2), 2937 (C-H, CH_2), 1641 (C=O), 1595-1300 (C=C), 1297 (C-N), 478 (Cp-Fe-Cp).

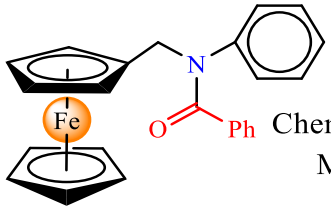

Chemical Formula: $C_{24}H_{21}FeNO$
Molecular Weight: 395.28

Figure III.5. Chemical structure of FMBA.

2.2.3. Synthesis of N-Ferrocenylmethyl-m-toluidine and its derivatives:

The synthesis of N-Ferrocenylmethyl-m-toluidine (3FMT) began by reacting the quaternary salt [1] with an excess of m-toluidine in distilled water (Scheme III.5). Following this,

the acylation of the obtained product was performed using chloride agents in the presence of pyridine as a base catalyst and toluene as a solvent, while maintaining the reaction temperature between 50 and 55 °C (Scheme III.6). Upon completion, the mixture was extracted with water three times, followed by washing with 6M hydrochloric acid (HCl). The organic phase was then evaporated, resulting in a yellow-brown oily compound. Both reactions were set up in a three-neck flask equipped with a condenser and submerged in an oil bath to maintain the required temperature, A continuous nitrogen flow was used throughout the process to provide an inert atmosphere. The Rf values were measured in a toluene/acetone eluent mixture (9:1).

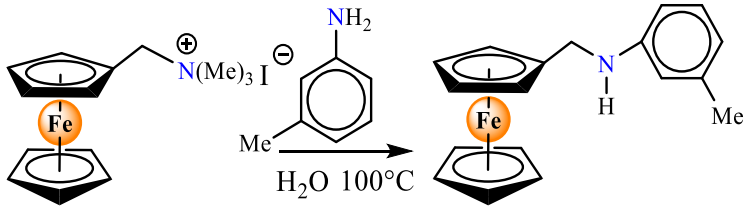

Scheme III.5. Synthesis pathway of 3FMT.

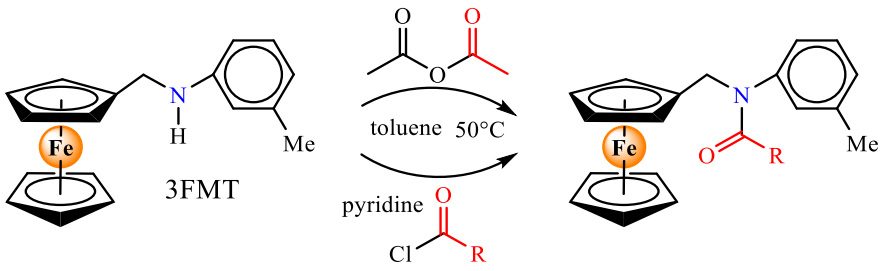

Scheme III.6. Acylation pathway of FMT.

➢ **Synthesis of N-Ferrocenylmethyl-m-toluidine (3FMT):**

The derivative N-ferrocenylmethyl-3-methylaniline (Figure III.6) was synthesized using 1 g of quaternary salt (2.6 mmol) and 562 mg of m-methylaniline (5.2 mmol, 99% purity), maintaining molar ratio of m-toluidine to quaternary salt set at 2:1. the reaction lasted for 16 hours at a temperatures range of 100-110 °C.

The final product was extracted using dichloromethane (DCM) three times, then washed with water three times. The organic phase was evaporated, yielding 600 mg of a brown-orange oily product with a 76% yield. Recrystallization from an ethanol/water mixture produce 550 mg (1.8 mmol) of a yellowish solid identified as 3FMT, with a final yield of 69% and Rf = 0.83.

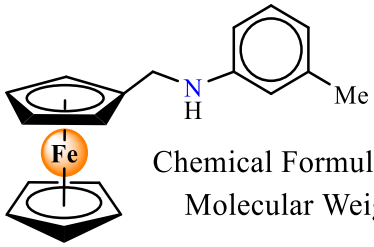

Chemical Formula: $C_{18}H_{19}FeN$
Molecular Weight: 305.20

Figure III.6. Chemical structure of 3FMT.

FTIR (KCl) ν (cm^{-1}): 3406 (NH), 3093-3035 (CH SP^2), 2935 (CH_3), 2858 (CH_2), 1600-1423 (C=C), 1300 (C-N), 486 (Cp-Fe-Cp).

^{1}H NMR (600 MHz, δ in ppm, $CDCl_3$): δ= 7.09 (td, *J*= 7.6, 0.8 Hz, 1H, C_6H_4), 6.56 (dt, *J*= 7.4, 1.6 Hz, 1H, C_6H_4), 6.51 – 6.46 (m, 2H, C_6H_4), 4.24 (t, *J*= 1.9 Hz, 2H, C_5H_4), 4.18 (s, 5H, C_5H_5), 4.14 (t, *J*= 1.8 Hz, 2H, C_5H_4), 3.95 (s, 2H, -CH_2-N), 2.30 (d, *J*= 0.7 Hz, 3H, CH_3-Ph).

^{13}C NMR (150 MHz, δ in ppm, $CDCl_3$): δ= 148.31 (C_q), 139.07 (C_q), 129.15 (CH_{Ar}), 118.48 (CH_{Ar}), 113.58 (CH_{Ar}), 110.00 (CH_{Ar}), 86.56 (C_q), 68.47 (C_5H_4), 68.06 (C_5H_5), 67.85 (C_5H_4), 43.39 (CH_2-N), 21.62 (CH_3).

- **Synthesis of N-Ferrocenylmethyl-N-acetyl-m-toluidine (3FMAT):**

The acylation process of the 3FMAT derivative (Figure III.7) commenced with 3FMT (100 mg; 0.33 mmol) and acetic anhydride (66.8 mg; 0.65 mmol). The reaction lasted for 30 minutes, and crystallization done by ethanol/water mixture yielded 85.2 mg (0.25 mmol) of a yellowish solid, corresponding to a 75% yield with an Rf value of 0.3.

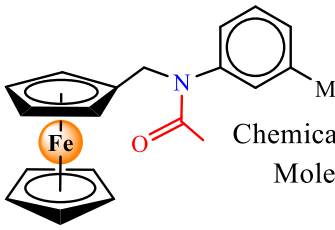

Chemical Formula: $C_{20}H_{21}FeNO$
Molecular Weight: 347.24

Figure III.7. Chemical structure of 3FMAT.

FTIR (KCl) ν (cm^{-1}): 3093-3039 (CH SP^2), 2981 (CH_3), 2927 (CH_2), 1643 (C=O), 1600-1392 (C=C), 1288 (C-N), 478 (Cp-Fe-Cp).

^{1}H NMR (600 MHz, δ in ppm, $CDCl_3$): δ= 7.23 – 7.18 (m, 1H), 7.11 (d, *J*= 7.7 Hz, 1H, C_6H_4), 6.81 (s, 1H, C_6H_4), 6.75 (d, *J*= 7.9 Hz, 1H, C_6H_4), 4.59 (d, *J*= 2.0 Hz, 2H, -CH_2-N), 4.09 (d, *J*= 2.0 Hz, 5H, C_5H_5), 4.07 – 4.03 (m, 4H, C_5H_4), 2.32 (d, *J*= 1.9 Hz, 3H, CH_3-Ph), 1.77 (d, *J*= 2.0 Hz, 3H, CH_3-CO).

^{13}C NMR (150 MHz, δ in ppm, $CDCl_3$): δ =169.80 (C=O), 129.10 (CH_{Ar}), 128.96 (CH_{Ar}), 128.54 (CH_{Ar}), 125.52 (CH_{Ar}),69.83 (C_5H_4), 68.46 (C_5H_4), 68.02 (C_5H_4), 48.39 (CH_2-N), 22.77 (CH_3), 21.25 (CH_3-CO).

- **Synthesis of N-Ferrocenylmethyl-N-propionyl-m-toluidine (3FMPT):**

The acylation of the 3FMPT derivative (Figure III.8) was carried out by reacting 3FMT (100 mg;0.33 mmol) with propionyl chloride (47 mg; 0.5 mmol). The reaction proceeded for 25 minutes. Purification through crystallization from ethanol/water yielded 87.3 mg (0.24 mmol) of yellowish wool of 3FMPT, corresponding to a 74% yield with an Rf value of 0.43.

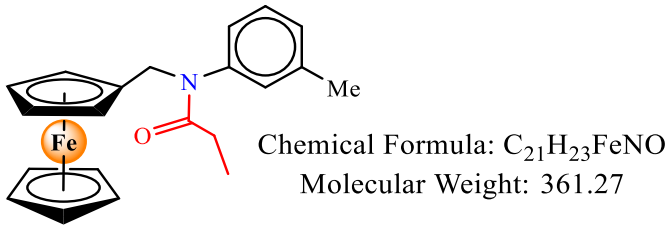

Figure III.8. Chemical structure of 3FMPT.

FTIR (KCl) ν (cm^{-1}): 3097-3032 (CH SP^2), 2970 (CH_3), 2924 (CH_2), 1654 (C=O), 1604-1400 (C=C), 1269 (C-N), 486 (C_p-Fe-C_p).

^{1}H NMR (600 MHz, δ in ppm, $CDCl_3$): δ = 7.20 (t, *J*= 7.5 Hz, 1H, C_6H_4), 7.11 (d, *J*= 7.7 Hz, 1H, C_6H_4), 6.79 (s, 1H, C_6H_4), 6.74 (d, *J*= 7.8 Hz, 1H, C_6H_4), 4.59 (s, 2H, -CH_2-N), 4.09 (d, *J*= 1.9 Hz, 5H, C_5H_5), 4.06 (d, *J*= 2.2 Hz, 2H, C_5H_4), 4.04 (d, J= 2.7 Hz, 2H, C_5H_4), 2.32 (d, *J*= 1.9 Hz, 3H, CH_3-Ph), 1.96 (q, *J*= 7.4 Hz, 2H, CH_2-CH_3), 1.00 (t, *J*= 7.3 Hz, 3H CH_3-CH_2).

^{13}C NMR (150 MHz, δ in ppm, $CDCl_3$): δ = 173.28 (C=O), 142.55 (C_q), 139.53 (C_q), 129.11 (CH_{Ar}), 129.27 (CH_{Ar}), 129.21 (CH_{Ar}), 128.63 (CH_{Ar}), 125.80 (CH_{Ar}), 83.47 (C_q), 70.00 (C_5H_4), 68.58 (C_5H_4), 67.11 (C_5H_4), 48.74 (CH_2-N), 27.89 (CH_2-C=O), 21.38 (CH_3-Ph), 9.73(CH_3-CH_2).

- **Synthesis of N-Ferrocenylmethyl-N-chloroacetyl-m-toluidine (3FMClAT):**

The acylation of 3FMClAT (Figure III.9) was performed using 3FMT (100 mg; 0.33 mmol) and chloroacetyl chloride (76 mg; 0.66 mmol). The reaction proceeded for 45 minutes. Purification through crystallization from ethanol/water yielded 104.2 mg (0.27 mmol; 82.7%) of a tawny solid, corresponding to Rf = 0.53.

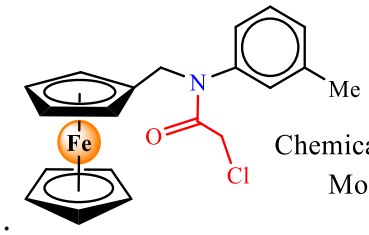

Chemical Formula: $C_{20}H_{20}ClFeNO$
Molecular Weight: 381.68

Figure III.9. Chemical structure of 3FMClAT.

FTIR (KCl) ν (cm^{-1}): 3101-3032 (CH SP^2), 2947 (CH_3) 2920 (CH_2), 1670 (C=O), 1604-1388 (C=C), 1300 (C-N), 470 (C_p-Fe-C_p).

^{1}H NMR (600 MHz, δ in ppm, $CDCl_3$): δ =7.23 (t, J= 7.8 Hz, 1H, C_6H_4), 7.16 (d, *J*= 7.6 Hz, 1H, C_6H_4), 6.84 (s, 1H, C_6H_4), 6.78 (d, *J*= 7.8 Hz, 1H, C_6H_4), 4.62 (s, 2H, -CH_2-N), 4.10 (d, *J*=2.0 Hz, 5H, C_5H_5), 4.07 (d, *J*= 2.0 Hz, 4H, C_5H_4), 3.75 (d, *J*= 2.0 Hz, 2H, CH_2-Cl), 2.33 (d, *J*= 2.0 Hz, 3H, CH_3-Ph).

^{13}C NMR (150 MHz, δ in ppm, $CDCl_3$): δ =165.46 (C=O), 140.75 (C_q), 139.89 (C_q), 129.45 (CH_{Ar}), 129.40 (CH_{Ar}), 128.91 (CH_{Ar}), 125.46 (CH_{Ar}), 82.25 (C_q), 68.52 (C_5H_4), 68.25 (C_5H_4), 49.55 (CH_2-N), 42.22 (Cl-CH_2-C=O), 21.25 (CH_3-Ph).

- **Synthesis of N-Ferrocenylmethyl-N-benzoyl-m-toluidine (3FMBT):**

The acylation of 3FMBT (Figure III.10) was carried out starting with 3FMT (98.5 mg; 0.32 mmol) and benzoyl chloride (92 mg; 0.65 mmol) over 35 minutes. The residue obtained was then crystallized from an ethanol/water mixture, producing 102.1 mg of a yellowish solid of 3FMBT (0.25 mmol; 77.3%.), with Rf value of 0.42.

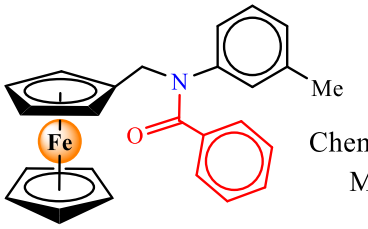

Chemical Formula: $C_{25}H_{23}FeNO$
Molecular Weight: 409.31

Figure III.10. Chemical structure of 3FMBT.

FTIR (KCl) ν (cm^{-1}): 3097-3024 (CH SP^2), 2943 (CH_3), 2920 (CH_2), 1643 (C=O), 1604-1357 (C=C), 1273 (C-N), 478 (C_p-Fe-C_p).

^{1}H NMR (600 MHz, δ in ppm, $CDCl_3$): δ=7.26 (dd, J= 7.4, 4.2 Hz, 2H, C_6H_5), 7.18 (t, J= 7.3 Hz, 1H, C_6H_4), 7.12 (t, J= 7.8 Hz, 2H, C_6H_5), 7.01 (t, J= 7.8 Hz, 1H, C_6H_5), 6.91 (d, J= 7.6 Hz, 1H, C_6H_4), 6.76 (s, 1H, C_6H_4), 6.65 (d, J= 7.9 Hz, 1H, C_6H_4), 4.84 (s, 2H, -CH_2-N), 4.16 (s, 2H,

C_5H_5), 4.12 (d, J= 2.0 Hz, 5H, C_5H_5), 4.07 (d, J= 2.2 Hz, 2H, C_5H_5), 2.20 (d, J= 1.9 Hz, 3H, CH_3-Ph).

^{13}C NMR (150 MHz, δ in ppm, $CDCl_3$): δ =169.97 (C=O), 143.32 (C_q), 138.79 (C_q), 136.27 (C_q), 129.38 (CH_{Ar}), 128.80 – 128.51 (m), 127.56 (CH_{Ar}), 127.42 (CH_{Ar}), 125.39 (CH_{Ar}), 83.26 (C_q), 69.85 (C_5H_4), 68.55 (C_5H_4), 68.02 (C_5H_4), 49.84 (CH_2-N), 21.22 (CH_3-Ph).

- **Synthesis of N-Ferrocenylmethyl-N-phthaloyl-m-toluidine (3FMPHT):**

The acylation of 3FMPHT (Figure III.11) was performed using 3FMT (75.2 mg; 0.25 mmol) and phthaloyl chloride (150 mg; 0.69 mmol) over 30 minutes. The residue obtained was then crystallized from an ethanol/water mixture, producing 80.4 mg of a yellowish solid of 3FMPHT (0.17 mmol; 69.2%), with an Rf value of 0.7.

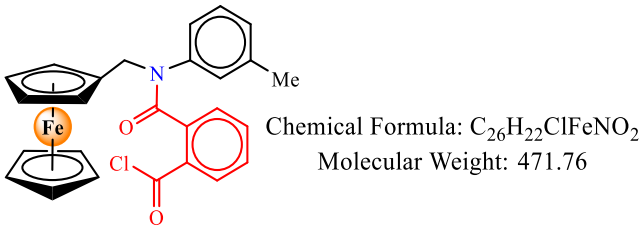

Figure III.11. Chemical structure of 3FMPHT.

- **Synthesis of N-Ferrocenylmethyl-N-(4-nitrobenzoyl)-m-toluidine (3FM4NBT):**

The acylation of 3FM4NBT (Figure III.12) was carried out starting from 3FMT (89.6 mg; 0.29 mmol) and 4-nitrobenzoyl chloride (110 mg; 0.59 mmol) over 30 minutes. The residue obtained was then crystallized from an ethanol/water mixture, producing 97.4 mg of a yellowish solid of 3FM4NBT (0.21 mmol; 73%), with an Rf value of 0.6.

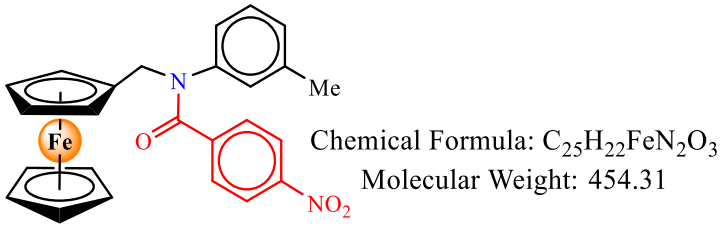

Figure III.12. Chemical structure of 3FM4NBT.

2.3. In Vitro Evaluation:

2.3.1. Anti-inflammatory activity:

The *in vitro* anti-inflammatory activity of the synthesized compounds was evaluated using the BSA denaturation method [8]. A 0.5% (w/v) Bovine Serum Albumin (BSA) solution was

prepared by dissolving 250 mg of BSA in 50 ml solution of phosphate buffer saline solution (PBS, pH 6.4). Three different solutions (each 500 µL) were prepared:

- The test solution consists of 450 µL of BSA solution and 50 µL of the tested compounds at varying concentration (2.1 to 1.28 × 10^{-4} mg/mL).
- The standard solution consists of 450 µL of BSA solution and 50 µL of the standard drug solution (diclofenac sodium) at varying concentration (12.9 to 7.9 × 10^{-4} mg mL).
- The control solution includes 450 µL of BSA solution and 50 µL of PBS.
- These solutions were incubated at 37°C for 20 minutes, followed by an increase in temperature to 70°C for 20 minutes. The absorbance was then measured at 660 nm [8]. The percentage inhibition (I%) of protein denaturation was calculated as follows:

$$I\% = \frac{A_S - A_C}{A_S} * 100 \qquad \text{(eq. III. 1)}$$

Wherein A_S denotes the sample's absorbance value, and A_C indicates the control's absorbance value.

The data obtained from UV-vis spectroscopy were then used to compute binding constant (K), applying the equation (III.2) of Benesi-Hildebrand [9].

$$\frac{A_S}{A_C - A_S} = \frac{\varepsilon_S}{\varepsilon_C - \varepsilon_S} - \frac{\varepsilon_S}{\varepsilon_C - \varepsilon_S}\frac{1}{K[C]} \qquad \text{(eq. III. 2)}$$

Where A_S and A_C are the absorbance value for the samples and control, respectively. ε_S and ε_C are their respective extinction coefficients, and [C] is the concentration of the studied compounds.

The binding free energy (ΔG) value was determined using the equation (III.3):

$$\Delta G = -RTlnK \qquad \text{(eq. III. 3)}$$

Where T represents the ambient temperature, 298K, and R stands for the universal gas constant, 8.32 $J.mol^{-1}.K^{-1}$.

2.3.2. Anti-diabetic activity:

The *in vitro* anti-diabetic activity of the synthesized compounds was evaluated using the α-amylase inhibition assay, based on the method of Thilagam et al. [10] with slight modifications. A solution of 4 mg α-amylase was prepared in 1 mL of PBS. A starch solution (2% w/v) was prepared by dissolving 0.5 g of starch in 25 mL PBS and 0.2 M potassium chloride. The method involves preparing three solutions, each consisting of 200 µL:

- The test solution consists of 100 µL of α-amylase and 100 µL of the tested compounds at varying concentration (2.1 to 1.28 × 10^{-4} mg/mL).
- The standard solution consists of 100 µL of α-amylase and 100 µL of the Acarbose (standard drug) at varying concentration (12.9 to 7.9 ×10^{-4} mg/mL).
- The control solution includes 100 µL of α-amylase and 100 µL of PBS, and incubated for 10 min at 37°C.

After an initial incubation at 37°C for 10 min, 50 µL of 2% starch solution was introduced into the mixtures, followed by further incubation at 37°C for 30 min. The reaction was then terminated by adding 1 µL of distilled water, 50 µL of HCl, and 100 µL of Lugol's iodine solution. For control, blank tubes were prepared by replacing the enzyme solution with 100 µL of distilled water. Absorbance readings were taken at 580 nm employing a spectrophotometer [10]. The percentages of α-amylase enzyme inhibition, binding constant (K), and binding free energy (ΔG) were determined using the equations (III.1-3).

2.3.3. Antibacterial activity:

The antibacterial properties of a substance *in vitro* can be identified through numerous traditional methods, whether in solid or liquid media. This research focuses on examining the antibacterial effectiveness of synthesized compounds by employing the paper disc diffusion technique, which allows for the determination of the inhibition zone diameter, providing insight into the effectiveness of the compounds against bacterial growth.

The antibacterial activity was tested against four pathogenic strains, including *E. coli* (ATCC 25922), *P. aeruginosa* (ATCC 27853), *K. pneumoniae* (ATCC 700603), and *S. aureus* (ATCC 25923). All bacterial strains were sourced from the Microbiology Laboratory at the University of El Oued.

- **Preparation of precultures:**

The selected strains were streaked onto nutrient agar and incubated at 37°C for 24 hours to ensure optimal growth. Following incubation, well-isolated colonies were transferred into 3 mL of sterile physiological saline solution (0.9%) and homogenized using a vortex mixer. The inoculum was then standardized to 0.5 McFarland, corresponding to an optical density of 0.08–0.10 at 620 nm, resulting in a final inoculum concentration of 10^7 CFU/mL.

- **Preparation of dilutions:**

Each compound was dissolved in DMSO at an initial concentration of 60 mg/ml. From these stock solutions, a series of dilutions were prepared with different concentrations (60, 50, 40, 30, 20, 10, 5, 1 mg/mL) in order to assess the antibacterial activity parameters of each compound.

- **Antibacterial testing procedure:**

The antibacterial activity was conducted following the solid medium diffusion method [11]. Sterile Whatman filter paper discs (6 mm diameter) were sterilized using autoclaving at 120°C for 20 min. Sterile Mueller-Hinton agar was poured into Petri dishes, and the bacterial strains were inoculated onto the agar surface using a sterile cotton swab. The prepared filter paper discs were then carefully placed on the inoculated agar surface with sterile forceps and saturated with 20 µL of the respective compound solution.

The inoculated plates were incubated for 20-24 hours at 37°C. Following incubation, the antibacterial effectiveness of each compound was determined by measuring the clear inhibition zones around the discs, indicating bacterial growth suppression. The diameter of these inhibition zones directly correlated with the sensitivity of the bacterial strain, with larger zones suggesting higher antibacterial activity [12].

To ensure the validity of results, negative controls using DMSO and distilled water were included to verify the absence of unintended bacterial growth [13], while amoxicillin serves as a positive control. The inhibition zone diameters were measured in millimeters (mm). Additionally, absorbance measurements at 620 nm were recorded to further quantify the antibacterial activity.

3. Theoretical procedures:

3.1. DFT Calculations:

The chemical structures of the synthesized compounds were optimized with the Gaussian 16, Revision B.01 program package [14], using density functional theory (DFT) at the B3LYP level of theory with the 6-311++G (d, p) basis set [15].

After geometry optimization, several global and electronic descriptors were calculated to evaluate the compounds' chemical reactivity and stability. These included:

- The highest occupied molecular orbital energy (E_{HOMO}), and lowest unoccupied molecular orbital energy (E_{LUMO}), which indicate the tendency to donate or accept electrons, respectively.
- Energy gap (ΔE_{L-H}) between LUMO and HOMO, which reflects molecular chemical stability and reactivity.
- Molecular electrostatic potential (MEP), describing charge distribution and potential reactive sites.
- Ionization potential (IP) and electron affinity (EA).
- electronegativity (χ); global hardness (η), global softness (σ), and electrophilicity index (ω), which characterize the compound's electronic chemical behavior.
- Other properties such as Polarizability (α), dipole moment (μ), Entropy (S) Thermal energy (Q) and Heat capacity (C_H) were also computed.

The descriptors were calculated using the following equations:

$$IP = -E_{HOMO} \quad \text{(eq. III. 4)}$$

$$EA = -E_{LUMO} \quad \text{(eq. III. 5)}$$

$$\chi = (IP_E + EA)/2 \quad \text{(eq. III. 6)}$$

$$\eta = (IP_E - EA)/2 \quad \text{(eq. III. 7)}$$

$$\sigma = 1/(2\eta) \quad \text{(eq. III. 8)}$$

$$\omega = \chi^2/(2\eta) \quad \text{(eq. III. 9)}$$

3.2. Molecular Docking Study:

The proteins associated with the previously mentioned disease were identified through a literature review, and their crystallographic structures were obtained from the Protein Data Bank [16]. The selected target proteins are as follows:

- α-amylase (PDB ID: 2QV4): Associated with anti-diabetic activity.
- BSA (PDB ID: 6QS9) and Cyclooxygenase-2 (PDB ID: 1PXX): Target for anti-inflammatory activity.
- DNA Gyrase Subunit B (DGB, PDB ID: 1KZN) and Peptide Deformylase (PDF, PDB ID: 1BSK): Related to *E. coli*.
- Dihydrofolate Reductase (DHFR, PDB ID: 4OR7) and DNA Topoisomerase IV (DTO4, PDB ID: 5EIX): Related to *K. pneumoniae*.

- Anthranilate-CoA Ligase (ACL, PDB ID: 5OE3), Peptide Deformylase (PDF, PDB ID: 1LRY), and Peptidoglycan D,D-Transpeptidase (PGDT, PDB ID: 6I1E): Related to *P. aeruginosa*.
- Dehydrosqualene Synthase (DSS, PDB ID: 2ZCQ), Dihydrofolate Reductase (DHFR, PDB ID: 3SRW), DNA Gyrase Subunit B (DGB, PDB ID: 3TTZ), Penicillin-Binding Protein 2a (PBP2a, PDB ID: 5M18), and Peptide Deformylase (PDF, PDB ID: 3U7K): Related to *S. aureus*.

These proteins were selected based on their relevance to the biological activities of the synthesized compounds, including anti-inflammatory, antidiabetic, and antibacterial properties. Molecular docking simulations were performed to predict the binding modes and affinities of the compounds with each target protein.

3.2.1. Receptor preparation:

Molecular docking studies were performed using AutoDock Tools 1.5.7 (ADT**)** software [17], executed on Windows 10 system with Intel i5 4 GHz processor and 8 GB RAM. Heteroatoms and water molecules were eliminated, Kollman and Gasteiger charges as well as polar hydrogen atoms, were incorporated into the protein for docking simulation analysis. After preparation, the receptor proteins were saved in pdbqt format for further analysis.

3.2.2. Ligand preparation:

The ligand structures, derived from DFT optimization, were saved as pdbqt files using ADT. The 3D-structures of the standard drug acarbose (ARE) diclofenac (DIF) and amoxicillin (AXL) were obtained from PubChem [18]. MMFF charges were added to these structures using the ADT software.

3.2.3. Docking simulation:

The crucial amino acids of the active site were identified by Discovery Studio Visualizer software (DSV) [19] based on their interaction with the co-crystallized ligand. Docking was carried out using a grid box with specific dimensions and center coordinates for each protein, as summarized in Table III.1. The grid spacing for all docking simulations was maintained at 0.375 Å.

Table III.1. Grid box dimensions and grid center coordinates of the target proteins.

	Box size			Center coordinates		
Proteins	X	Y	Z	X	Y	Z
2QV4	50	40	40	12.942	47.169	26.2
6QS9	30	30	30	-11.134	-8.424	14.203
1PXX	40	40	40	27.131	24.348	14.747
1KZN	30	40	50	19.150	30.393	34.745
1BSK	30	16	32	42.286	53.094	78.287
4OR7	30	22	24	55.072	27.911	17.633
5EIX	16	22	34	198.496	35.203	-11.183
5OE3	34	28	26	38.587	-3.785	15.64
1LRY	24	36	16	11.091	36.189	37.456
6I1E	22	24	16	-4.973	40.421	-16.175
2ZCQ	30	24	26	18.085	52.275	37.826
3SRW	22	30	20	-5.147	-32.121	6.066
3TTZ	26	36	18	0.318	2.989	24.168
5M18	16	24	10	19.422	-18.162	-52.577
3U7K	28	24	28	-15.993	84.614	70.14

The validity of the docking protocol was confirmed through re-docking the co-crystalized (native) ligands within the binding sites of their corresponding proteins. As cited in literature [20], the docking results are considered reliable when the root mean square deviation (RMSD) between the docked pose and the experimental crystal structure is less than 2.0 Å, ensuring that the computational approach accurately replicates the ligand's experimental binding position.

Lamarckian genetic algorithms were employed for docking calculations, with each experiment consisting of 50 runs. After docking, various ligand binding energies and corresponding conformations were obtained. The best conformation, characterized by the lowest binding energy, was selected as the optimal pose and employed for further ligand-protein interaction analysis [21–25].

3.3. ADMET Studies:

In the process of developing therapeutic drugs, a significant portion of failures can be attributed to inadequate bioavailability, drug-likeness, pharmacokinetics, pharmacodynamic, and toxicity profiles (ADME-Tox) [26–28]. For a drug to be considered an ideal candidate, it must exhibit favorable ADMET characteristics at therapeutic doses while effectively reaching the target site [29].

Understanding the toxicological profile is crucial, as it provides insights into the harmful properties and effects of drug compounds, facilitating a more precise evaluation of their adverse impacts on human health and the environment [30]. Assessing these properties early in drug development can

significantly reduce the likelihood of failure related to drug-likeness and pharmacokinetics. In silico predictive models have become a standard method for preliminary evaluations, as they can provide rapid assessments of the compound's ADMET profiles and toxicity risks, thereby minimizing the need for extensive experimental testing.

- A common challenge in drug development is the low success rate of screened compounds , often due to:

(1) Structural properties of the molecule being incompatible with effective bioavailability.
(2) Inability to achieve adequate pharmacokinetics.
(3) Difficulty in managing the lethal dose concentration.
(4) Toxicity risk
(5) Appearance of unfavorable side effects.
(6) Failure to elicit the desired biological response or achieve therapeutic objectives.

In this research, we focused on evaluating the drug-like properties of candidate molecules with respect to oral absorption utilizing Veber's and Lipinski's bioavailability rules [31–33]. Moreover, the pharmacodynamic and pharmacokinetic properties of these molecules were evaluated using several computational tools. These include SwissADME [34], PKCSM [35] and Pro-Tox [36] web servers, which collectively provide a comprehensive prediction of the compounds' ADMET profiles and potential toxicity.

Chapter IV: Results and Discussion

1. Structural Analysis and Identification of Synthesized Derivatives:

Following the organic synthesis of ferrocene derivatives, the structures of the resulting products were identified using a combination of spectroscopic analysis and electrochemical characterization. Specifically, the newly synthesized compounds were characterized by IR, ^{1}H NMR, ^{13}C NMR (Figures S4-S31), UV-Vis, and cyclic voltammetry. However, FMA, FMAA, and FMBA were characterized only by IR (Figures S1-S3), UV-Vis, and cyclic voltammetry.

1.1. FT-IR Analysis:

The FT-IR spectra of the synthesized derivatives revealed characteristic absorption bands, providing evidence of successful functionalization. Medium-frequency stretching bands observed at 3398 and 3406 cm^{-1} (Table IV.1) were assigned to N-H stretching vibrations in the secondary amine groups of FMA and 3FMT, respectively. These bands were absent in the spectra of the acylated derivatives, confirming successful acylation. The disappearance of the N-H stretches and the appearance of a strong carbonyl (C=O) stretching band in the range of 1641-1670 cm^{-1} (Table IV.1) further validated this modification.

The spectra also exhibited the typical C-H stretching frequencies, with aromatic (CH sp^2) and aliphatic (CH sp^3) proton stretches appearing in the ranges of 3101-3024 cm^{-1} and 2981-2843 cm^{-1}, respectively. Importantly, the characteristic absorption peaks associated with the ferrocene moiety were identified at 470-491 cm^{-1} (Table IV.1), which aligns with previous studies [37–40]. These bands correspond to the Fe-C bond stretching vibrations, confirming the retention of the ferrocene core in the synthesized derivatives.

Table IV.1. FT-IR (ν cm^{-1}) spectroscopic data of ferrocene derivatives.

Compounds	ν_{NH}	$\nu_{HC=C}$	ν_{CH3}	ν_{CH2}	$\nu_{C=O}$	$\nu_{Cp-Fe-Cp}$
FMA	3398	3095-3035	-	2843	-	491
FMAA	-	3088-3039	-	2980	1652	476
FMBA	-	3097-3030	-	2937	1641	478
3FMT	3406	3093-3035	2935	2858	-	486
3FMAT	-	3093-3039	2981	2927	1643	478
3FMPT	-	3097-3032	2970	2924	1654	486
3FMClAT	-	3101-3032	2947	2920	1670	470
3FMBT	-	3097-3024	2943	2920	1643	478

1.2. ^{1}H NMR and ^{13}C NMR Analysis:

The ^{1}H-NMR spectra of the new synthetized compounds displayed characteristic signal patterns corresponding to the ferrocene fragments. Three distinct sets of signals were observed: one at δ =4.00-4.14 (2H), another δ =4.02-4.18 (5H) and a third at δ =4.06-4.24 (2H). These signals align with the known splitting patterns of ferrocene, where the five-membered cyclopentadienyl rings contribute to the observed chemical shifts [39,41–49].

In compound 3FMT, the methylene group signal appeared at 3.95 ppm. Following acylation, this signal shifts to the range of 4.53-4.77 ppm, indicating the electronic influence of the acyl group on the adjacent protons. Additionally, all compounds exhibited signals between 2.13 and 2.32 ppm, assigned to the methyl protons, and in the region of 6.46-7.20 ppm, corresponding to the aromatic phenyl protons.

The ^{13}C NMR spectra provided further structural confirmation. The methyl group carbon signals in the phenyl ring appeared between 21.22 and 22.77 ppm. For the methylene g carbon in the ferrocene ring was observed in the range of 43.39-49.84 ppm. The ferrocenyl carbons were detected at 67.11-86.56 ppm. Following acylation, the (C=O) peaks were detected at 165.46–173.28 ppm. The aromatic and aliphatic carbon signals appeared in their expected regions, further confirming the integrity of the synthesized structures.

1.3. UV-Vis Spectroscopy Analysis:

Ferrocene derivatives exhibit color variations ranging from yellow-orange to dark brown, corresponding to their absorption of light in the UV-visible spectrum. These absorptions indicate electronic transitions, which are influenced by the conjugation and electronic properties of the substituents on the ferrocene framework. UV-Vis absorption spectra of the synthesized ferrocene derivatives were recorded in DMF, scanning wavelengths from 200 to 900 nm, as shown in Figure IV.1.

The UV spectra of FMA and FMBA exhibit a single absorption band in the visible region at λ_{max} = 439.2 nm and 432.4 nm, respectively, attributed to the π→π* electronic transition. In contrast, FMAA displays two characteristic bands: one in the ultraviolet region at λ_{max1} = 321.4 nm and a second band in the visible region at λ_{max2} = 438.2 nm, attributed to the n→π* and π→π* transition, respectively.

Similarly, the UV spectra of 3FMT, 3FMBT, and 3FMPHT each display a single band in the visible region at λ_{max} = 437 nm, 438 nm, and 439.2 nm, respectively. On the other hand, 3FMAT, 3FMPT, and 3FMClAT exhibit two characteristic bands: λ_{max1} in the ultraviolet region at 320.2 nm, 320.8 nm, and 321.6 nm, respectively, attributed to n→π* transitions, and λ_{max2} in the visible region at 438.2 nm, 439.6 nm, and 443.4 nm, respectively, corresponding to π→π* transitions.

The observed electronic transitions align with the typical behavior of ferrocene derivatives, where n→π* and π→π* transitions dominate in both the UV and visible regions [50], confirming the successful synthesis and structural integrity of the compounds.

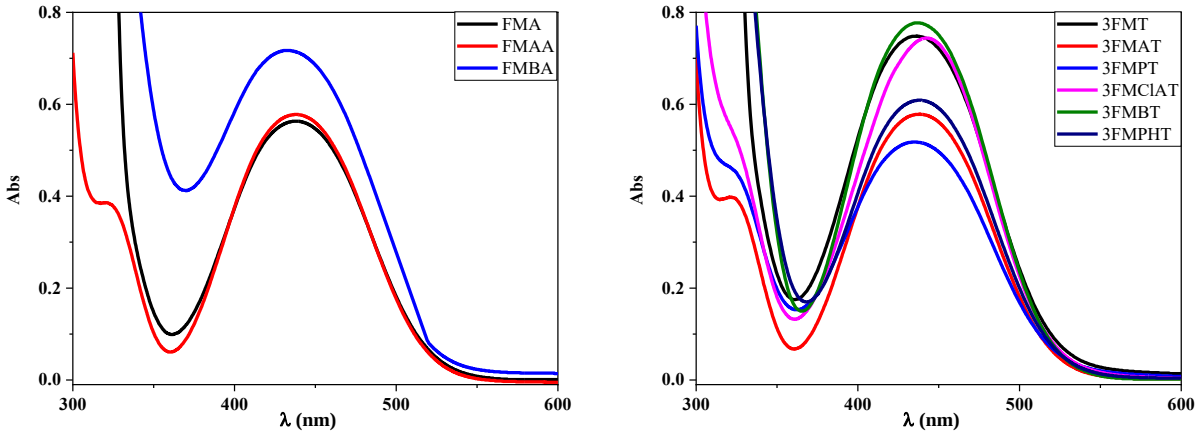

Figure IV.1. UV-visible absorption spectra of (left) FMA and its derivatives, (right) 3FMT and its derivatives in DMF at 298K.

1.4. Cyclic Voltammetry Analysis:

The synthesized compounds were characterized by CV in a 10 mM DMF solution containing Bu_4NBF_4 as the electrolyte, using a platinum electrode at a scan rate of 100 mV/s. The potential range scanned was 0 to 800 mV. The obtained voltammograms are shown in Figure IV.2, where each voltammogram displays one reversible process with a cathodic wave and an anodic wave. This behavior is indicative of the one electron reversible Fe^{2+}/Fe^{3+} redox system of the ferrocenyl moiety. The electrochemical parameters extracted from the cyclic voltammograms are summarized in Table IV.2.

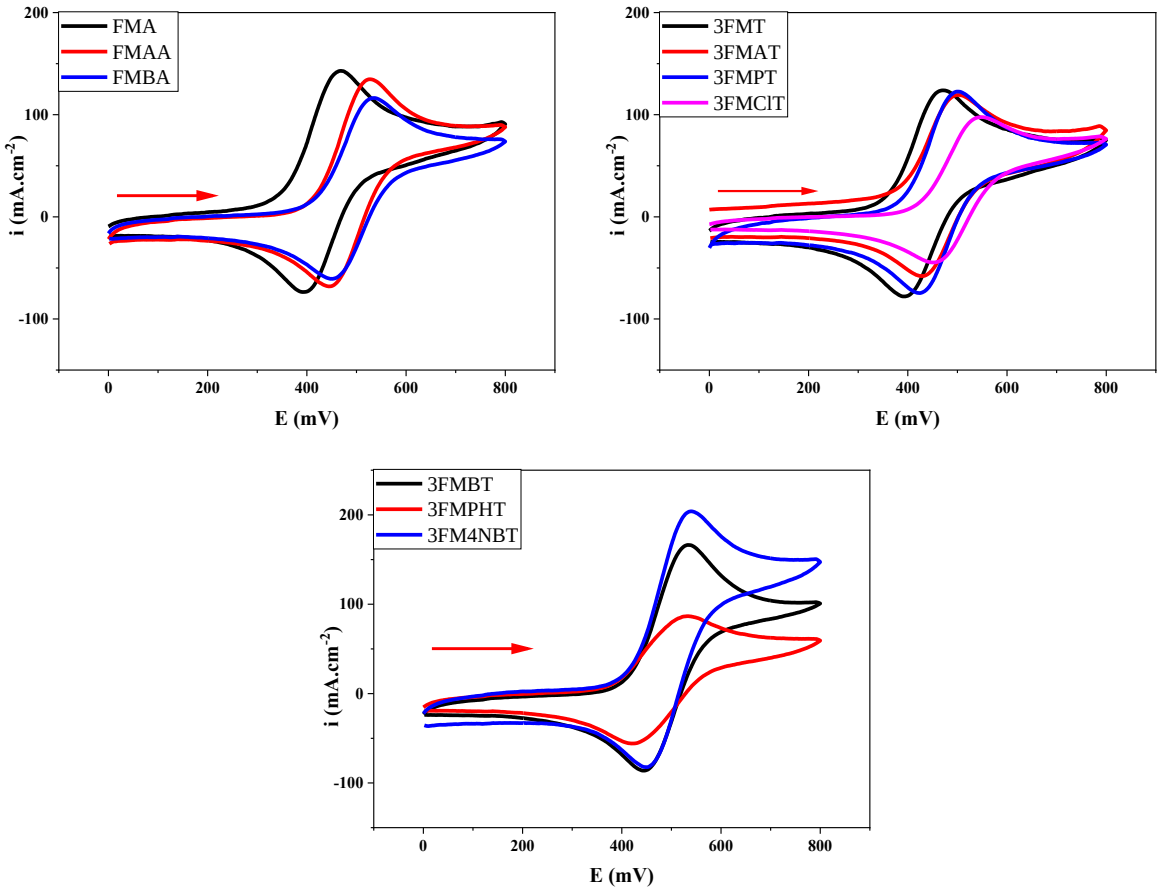

Figure IV.2. Cyclic voltammogram of the studied compounds on platinum electrode at scan rate 100 mV/s.

Based on the anodic-to-cathodic peak current ratio (Ip_a/Ip_c) for all the examined compounds, which ranged from 1.04 to 1.19 (Table IV.2), it can be inferred that these ratios are relatively close to one, indicating reversible redox behavior. This behavior aligns with observations in similar ferrocenyl Schiff base derivatives [48]. The potential difference between the anodic and cathodic peaks (ΔEp) ranged from 71 to 113 mV, exceeding the theoretical value of 59 mV. This deviation can be attributed to the uncompensated solution resistance [51].

The formal potential (E°) of FMA and 3FMT exhibit similar values (431.00 mV and 431.50 mV, respectively), with a small positive shift of 0.5 mV. Similarly, the acylated compounds 3FMPT and 3FMAT demonstrate comparable E° values (463.50 mV and 464.50 mV, respectively), with a small positive shift of 1 mV. Among the synthesized derivatives, 3FMClAT had the highest E°(502.00 mV), likely due the electron-withdrawing nature of the chloride group. making it the most favorable for the reduction of the iron center. Conversely, FMA and 3FMT had the lowest E° values, making them the least favorable for reduction.

The anodic peak potential (Epa) and cathodic peak potential (Epc) ranged from 469 to 546 mV and 393 to 458 mV, respectively. FMA and 3FMT exhibit comparable Epa and Epc values 469/393 mV and 469/394 mV, respectively), suggesting that the addition of a methyl group (Me) to the phenyl ring does not significantly affect these redox potentials. A similar trend was observed in 3FMPT, 3FMAT, FMBA and 3FMBT, where Epa and Epc values remained within a close range. All the acylated compounds show higher Epa and Epc value compared to FMA and 3FMT under similar conditions, which is likely due to the electron-withdrawing effect of the amide group.

Table IV.2. Electrochemical parameters extracted from the cyclic voltammogram.

	Ep_a (mV)	Ep_c (mV)	Ip_a (µA)	Ip_c (µA)	ΔEp (mV)	E_0 (mV)	Ip_a/ Ip_c
FMA	469.00	393.00	142.96	119.72	76.0	431.00	1.1941196
FMAA	527.00	446.00	158.19	142.22	81.0	486.50	1.1122908
FMBA	534.00	452.00	106.84	116.39	82.0	493.00	1.0893860
3FMT	469.00	394.00	123.87	108.24	75.0	431.50	1.1444013
3FMAT	500.00	429.00	119.34	101.41	71.0	464.50	1.1768070
3FMPT	501.00	426.00	122.44	114.10	75.0	463.50	1.0730938
3FMClAT	546.00	458.00	150.45	130.58	88.0	502.00	1.1521673
3FMBT	534.00	445.00	200.68	187.95	89.0	489.50	1.0677308
3FMPHT	532.00	419.00	108.98	104.53	113.0	475.50	1.0425715
3FM4NBT	536.00	452.00	203.63	186.72	84.0	494.00	1.0905634

The cyclic voltammograms of the synthesized compounds were recorded on a platinum electrode at various scan rates. The vertical arrow in Figure IV.3 indicates the direction of increasing scan rates. As expected, the anodic and cathodic peak currents increased with the scan rate, confirming a diffusion-controlled process. In the inset, the linear regression plots of the peak current (i_p) versus the square root of the scan rate ($v^{1/2}$) are shown in Figure IV.3. These plots were used to calculate the diffusion coefficients of the synthesized ferrocene derivatives.

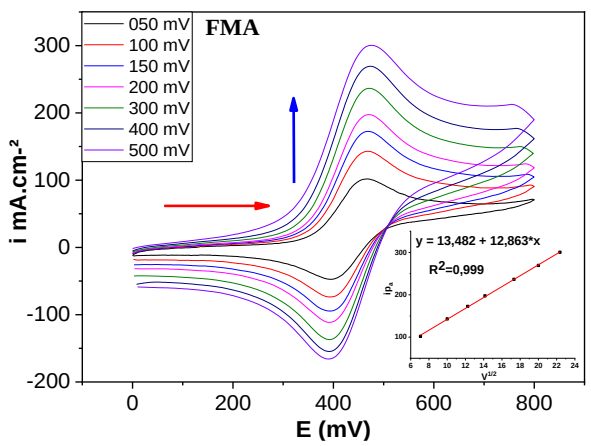
FMA
050 mV
100 mV
150 mV
200 mV
300 mV
400 mV
500 mV
y = 13,482 + 12,863*x
R2=0,999
i mA.cm-2
E (mV)

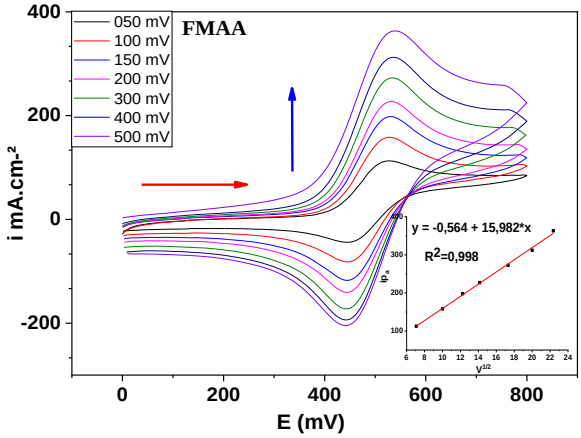
FMAA
050 mV
100 mV
150 mV
200 mV
300 mV
400 mV
500 mV
y = -0,564 + 15,982*x
R2=0,998
i mA.cm-2
E (mV)

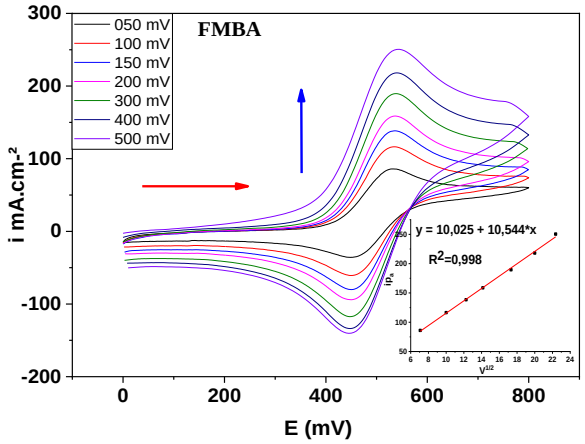
FMBA
050 mV
100 mV
150 mV
200 mV
300 mV
400 mV
500 mV
y = 10,025 + 10,544*x
R2=0,998
i mA.cm-2
E (mV)

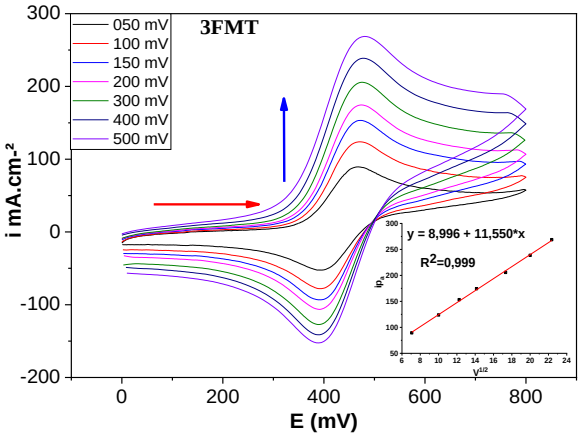
3FMT
050 mV
100 mV
150 mV
200 mV
300 mV
400 mV
500 mV
y = 8,996 + 11,550*x
R2=0,999
i mA.cm-2
E (mV)

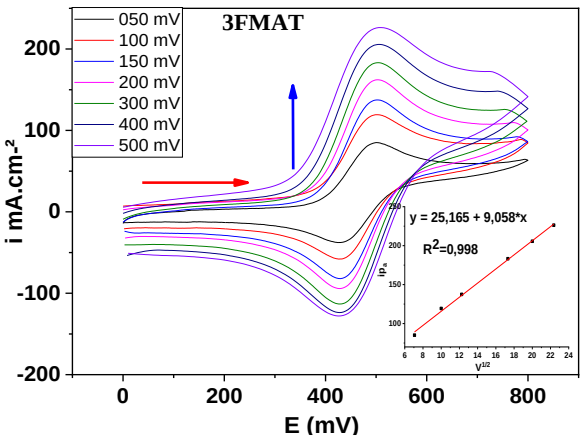
3FMAT
050 mV
100 mV
150 mV
200 mV
300 mV
400 mV
500 mV
y = 25,165 + 9,058*x
R2=0,998
i mA.cm-2
E (mV)

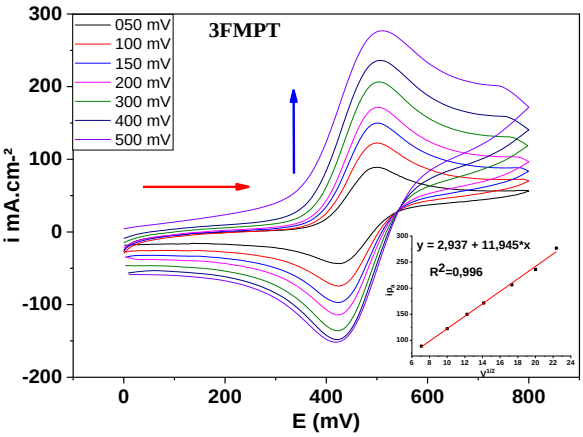
3FMPT
050 mV
100 mV
150 mV
200 mV
300 mV
400 mV
500 mV
y = 2,937 + 11,945*x
R2=0,996
i mA.cm-2
E (mV)

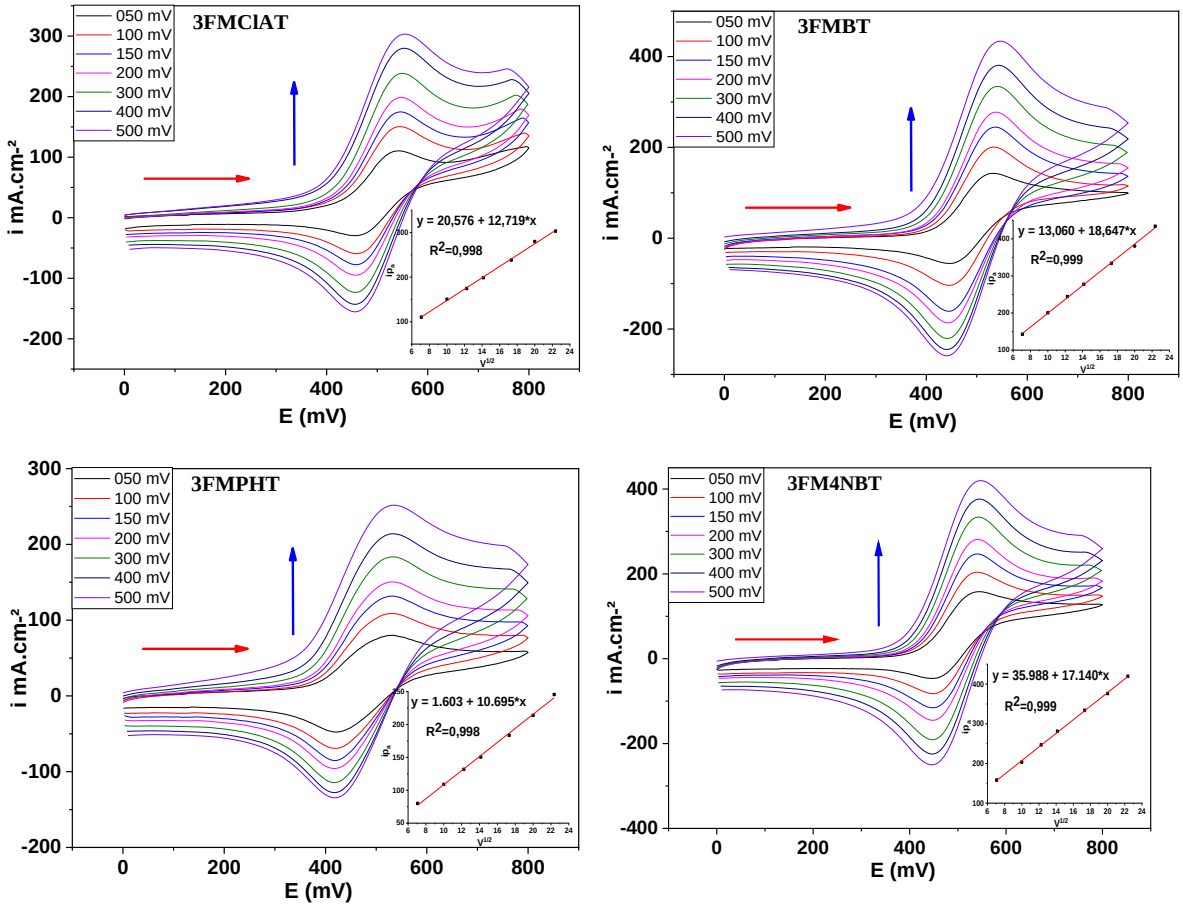

Figure IV.3. Succession of cyclic voltammograms of the synthetized compounds on a platinum electrode at different scan rates.

The linear regression equations obtained from the peak currents and their correlation coefficients (R^2) are presented in Table IV.3. The diffusion constants were calculated based on these relationships using the Randles-Sevcik equation IV.1, reflecting the rate at which each compound diffuses through the DMF solution under the experimental conditions.

$$i_P = 2.69.10^5\left(\sqrt{n}\right)^3 SC\sqrt{D}\sqrt{v} \qquad \text{(eq IV. 1)}$$

where i_p is the peak current, n is the number of electrons transferred, S is the electrode surface area, C is the concentration, D is the diffusion coefficient, and v is the scan rate.

The diffusion coefficients (D) of the synthesized ferrocene derivatives, summarized in Table IV.3, range from 11.20 × 10^{-6} cm^2 s^{-1} (FMA) to 52.04 × 10^{-6} cm^2 s^{-1} (3FMPHT). This variation reflects the influence of molecular structure, particularly molecular weight (MW) and polarity, on diffusion behavior in DMF solution.

Among the studied compounds, FMA exhibits the lowest diffusion coefficient (11.20×10^{-6} $cm^2\ s^{-1}$) , while its methylated analogue (3FMT), exhibits a slightly higher value (11.68×10^{-6} $cm^2\ s^{-1}$), indicating that the addition of a methyl group has a minimal impact on diffusion. However, as the MW increases through acetylation (FMAA, 13.80×10^{-6} $cm^2\ s^{-1}$) and benzoylation (FMBA, 35.51×10^{-6} $cm^2\ s^{-1}$), the diffusion coefficient rises significantly. This enhancement is attributed to increased molecular polarity due to the presence of electron-withdrawing groups.

A similar trend is observed in the toluidine-based derivatives. 3FMAT (14.04×10^{-6} $cm^2\ s^{-1}$), 3FMPT (16.92×10^{-6} $cm^2\ s^{-1}$), and 3FMClAT (20.05×10^{-6} $cm^2\ s^{-1}$), show a gradual increase in diffusion values, reflecting the influence of increasingly polar functional groups. Notably, the highest diffusion coefficients are recorded for derivatives containing bulky, highly polar substituents such as benzoyl, phthaloyl, and 4-nitrobenzoyl. The compounds 3FMBT, 3FMPHT, and 3FM4NBT demonstrate diffusion coefficients of 37.80, 52.04, and 51.60×10^{-6} $cm^2 \cdot s^{-1}$, respectively. These results suggest that the presence of strong electron-withdrawing groups significantly enhances diffusion, likely by promoting better interaction with the solvent environment.

In summary, diffusion in DMF for this series of ferrocene derivatives appears to be governed primarily by molecular weight and the polarity of the substituents. Compounds bearing highly polar or electron-withdrawing groups diffuse more readily, whereas those with less polar or smaller groups exhibit lower diffusion rates. This behavior underscores the importance of electronic structure in determining the electrochemical properties of these molecules.

Table IV. 3. Diffusion constants values of FMA, 3FMT and their derivatives.

Compound	Equation	R^2	$D.10^{-6}$ $cm^2.s^{-1}$
FMA	$Y = 12.863x + 13.482$	0.999	11.20
FMAA	$Y = 15.982x - 0.564$	0.998	13.80
FMBA	$Y = 10.544x + 10.025$	0.998	35.51
3FMT	$Y = 11.550x + 8.996$	0.999	11.68
3FMAT	$Y = 9.058x + 25.165$	0.998	14.04
3FMPT	$Y = 11.945x + 2.937$	0.996	16.92
3FMClAT	$Y = 12.719x + 20.576$	0.998	20.05
3FMBT	$Y = 18.647x + 13.060$	0.999	37.80
3FMPHT	$Y = 10.695x + 1.603$	0.998	52.04

3FM4NBT	$Y = 17.140x + 35.988$	0.999	51.60

2. In Vitro Biological Activity Results:

2.1. Antidiabetic Activity:

A dose-dependent inhibition of α-amylase activity was observed for the synthesized compounds within a concentration range of 5.13 10^{-4} to 2.1 mg/mL, while the standard drug acarbose (ARE) exhibited activity within a range of 5.05 10^{-2} to 12.9 mg/mL, as illustrated in Figure IV.4.

At a concentration of 12.94 mg/mL, ARE achieved maximum inhibition of α-amylase enzyme, with an inhibition rate of 94.73%. In contrast, the synthesized compounds demonstrated inhibition ranging from 80% to 95.23% at a significantly lower concentration of 2.1 mg/mL. FMA and its derivatives displayed inhibition between. While 3FMT and its derivatives showed inhibition rates ranging from 84.93% to 95.23%.

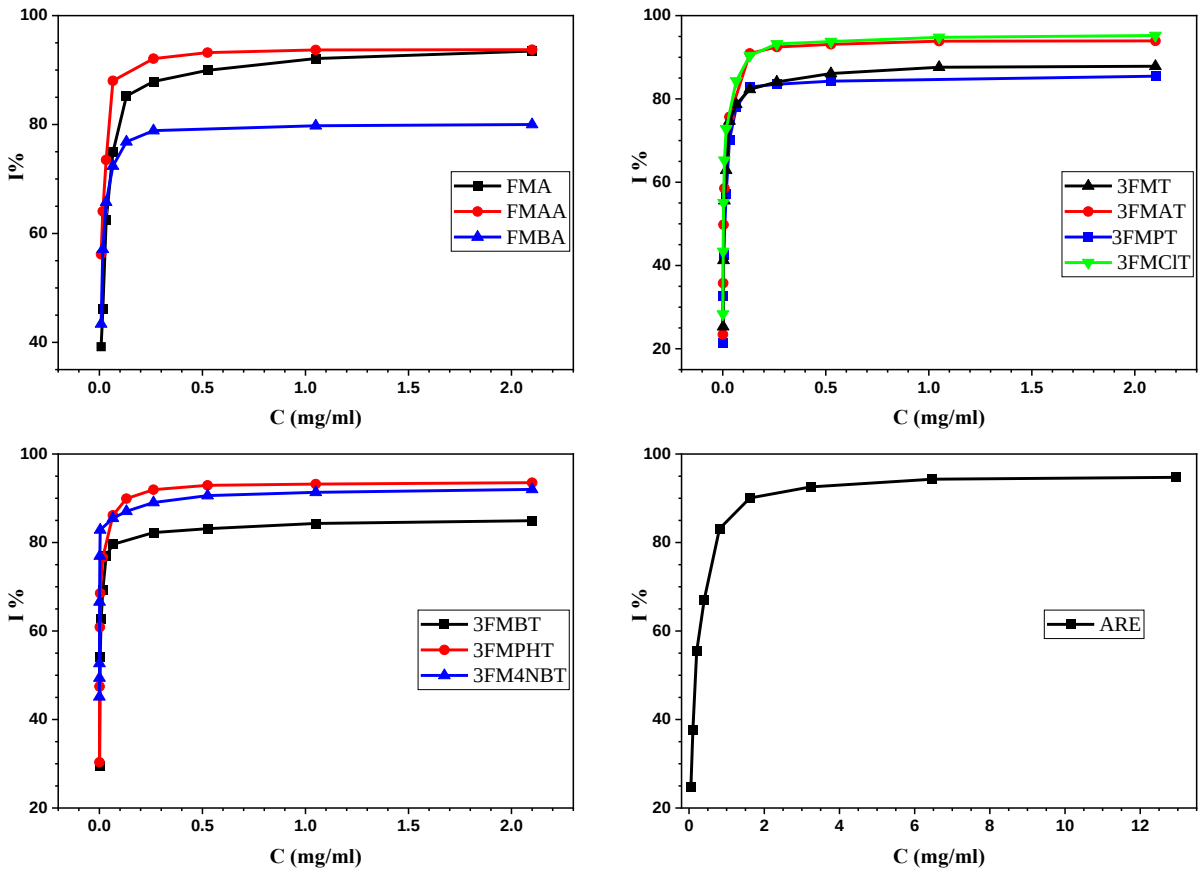

Figure IV.4. Percentage inhibition activity of α-amylase enzyme at deferent concentration of the synthetized compounds and acarbose.

The IC_{50} values were determined by analyzing the variation in absorbance values with increasing α-amylase concentration. The summarized data in Table IV.4 reveal that all tested compounds exhibit lower IC_{50} than ARE (259 µM), indicating stronger inhibitory activity.

The calculated IC_{50} values for these compounds ranged from 0.69 to 64.5 µM, which are significantly lower than that of ARE (259 µM). These results indicate that all tested compounds exhibit a stronger antidiabetic effect against α-amylase than the standard drug ARE. Notably, 3FM4NBT (IC_{50} = 0.69 µM) and 3FMPHT (IC_{50} = 2.74 µM) exhibited the strongest inhibitory effects, suggesting their potential as potent α-amylase inhibitors.

Table IV.4. IC_{50} values of the synthetized compound and acarbose for α-amylase.

ligands	Equation	R^2	IC_{50} mg/ml	IC_{50} uM
ARE	$I\% = 93.861 - 83.645 * \exp^{-3.868x}$	0.996	167 10^{-3}	259
FMA	$I\% = 91.877 - 64.756 * \exp^{-23.233x}$	0.997	18.80 10^{-3}	64.5
FMAA	$I\% = 93.613 - 49.198 * \exp^{-32.190x}$	0.999	3.74 10^{-3}	11.2
FMBA	$I\% = 79.436 - 31.903 * \exp^{-21.978x}$	0.996	3.66 10^{-3}	9.27
3FMT	$I\% = 87.067 - 81.027 * \exp^{-124.426x}$	0.997	6.29 10^{-3}	17.4
3FMAT	$I\% = 92.834 - 65.724 * \exp^{-84.995x}$	0.994	5.04 10^{-3}	14.5
3FMPT	$I\% = 83.986 - 74.782 * \exp^{-156.271x}$	0.997	5.05 10^{-3}	16.5
3FMClAT	$I\% = 94.247 - 57.550 * \exp^{-60.184x}$	0.999	4.37 10^{-3}	11.4
3FMBT	$I\% = 84.122 - 41.577 * \exp^{-80.558x}$	0.998	2.45 10^{-3}	5.99
3FMPHT	$I\% = 92.862 - 76.868 * \exp^{-452.078x}$	0.996	1.29 10^{-3}	2.74
3FM4NBT	$I\% = 90.739 - 49.729 * \exp^{-640.711x}$	0.996	0.31 10^{-3}	0.69

2.1.1. Binding free energy and binding constant:

The plots of $\frac{A_S}{A_C - A_S}$ as a function with $\frac{1}{[C]}$ are illustrated in Figure S.32. The results of binding constant K and binding free energy ΔG are summarized in Table IV.5.

The binding energy values for FMA and its derivatives range from -24.10 to -27.20 kJ/mol, while those for 3FMT and its derivatives range from -27.46 to -34.78 kJ/mol. These values are lower than that of ARE (-20.82 kJ/mol), indicating that the synthesized compounds exhibit stronger

binding interactions with α-amylase compared to the standard drug. This enhanced interaction implies a greater affinity for the enzyme, potentially leading to improved inhibitory effects.

Similarly, the binding constant follows a similar trend, showing a significant increase with structural modifications. The introduction of acetyl (-COMe) or benzoyl (-COPh) groups to FMA leads to a considerable enhancement in K, increasing it from 1.67 10^4 M^{-1} to 5.82 10^4 M^{-1}. For 3FMT, the addition of a methyl (-Me) group to the phenyl ring further raises the K to 6.27 × 10^4 M^{-1}, demonstrating the impact of even minor modifications on binding affinity. Further acylation of 3FMT, particularly through the incorporation of benzoyl (-COPh) or 4-nitrobenzoyl (-CO4NO$_2$Ph) groups, results in an even greater enhancement, with K values reaching 24.13 10^4 M^{-1} and 123.94 10^4 M^{-1}, respectively.

These findings highlight the crucial role of structural modifications, particularly the introduction of electron-withdrawing acyl groups, in significantly enhancing ligand affinity toward α-amylase. Among all the tested compounds, 3FM4NBT exhibits the strongest interaction, indicating its potential as a highly potent α-amylase inhibitor. The progressive increase in K and ΔG change across the derivatives suggests that targeted chemical modifications can be an effective strategy to develop stronger enzyme inhibitors, potentially surpassing the efficacy of the standard drug ARE.

Table IV.5. ΔG and K for the studied ligands with α-amylase at T= 298K using UV-visible.

Ligand	Equation	R^2	K (M^{-1})	-ΔG (kj.mol^{-1})
Acarbose	$A/(A_0 - A) = -1.050 - 0.153\ 1/[C]$	0.998	0.44 10^4	20.82
FMA	$A/(A_0 - A) = -1.049 - 0.018\ 1/[C]$	0.999	1.67 10^4	24.10
FMAA	$A/(A_0 - A) = -1.123 - 0.007\ 1/[C]$	0.997	5.11 10^4	26.88
FMBA	$A/(A_0 - A) = -1.245 - 0.008\ 1/[C]$	0.997	5.82 10^4	27.20
3FMT	$A/(A_0 - A) = -1.098 - 0.006\ 1/[C]$	0.997	6.27 10^4	27.46
3FMAT	$A/(A_0 - A) = -1.257 - 0.003\ 1/[C]$	0.999	14.08 10^4	29.39
3FMPT	$A/(A_0 - A) = -1.349 - 0.003\ 1/[C]$	0.997	12.40 10^4	29.08
3FMClAT	$A/(A_0 - A) = -1.232 - 0.002\ 1/[C]$	0.999	20.18 10^4	30.28
3FMBT	$A/(A_0 - A) = -1.279 - 0.002\ 1/[C]$	0.997	24.13 10^4	30.73
3FMPHT	$A/(A_0 - A) = -1.243 - 0.0009\ 1/[C]$	0.998	66.88 10^4	33.26
3FM4NBT	$A/(A_0 - A) = -1.107 - 0.0004\ 1/[C]$	0.999	123.94 10^4	34.79

2.2. Anti-inflammatory Activity:

Inflammation results from tissue and cellular damage caused by an imbalance in the regulatory mechanisms controlling the inflammatory process [52]. Diabetes has been shown to increase the susceptibility to inflammation, making effective management of inflammatory responses crucial for preventing the worsening of diabetic complications [53].

2.2.1. BSA denaturation assay:

In this study, a dose-dependent activity profile was observed for the synthesized compounds within a concentration range of 2.56 10^{-4} to 2.1 mg/mL. For the standard drug diclofenac (DIF), the activity was measured within a concentration range of 6.1 10^{-4} to 10 mg/mL, as depicted in Figure IV.5.

At a concentration of 10 mg/mL, DIF achieved the highest inhibition of protein denaturation in BSA, with an inhibition rate of 93.53%. For the compounds FMA and its derivative, inhibition rates ranging from 68.09% to 71.72% at a concentration of 2.1 mg/ml. Similarly, 3FMT and its derivative exhibited inhibition rates between 72.07% and 96.87% at the same concentration.

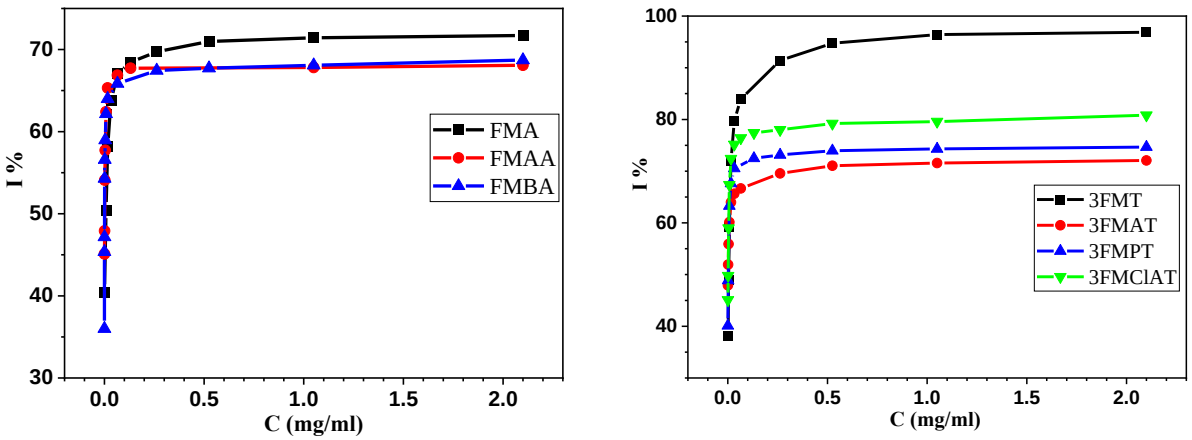

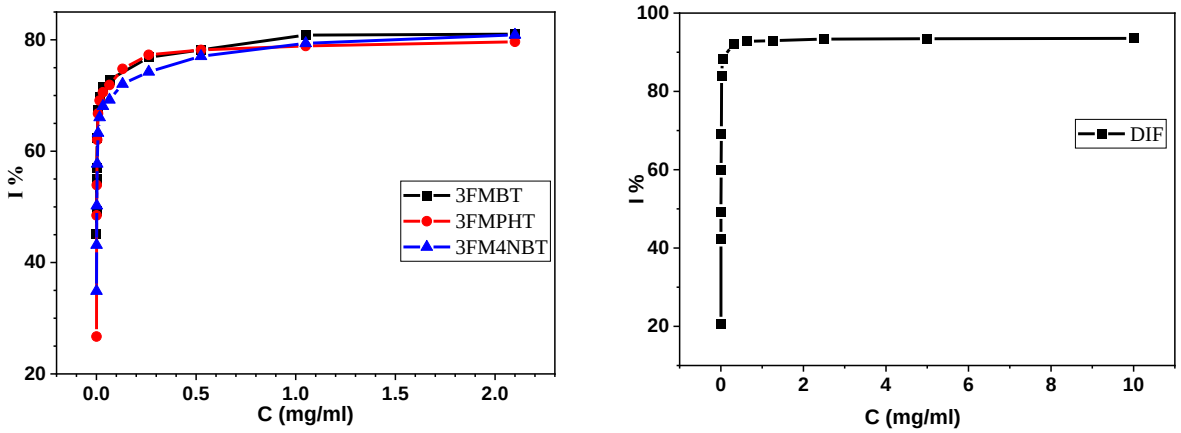

Figure IV.5. Percentage inhibition of BSA denaturation at deferent concentration of the synthetized compounds and DIF.

The IC_{50} values were determined by analyzing the variation in absorbance values with increasing BSA concentration, as summarized in Table IV.6.

The IC_{50} values for 3FMT (18.95 µM) and FMA (24.79 µM) were higher than that of DIF (15.81 µM), indicating a weaker anti-inflammatory effect. However, the acylated derivatives of both 3FMT and FMA demonstrated IC_{50} values ranging from 1.72 µM to 7.26 µM, indicating a stronger anti-inflammatory effect compared to DIF. The lower IC_{50} values of the acylated derivatives suggest a more potent anti-inflammatory activity, suggesting that structural modifications, particularly acylation, significantly enhance the inhibitory activity against BSA denaturation.

Table IV.6. IC_{50} values of the synthetized compounds and DIF for BSA denaturation.

Ligands	Equation	R^2	IC_{50} mg/ml	IC_{50} uM
DIF	$I\% = 92.480 - 77.083 * \exp^{-118.496x}$	0.997	5.03 10^{-3}	15.81
FMA	$I\% = 70.965 - 30.983 * \exp^{-54.116x}$	0.997	7.22 10^{-3}	24.79
FMAA	$I\% = 67.400 - 24.314 * \exp^{-205.368x}$	0.994	1.63 10^{-3}	4.89
FMBA	$I\% = 67.915 - 35.806 * \exp^{-983.385x}$	0.998	0.70 10^{-3}	1.78
3FMT	$I\% = 96.012 - 65.672 * \exp^{-61.527x}$	0.999	5.78 10^{-3}	18.95
3FMAT	$I\% = 71.563 - 26.756 * \exp^{-135.149x}$	0.998	1.60 10^{-3}	4.60
3FMPT	$I\% = 73.977 - 35.927 * \exp^{-154.197x}$	0.997	2.62 10^{-3}	7.26
3FMClAT	$I\% = 79.841 - 40.388 * \exp^{-149.658x}$	0.998	2.02 10^{-3}	5.30

3FMBT	$I\% = 80.903 - 38.707 * \exp^{-184.982x}$	0.999	$1.22\ 10^{-3}$	2.97
3FMPHT	$I\% = 78.912 - 31.806 * \exp^{-117.301x}$	0.998	$0.81\ 10^{-3}$	1.72
3FM4NBT	$I\% = 80.114 - 50.921 * \exp^{-271.290x}$	0.997	$1.94\ 10^{-3}$	4.26

2.2.2. Binding free energy and binding constant:

The values for the K and ΔG were determined based on changes in absorbance as the BSA concentration increased, using equation III.2. The plots of $\frac{A_S}{A_C - A_S}$ as a function with $\frac{1}{[C]}$ are shown in Figure S.33. The results of K and ΔG are summarized in Table IV.7.

The calculated ΔG values indicate that the interactions between the studied compounds and BSA are thermodynamically favorable, as evidenced by the negative free energy changes. The reference drug DIF exhibited a ΔG value of -29.61 kJ/mol with a binding constant of 1.54×10^5 M^{-1}.

Among the synthesized compounds, FMA and 3FMT showed comparable binding affinities to DIF, with ΔG values of -28.16 kJ/mol and -28.38 kJ/mol, respectively. However, the acylated derivatives of both FMA and 3FMT exhibited significantly stronger interactions with BSA, as reflected by their higher ΔG values ranging from -31.06 to -33.36 kJ/mol. Notably, the highest binding affinity was observed for FMBA and 3FMPHT, with ΔG values of -33.32 kJ/mol and -33.36 kJ/mol, respectively. These values indicate a stronger interaction with BSA than DIF, suggesting enhanced stability and potentially improved pharmacokinetics for these compounds.

The increase in K and ΔG across different derivatives suggests that structural modifications enhance ligand binding to BSA. Particularly, Acylation of FMA leads to a substantial increase in K, reaching up to 6.87×10^5 M^{-1} for FMBA, significantly strengthening protein-ligand interactions. Similarly, substitutions in 3FMT, particularly in derivatives like 3FMPHT and 3FM4NBT, further enhance binding affinity, with binding constants exceeding 5×10^5 M^{-1}. The presence of electron-withdrawing groups, such as benzoyl (-COPh) and nitro ($-NO_2$) groups, likely enhances ligand interaction with BSA binding sites by increasing hydrogen bonding and hydrophobic interactions, contributing to stronger and more stable binding.

These findings indicate that the synthesized compounds, particularly FMBA and 3FMPHT, exhibit stronger binding affinities toward BSA than DIF. The introduction of acyl and electron-withdrawing groups significantly enhances binding stability and interaction strength, suggesting that these modifications could improve the bioavailability and pharmacokinetic properties of the

compounds. This makes them promising candidates for further anti-inflammatory drug development.

Table IV.7. Binding free energies and binding constants for the studied compounds with BSA at T= 298K using UV-visible spectroscopy.

ligand	Equation	R^2	K (M^{-1})	-ΔG ($kj.mol^{-1}$)
DIF	$A/(A_0 - A) = -0.002\ 1/[C] - 1.076$	0.997	$1.54\ 10^5$	29.61
FMA	$A/(A_0 - A) = -0.005\ 1/[C] - 1.424$	0.999	$0.86\ 10^5$	28.16
FMAA	$A/(A_0 - A) = -0.001\ 1/[C] - 1.471$	0.998	$4.58\ 10^5$	32.32
FMBA	$A/(A_0 - A) = -0.001\ 1/[C] - 1.506$	0.997	$6.87\ 10^5$	33.32
3FMT	$A/(A_0 - A) = -0.004\ 1/[C] - 1.146$	0.999	$0.94\ 10^5$	28.38
3FMAT	$A/(A_0 - A) = -0.002\ 1/[C] - 1.472$	0.996	$3.28\ 10^5$	31.49
3FMPT	$A/(A_0 - A) = -0.002\ 1/[C] - 1.364$	0.998	$2.75\ 10^5$	31.06
3FMClAT	$A/(A_0 - A) = -0.002\ 1/[C] - 1.279$	0.999	$2.89\ 10^5$	31.17
3FMBT	$A/(A_0 - A) = -0.001\ 1/[C] - 1.365$	0.997	$5.65\ 10^5$	32.84
3FMPHT	$A/(A_0 - A) = -0.001\ 1/[C] - 1.384$	0.996	$6.98\ 10^5$	33.36
3FM4NBT	$A/(A_0 - A) = -0.001\ 1/[C] - 1.431$	0.998	$5.24\ 10^5$	32.65

2.3. Antibacterial Activity:

The synthesized compounds FMA, 3FMT, and their acylated derivatives were evaluated for their antibacterial activity against four bacterial strains: *E. coli*, *P. aeruginosa*, *K. pneumoniae*, and *S. aureus*. To assess their efficacy, the compounds were tested at concentrations ranging from 1 to 60 mg/mL, while the standard antibiotic Amoxicillin (AXL) was examined at concentrations between 0.12 and 30 mg/mL. The antibacterial activity was measured in terms of inhibition diameters (in mm) following 24 hours of incubation at 37°C.

The results, detailing the inhibition diameters (DI) for each bacterial strain at different concentrations, are presented in Supplementary Tables S1-S4. to facilitate the interpretation of these data, the values were also represented graphically in Figures IV.6-9, allowing for a clearer comparison of antibacterial activity among the synthesized compounds.

As illustrated in Figure IV.6, the antibacterial activity of the compounds against ***E. coli*** varied depending on the structural modifications. FMA and FMAA exhibited the highest DI, measuring 9 mm and 8 mm, respectively, at a concentration of 50 mg/mL. Similarly, FMBA and

3FMT demonstrated significant antibacterial activity, with DI of 11 mm and 9 mm, respectively, at 40 mg/mL. Notably, the acylated derivative 3FMT displayed DI ranging from 8 mm to 12 mm at the maximum tested concentration of 60 mg/mL. Among all tested compounds, 3FM4NBT, 3FMPHT, and FMBA exhibited the most potent antibacterial effects, achieving DI of 12 mm, 11.5 mm, and 11 mm, respectively, at 60 mg/mL.

These findings indicate that all synthesized compounds demonstrate antibacterial activity against *E. coli*, although their potency varies depending on the presence of acyl and electron-withdrawing functional groups. The most effective compounds, particularly 3FM4NBT, 3FMPHT, and FMBA, show promising antibacterial potential, suggesting that further structural modifications could enhance their therapeutic applications.

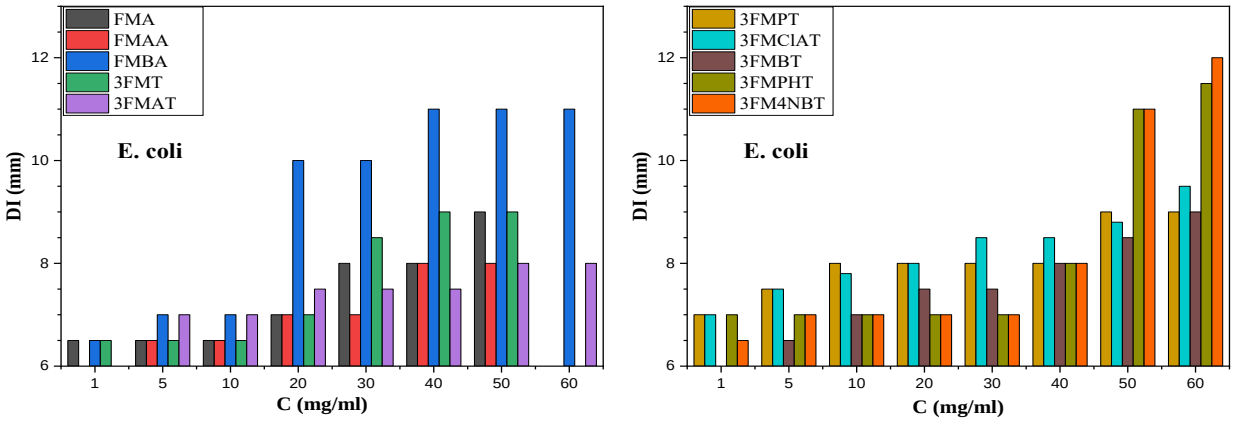

Figure IV.6. Inhibition zones of the synthesized compounds against *E. coli*.

Among the synthesized compounds, FMA, FMAA, 3FMT, and 3FMAT exhibited maximum DI of 9 mm at the highest tested concentration of 60 mg/mL against *K. pneumoniae* (Figure IV.7). However, 3FMT and 3FMAT displayed the minimum DI of 6.5 mm at 30 mg/mL, whereas FMA and FMAA displayed similar DI of 6.5 mm at a lower concentration of 1 mg/mL, suggesting a consistent level of antibacterial activity across different concentrations.

A more pronounced antibacterial effect was observed for the acylated derivatives of 3FMT and FMA, particularly FMBA, 3FMClAT, 3FMBT, 3FMPHT, and 3FM4NBT, which exhibited the highest DI ranging from 10 mm to 12 mm at 60 mg/mL. These compounds demonstrated significantly greater antibacterial potency against *K. pneumoniae* compared to their non-acylated counterparts. Conversely, 3FMPT showed the lowest DI (8.5 mm at 60 mg/mL), indicating weaker antibacterial activity than the other derivatives.

Overall, the results suggest that structural modifications, particularly acylation and the incorporation of electron-withdrawing groups, enhance antibacterial activity against *K. pneumoniae*. The superior DI observed for FMBA, 3FMClAT, 3FMBT, 3FMPHT, and 3FM4NBT highlight their potential as promising antibacterial agents against this bacterial strain.

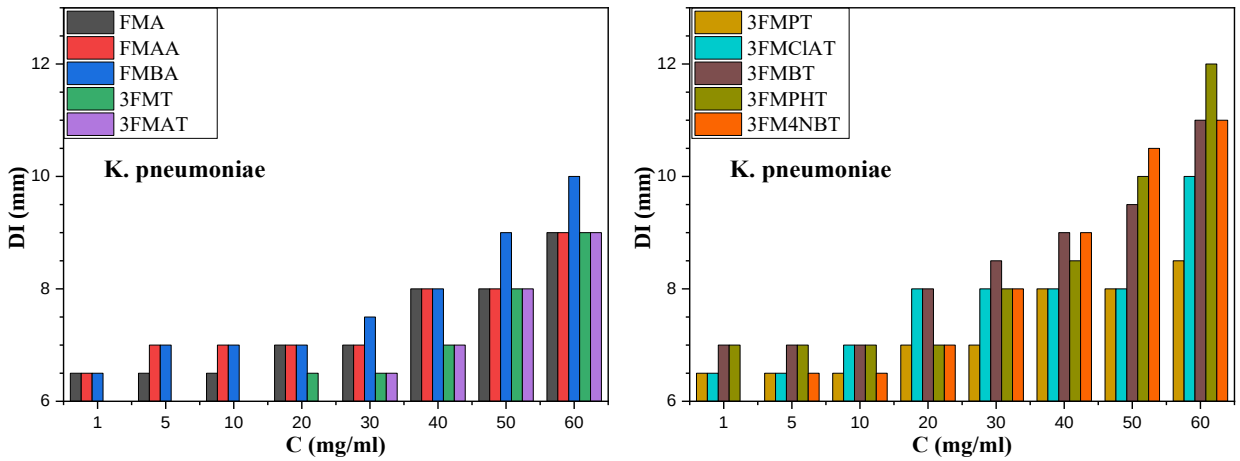

Figure IV.7. Inhibition zones of the synthesized compounds against *K. pneumoniae*.

Regarding *P. aeruginosa*, the synthesized compounds 3FMAT, FMA, 3FMClAT and 3FMPT exhibited the highest antibacterial activity, with DI ranging from 11 to 12 mm at a concentration of 60 mg/mL (Figure IV.8). At 50 mg/mL, both FMBA and 3FMT displayed DI of 11 mm. Among all tested compounds, 3FMPHT showed the weakest antibacterial effect, maintaining a minimal DI of 7 mm across all concentrations.

These results indicate that most of the synthesized compounds exhibit moderate to high antibacterial activity against *P. aeruginosa*, with 3FMAT, FMA, and 3FMPT being the most effective. The enhanced activity of these compounds may be attributed to structural modifications that improve their interaction with bacterial cell components, reinforcing their potential as antibacterial agents.

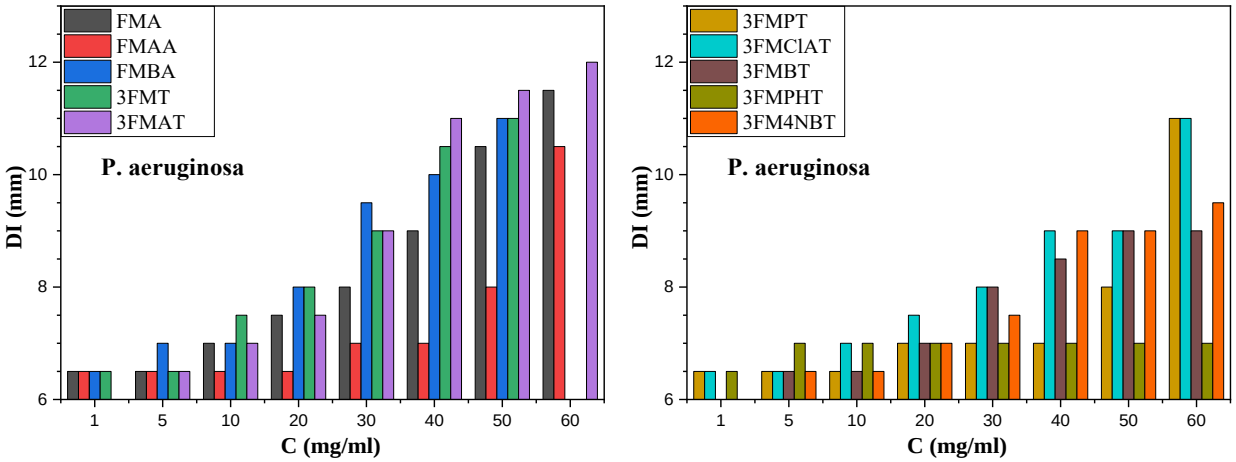

Figure IV.8. Inhibition zones of the synthesized compounds against *P. aeruginosa*.

Regarding *S. aureus*, the synthesized compounds exhibited varying degrees of antibacterial activity, with DI ranging from 6 to 14 mm across different concentrations (Figure IV.9). At the highest tested concentration (60 mg/mL), 3FM4NBT and 3FMPHT demonstrated the strongest antibacterial effects, with DI of 14 mm, followed by FMBA and 3FMBT, which reached 10 mm. Moderate antibacterial activity was observed for FMAA, 3FMAT, 3FMPT, and 3FMClAT, with DI between 9 and 9.5 mm at 60 mg/mL. Meanwhile, FMA and 3FMT exhibited the weakest inhibition, with DI of 8 mm and 7 mm, respectively.

These findings suggest that structural modifications, particularly those in 3FM4NBT and 3FMPHT, significantly enhance antibacterial activity against *S. aureus*. The presence of electron-withdrawing substituents in these compounds likely contributes to their superior inhibitory effects, making them promising candidates for further antibacterial studies.

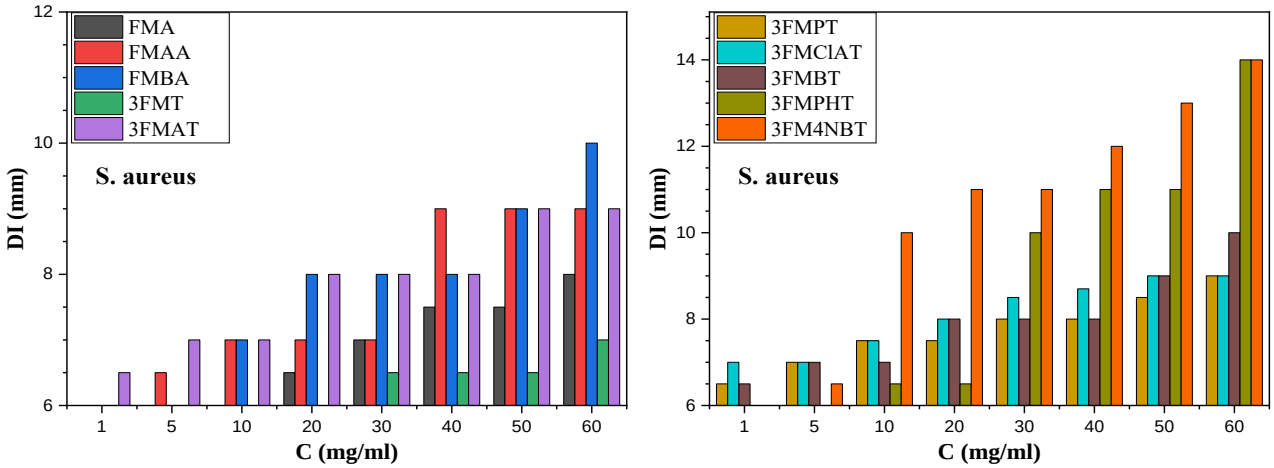

Figure IV.9. Inhibition zones of the synthesized compounds against *S. aureus*.

For the standard drug AXL, a dose-dependent antibacterial activity was observed against all four bacterial strains (Table IV.8). Against *E. coli*, AXL exhibited a high DI of 24 mm at 20 mg/mL, with a consistent maximum inhibition of 24 mm at higher concentrations. The strongest antibacterial effect was observed against *P. aeruginosa*, with an DI reaching 33 mm at 30 mg/mL. Similarly, *K. pneumoniae* showed a high DI of 30 mm at 30 mg/mL, while *S. aureus* exhibited a lower but still significant inhibition of 22 mm at the same concentration.

The antibacterial activity of the synthesized compounds varied across the tested bacterial strains, with notable effectiveness against *E. coli*, *K. pneumoniae*, and *P. aeruginosa*. Among the tested compounds, FMBA, 3FMClAT, 3FMBT, 3FMPHT, and 3FM4NBT exhibited the highest inhibition zones, particularly at higher concentrations, indicating moderate antibacterial activity. However, their effectiveness was generally lower than that of AXL, which demonstrated superior inhibition across all strains.

Table IV.8. Inhibition diameters (mm) of AXL at different concentrations (mg/mL).

bacterial strains	0.12	0.25	0.50	1.00	5.00	10.00	15.00	20.00	25.00	30.00
E. coli	6.5	6.5	7	10	20	20	22	24	24	24
K. pneumoniae	6	9	14	14	22	24	25	28	28	30
P. aeruginosa	14	15	20	20	25	25	25	25	30	33
S. aureus	6.5	6.5	6.5	6.5	19	19	19	21	21	22

3. In Silico Drug-Likeness and Pharmacokinetics Analysis:

As previously described, we assessed the drug-like properties of the synthesized ferrocenyl compounds to evaluate their potential as therapeutic agents. Additionally, we analyzed their pharmacokinetic (ADME) properties, focusing on how these compounds are absorbed

(Gastrointestinal (GI) Absorption and Cell Permeability), distributed (Blood-Brain Barrier (BBB) Permeability and Volume of Distribution (VDss)), metabolized (Cytochrome P450 Interactions), and excreted (Total Clearance) within the body.

3.1. Drug-Like:

To assess the drug-like properties of our synthesized compounds, we employed several established guidelines, including Lipinski's Rule of Five, the Ghose Filter, Veber's Rule, and the Egan Rule. These criteria assess key physicochemical parameters that influence bioavailability and drug efficacy:

- **Lipinski's Rule of Five:** This rule serves as a fundamental criterion for evaluating the drug-like properties of compounds by assessing key physicochemical parameters such as molecular weight (MW < 500 g/mol), permeability (MLogP < 4.15), rotatable bonds (ROTB < 10), hydrogen bond donors and acceptors (HBD < 5 and HBA < 10), and total polar surface area (TPSA < 140 $Å^2$).
- **Ghose Filter**: This filter extends the evaluation by considering additional criteria such as LogP (-0.4 < WLogP < 5.6), molar refractivity (40 < MR < 130), 160 < MW < 480, atom count (20 to 70 atoms), and TPSA < 140 $Å^2$ [54].
- **Veber's rule:** Emphasizes molecular flexibility and hydrophilicity, suggesting that good oral bioavailability is associated with TPSA ≤ 140 $Å^2$ and ROTB < 10 [55].
- **Egan Rule:** Predicts oral absorption based on WLogP (−1.0 ≤ WLogP ≤ 5.8) and its TPSA remains below 130 $Å^2$ [56].

According to Table IV.9, all synthesized compounds adhered to Lipinski's Rule, with only FMA demonstrating full compliance without any violations, while the remaining compounds showed a single violation (MLOGP > 4.15). Regarding the Ghose and Egan criteria, all compounds except FMBA, 3FMBT, 3FMPHT, and 3FM4NBT met the criteria. These four compounds exceeded the limits for both MLOGP (>5.6) and WLogP (>5.88), indicating higher lipophilicity. Despite these exceptions, all compounds met Veber criteria, reinforcing their potential as orally bioavailable drug candidates.

In comparison, the standard drug DIF adhered to all four drug-likeness rules, underscoring its favorable pharmacokinetic profile. Conversely, ARE displayed multiple violations: three in Lipinski's Rule (MW > 500, HBA > 10, HBD > 5), four in the Ghose Filter (MW > 480, WLogP < -0.4, MR > 130, atom count > 70), and additional violations in Veber's (TPSA > 140) and Egan's

(TPSA > 131.6) rules. This contrast highlights that while the synthesized compounds may require further optimization, they exhibit more balanced and favorable drug-like properties than ARE.

These findings suggest that most of the synthesized ferrocenyl compounds align with established drug-likeness criteria, making them promising candidates for further pharmacokinetic and biological evaluation.

Table IV.9. Drug-Likeness Properties of the synthetized ferrocenyl compounds.

Rule	**FMA**	**FMAA**	**FMBA**	**3FMT**	**3FMAT**	**3FMPT**
MW	291.17	333.21	395.27	305.2	347.23	361.26
ROTB	3	4	5	3	4	5
HBA	0	1	1	0	1	1
HBD	1	0	0	1	0	0
TPSA	12.03	20.31	20.31	12.03	20.31	20.31
MR	71.13	81.04	100.94	76.1	86.01	90.82
XlogP	2.98	2.35	4.01	3.34	2.72	3.19
WLogP	4.67	4.8	6.09	4.98	5.11	5.5
MlogP	4.22	4.08	5.2	4.46	4.31	4.53
Lipinski	Yes; 1V	Yes; 0v	Yes; 1V	Yes; 1V	Yes; 1V	Yes; 1V
Ghose	Yes	Yes	No; 1V	Yes	Yes	Yes
Veber	Yes	Yes	Yes	Yes	Yes	Yes
Egan	Yes	Yes	No; 1V	Yes	Yes	Yes
	3FMClAT	**3FMBT**	**3FMPHT**	**3FM4NBT**	**ARE**	**DIF**
MW	381.68	409.30	471.76	454.30	645.60	318.13
ROTB	5	5	6	6	9	4
HBA	1	1	2	3	19	2
HBD	0	0	0	0	14	1
TPSA	20.31	20.31	37.38	66.13	321.17	52.16
MR	90.8	105.91	116.09	114.73	136.69	75.61
XlogP	3.34	4.38	4.89	4.21	-8.53	4.4
WLogP	5.5	6.4	6.78	6.31	-8.56	3.03
MlogP	4.53	5.4	5.12	4.32	-6.94	3.84
Lipinski	Yes; 1V	Yes; 1V	Yes; 1V	Yes; 1V	No, 3V	Yes; 0v
Ghose	Yes	No; 1V	No; 1V	No; 1V	No, 4V	Yes
Veber	Yes	Yes	Yes	Yes	No	Yes
Egan	Yes	No; 1V	No; 1V	No; 1V	No	Yes

3.2. Absorption:

Absorption is a crucial step in pharmacokinetics, as it determines how a drug is taken up into the systemic circulation after administration. While drugs can be delivered through various routes, oral administration is the most common, with absorption primarily occurring in the intestine due to its large surface area. Factors such as solubility, permeability, and surface area influence the extent of absorption [57].

As presented in Table IV.10, all synthesized compounds exhibit good water solubility, with $logS_{wat}$ values ranging from -4.087 (3FMPT) to -3.666 (3FM4NBT), well above the recommended threshold of -5.7. This suggests favorable oral absorption potential. Additionally, their gastrointestinal (GI) absorption rates range from 84.23% (3FMT) to 88.98% (FMBA), surpassing the minimum absorption threshold of 30% [58]. Notably, these values are higher than that of the standard drug DIF (77.74%) and significantly superior to ARE (4.17%), confirming the improved absorption profile of the synthesized compounds.

Caco-2 cell permeability is a key predictor of intestinal absorption. Compounds with permeability values above 0.90×10^{-6} cm/s are classified as highly permeable [59]. Based on this criterion, all synthesized compounds exhibited high permeability, except 3FM4NBT (-0.05×10^{-6} cm/s) and ARE (-0.48×10^{-6} cm/s), which demonstrated poor permeability. The highest permeability was observed for 3FMAT (1.86×10^{-6} cm/s) and FMAA (1.85×10^{-6} cm/s), indicating their strong potential for efficient intestinal absorption.

Skin permeability is another important factor, particularly for transdermal drug delivery systems [59,60]. The more negative the log Kp value (with Kp in cm/s), the lower the compound's ability to penetrate the skin [34]. All compounds showed log Kp values ranging from -2.76 (FMA and 3FMT) to -2.72 (FMBA and 3FMPT), which are comparable to the reference drugs DIF (-2.72) and ARE (-2.74). These values indicate that the synthesized compounds have skin permeability properties similar to those of the reference drugs, making them potentially suitable for transdermal applications.

P-glycoprotein (P-gp) plays a vital role in drug absorption, distribution, and elimination [34]. Predicting whether a compound acts as a substrate or inhibitor of P-gp is vital during the early stages of drug discovery, as it influences the compound's bioavailability and potential for drug-drug interactions [60]. All synthesized compounds were predicted to be P-gp substrates, similar to

the standard drugs DIF and ARE, indicating their likelihood of being actively transported and possibly affecting their overall pharmacokinetic profiles.

These findings collectively highlight the strong absorption potential of the synthesized ferrocenyl compounds, with high GI absorption (≥84.23%), favorable solubility (logSwat > -4.1), and good permeability (Caco-2 > 0.90 × 10^{-6} cm/s in most cases). Their enhanced absorption profiles compared to DIF and ARE further support their potential as promising orally and transdermally bioavailable drug candidates.

Table IV.10. Absorption profile of the synthetized ferrocenyl compounds.

Rule	FMA	FMAA	FMBA	3FMT	3FMAT	3FMPT
GI absorption	84.43%	88.23%	88.98%	84.23%	88.03%	87.75%
$logS_{wat}$ (mol/L)	-3.886	-3.971	-3.736	-3.937	-4.05	-4.087
Caco2 perm	1.40	1.85	1.08	1.40	1.86	1.76
log Kp (cm/s)	-2.76	-2.74	-2.72	-2.76	-2.75	-2.72
P-gp substrate	Yes	Yes	Yes	Yes	Yes	Yes
	3FMClAT	**3FMBT**	**3FMPHT**	**3FM4NBT**	**ARE**	**DIF**
GI absorption	87.47%	88.78%	87.56%	86.96%	4.17%	77.74%
$logS_{wat}$ (mol/L)	-4.069	-3.77	-3.794	-3.666	-1.482	-3.405
Caco2 perm	1.77	1.08	1.05	-0.05	-0.48	1.225
log Kp (cm/s)	-2.73	-2.72	-2.73	-2.74	-2.74	-2.72
P-gp substrate	Yes	Yes	Yes	Yes	Yes	Yes

3.3. Distribution:

The steady-state volume of distribution (VDss) is a critical pharmacokinetic parameter that helps determine the appropriate drug dosage regimen [61]. It represents the hypothetical volume of plasma or blood in which the compound appears to be evenly distributed at equilibrium [62]. A VDss value is considered low if log L/kg is below -0.15 and high if it exceeds 0.45. Compounds with higher VDss values tend to be more distributed in tissues than in plasma [59].

According to the predictions (Table IV.11), all synthesized compounds, except 3FM4NBT, exhibit high VDss values, ranging from 0.45 (3FMPHT) to 1.00 (3FMT). This indicates that most of these compounds undergo extensive tissue distribution. In contrast, 3FM4NBT (0.14 L/kg), ARE (-0.84 L/kg) and DIF (-1.41 L/kg) demonstrate significantly lower VDss values, suggesting they primarily distributed in plasma rather than tissues.

Predicting whether a compound can cross the blood-brain barrier (BBB) is crucial in drug design, as it helps mitigate toxicities and enhances drug the effectiveness of drugs targeting the

brain [59]. Compounds with a log BB greater than 0.3 are likely to cross the BBB, while those below -1 exhibit poor brain distribution [59].

Based on the data (Table IV.11), all synthesized compounds, except 3FMPHT (-0.05) and 3FM4NBT (-0.59), have log BB values above 0.3, suggesting that they can effectively penetrate the brain. FMA and 3FMT show the highest BBB permeability (0.60), indicating their potential utility for central nervous system (CNS) related applications. On the other hand, ARE (-1.72) and DIF (0.07) demonstrate limited and moderate BBB penetration, respectively.

The blood-brain permeability–surface area product (log PS) provides a more accurate measure of CNS penetration than traditional BBB permeability assessments. Compounds with log PS values higher than -2 are expected to penetrate the CNS effectively, while those below -3 are unlikely to do so [59].

According to the results (Table IV.11), only FMA (-1.27), FMBA (-1.89), 3FMT (-1.32), and 3FMBT (-1.88) exceed the log PS threshold (-2), indicating strong CNS penetration potential. In contrast, FMAA (-2.10), 3FMAT (-2.15), 3FMPT (-2.18), and 3FMClAT (-2.18) show moderate CNS penetration, while 3FM4NBT (-1.74) remains borderline. However, ARE (-6.44) exhibits extremely poor CNS permeability, making it unlikely to reach therapeutic brain concentrations.

Overall, these findings suggest that most of the synthesized ferrocenyl compounds exhibit significant tissue distribution, high BBB permeability, and good CNS penetration, reinforcing their potential for CNS-related therapeutic applications.

Table IV.11. Distribution profile of the synthetized ferrocenyl compounds.

Rule	**FMA**	**FMAA**	**FMBA**	**3FMT**	**3FMAT**	**3FMPT**
VDss human	0.99	0.92	0.58	1.00	0.92	0.87
BBB perm	0.60	0.40	0.60	0.60	0.40	0.45
CNS perm	-1.27	-2.10	-1.89	-1.32	-2.15	-2.18
	3FMClAT	**3FMBT**	**3FMPHT**	**3FM4NBT**	**ARE**	**DIF**
VDss human	0.82	0.59	0.45	0.14	-0.84	-1.41
BBB perm	0.44	0.59	-0.05	-0.59	-1.72	0.07
CNS perm	-2.18	-1.88	-1.94	-1.74	-6.44	-2.75

Perm: permeability

3.4. Metabolism:

The cytochrome P450 (CYP450) enzymes play a crucial role in drug metabolism, processing approximately 95% of all drugs [63]. Among them, CYP1A2, CYP2C9, CYP2C19,

CYP2D6, and CYP3A4 are the most significant [64], which together manage around 90% of drug metabolism. The interaction of drugs with these enzymes directly influences their ADMET profiles [59]. Substrates are compounds that bind to the active site of an enzyme and are metabolized into either inactive form for clearance or active forms in the case of prodrugs [65].

All synthesized compounds were predicted to be substrates of CYP3A4 (Table IV.12), indicating that they are likely to be metabolized when interacting with this enzyme. This differs from the standard drugs DIF and ARE, which are not predicted to be CYP3A4 substrates, implying a potentially different metabolic pathway.

Inhibitors are compounds that bind to an enzyme's active site or another crucial binding site, thereby blocking the enzyme's ability to process its substrate and altering its catalytic activity. This inhibition can lead to drug-drug interactions (DDIs), affecting the clearance of co-administered drugs and increasing the risk of toxicity or reduced therapeutic efficacy in prodrugs requiring metabolic activation [66].

In this context, FMA, FMAA, FMBA, and 3FMT were predicted to inhibit both CYP1A2 and CYP2C19 by SwissADME, suggesting that they may interfere with the metabolism of drugs dependent on these enzymes, whereas PKCSM predicted no inhibition for these enzymes, highlighting potential model-dependent differences. Additionally, 3FMAT, 3FMPT, and 3FMClAT were identified as CYP2C19 inhibitors by SwissADME, which could further contribute to potential DDIs when co-administered with CYP2C19-metabolized drugs, but not by PKCSM, suggesting that further experimental validation is needed to confirm these inhibitory effects.

According to PKCSM, all synthesized compounds (except ARE and DIF) were predicted to be CYP3A4 inhibitors, implying their potential to affect the metabolism of other drugs processed by this enzyme. However, SwissADME predicted that none of the synthesized compounds inhibit CYP3A4, indicating a discrepancy between the two predictive models.

Table IV.12. Metabolism and excretion profiles of the synthetized ferrocenyl compounds.

Rule	FMA	FMAA	FMBA	3FMT	3FMAT	3FMPT
CYP2D6 sub	Yes	Yes	No	Yes	Yes	Yes
CYP3A4 sub	Yes	Yes	Yes	Yes	Yes	Yes
CYP1A2 inhi	No[a],Yes[b]	No[a],Yes[b]	No[a],Yes[b]	No[a],Yes[b]	No[a], No[b]	No[a], No[b]
CYP2C19 inhi	No[a],Yes[b]	No[a],Yes[b]	No[a],Yes[b]	No[a],Yes[b]	No[a],Yes[b]	No[a],Yes[b]
CYP2C9 inhi	No[a], No[b]	No[a], No[b]	No[a], No[b]	No[a], No[b]	No[a], No[b]	No[a], No[b]
CYP2D6 inhi	No[a], No[b]	No[a], No[b]	No[a], No[b]	No[a], No[b]	No[a], No[b]	No[a], No[b]
CYP3A4 inhi	Yes[a],No[b]	Yes[a],No[b]	Yes[a],No[b]	Yes[a],No[b]	Yes[a],No[b]	Yes[a],No[b]

CL_{tot}	0.07	0.05	0.03	0.05	0.04	0.04
Renal OCT2	No	No	No	No	No	No
	3FMClAT	**3FMBT**	**3FMPHT**	**3FM4NBT**	**ARE**	**DIF**
CYP2D6 sub	Yes	No	No	No	No	No
CYP3A4 sub	Yes	Yes	Yes	Yes	No	No
CYP1A2 inhi	No[a], No[b]	No[a], No[b]	No[a], No[b]	No[a], No[b]	No[a], No[b]	No[a], No[b]
CYP2C19 inhi	No[a],Yes[b]	No[a], No[b]	No[a], No[b]	No[a], No[b]	No[a], No[b]	No[a], No[b]
CYP2C9 inhi	No[a], No[b]	No[a], No[b]	No[a], No[b]	No[a], No[b]	No[a], No[b]	No[a], No[b]
CYP2D6 inhi	No[a], No[b]	No[a], No[b]	No[a], No[b]	No[a], No[b]	No[a], No[b]	No[a], No[b]
CYP3A4 inhi	Yes[a],No[b]	Yes[a],No[b]	Yes[a],No[b]	Yes[a],No[b]	No[a], No[b]	No[a], No[b]
CL_{tot}	0.76	0.02	0.59	0.01	2.68	0.15
Renal OCT2	No	No	No	No	No	No

Sub: substrate, inhi: inhibitor, [a]pKCSM, [b]SwissADME, CL_{tot}: Total clearance (ml/min).

3.5. Excretion:

Total clearance (CL_{tot}) represents the combined hepatic and renal clearances and directly relates to a compound's bioavailability. It plays a critical role in determining the dosing regimen needed to maintain steady-state drug concentrations [59].

As shown in Table IV.12, the predicted total clearance values for the ferrocenyl compounds are presented in ml/min for clarity. These values range between 0.01 and 0.76 ml/min, indicating that these compounds are poorly eliminated by the kidneys, as their clearance values fall below 5 ml/min [67]. When compared to standard drugs, ARE exhibits a total clearance of 2.68 ml/min/, which is significantly higher than those of the ferrocenyl compounds. In contrast, DIF shows a lower clearance value of 0.15 ml/min, which is still exceeded by 3FMClAT (0.76 ml/min) and 3FMPHT (0.59 ml/min).

Since approximately 40% of marketed drugs are cationic [68], the renal organic cation transporter 2 (OCT2) plays a significant role in their excretion. Inhibiting OCT2 can lead to decreased clearance of its substrates, increasing the risk of drug-drug interactions [69]. However, none of the ferrocenyl compounds were predicted to inhibit OCT2 (Table IV.12), suggesting a minimal risk of adverse interactions related to this transporter.

3.6. Toxicity:

The Ames test is a widely utilized assay that employs bacteria to evaluate the mutagenic potential of compounds, offering early insights into their genotoxicity during the drug development

process [59]. Detecting mutagenicity at this stage is crucial for filtering out harmful compounds that could pose health risks later on [60]. All the synthesized ferrocenyl compounds tested negative in the Ames toxicity assay (Table IV.13), suggesting a low risk of mutagenicity.

Acute toxicity is assessed using the median lethal dose (LD50), which represents the dose required to cause mortality in 50% of a test population (usually rats) [59]. The LD50 values of the ferrocenyl compounds in this study range from 2.22 and 3.05 mol/kg (Table IV.13). where 3FMPHT exhibited the lowest LD50 (2.22 mol/kg), followed closely by 3FM4NBT, 3FMAT, and 3FMAA with an LD50 of 2.60 mol/kg, marking them as the most toxic. In contrast, 3FMBA, 3FMClAT, and 3FMBT had the highest LD50 values (3.03–3.05 mol/kg), marking them as the least toxic.

Liver toxicity remains a critical safety issue during drug development, often leading to drug discontinuation or withdrawal from the market [59]. Similarly, drug-induced skin sensitization can cause allergic contact dermatitis and severe immune responses [60]. In this study, none of the ferrocenyl compounds were predicted to cause hepatotoxicity or skin sensitization (Table IV.13), reinforcing their favorable safety profile in these areas.

When evaluating toxicity endpoints like carcinogenicity, immunotoxicity, mutagenicity, and cytotoxicity, the majority of compounds were predicted to be inactive. However, FMBA, 3FMBT, 3FMPHT, and 3FM4NBT exhibited potential mutagenicity, with a probability ranging from 51% to 79%, indicating a moderate risk of inducing genetic mutations (Table IV.10), suggesting that these compounds are unlikely to cause adverse toxic effects. Additionally, 3FM4NBT showed a 66% probability of carcinogenicity, indicating a possible cancer-causing risk.

These findings suggest that while most synthesized ferrocenyl compounds demonstrated a low toxicity profile, but FMBA, 3FMBT, 3FMPHT, and especially 3FM4NBT require further evaluation due to their mutagenic and carcinogenic potential. The high-risk profile of 3FM4NBT necessitates additional studies before its consideration as a drug candidate.

Overall, the ferrocenyl compounds exhibit promising ADMET properties, including good absorption, tissue distribution, and predictable metabolic pathways. However, careful consideration of toxicity risks is essential during drug development to ensure safety and efficacy.

Table IV.13. Toxicity profile of the synthetized ferrocenyl compounds.

Rule	FMA	FMAA	FMBA	3FMT	3FMAT	3FMPT
Ames toxicity	No	No	No	No	No	No

LD50 (mol/kg)	2.80	2.60	3.03	2.81	2.60	2.68
Skin Sens	No	No	No	No	No	No
hepatotoxicity	No 0.71	No 0.77	No 0.73	No 0.71	No 0.79	No 0.82
Carcinogenicity	No 0.60	No 0.55	No 0.5	No 0.59	No 0.58	No 0.59
Immunotoxicity	No 0.99	No 0.99	No 0.99	No 0.98	No 0.99	No 0.99
Mutagenicity	No 0.54	No 0.51	Yes 0.54	No 0.54	No 0.52	No 0.58
Cytotoxicity	No 0.65	No 0.68	No 0.68	No 0.63	No 0.67	No 0.67
	3FMClAT	**3FMBT**	**3FMPHT**	**3FM4NBT**	**ARE**	**DIF**
Ames toxicity	No	No	No	No	No	No
LD50 (mol/kg)	3.04	3.05	2.22	2.59	2.45	2.16
Skin Sens	No	No	No	No	No	No
hepatotoxicity	No 0.77	No 0.73	No 0.62	No 0.60	Yes 0.65	Yes 0.65
Carcinogenicity	No 0.58	No 0.50	No 0.52	Yes 0.66	No 0.84	No 0.63
Immunotoxicity	No 0.94	No 0.99	No 0.98	No 0.95	Yes 0.99	No 0.97
Mutagenicity	No 0.50	Yes 0.54	Yes 0.51	Yes 0.79	No 0.76	No 0.78
Cytotoxicity	No 0.67	No 0.67	No 0.61	No 0.56	No 0.70	No 0.76

Skin Sens: Skin Sensitization

4. Molecular Docking Analysis:

To complement the findings from *in vitro* studies and provide a mechanistic explanation for the potent activity of ferrocenyl compounds, molecular docking was employed. This technique investigated the binding interactions of the ligand molecules with the active-site residues of α-amylase, BSA, COX-2, and several bacterial strains.

As describe before, the docking protocol was validated by re-docking the co-crystallized ligands into the binding sites of their respective proteins. The validation experiments demonstrated a satisfactory alignment between the docked poses of the co-crystallized ligands and their native structures, with RMSD values of 0.759 Å, 1.416 Å, and 1.555 Å for α-amylase, BSA, and COX-2, respectively, as illustrated in Figure IV.10.

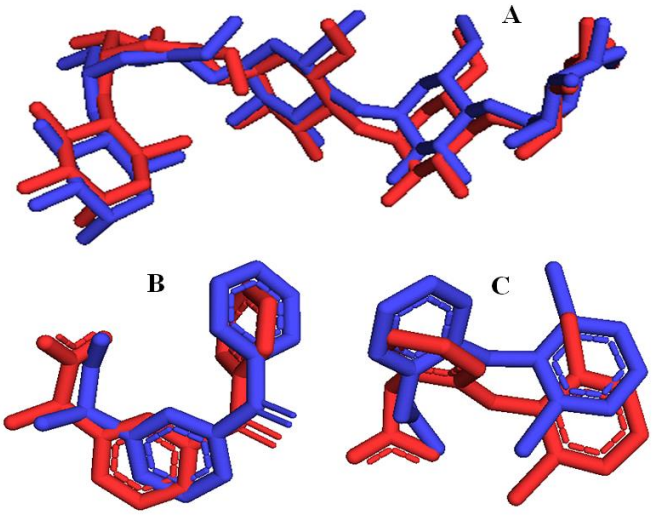

Figure IV.10. Native co-crystal (Blue) and dock pose (Red) in the active site of A:2QV4, B:6QS9 and C:1PXX.

4.1. Binding Energy Analysis:

The binding free energies for the docked ligands with α-amylase, BSA, and COX-2 are summarized in Table IV.14. The results highlight the varying affinity of the synthesized ferrocenyl derivatives towards these proteins, correlating with their potential biological activity.

Table IV.14. Binding energy (Kcal/mol) and inhibit constant (uM) of the docked ligands with 2QV4, 6QS9 and 1PXX proteins.

Protein	2QV4	6QS9	1PXX
RMSD (Å)	0.759	1.416	1.555

Ligand	-ΔG	C	-ΔG	C	-ΔG	C
Native	11.65	2.88 10^{-03}	7.82	1.85	7.91	1.6
Drug	4.88	253.63	7.79	1.95	7.70	2.26
FMA	5.85	51.80	6.89	8.97	8.17	1.03
FMAA	6.44	19.18	8.56	0.53	8.90	0.30
FMBA	7.33	4.24	9.92	0.05	10.68	0.01
3FMT	6.07	35.64	7.28	4.64	8.29	0.84
3FMAT	6.54	15.95	8.58	0.51	8.84	0.33
3FMPT	6.51	16.93	8.04	1.27	9.11	0.21
3FMClAT	6.78	10.68	8.35	0.75	9.16	0.19
3FMBT	7.23	5.04	9.28	0.16	10.95	0.01
3FMPHT	7.84	1.79	10.49	0.02	11.97	0.00
3FM4NBT	7.70	2.29	9.11	0.21	10.94	0.01

4.1.1. *α*-amylase:

The calculated ΔG values indicate a strong binding affinity between α-amylase and the studied compounds. FMA, 3FMT, and their acylated derivatives demonstrated the best fit, with ΔG values ranging from -5.85 to -7.84 kcal/mol (Table IV.14), which are lower (indicating stronger binding) than that of ARE, which has a ΔG of -4.88 kcal/mol. These results are consistent with those obtained *in vitro* results.

4.1.2. BSA:

Concerning BSA, FMA and 3FMT displayed lower affinities, with ΔG values of -6.89 kcal/mol and -7.28 kcal/mol, respectively, compared to the standard drug DIF (ΔG = -7.79 kcal/mol). However, the acylated derivatives of both FMA and 3FMT exhibited stronger binding affinities, with ΔG values ranging from -8.04 to -10.49 kcal/mol, indicating a better fit than DIF and highlighting their enhanced potential. These observations are consistent with the *in vitro* results and suggest that acylation improves the interaction between these compounds and BSA.

4.1.3. COX-2:

The agreement between experimental studies and molecular docking for α-amylase and BSA validates the experimental assays and reinforces the reliability of our conclusions. Given this consistency, molecular docking was extended to COX-2 despite the absence of *in vitro* data for this target. The strong correlation observed for α-amylase and BSA suggests that the docking predictions for COX-2 are also reliable, providing a basis for exploring the COX-2 inhibitory activity of these compounds in future experimental investigations.

The calculated ΔG reveal a strong interaction between the COX-2 enzyme and the ferrocenyl compounds. FMA, 3FMT, and their acylated derivatives exhibited favorable binding, with ΔG values ranging from -8.17 to -11.97 kcal/mol (Table IV.14), surpassing the standard drug DIF (ΔG = -7.70 kcal/mol). These findings suggest that all the ferrocenyl compounds possess significant anti-inflammatory potential against COX-2 protein.

4.1.4. Antibacterial:

As mentioned before, binding affinities of the synthesized ferrocenyl compounds were evaluated against various target proteins associated with the bacterial strains. The studied proteins include:

E. coli: DGB (PDB ID: 1KZN) and PDF (PDB ID: 1BSK).

K. pneumoniae: the targets are DHFR (PDB ID: 4OR7) and DTO4 (PDB ID: 5EIX).

P. aeruginosa: ACL (PDB ID: 5OE3), PDF (PDB ID: 1LRY), and PGDT (PDB ID: 6I1E).

S. aureus: DSS (PDB ID: 2ZCQ), DHFR (PDB ID: 3SRW), DGB (PDB ID: 3TTZ), PBP2a (PDB ID: 5M18), and PDF (PDB ID: 3U7K).

To ensure the accuracy of the docking procedure, each target protein underwent validation through redocking of their co-crystallized ligands into their respective active sites, with RMSD values presented in Table IV.15. The binding energy data of all ferrocenyl compounds, alongside the standard drug AXL and the co-crystallized ligands for each protein, are included in the supplementary materials (Table S5). Additionally, a radar plot visualizing these results is provided in Figure IV.11, facilitating comparative analysis of the antibacterial potential of these compounds.

Table IV.15. RMSD (Å) values for bacterial strain proteins after redocking of co-crystallized ligands.

Protein	RMSD	Protein	RMSD	Protein	RMSD
1KZN	1.104	5OE3	1.330	3SRW	0.906
1BSK	1.304	1LRY	1.851	3TTZ	1.058
4OR7	0.771	6I1E	1.459	5M18	1.703
5EIX	1.854	2ZCQ	1.783	3U74	1.903

As shown in Figure IV.11, the standard drug AXL exhibits higher ΔG of -7.95, -6.97, -7.77 and -6.85 with 1BSK, 6I1E, 2ZCQ and 5M18, respectively, compared to their co-crystallized ligands. This suggests that AXL has a stronger interaction potential with these proteins.

All synthesized compounds demonstrate ΔG ranging from -5.96 to -7.99 kcal/mol surpassing the native ligand of 6I1E (-4.74 kcal/mol), and between -6.25 to -7.81 kcal/mol for 5M18, exceeding its native ligand (-4.17 kcal/mol). Most compounds, except FMA, 3FMT, and 3FMPT, show ΔG between -7.96 and -8.76 kcal/mol against the native ligand of 1BSK (-7.92 kcal/mol).

exhibited binding energies of -4.99, -5.46, -5.58, and -5.77 kcal/mol, respectively, which are higher than the native ligand of 5EIX (-4.94 kcal/mol).

Additionally, all compounds except FMA and 3FMT display ΔG ranging from -7.32 to -8.99 kcal/mol, surpassing the native ligand of 2ZCQ (-7.19 kcal/mol). Specifically, 3FMClT, 3FMBT, FMBA, and 3FMPHT show ΔG of -4.99, -5.46, -5.58, and -5.77 kcal/mol, respectively, which are higher than the native ligand of 5EIX (-4.94 kcal/mol).

Furthermore, FMBA, 3FMBT, 3FM4NBTA, and 3FMPHT had ΔG of -11.36, -11.97, -12.82, and -13.01 kcal/mol, respectively, surpassing the native ligand of ligand of 5OE3 (-10.45 kcal/mol). Additionally, 3FMPHT, 3FMPHT, and 3FM4NBT demonstrate higher ΔG than the native ligands of proteins 1LRY, 3SRW, and 3TTZ, respectively, indicating a strong interaction potential.

These results indicate that the synthesized compounds predominantly target Peptidoglycan D,D-transpeptidase in *P. aeruginosa* (6I1E) and Penicillin-binding protein 2a in *S. aureus* (5M18). Additionally, all compounds except FMA and 3FMT can also interact with *S. aureus* Dehydrosqualene synthase (2ZCQ), while 3FMPHT and 3FM4NBT exhibit interactions with Dihydrofolate reductase (3SRW) and DNA gyrase subunit B (3TTZ) in *S. aureus*, respectively.

Moreover, FMBA, 3FMBT, and 3FM4NBT interact with *P. aeruginosa* Anthranilate-CoA ligase (5OE3), and 3FMPHT interacts with both *P. aeruginosa* Anthranilate-CoA ligase (5OE3) and Peptide deformylase (1LRY). Additionally, all compounds except FMA, 3FMT, and 3FMPT interact with *E. coli* Peptide deformylase (1BSK), while compounds 3FMClT, 3FMBT, FMBA, and 3FMPHT interact with *K. pneumoniae* DNA topoisomerase IV (5EIX).

These provide insights into the mechanisms of action of these compounds against the studied bacterial strains.

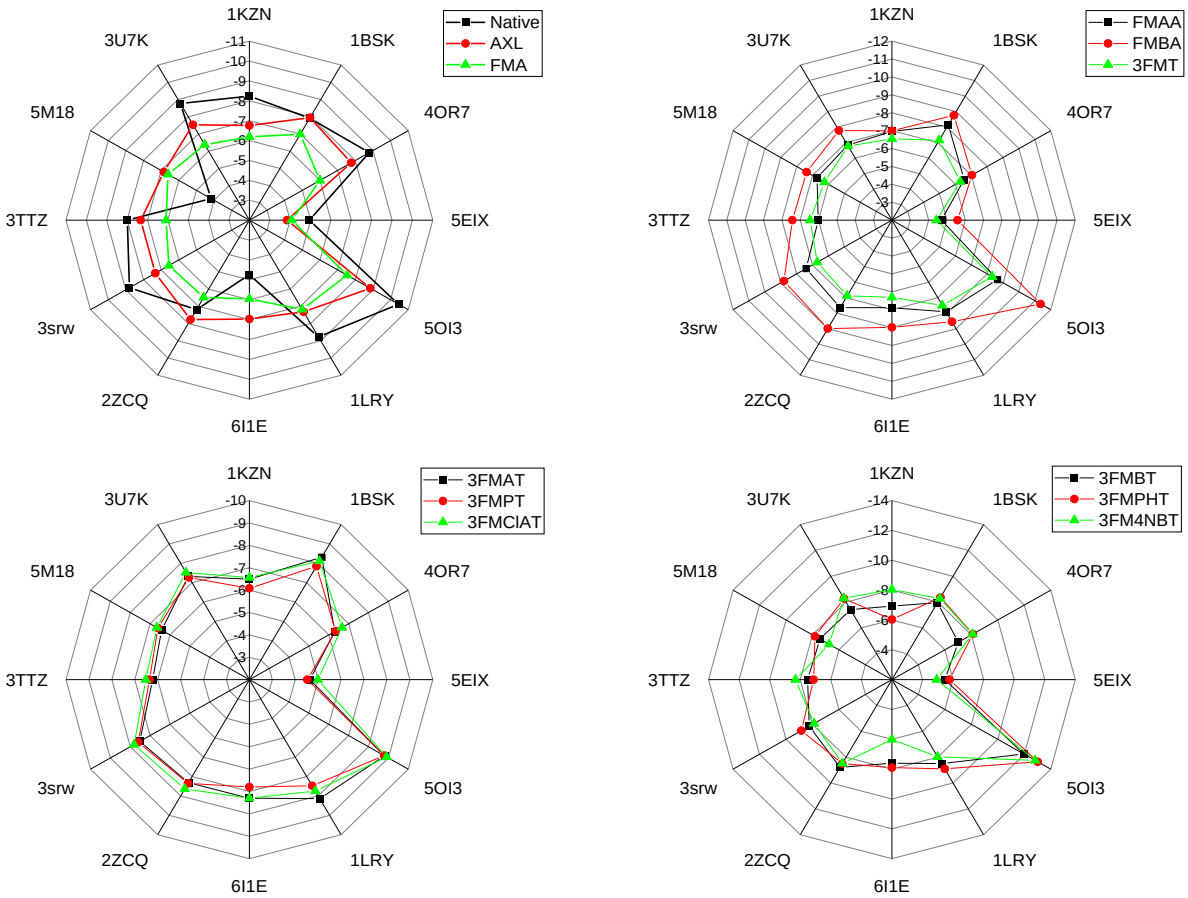

Figure IV.11. Binding energy values (kcal/mol) of docked ligands with bacterial strain proteins.

4.2. Binding Interaction Analysis:

4.2.1. *α*-amylase:

The re-docking of the co-crystallized ligand QV4 (Table S6, Figure IV.12) revealed the formation of seventeen hydrogen bonds (H-bonds) with various amino acid residues, including TYR A:62 (two interactions), GLN A:63, ASN A:105, ALA A:106 (two interactions), VAL A:107, THR A:163, GLY A:164, ARG A:195, ALA A:198, GLU A:233, HIS A:299 (two interactions), ASP A:300 (two interactions), and HIS A:305.

In comparison, the standard drug ARE forms eleven H-bonds, one hydrophobic interaction, and one unfavorable donor-donor (D-D) bond with residues such as TRP A:59, THR A:163 (three interactions), LEU A:165, LYS A:200 (two interactions), HIS A:201 (two interactions), GLU A:233 (two interactions), ILE A:235, and HIS A:305.

All the synthesized compounds formed one H-bond as shown in Figure IV.12 (Table S6). Specifically, FMA and 3FMT interacted with TRP A:59, while FMAA, 3FMAT, 3FMPT, and 3FMClAT interacted with HIS A:305. FMBA, 3FMBT, and 3FM4NBT interacted with HIS A:101, and 3FMPHT bonded with LYS A:200.

Additionally, these compounds exhibited between five to thirteen hydrophobic interactions with residues such as TRP A:59, TYR A:62, HIS A:101, LEU A:162, LEU A:165, ALA A:198, HIS A:299, and HIS A:305. Notably, 3FMBT and 3FMAT formed Pi-anion bonds with ASP A:197 and ASP A:300, respectively, further enhancing their binding stability.

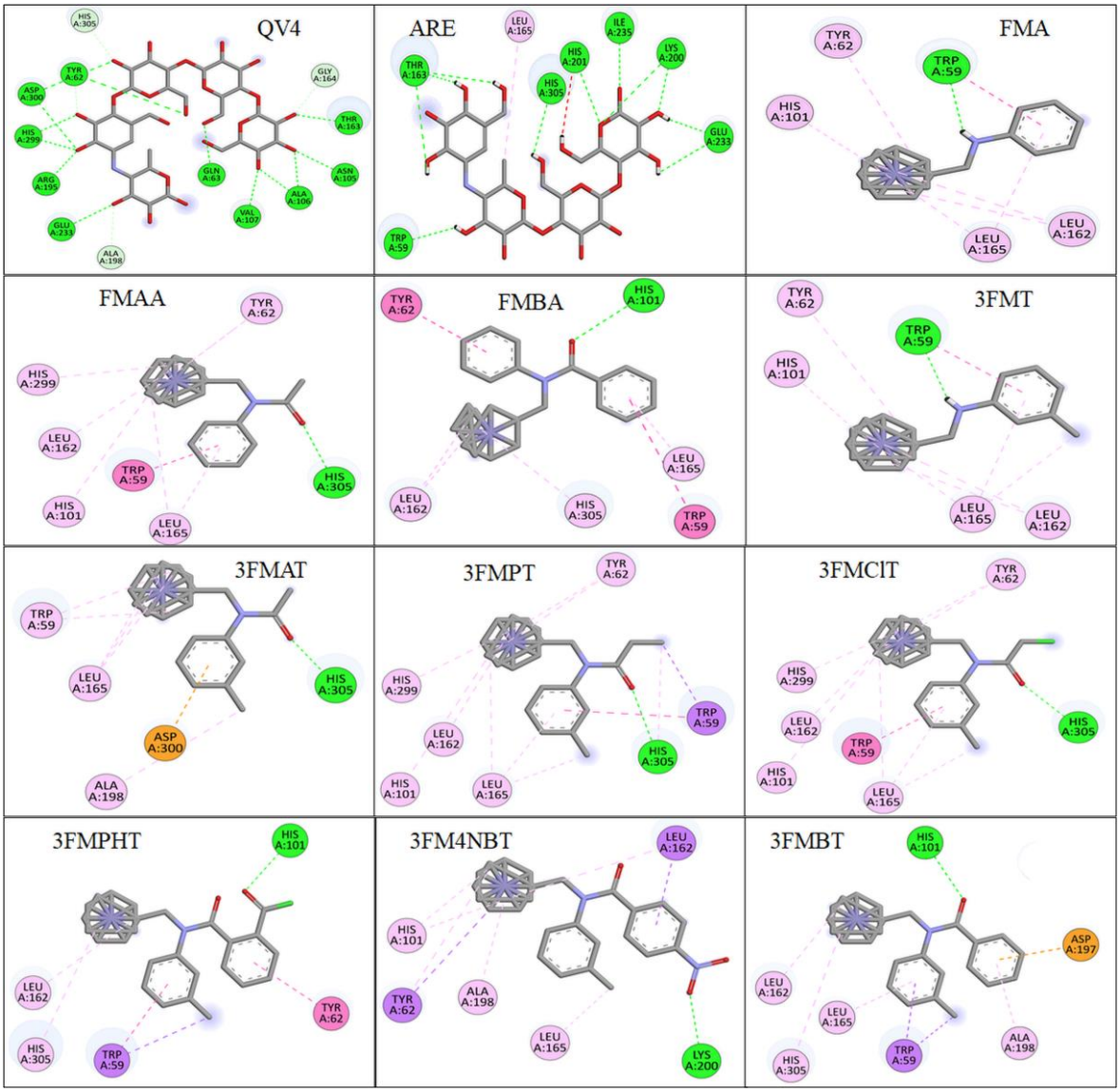

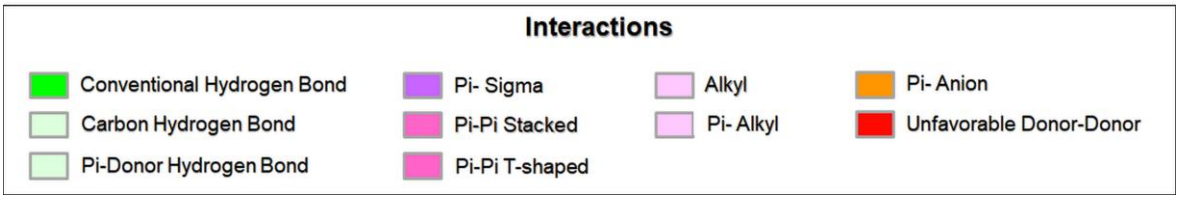

Figure IV.12. 2D illustration of possible interactions of the studied compounds with α-amylase protein.

4.2.2. BSA:

The re-docking of the co-crystallized ligand JGE into BSA protein (Table S7, Figure IV.13) revealed the formation of three H-bonds with amino acid residues, specifically TYR A:149 and ARG A:256 (two interactions). Additionally, it establishes two electrostatic bonds with HIS A:241 and ARG A:256, along with nine hydrophobic interactions involving LEU A:218, LEU A:237 (two interactions), HIS A:241, ARG A:256, LEU A:259, ALA A:260, ILE A:289, and ALA A:290.

When comparing the synthesized compounds to JGE, FMBA, 3FMPT, 3FMClAT, and 3FM4NBT exhibit the same number of H-bonds with the same amino acids. Notably, 3FM4NBT also forms an additional H-bond with HIS A:241. Both 3FMBT and the standard drug DIF each form only two H-bonds with the same residues, while 3FMPHT shows four H-bonds with ARG A:198 and ARG A:217. On the other hand, FMA, FMAA, 3FMT, and 3FMAT do not form any H-bonds.

Electrostatic interactions are also observed, with FMBA and 3FMBT interacted with HIS A:241, while 3FMPHT interacted with ARG A:217. Additionally, 3FM4NBT and 3FMPT each exhibited two electrostatic bonds involving ARG A:256 and ARG A:198 with 3FM4NBT, ARG A:198 and ARG A:217 with 3FMPT.

The standard drug DIF exhibits five hydrophobic interactions with LEU A:218, LEU A:259, ALA A:260, ILE A:263 and ILE A:289. These interactions were almost identical to those of JGE, except for an additional interaction with ILE A:263 in DIF. All the synthesized compounds exhibit between twelve to eighteen hydrophobic interactions. Notably, all compounds interacted with LEU A:259, ALA A:290, ALA260, ILE289 and ARG256 except 3FMClAT.

Interaction with LEU A:218 was observed across all compounds except 3FMPT. Additionally, FMBA, 3FMPT, 3FMClAT, 3FMBT, and 3FM4NBT interacted with LEU A:237, while only FMBA and 3FMBT formed interactions with HIS A:241 and VAL A:292. All of these interactions, except for VAL A:292, align with those observed in JGE. Furthermore, all compounds

except 3FMPHT interact with LYS A:221 and apart from FMA, 3FMBT, and 3FM4NBT, all compounds interact with ILE A:263. Additionally, FMA, 3FMBT, 3FM4NBT, and 3FMPHT also interacted with PHE A:222, whereas 3FMAT, 3FMPT, and 3FMClAT interacted with ARG A:217. Lastly, 3FMClAT and 3FMPHT interacted with LEU A:233, while 3FMPT, 3FMBT, and 3FMPHT interacted with TYR A:149, TRP A:213, and LEU A:274, respectively.

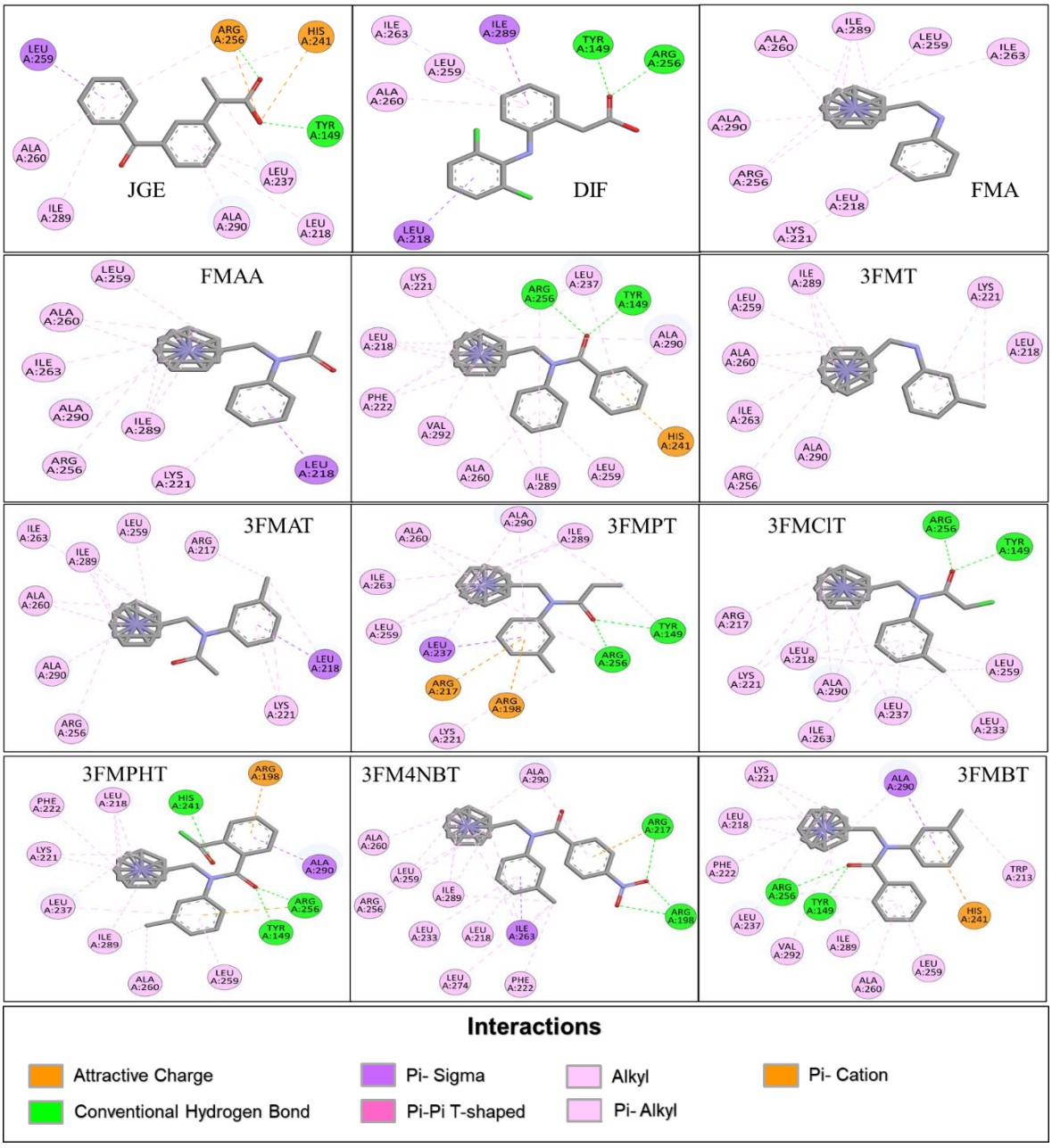

Figure IV.13. 2D illustration of possible interactions of studied compounds with the BSA protein.

4.2.3. COX-2:

The re-docking of the co-crystallized ligand CO-DIF into the COX-2 protein (Table S8, Figure IV.14) revealed that it forms two H-bonds with the amino acid residues ALA A:527 and SER A:530, one Pi-sulfur interaction with MET A:522, and four hydrophobic interactions involving VAL A:349, TRP A:387, VAL A:523, and ALA A:527. Additionally, the standard drug replicates these interactions while also forming an extra H-bond with TYR A:385.

Among the synthesized compounds, only FMA, 3FMPT, and 3FMPHT exhibit one H-bond each with SER A:530, SER A:530, and SER A:353, respectively. Both FMA and 3FMAT also show a Pi-sulfur interaction with MET A:522, similar to the native ligand, while FMA uniquely forms a Pi-lone pair bond with SER A:530.

All synthesized compounds demonstrate hydrophobic interactions with both VAL A:523 and ALA A:527. Most compounds, except 3FMT and 3FMBT, also interacted with TRP A:387, while only FMA did not interact with VAL A:349.

Furthermore, FMA engaged with additional residues such as PHE A:205, VAL A:344, LEU A:352, PHE A:381, TYR A:385, and LEU A:534. FMAA, on the other hand, interacted with TYR A:355 and LEU A:531. FMBA, 3FMT, 3FMClAT, 3FMBT, and 3FMPHT shared common interactions with LEU A:352, TYR A:385, PHE A:518, and MET A:522. FMBA uniquely interacted with SER A:553, while both 3FMBT and 3FMPHT interacted with SER A:353 and LEU A:531.

3FMPT and 3FMClAT consistently interacted with LEU A:359, while PHE A:381 interactions were observed in 3FMT, 3FMPT, 3FMClAT, and 3FMPHT. Interactions with TYR A:355 were found in 3FMT, 3FMAT, and 3FMClAT, with 3FMT also engaging with HIS A:90.

Additionally, 3FMAT and 3FMPT shared interactions with PHE A:518 and LEU A:531, while 3FMPHT also targeted PHE A:518. Furthermore, 3FMAT formed an extra interaction with MET A:522. Both 3FMPT and 3FMPHT engaged with TYR A:385, with 3FMPHT also forming a bond with SER A:353, while 3FMPT interacted with VAL A:116, LEU A:352, LEU A:384, and LEU A:534.

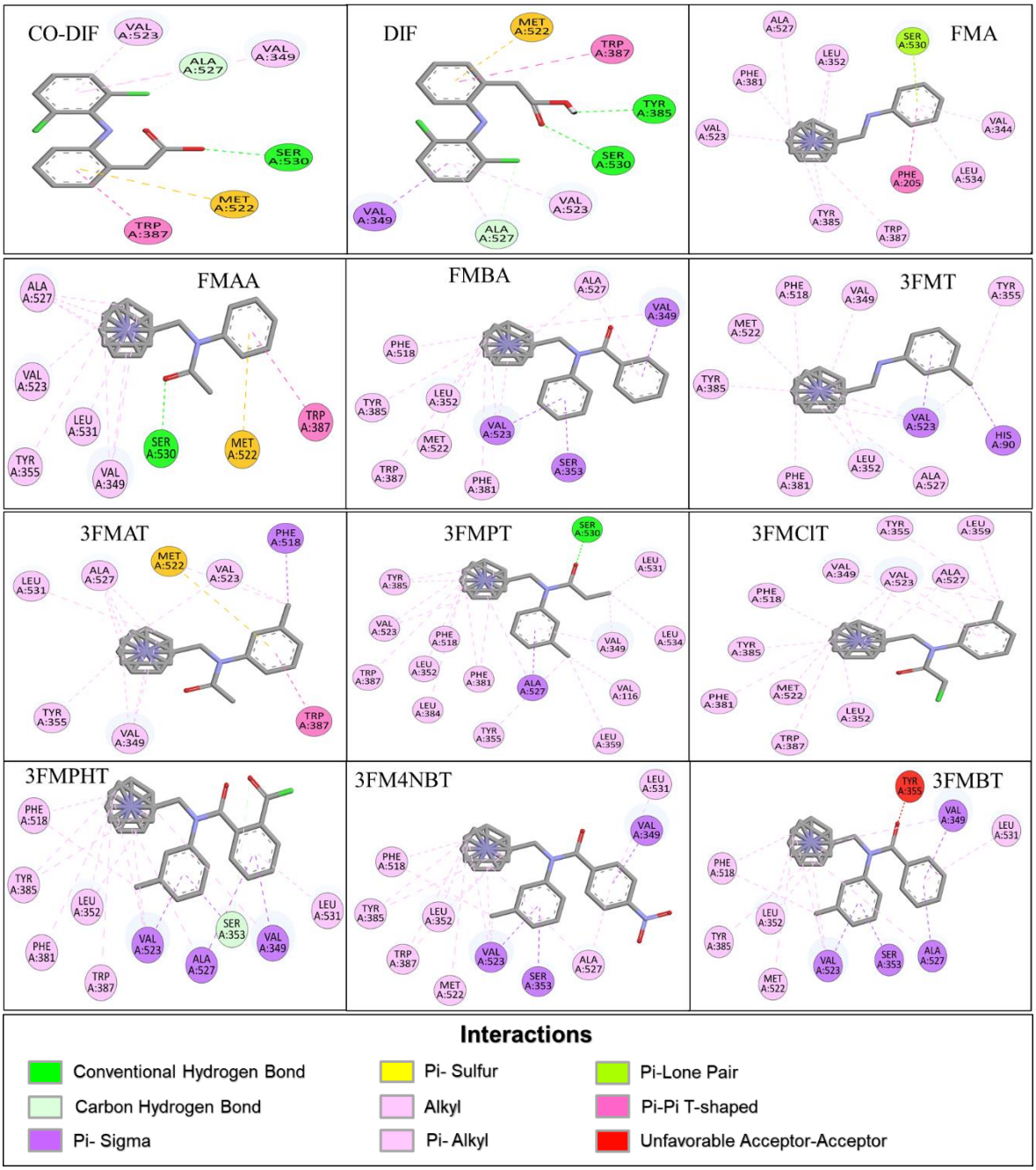

Figure IV.14. 2D illustration of possible interactions of studied compounds, with COX-2 protein.

5. DFT Analysis:

5.1. Geometry Optimization:

Geometry optimization is a fundamental step in quantum chemical calculations, essential for identifying the most stable molecular conformations [70]. This process minimizes the system's

energy, providing a deeper understanding of the structural properties of the studied compounds [71].

In this study, geometry optimization was conducted to gain deeper insights into the molecular structure of the synthesized compounds and their interactions with the previously mentioned target activities. The most stable conformer of the synthesized compounds was obtained in the gas phase using the B3LYP/6–311++G(d,p) level of DFT (Figure IV.15).

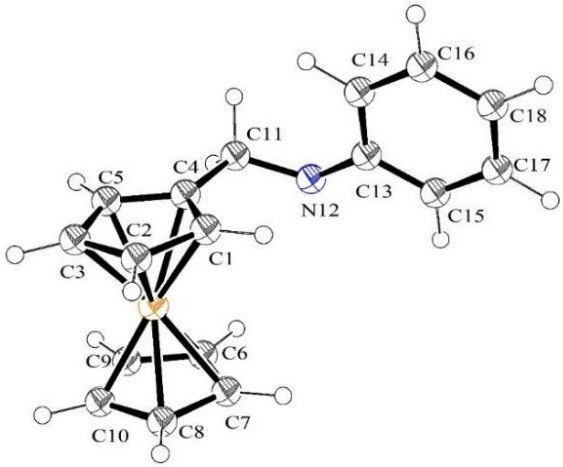

Figure IV.15. General conformation of synthetized compounds (ORTEP View 03, V1.08); color codes are White (Hydrogen), Grey (Carbon), Blue (Nitrogen), Orange (Iron).

The calculations revealed that the lowest energy-minimized structures exhibit a common design featuring cyclopentane and phenyl rings. Notably, the average bond distances between the carbons of the cyclopentane rings and the iron atom (Table IV.16) ranged from 2.076 Å to 2.077 Å, which closely aligns with the X-ray data value of 2.076 Å. Additionally, the average bond distances between the carbons (C=C) in the cyclopentane rings ranged from 1.426 Å to 1.427 Å, while the X-ray data value was 1.423 Å, showing only a slight variation. These findings indicate that the iron atom is nearly equidistant from the adjacent carbons, implying an equal electronic distribution across the two rings.

The average bond distances for C4-C11, C11-N12, and N12-C13 in FMA and 3FMT were 1.452 Å, Upon the addition of -COMe (FMAA, 3FMAT) and -COPh (FMBA, 3FMBT) groups increased these distances to 1.473 Å–1.477 Å, with only a negligible variation of 0.001 Å Similarly, the addition of -COEt (3FMPT) and COMeCl (3FMClT) groups to 3FMT resulted in bond distances remaining at 1.473 Å. For the remaining acylated compounds, the average bond distances ranged from 1.475 Å to 1.477 Å. Furthermore, the average bond distances between the carbons in

the phenyl rings ranged from 1.394 Å to 1.398 Å, slightly deviating from the X-ray data value of 1.410 Å by 0.012–0.016 Å.

Table IV.16. Theoretical geometric parameters of FMA, 3FMT and their acylated compounds.

	C1–Fe	C2–Fe	C3–Fe	C4–Fe	C5–Fe	C6–Fe	C7–Fe	C8–Fe	C9–Fe	C10–Fe	Average
FMA	2.079	2.073	2.072	2.085	2.071	2.08	2.08	2.078	2.079	2.077	**2.077**
FMAA	2.074	2.077	2.074	2.073	2.072	2.077	2.077	2.077	2.078	2.078	**2.076**
FMBA	2.072	2.077	2.076	2.072	2.073	2.078	2.078	2.077	2.078	2.077	**2.076**
3FMT	2.079	2.073	2.072	2.085	2.071	2.08	2.08	2.078	2.079	2.077	**2.077**
3FMAT	2.074	2.076	2.074	2.073	2.072	2.077	2.077	2.077	2.078	2.078	**2.076**
3FMPT	2.074	2.076	2.074	2.074	2.072	2.077	2.077	2.077	2.078	2.078	**2.076**
3FMClT	2.074	2.077	2.075	2.072	2.072	2.078	2.078	2.077	2.078	2.078	**2.076**
3FMBT	2.072	2.077	2.076	2.073	2.073	2.078	2.078	2.077	2.078	2.078	**2.076**
3FMPHT	2.075	2.078	2.076	2.074	2.074	2.078	2.078	2.077	2.078	2.077	**2.077**
3FM4NBT	2.071	2.077	2.077	2.071	2.073	2.079	2.079	2.078	2.078	2.077	**2.076**
X-ray	2.072[a]	2.079[a]	2.077[a]	2.073[a]	2.073[a]	2.079[a]	2.078[a]	2.077[a]	2.078[a]	2.078[a]	**2.076**
	C1-C2	**C1-C4**	**C2-C3**	**C3-C5**	**C5-C4**	**C6-C7**	**C6-C9**	**C7-C8**	**C8-C10**	**C10-C9**	**Average**
FMA	1.426	1.429	1.425	1.426	1.431	1.427	1.426	1.426	1.426	1.426	**1.427**
FMAA	1.424	1.431	1.427	1.425	1.431	1.426	1.427	1.426	1.426	1.426	**1.427**
FMBA	1.424	1.432	1.426	1.424	1.43	1.426	1.426	1.426	1.426	1.426	**1.427**
3FMT	1.426	1.429	1.425	1.426	1.431	1.427	1.426	1.426	1.426	1.426	**1.427**
3FMAT	1.425	1.431	1.427	1.425	1.431	1.426	1.427	1.426	1.426	1.426	**1.427**
3FMPT	1.425	1.431	1.427	1.425	1.431	1.426	1.427	1.426	1.426	1.426	**1.427**
3FMClT	1.424	1.431	1.427	1.425	1.431	1.426	1.427	1.426	1.426	1.426	**1.427**
3FMBT	1.425	1.432	1.426	1.424	1.43	1.426	1.426	1.426	1.426	1.426	**1.427**
3FMPHT	1.424	1.43	1.426	1.424	1.43	1.426	1.427	1.426	1.426	1.426	**1.426**
3FM4NBT	1.424	1.432	1.426	1.424	1.43	1.426	1.426	1.426	1.426	1.426	**1.427**
X-ray	1.420[b]	1.430[b]	1.424[b]	1.425[b]	1.433[b]	1.410[b]	1.408[b]	1.416[b]	1.420[b]	1.441[b]	**1.423**
	C4-C11	**C11-N12**	**N12-C13**	**Average**	**C13-C14**	**C13-C15**	**C14-C16**	**C15-C17**	**C16-C18**	**C17-C18**	**Average**
FMA	1.512	1.452	1.392	**1.452**	1.405	1.409	1.394	1.388	1.392	1.396	**1.397**
FMAA	1.504	1.481	1.434	**1.473**	1.397	1.398	1.394	1.393	1.394	1.395	**1.395**
FMBA	1.505	1.483	1.441	**1.476**	1.395	1.395	1.393	1.394	1.394	1.393	**1.394**
3FMT	1.512	1.452	1.393	**1.452**	1.403	1.41	1.394	1.391	1.39	1.402	**1.398**
3FMAT	1.504	1.48	1.435	**1.473**	1.394	1.398	1.394	1.396	1.392	1.401	**1.396**
3FMPT	1.504	1.481	1.435	**1.473**	1.395	1.398	1.394	1.397	1.392	1.4	**1.396**
3FMClT	1.503	1.483	1.437	**1.474**	1.394	1.399	1.395	1.396	1.391	1.401	**1.396**
3FMBT	1.505	1.483	1.442	**1.477**	1.393	1.398	1.395	1.399	1.392	1.393	**1.395**
3FMPHT	1.504	1.48	1.442	**1.475**	1.392	1.394	1.392	1.398	1.393	1.398	**1.395**
3FM4NBT	1.504	1.484	1.443	**1.477**	1.393	1.394	1.392	1.398	1.393	1.398	**1.395**
X-ray	1.535[b]	1.479[b]	1.371[b]	**1.462**	1.429[b]	1.435[b]	1.393[b]	1.418[b]	1.410[b]	1.379[b]	**1.41**

a [72]. b [73]

5.2. FMO Analysis:

According to frontier molecular orbitals (FMOs) theory, the HOMO and the LUMO of compounds are crucial for intermolecular interactions [74]. Additionally, the energy gap (ΔE_{H-L}) between HOMO and LUMO reflects the energy contribution to the formation of covalent bonds [75]. The distribution and energies of the HOMO and LUMO, along with their corresponding ΔE_{H-L}, were calculated in vacuum for FMA, 3FMT, and their acylated derivatives. These results are illustrated in Figure IV.16 and summarized in Table IV.14.

From Figure IV.16, it can be observed that the HOMO and LUMO orbital distributions remain consistent across all acylated compounds, except for FMA and 3FMT. Specifically, in most compounds (FMAA, FMBA, 3FMAT, 3FMPT, and 3FMClT), the HOMO orbitals are predominantly localized on the cyclopentane rings, while the LUMO orbitals are concentrated on the phenyl ring (aniline in FMAA and FMBA, toluidine in 3FMAT, 3FMPT, and 3FMClT) and the amide group (N-C=O). This orbital distribution indicates that the cyclopentane ring acts as an electron donor, while the phenyl ring and amide group act as electron acceptors, facilitating potential charge transfer during molecular interactions.

For 3FMBT, 3FMPHT, and 3FM4NBT, the LUMO orbitals are found on the second phenyl ring (benzoyl group) and the amide group (N-C=O), indicating a shift in the electron-accepting region. This shift suggests that these compounds may exhibit different electronic properties and reactivity patterns, particularly in binding interactions involving the carbonyl group and the extended π-system of the benzoyl moiety. These variations could lead to enhanced binding affinities in biological systems by stabilizing interactions with electron-deficient regions of the target protein.

In contrast, the HOMO distribution for FMA and 3FMT differs from the acylated derivatives. In these compounds, the HOMO orbitals are distributed over the phenyl ring (aniline in FMA, toluidine in 3FMT), the amine group (CH_2-NH), and the attached cyclopentane ring, highlighting these regions as the primary electron-donating sites. Meanwhile, the LUMO orbitals extend over the entire molecule, excluding the amine group (NH), in both FMA and 3FMT. This extensive LUMO distribution implies that these compounds might participate in widespread electron-accepting interactions, potentially enhancing their reactivity toward electrophilic species.

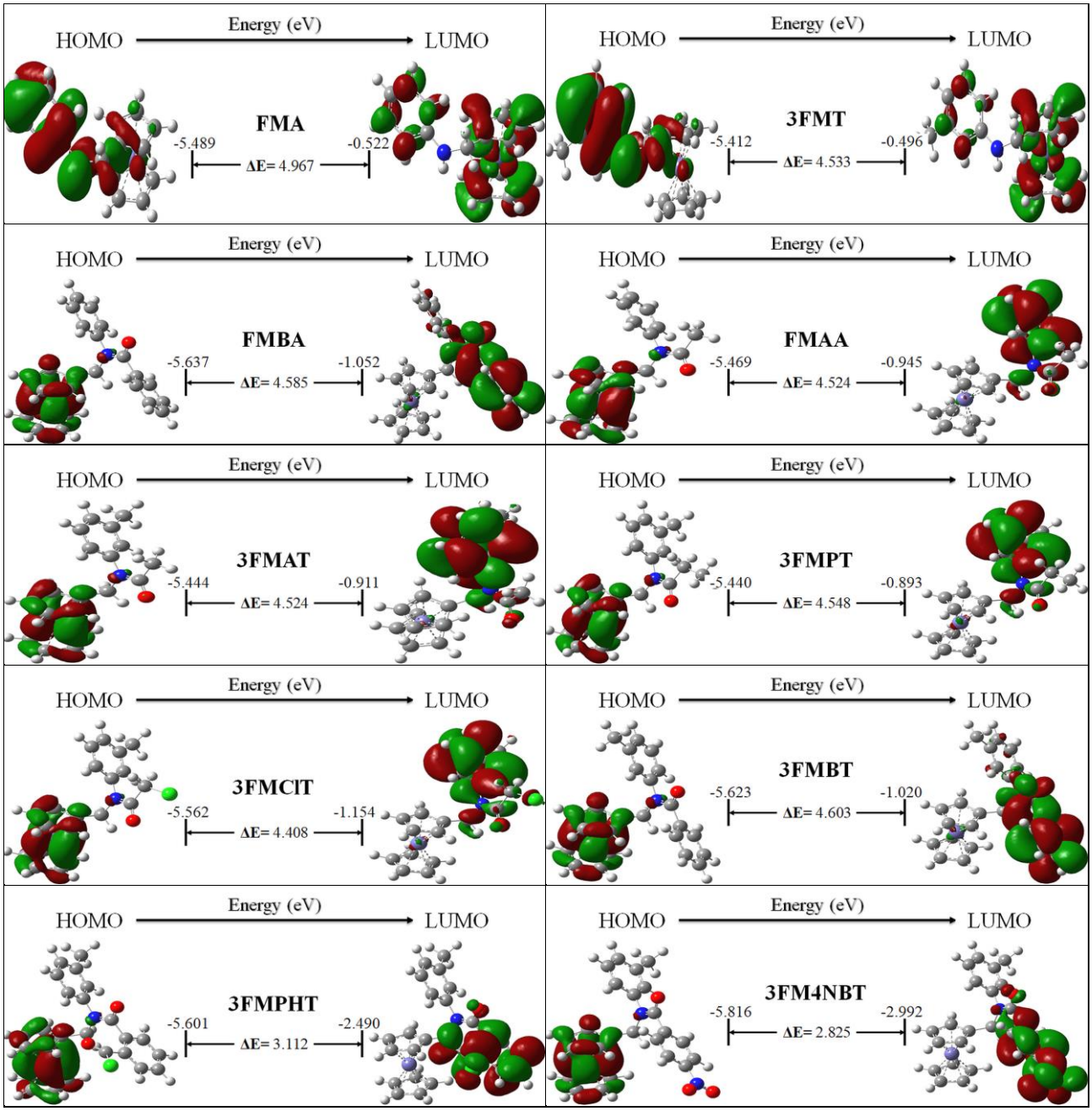

Figure IV.16. HOMO and LUMO orbitals distribution for the optimized molecules in the gas phase.

From Table IV.17, the HOMO energy values range from -5.41 eV for 3FMT to -5.82 eV for 3FM4NBT. The LUMO energy values, which represent the electron-accepting capabilities of the compounds, exhibit greater variation. Among these, 3FM4NBT (-2.99 eV) and 3FMPHT (-2.49 eV) have the lowest LUMO energies, indicating a high electron-accepting ability. On the other

hand, FMA (-0.52 eV) and 3FMT (-0.50 eV) show the highest LUMO energies, suggesting a lower tendency to accept electrons and relatively less reactivity.

The electronic properties derived from the FMOs suggest that acylated derivatives, particularly 3FMBT, 3FMPHT, 3FM4NBT, and FMBA, may exhibit enhanced electron-donating and electron-accepting capacities due to extended conjugation over the benzoyl group. This feature can contribute to stronger binding interactions and potentially higher biological activity. The differences in orbital localization and energy levels provide valuable insights into the reactivity and binding behavior of these compounds, emphasizing their importance in drug design and molecular recognition processes.

The ΔE_{H-L} values for FMA and 3FMT are 4.94 eV and 4.92 eV, respectively. Meanwhile, for acylated derivatives, ΔE_{H-L} values range from 2.83 eV to 4.60 eV. The slightly larger ΔE_{H-L} values for FMA and 3FMT suggest that these compounds may exhibit relatively lower reactivity and higher stability. However, compounds with smaller ΔE_{H-L} values, such as 3FM4NBT (2.83 eV) and 3FMPHT (3.11 eV), are expected to be more reactive, showing stronger interactions with electron-deficient regions in target proteins.

The decreasing ΔE_{H-L} trend for acylated derivatives (FMAA, FMBA, 3FMAT, etc.) suggests that the introduction of functional groups like -COMe, -COPh, -COEt, and others effectively reduces the energy gap, thereby enhancing the compounds' potential for intermolecular interactions, particularly with biological targets. This effect is particularly pronounced in 3FM4NBT, where the significantly lower ΔE_{H-L} suggests higher reactivity and greater likelihood of strong binding to electron-deficient regions of the target enzyme or receptor.

These observations highlight the critical role of functional group modifications in improving the biological activity of the synthesized compounds. This is further supported by molecular docking studies, which reveal strong binding affinities toward target proteins such as α-amylase, BSA, COX-2, and antibacterial activity against *E. coli*, *S. aureus*, and *K. pneumoniae*.

5.3. Quantum Chemical Descriptors:

Table IV.17 presents the calculated quantum reactivity descriptors for the synthesized compounds, providing insight into their electronic properties and reactivity [76].

The ionization potential (IP) values range from 5.41 eV to 5.82 eV, indicating relative stability across the studied compounds. Notably, 3FM4NBT exhibits the highest IP (5.82 eV),

indicating greater difficulty in electron removal, followed by 3FMBT (5.62 eV), 3FMPhT (5.60 eV), and FMBA (5.64 eV). In contrast, 3FMT (5.41 eV) and FMA (5.46 eV) have the lowest IP values, implying a slightly easier electron removal process

Regarding electron affinity (EA), 3FM4NBT (2.99 eV) and 3FMPhT (2.49 eV) exhibit the highest values, indicating a greater tendency to accept electrons. FMA (0.52 eV) and 3FMT (0.50 eV) have the lowest EA values, suggesting reduced electron-accepting ability.

Electronegativity (χ), which indicates the ability of a molecule to attract electrons, ranges from 2.95 eV (3FMT) to 4.40 eV (3FM4NBT). The highest values for 3FM4NBT (4.40 eV) and 3FMPhT (4.05 eV) suggest enhanced electron attraction and reactivity, while FMA (2.99 eV) and 3FMT (2.95 eV) exhibit the lowest electronegativity values.

Chemical hardness (η), which represents a molecule's resistance to electronic deformation, is lowest for 3FM4NBT (1.41 eV) and 3FMPhT (1.56 eV), indicating higher reactivity. Conversely, FMA (2.47 eV) and 3FMT (2.46 eV) exhibit the highest hardness values, suggesting lower reactivity.

In agreement with these findings, softness (σ) values are highest for 3FM4NBT (0.35 eV^{-1}) and 3FMPhT (0.32 eV^{-1}), reinforcing their greater reactivity, while FMA and 3FMT (both 0.20 eV^{-1}) have the lowest softness values, indicating reduced chemical flexibility.

The electrophilicity index (ω) is highest for 3FM4NBT (6.87 eV) and 3FMPhT (5.26 eV), suggesting they are the most electrophilic compounds, making them strong electron acceptors. In contrast, FMA (1.81 eV) and 3FMT (1.77 eV) have the lowest electrophilicity indices, indicating weaker electrophilic behavior.

The electron-donating (ω^-) and electron-accepting (ω^+) capacities further support these trends. 3FM4NBT (ω^- = 9.24 eV, ω^+ = 4.84 eV) and 3FMPhT (ω^- = 7.48 eV, ω^+ = 3.43 eV) exhibit the highest values, confirming strong redox potential. Conversely, FMA (ω^- = 3.62 eV, ω^+ = 0.62 eV) and 3FMT (ω^- = 3.56 eV, ω^+ = 0.61 eV) exhibit the lowest values, indicating lower reactivity.

These quantum descriptors align with the trends observed in FMO analysis, indicating that 3FM4NBT and 3FMPhT exhibit the highest reactivity and strongest electron-accepting abilities. This reinforces their potential biological activity, consistent with molecular docking and *in vitro* studies, which demonstrate high binding affinity toward α-amylase, BSA, COX-2, and significant antibacterial activity against *E. coli*, *S. aureus*, and *K. pneumoniae* species.

Table IV.17. Calculated quantum reactivity descriptors for synthetized compounds computed.

	FMA	FMAA	FMBA	3FMT	3FMAT
HOMO (eV)	-5.46	-5.47	-5.64	-5.41	-5.44
LUMO (eV)	-0.52	-0.95	-1.05	-0.50	-0.91
ΔE (eV)	4.94	4.52	4.59	4.92	4.53
IP (eV)	5.46	5.47	5.64	5.41	5.44
EA (eV)	0.52	0.95	1.05	0.50	0.91
χ (eV)	2.99	3.21	3.34	2.95	3.18
η (eV)	2.47	2.26	2.29	2.46	2.27
σ (eV^{-1})	0.20	0.22	0.22	0.20	0.22
ω (eV)	1.81	2.27	2.44	1.77	2.23
ω^- (eV)	3.62	4.16	4.40	3.56	4.10
ω^+ (eV)	0.62	0.95	1.05	0.61	0.92
Q (kcal/mol)	194.85	220.39	255.47	213.03	238.56
C_H (cal/mol.k)	65.68	76.96	90.33	71.83	83.14
S (Cal/mol.K)	131.74	150.63	168.84	143.31	164.10
α ($A^{\circ 3}$)	31.76	35.37	43.46	33.80	37.46
μ (Debye)	1.79	3.86	3.64	1.49	4.22
	3FMPT	**3FMClT**	**3FMBT**	**3FMPHT**	**3FM4NBT**
HOMO (eV)	-5.44	-5.56	-5.62	-5.60	-5.82
LUMO (eV)	-0.89	-1.15	-1.02	-2.49	-2.99
ΔE (eV)	4.55	4.41	4.60	3.11	2.83
IP (eV)	5.44	5.56	5.62	5.60	5.82
EA (eV)	0.89	1.15	1.02	2.49	2.99
χ (eV)	3.17	3.36	3.32	4.05	4.40
η (eV)	2.27	2.20	2.30	1.56	1.41
σ (eV^{-1})	0.22	0.23	0.22	0.32	0.35
ω (eV)	2.20	2.56	2.40	5.26	6.87
ω^- (eV)	4.07	4.51	4.35	7.48	9.24
ω^+ (eV)	0.91	1.15	1.02	3.43	4.84
Q (kcal/mol)	257.26	233.81	273.69	275.66	276.73
C_H (cal/mol.k)	87.99	85.73	96.44	106.90	105.13
S (Cal/mol.K)	169.16	171.56	178.21	195.15	194.24
α ($A^{\circ 3}$)	39.32	39.41	45.48	50.04	48.72
μ (Debye)	4.04	5.90	3.42	5.28	6.67

5.4. Molecular Electrostatic Potential Analysis:

The determination of the MEP region is the best fit for identifying regions within a molecule that are likely to engage in intra- and intermolecular interactions. MEP maps visualize how different areas of a molecule may attract or repel electrons, helping to pinpoint potential reactive sites [77]. The color coding on the MEP surface offers a clear representation:

- **Red/Yellow regions** correspond to areas of negative electrostatic potentials typically indicating electron-rich zones. These regions are more susceptible to electrophilic attacks.
- **Blue regions** represent areas of positive electrostatic potential, which are electron-deficient and prone to nucleophilic attacks.
- **Green areas** signify neutral potential, marking regions that are relatively balanced in terms of electron distribution.

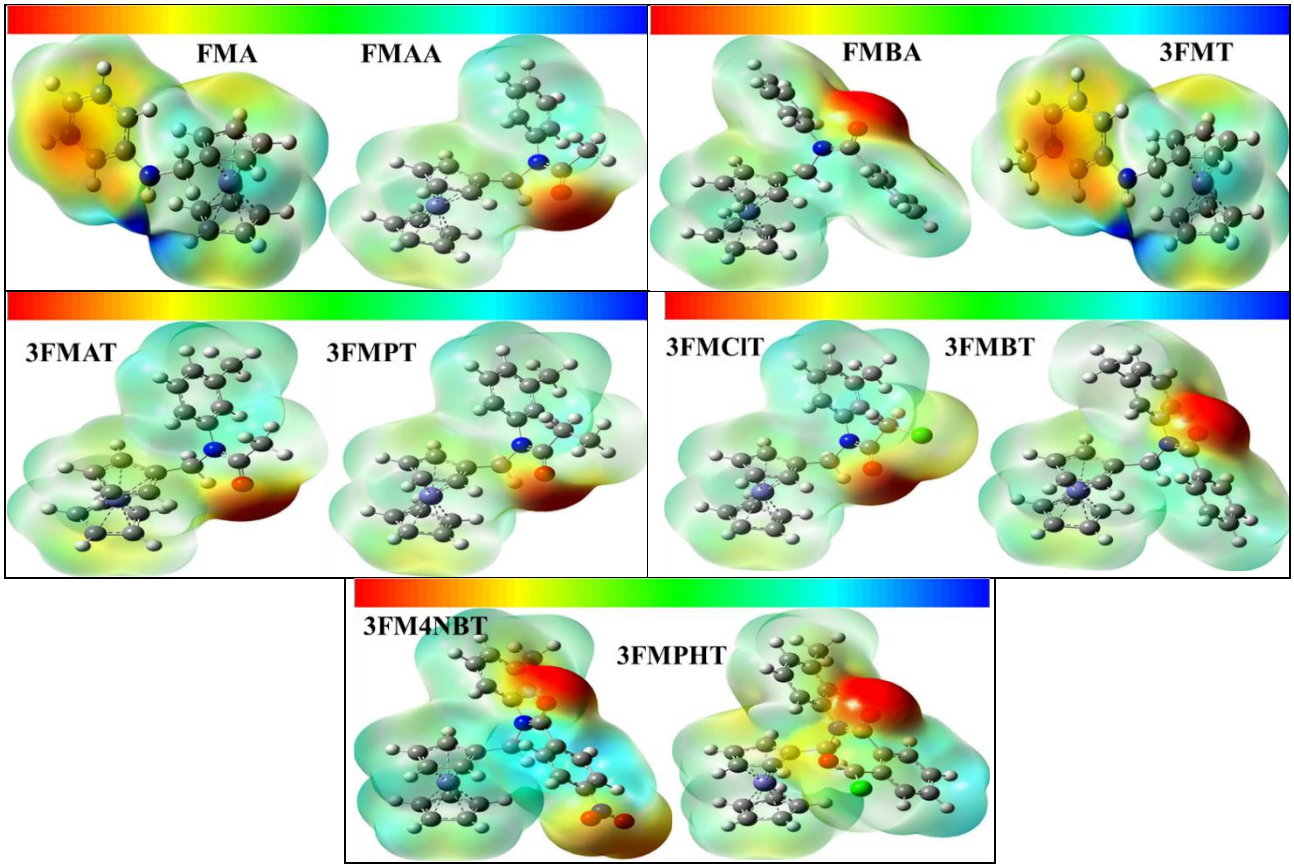

Figure IV.17. MEP surface of the investigated ferrocene compounds.

The electrostatic potential (ESP) range for the synthesized compounds is as follows (in kcal/mol):

- FMA: -25.11 to 25.11 3FMT: -24.61 to 24.61 FMAA: -37.41 to 37.41
- FMBA: -40.86 to 40.86 3FMAT: -38.10 to 38.10 3FMPT: -37.13 to 37.13
- 3FMClT: -41.18 to 41.18 3FMBT: -40.86 to 40.86 3FMPHT: -40.52 to 40.52
- 3FM4NBT: -35.78 to 35.78

As illustrated in Figure IV.14, the highly negative electrostatic potential regions are concentered over the oxygen atoms of all the acylated derivatives. However, in non-acylated

compounds (FMA and 3FMT), these regions are localized around the aromatic system (phenyl and cyclopentadienyl rings), suggesting that these sites are most favorable for nucleophilic interactions.

In contrast, the highly positive electrostatic potential regions in acylated derivatives are uniformly distributed across the whole molecule, covering both the cyclopentadiene and phenyl rings, except for the oxygen and chlorine atoms. while for FMA and 3FMT these regions are concentered in the nitrogen atom (NH) and the hydrogen atoms across the molecule, highlighting their importance as potential sites for electrophilic attack.

For the acylated derivatives, the most negative electrostatic potential values regions near the oxygen atoms fall in the range of -37.13 to -40.86 kcal/mol, suggesting a strong attraction for electrophilic agents. In comparison, the synthesized compounds (FMA and 3FMT) show slightly weaker negative potential over the phenyl rings, with values ranging between -24.61 and -25.11 kcal/mol.

The quantification of electrostatic potential distribution highlights the impact of acylation on molecular reactivity. The acylated derivatives exhibit stronger negative and positive regions than their non-acylated counterparts, suggesting that acylation enhances the charge separation within the molecules. This increased polarization may significantly improve binding properties and molecular recognition, particularly in biological environments.

These findings reinforce the results from molecular docking and *in vitro* studies, where the acylated derivatives exhibited stronger interactions with target proteins such as α-amylase, BSA, and COX-2, as well as higher antibacterial activity against *E. coli*, *S. aureus*, and *K. pneumoniae*.

General Conclusion

The primary objective of this thesis was to assess the biological activity of several ferrocenyl derivatives synthesized in the laboratory, utilizing both *in vitro* assays and in silico analyses. The study primarily focused on ferrocenylmethylaniline (FMA), ferrocenylmethyl-m-toluidine (3FMT), and their acylated derivatives. Characterization of these compounds was successfully achieved using UV-Visible spectroscopy, electrochemistry, infrared (IR) spectroscopy, and nuclear magnetic resonance (NMR) spectroscopy, confirming their structural integrity.

The spectroscopic parameters, such as binding free energy (ΔG) and binding constant (K), for interactions with specific biological targets, including α-amylase, bovine serum albumin (BSA) and bacterial strains like *E. coli*, *S. aureus*, *K. pneumoniae* and *P. aeruginosa*. Both *in vitro* and in silico studies revealed spontaneous interactions, indicating the potential of these ferrocenyl derivatives as bioactive agents.

Regarding antidiabetic activity, the compounds' interaction with α-amylase demonstrated their strong inhibitory potential. The ΔG values ranged from -24.1 to -34.78 kJ/mol, surpassing the activity of the standard drug acarbose (ARE), which exhibited a ΔG of -20.82 kJ/mol. The spectroscopic assays produced IC_{50} values between 0.69 and 64.5 µM, highlighting the effectiveness of these ferrocenyl derivatives as potential anti-diabetic agents.

In addition, the anti-inflammatory activity was assessed through interactions with BSA, where all synthesized compounds, except for FMA and 3FMT, exhibited notable anti-inflammatory effects. These compounds effectively inhibited BSA denaturation, with IC_{50} values ranging from 1.72 to 7.26 µM and ΔG values between -33.36 and -31.06 kJ/mol. These values were significantly better than those of diclofenac (DIF), which exhibited an IC_{50} of 15.81 µM and a ΔG of -29.61 kJ/mol, highlighting the superior potential of these ferrocene derivatives in managing inflammation.

Furthermore, the antibacterial activity of these compounds was evaluated, revealing moderate to strong antibacterial effects. However, their effectiveness was generally lower than that of amoxicillin, which demonstrated superior inhibition across all strains.

The molecular docking results reinforced the *in vitro* findings by confirming the interactions between the synthesized ferrocene derivatives and their respective target proteins. Docking studies demonstrated that these compounds have strong binding affinities for α-amylase

(ΔG ranging from -5.85 to -7.84 kcal/mol), BSA (ΔG ranging from -8.04 to -10.49 kcal/mol), and COX-2 (ΔG ranging from -8.17 to -11.97 kcal/mol), suggesting their potential as significant inhibitors of key anti-diabetic and anti-inflammatory targets.

Regarding antibacterial activity, molecular docking revealed that these compounds act through various mechanisms, targeting essential bacterial enzymes and proteins. Specifically, they interact with peptidoglycan D,D-transpeptidase in *P. aeruginosa*, as well as penicillin-binding protein 2a, dihydrofolate reductase, and DNA gyrase subunit B in *S. aureus*. Additionally, they exhibit interactions with anthranilate-CoA ligase and peptide deformylase in *P. aeruginosa* and *E. coli*, as well as DNA topoisomerase IV in *K. pneumoniae*. These findings suggest that ferrocenyl derivatives could serve as promising antibacterial agents by interfering with key bacterial pathways.

The ADMET profile of the synthesized ferrocene derivatives also supports their potential as drug candidates. These compounds demonstrated favorable pharmacokinetic properties, including high solubility, high intestinal absorption rates, and the ability to cross the blood-brain barrier. Additionally, most compounds were found to be non-mutagenic and non-carcinogenic, reinforcing their safety and viability as drug candidates.

Moreover, quantum chemical calculations further supported the stability of these compounds, providing insight into the molecular orbital energies (HOMO, LUMO), molecular electrostatic potential (MEP) plots. These analyses helped explain the reactivity of the compounds within the active sites of target proteins, thus underscoring their potential as drug candidates.

In conclusion, this thesis effectively demonstrates that the synthesized ferrocenyl derivatives, particularly FMA, 3FMT, and their acylated forms, exhibit promising anti-diabetic, anti-inflammatory, and antibacterial activities. The combination of *in vitro* and in silico methods, coupled with ADMET profiling and quantum chemical calculations, highlights the strong potential of these compounds as candidates for further development in drug therapies targeting diabetes, inflammatory conditions, and bacterial infections.

Future research will focus on optimizing the structure-activity relationship (SAR) of these derivatives to enhance their binding affinities and pharmacokinetic profiles further. Additionally, in vivo studies will be conducted to validate the *in vitro* and *in silico* findings, ensuring the safety and efficacy of these compounds in a physiological environment. Exploring potential drug-drug interactions and assessing long-term toxicity effects will also be prioritized to better understand the clinical relevance of these ferrocenyl derivatives.

Reference

[1] J.M. Osgerby, P.L. Pauson, 900. Ferrocene derivatives. Part VIII. Tetrahydropyridoferrocenes, Journal of the Chemical Society (Resumed) (1961) 4600. https://doi.org/10.1039/jr9610004600.

[2] D. LEDNICER, J.K. LINDSAY, C.R. HAUSER, Reaction of the Methiodide of N,N-Dimethylaminomethylferrocene with Potassium Cyanide to Form Ferrocylacetonitrile 1, J Org Chem 23 (1958) 653–655. https://doi.org/10.1021/jo01099a001.

[3] J.K. LINDSAY, C.R. HAUSER, Aminomethylation of Ferrocene to Form N,N-Dimethylaminomethylferrocene and Its Conversion to the Corresponding Alcohol and Aldehyde 1, J Org Chem 22 (1957) 355–358. https://doi.org/10.1021/jo01355a001.

[4] N,N-DIMETHYLAMINOMETHYLFERROCENE METHIODIDE, Organic Syntheses 40 (1960) 31. https://doi.org/10.15227/orgsyn.040.0031.

[5] A. Yahiaoui, N. Benyza, A. Messai, T. Lanez, E. Lanez, Voltametric and molecular docking investigations of ferrocenylmethylaniline and its N-acetylated derivative interacting with DNA, Journal of Electrochemical Science and Engineering (2023). https://doi.org/10.5599/jese.2061.

[6] A. Khelef, M.S. Mahboub, T. Lanez, N -Ferrocenymethyl- N -phenylacetamide, IUCrdata 1 (2016) x160203. https://doi.org/10.1107/S2414314616002030.

[7] E. Lanez, A. Kedadra, T. Lanez, A. Adaika, N. Zegheb, In vitro antioxidant activity, QSAR, in silico toxicity prediction, molecular docking studies, and molecular dynamics of a series of N-ferrocenylmethylanilines as potent antioxidant agents, J Organomet Chem 1017 (2024) 123284. https://doi.org/10.1016/j.jorganchem.2024.123284.

[8] D. Anokwah, E.A. Kwatia, I.K. Amponsah, Y. Jibira, B.K. Harley, E.O. Ameyaw, E. Obese, R.P. Biney, A.Y. Mensah, Evaluation of the anti-inflammatory and antioxidant potential of the stem bark extract and some constituents of Aidia genipiflora (DC.) dandy (rubiaceae), Heliyon 8 (2022) e10082. https://doi.org/10.1016/j.heliyon.2022.e10082.

[9] H.A. Benesi, J.H. Hildebrand, A Spectrophotometric Investigation of the Interaction of Iodine with Aromatic Hydrocarbons, J Am Chem Soc 71 (1949) 2703–2707. https://doi.org/10.1021/ja01176a030.

[10] E. Thilagam, B. Parimaladevi, C. Kumarappan, S. Chandra Mandal, α-Glucosidase and α-Amylase Inhibitory Activity of Senna surattensis, J Acupunct Meridian Stud 6 (2013) 24–30. https://doi.org/10.1016/j.jams.2012.10.005.

[11] F. Medini, H. Fellah, R. Ksouri, C. Abdelly, Total phenolic, flavonoid and tannin contents and antioxidant and antimicrobial activities of organic extracts of shoots of the plant *Limonium delicatulum*, Journal of Taibah University for Science 8 (2014) 216–224. https://doi.org/10.1016/j.jtusci.2014.01.003.

[12] M.-D. Tsay, C.-C. Tseng, N.-X. Wu, C.-Y. Lai, Size distribution and antibiotic-resistant characteristics of bacterial bioaerosol in intensive care unit before and during visits to patients, Environ Int 144 (2020) 106024. https://doi.org/10.1016/j.envint.2020.106024.

[13] A.R. Jalalvand, M. Zhaleh, S. Goorani, M.M. Zangeneh, N. Seydi, A. Zangeneh, R. Moradi, Chemical characterization and antioxidant, cytotoxic, antibacterial, and antifungal properties of ethanolic extract of Allium Saralicum R.M. Fritsch leaves rich in linolenic acid, methyl ester, J Photochem Photobiol B 192 (2019) 103–112. https://doi.org/10.1016/j.jphotobiol.2019.01.017.

[14] E.U.A.-R.-S.R.P. Frisch, M.J., Trucks, G.W., Schlegel, H.B., Scuseria, G.E., Robb, M.A., Cheeseman, J.R.; Scalmani, G.; Barone, V.; Petersson, G.A.; Nakatsuji, H.; Li, X.; Caricato, M.; Marenich, A.V.; Bloino, J., Janesko, B.G., Gomperts, R., Mennucci, B., Hratchian, H.P., Gaussian 16, Revision B.01, (2016) Gaussian 16, Revision A.03, Gaussian, Inc., Wallin.

[15] A.D. Becke, Density-functional thermochemistry. III. The role of exact exchange, J Chem Phys 98 (1993) 5648–5652. https://doi.org/10.1063/1.464913.

[16] H.M. Berman, The Protein Data Bank, Nucleic Acids Res 28 (2000) 235–242. https://doi.org/10.1093/nar/28.1.235.

[17] G.M. Morris, R. Huey, W. Lindstrom, M.F. Sanner, R.K. Belew, D.S. Goodsell, A.J. Olson, AutoDock4 and AutoDockTools4: Automated docking with selective receptor flexibility, J Comput Chem 30 (2009) 2785–2791. https://doi.org/10.1002/jcc.21256.

[18] S. Kim, J. Chen, T. Cheng, A. Gindulyte, J. He, S. He, Q. Li, B.A. Shoemaker, P.A. Thiessen, B. Yu, L. Zaslavsky, J. Zhang, E.E. Bolton, PubChem 2023 update, Nucleic Acids Res 51 (2023) D1373–D1380. https://doi.org/10.1093/nar/gkac956.

[19] BIOVIA, Dassault Systèmes, Discovery Studio Visualizer, v21.1.0.20298; San Diego: Dassault Systèmes, (2020). https://discover.3ds.com/discovery-studio-visualizer-download (accessed February 18, 2025).

[20] R. Wang, Y. Lu, S. Wang, Comparative Evaluation of 11 Scoring Functions for Molecular Docking, J Med Chem 46 (2003) 2287–2303. https://doi.org/10.1021/jm0203783.

[21] A. Sagaama, O. Noureddine, S.A. Brandán, A.J. Jędryka, H.T. Flakus, H. Ghalla, N. Issaoui, Molecular docking studies, structural and spectroscopic properties of monomeric and dimeric species of benzofuran-carboxylic acids derivatives: DFT calculations and biological activities, Comput Biol Chem 87 (2020) 107311. https://doi.org/10.1016/j.compbiolchem.2020.107311.

[22] T. Ben Issa, A. Sagaama, N. Issaoui, Computational study of 3-thiophene acetic acid: Molecular docking, electronic and intermolecular interactions investigations, Comput Biol Chem 86 (2020) 107268. https://doi.org/10.1016/j.compbiolchem.2020.107268.

[23] S. Ramalakshmi, K. Sonanki, R. Prakash, G. Usha, K. Karpagalakshmi, E.R. Nagarajan, N. Selvapalam, In-silico approach of effect of protein on complexation of cucurbit[7]uril with N- (ferrocenylmethyl) aniline, Mater Today Proc 51 (2021) 1733–1737. https://doi.org/10.1016/j.matpr.2020.11.720.

[24] B. Kurt, H. Temel, M. Atlan, S. Kaya, Synthesis, characterization, DNA interaction and docking studies of novel Schiff base ligand derived from 2,6-diaminopyridine and its complexes, J Mol Struct 1209 (2020) 127928. https://doi.org/10.1016/j.molstruc.2020.127928.

[25] A. Arunadevi, N. Raman, Indole-derived water-soluble N, O bi-dentate ligand-based mononuclear transition metal complexes: in silico and in vitro biological screening, molecular docking and macromolecule interaction studies, J Biomol Struct Dyn 38 (2020) 1499–1513. https://doi.org/10.1080/07391102.2019.1611475.

[26] O. Daoui, S. Elkhattabi, S. Chtita, Design and Prediction of ADME/Tox Properties of Novel Magnolol Derivatives as Anticancer Agents for NSCLC Using 3D-QSAR, Molecular Docking, MOLCAD and MM-GBSA Studies, Lett Drug Des Discov 20 (2023) 545–569. https://doi.org/10.2174/1570180819666220510141710.

[27] A. Dhaundiyal, P. Kumari, S. Kalra, Pharmacophore-based Screening for Identification of Human Acyl-CoA Cholesterol Acyltransferase Inhibitors: An In-silico Study, Lett Drug Des Discov 18 (2021) 816–829. https://doi.org/10.2174/1570180818999201231200643.

[28] L. Rasheed, W. Rehman, F. Rahim, Z. Ali, A.S. Alanazi, R. Hussain, I. Khan, M.M. Alanazi, M. Naseer, M.H. Abdellattif, R. Hussain, S. Khan, M. Taha, S.A. Ali Shah, Molecular Modeling and Synthesis of Indoline-2,3-dione-Based Benzene Sulfonamide Derivatives and Their Inhibitory Activity against α-Glucosidase and α-Amylase Enzymes, ACS Omega 8 (2023) 15660–15672. https://doi.org/10.1021/acsomega.3c01130.

[29] C.-Y. Jia, J.-Y. Li, G.-F. Hao, G.-F. Yang, A drug-likeness toolbox facilitates ADMET study in drug discovery, Drug Discov Today 25 (2020) 248–258. https://doi.org/10.1016/j.drudis.2019.10.014.

[30] M.A. Shabbir, M. Naveed, S. ur Rehman, N. ul Ain, T. Aziz, M. Alharbi, A. Alsahammari, A.F. Alasmari, Synthesis of Iron Oxide Nanoparticles from Madhuca indica Plant Extract and Assessment of Their Cytotoxic, Antioxidant, Anti-Inflammatory, and Anti-Diabetic Properties via Different Nanoinformatics Approaches, ACS Omega 8 (2023) 33358–33366. https://doi.org/10.1021/acsomega.3c02744.

[31] C.A. Lipinski, Lead- and drug-like compounds: the rule-of-five revolution, Drug Discov Today Technol 1 (2004) 337–341. https://doi.org/10.1016/j.ddtec.2004.11.007.

[32] D.F. Veber, S.R. Johnson, H.-Y. Cheng, B.R. Smith, K.W. Ward, K.D. Kopple, Molecular Properties That Influence the Oral Bioavailability of Drug Candidates, J Med Chem 45 (2002) 2615–2623. https://doi.org/10.1021/jm020017n.

[33] W.J. Egan, K.M. Merz,, J.J. Baldwin, Prediction of Drug Absorption Using Multivariate Statistics, J Med Chem 43 (2000) 3867–3877. https://doi.org/10.1021/jm000292e.

[34] A. Daina, O. Michielin, V. Zoete, SwissADME: a free web tool to evaluate pharmacokinetics, drug-likeness and medicinal chemistry friendliness of small molecules, Sci Rep 7 (2017) 42717. https://doi.org/10.1038/srep42717.

[35] C. Lou, H. Yang, H. Deng, M. Huang, W. Li, G. Liu, P.W. Lee, Y. Tang, Chemical rules for optimization of chemical mutagenicity via matched molecular pairs analysis and machine learning methods, J Cheminform 15 (2023) 35. https://doi.org/10.1186/s13321-023-00707-x.

[36] P. Banerjee, A.O. Eckert, A.K. Schrey, R. Preissner, ProTox-II: a webserver for the prediction of toxicity of chemicals, Nucleic Acids Res 46 (2018) W257–W263. https://doi.org/10.1093/nar/gky318.

[37] V. Kudar, V. Zsoldos-Mády, K. Simon, A. Csámpai, P. Sohár, Synthesis, IR-, NMR- and X-ray investigations on some novel N-hetaryl-dihydro-pyrazolyl ferrocenes. Study on ferrocenes, part 16, J Organomet Chem 690 (2005) 4018–4026. https://doi.org/10.1016/j.jorganchem.2005.05.045.

[38] D.-G. Jia, J.-A. Zheng, Y.-R. Fan, J.-Q. Yu, X.-L. Wu, B.-J. Wang, X.-B. Yang, Y. Huang, Ferrocene appended naphthalimide derivatives: Synthesis, DNA binding, and in vitro

cytotoxic activity, J Organomet Chem 888 (2019) 16–23. https://doi.org/10.1016/j.jorganchem.2019.03.001.

[39] E.M. NJOGU, B. OMONDI, V.O. NYAMORI, Synthesis, physical and antimicrobial studies of ferrocenyl-N-(pyridinylmethylene)anilines and ferrocenyl-N-(pyridinylmethyl)anilines, South African Journal of Chemistry 69 (2016) 51–66. https://doi.org/10.17159/0379-4350/2016/v69a7.

[40] R. Sun, L. Wang, H. Yu, Zain-ul-Abdin, Y. Chen, H. Khalid, N. Abbasi, M. Akram, Synthesis of Ferrocene-Based Hyperbranched Polyether and Its Catalytic Performance for Thermal Decomposition of Ammonium Perchlorate, J Inorg Organomet Polym Mater 24 (2014) 1063–1069. https://doi.org/10.1007/s10904-014-0084-2.

[41] J.-N. Wei, Z.-D. Jia, Y.-Q. Zhou, P.-H. Chen, B. Li, N. Zhang, X.-Q. Hao, Y. Xu, B. Zhang, Synthesis, characterization and antitumor activity of novel ferrocene-coumarin conjugates, J Organomet Chem 902 (2019) 120968. https://doi.org/10.1016/j.jorganchem.2019.120968.

[42] B. Lal, A. Badshah, A.A. Altaf, M.N. Tahir, S. Ullah, F. Huq, Synthesis, characterization and antitumor activity of new ferrocene incorporated N,N′-disubstituted thioureas, Dalton Transactions 41 (2012) 14643–14650. https://doi.org/10.1039/c2dt31570j.

[43] X.-F. Huang, L.-Z. Wang, L. Tang, Y.-X. Lu, F. Wang, G.-Q. Song, B.-F. Ruan, Synthesis, characterization and antitumor activity of novel ferrocene derivatives containing pyrazolyl-moiety, J Organomet Chem 749 (2014) 157–162. https://doi.org/10.1016/j.jorganchem.2013.08.043.

[44] E. Lanez, L. Bechki, T. Lanez, Ferrocenylmethylnucleobases Synthesis, DFT Calculations, Electrochemical and Spectroscopic Characterization, Chemistry and Chemical Technology 14 (2020) 146–153. https://doi.org/10.23939/chcht14.02.146.

[45] A. Irfan, F.K. Al-Zeidaneen, I. Ahmed, A.G. Al-Sehemi, M.A. Assiri, S. Ullah, G. Abbas, Synthesis, characterization and quantum chemical study of optoelectronic nature of ferrocene derivatives, Bulletin of Materials Science 43 (2020) 45. https://doi.org/10.1007/s12034-019-1992-0.

[46] E. Lanez, L. Bechki, T. Lanez, Synthesis, characterization and in vitro and in silico study of biological activities of some ferrocenylmethyl-nucleic bases derivatives, 2019. https://doi.org/10.13140/RG.2.2.22090.80320.

[47] L. Tabrizi, T.L.A. Nguyen, H.D.T. Tran, M.Q. Pham, D.Q. Dao, Antioxidant and Anticancer Properties of Functionalized Ferrocene with Hydroxycinnamate Derivatives—An Integrated

Experimental and Theoretical Study, J Chem Inf Model 60 (2020) 6185–6203. https://doi.org/10.1021/acs.jcim.0c00730.

[48] V. Kovač, A. Višnjevac, V. Rapić, B. Kojić-Prodić, Ferrocene compounds. XL. Synthesis and characterization of ferrocene Schiff bases, J Mol Struct 687 (2004) 107–110. https://doi.org/10.1016/j.molstruc.2003.09.014.

[49] S. Benabdesselam, H. Izza, T. Lanez, E.K. Guechi, Synthesis, antioxidant and antibacterial activities of 3-nitrophenyl ferrocene, IOP Conf Ser Mater Sci Eng 323 (2018) 012007. https://doi.org/10.1088/1757-899X/323/1/012007.

[50] F. Javed, A.A. Altaf, A. Badshah, M.N. Tahir, M. Siddiq, A. Shah, S. Ullah, B. Lal, New supramolecular ferrocenyl amides: synthesis, characterization, and preliminary DNA-binding studies, J Coord Chem 65 (2012) 969–979. https://doi.org/10.1080/00958972.2012.664769.

[51] I.V. Smolyaninov, A.I. Poddel'sky, S.V. Baryshnikova, V.V. Kuzmin, E.O. Korchagina, M.V. Arsenyev, S.A. Smolyaninova, N.T. Berberova, Electrochemical transformations and evaluation of antioxidant activity of some Schiff bases containing ferrocenyl and (thio-)phenol, catechol fragments, Appl Organomet Chem 32 (2018). https://doi.org/10.1002/aoc.4121.

[52] H. Agarwal, A. Nakara, V.K. Shanmugam, Anti-inflammatory mechanism of various metal and metal oxide nanoparticles synthesized using plant extracts: A review, Biomedicine & Pharmacotherapy 109 (2019) 2561–2572. https://doi.org/10.1016/j.biopha.2018.11.116.

[53] S.T. Mathews, V. Kothari, J. Galdo, Hypoglycemic agents and potential anti-inflammatory activity, J Inflamm Res (2016) 27. https://doi.org/10.2147/JIR.S86917.

[54] A.K. Ghose, V.N. Viswanadhan, J.J. Wendoloski, A Knowledge-Based Approach in Designing Combinatorial or Medicinal Chemistry Libraries for Drug Discovery. 1. A Qualitative and Quantitative Characterization of Known Drug Databases, J Comb Chem 1 (1999) 55–68. https://doi.org/10.1021/cc9800071.

[55] C.A. Lipinski, Drug-like properties and the causes of poor solubility and poor permeability, J Pharmacol Toxicol Methods 44 (2000) 235–249. https://doi.org/10.1016/S1056-8719(00)00107-6.

[56] W.J. Egan, K.M. Merz,, J.J. Baldwin, Prediction of Drug Absorption Using Multivariate Statistics, J Med Chem 43 (2000) 3867–3877. https://doi.org/10.1021/jm000292e.

[57] X.E.N. Bucao, J.N. Solidum, In Silico Evaluation of Antidiabetic Activity and ADMET Prediction of Compounds from Musa acuminata Colla Peel, Philipp J Sci 151 (2022) 171–192. https://doi.org/10.56899/151.01.13.

[58] D. Lagorce, D. Douguet, M.A. Miteva, B.O. Villoutreix, Computational analysis of calculated physicochemical and ADMET properties of protein-protein interaction inhibitors, Sci Rep 7 (2017) 46277. https://doi.org/10.1038/srep46277.

[59] D.E. V. Pires, T.L. Blundell, D.B. Ascher, pkCSM: Predicting Small-Molecule Pharmacokinetic and Toxicity Properties Using Graph-Based Signatures, J Med Chem 58 (2015) 4066–4072. https://doi.org/10.1021/acs.jmedchem.5b00104.

[60] X.E.N. Bucao, J.N. Solidum, In Silico Evaluation of Antidiabetic Activity and ADMET Prediction of Compounds from Musa acuminata Colla Peel, 151 (2022) 171–192.

[61] Z.D. Zhivkova, T. Mandova, I. Doytchinova, Quantitative Structure – Pharmacokinetics Relationships Analysis of Basic Drugs: Volume of Distribution, Journal of Pharmacy & Pharmaceutical Sciences 18 (2015) 515. https://doi.org/10.18433/J3XC7S.

[62] A.A. Freitas, K. Limbu, T. Ghafourian, Predicting volume of distribution with decision tree-based regression methods using predicted tissue:plasma partition coefficients, J Cheminform 7 (2015) 6. https://doi.org/10.1186/s13321-015-0054-x.

[63] U.M. Zanger, M. Schwab, Cytochrome P450 enzymes in drug metabolism: regulation of gene expression, enzyme activities, and impact of genetic variation., Pharmacol Ther 138 (2013) 103–41. https://doi.org/10.1016/j.pharmthera.2012.12.007.

[64] F. Cheng, Y. Yu, Y. Zhou, Z. Shen, W. Xiao, G. Liu, W. Li, P.W. Lee, Y. Tang, Insights into molecular basis of cytochrome p450 inhibitory promiscuity of compounds., J Chem Inf Model 51 (2011) 2482–95. https://doi.org/10.1021/ci200317s.

[65] M. Deodhar, S.B. Al Rihani, M.J. Arwood, L. Darakjian, P. Dow, J. Turgeon, V. Michaud, Mechanisms of CYP450 Inhibition: Understanding Drug-Drug Interactions Due to Mechanism-Based Inhibition in Clinical Practice., Pharmaceutics 12 (2020). https://doi.org/10.3390/pharmaceutics12090846.

[66] P. Kokkonen, A. Beier, S. Mazurenko, J. Damborsky, D. Bednar, Z. Prokop, Substrate inhibition by the blockage of product release and its control by tunnel engineering., RSC Chem Biol 2 (2021) 645–655. https://doi.org/10.1039/d0cb00171f.

[67] R.B. Diasio, Principles of Drug Therapy, Goldman's Cecil Medicine: Twenty Fourth Edition 1 (2012) 124–132. https://doi.org/10.1016/B978-1-4377-1604-7.00028-2.

[68] M. Belzer, M. Morales, B. Jagadish, E.A. Mash, S.H. Wright, Substrate-Dependent Ligand Inhibition of the Human Organic Cation Transporter OCT2, Journal of Pharmacology and Experimental Therapeutics 346 (2013) 300–310. https://doi.org/10.1124/jpet.113.203257.

[69] K. Hacker, R. Maas, J. Kornhuber, M.F. Fromm, O. Zolk, Substrate-Dependent Inhibition of the Human Organic Cation Transporter OCT2: A Comparison of Metformin with Experimental Substrates, PLoS One 10 (2015) e0136451. https://doi.org/10.1371/journal.pone.0136451.

[70] Ö. Farkas, H.B. Schlegel, Geometry optimization methods for modeling large molecules, Journal of Molecular Structure: THEOCHEM 666–667 (2003) 31–39. https://doi.org/10.1016/J.THEOCHEM.2003.08.010.

[71] G.W. Watson, P. Tschaufeser, A. Wall, R.A. Jackson, S.C. Parker, Lattice Energy and Free Energy Minimization Techniques, Computer Modeling in Inorganic Crystallography (1997) 55–81. https://doi.org/10.1016/B978-012164135-1/50004-6.

[72] M. Hanane, T. Lanez, I. Zafar, M.S. Afghan, N. Zegheb, N'-Ferrocenylmethyl-N'-phenylbenzohydrazide as a potential DNA binding compound: a combined experimental and computational study, J Coord Chem 76 (2023) 1984–1998. https://doi.org/10.1080/00958972.2023.2275247.

[73] O. Rahim, A. Khelef, B. Terki, M.S. Mahboub, T. Lanez, N -Ferrocenylmethyl-2-nitroaniline, Acta Crystallogr Sect E Struct Rep Online 68 (2012) m1318–m1318. https://doi.org/10.1107/S1600536812039177.

[74] K. Fukui, Role of Frontier Orbitals in Chemical Reactions, Science (1979) 218 (1982) 747–754. https://doi.org/10.1126/science.218.4574.747.

[75] M.M. Hammoud, M. Khattab, M. Abdel-Motaal, J. Van der Eycken, R. Alnajjar, H.S. Abulkhair, A.A. Al-Karmalawy, Synthesis, structural characterization, DFT calculations, molecular docking, and molecular dynamics simulations of a novel ferrocene derivative to unravel its potential antitumor activity, J Biomol Struct Dyn (2022) 1–18. https://doi.org/10.1080/07391102.2022.2082533.

[76] S. Tighadouini, S. Radi, F. Abrigach, R. Benabbes, D. Eddike, M. Tillard, Novel β-keto–enol Pyrazolic Compounds as Potent Antifungal Agents. Design, Synthesis, Crystal Structure, DFT, Homology Modeling, and Docking Studies, J Chem Inf Model 59 (2019) 1398–1409. https://doi.org/10.1021/acs.jcim.8b00828.

[77] Y. Kaddouri, F. Abrigach, E.B. Yousfi, M. El Kodadi, R. Touzani, New thiazole, pyridine and pyrazole derivatives as antioxidant candidates: synthesis, DFT calculations and molecular docking study, Heliyon 6 (2020) e03185. https://doi.org/10.1016/j.heliyon.2020.e03185.

Supplementary information

Supplementary Information

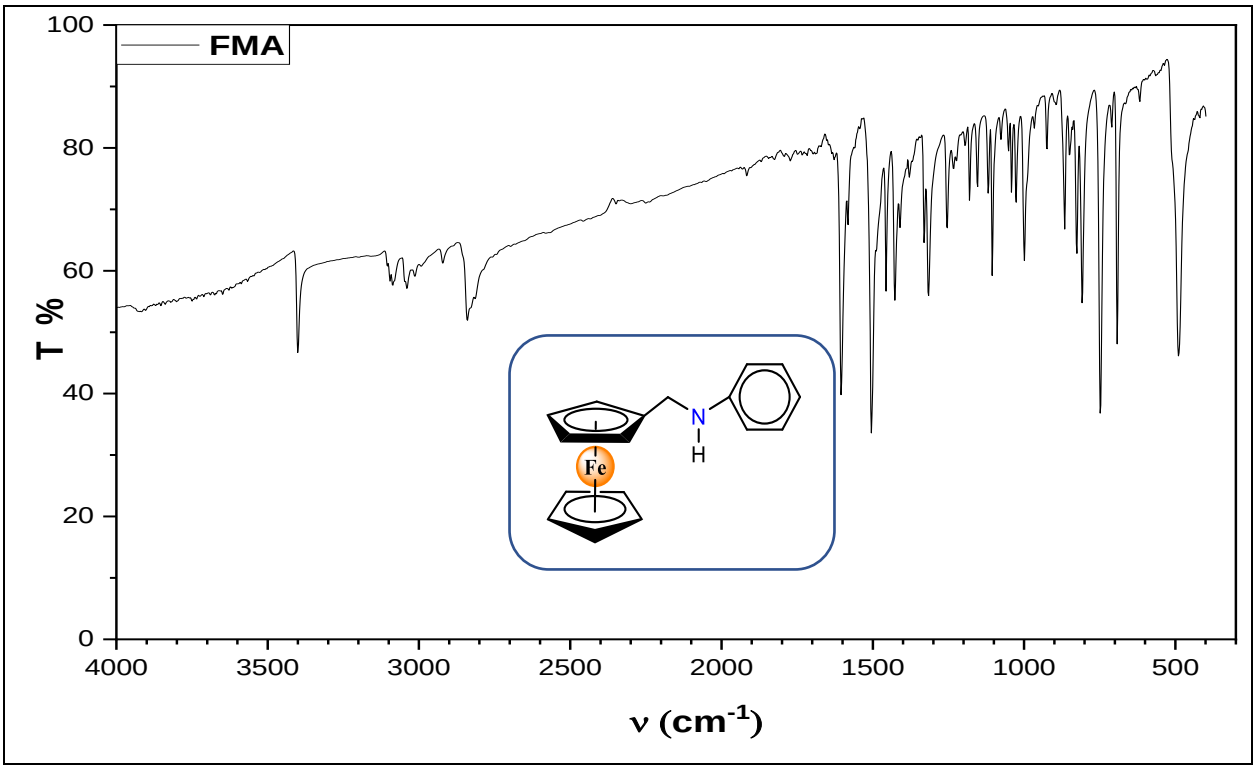

Figure S1. IR spectrum of FMA.

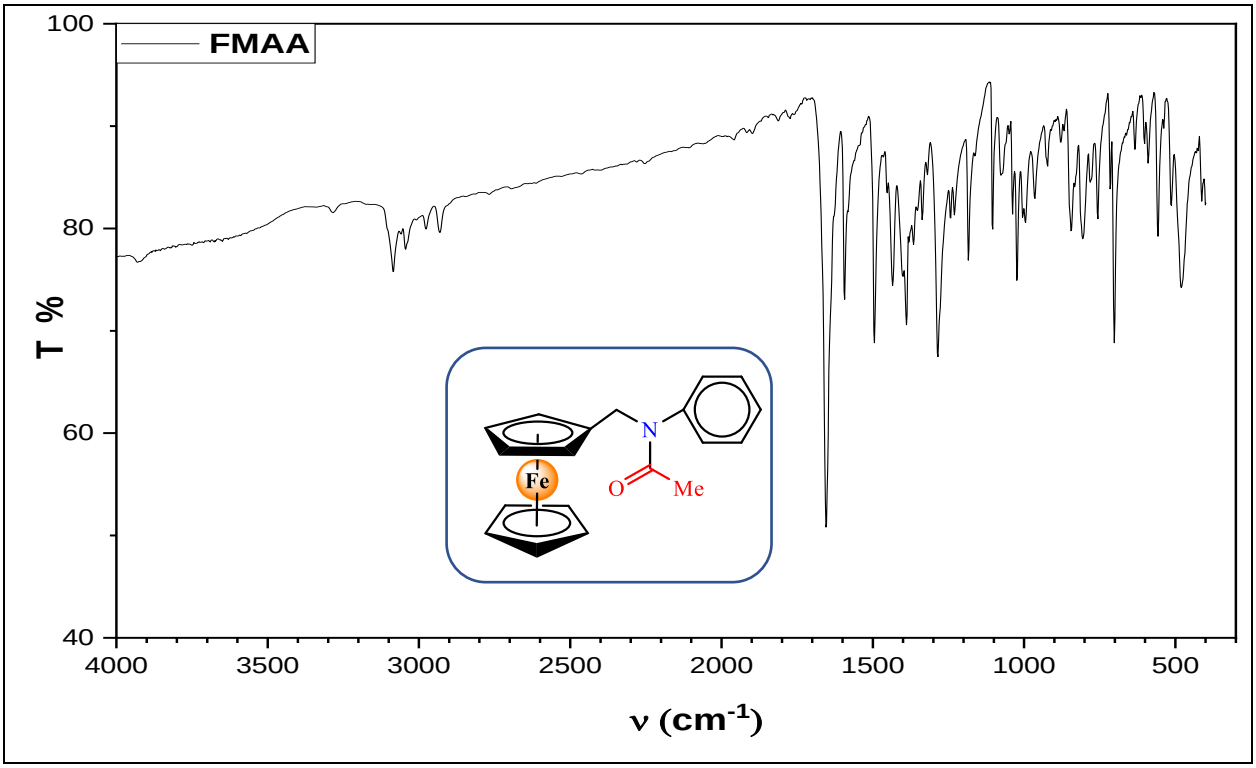

Figure S2. IR spectrum of FMAA.

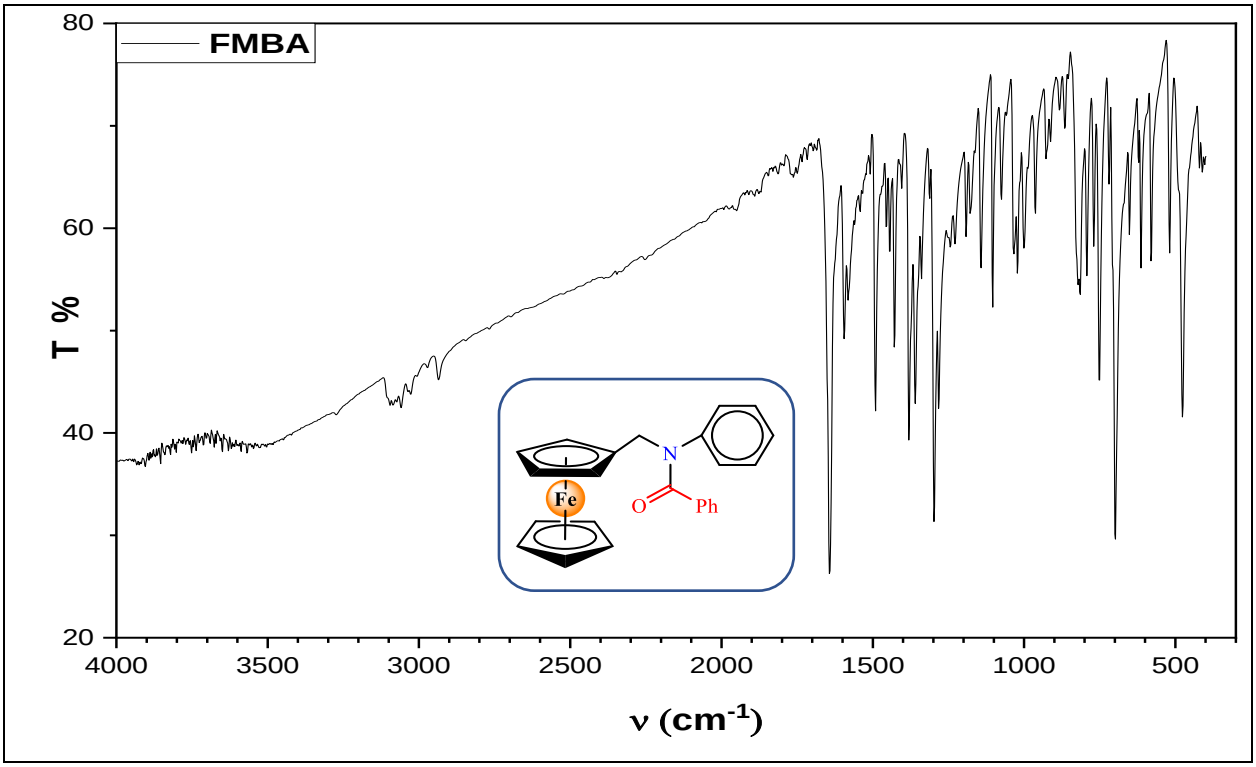

Figure S3. IR spectrum of FMBA.

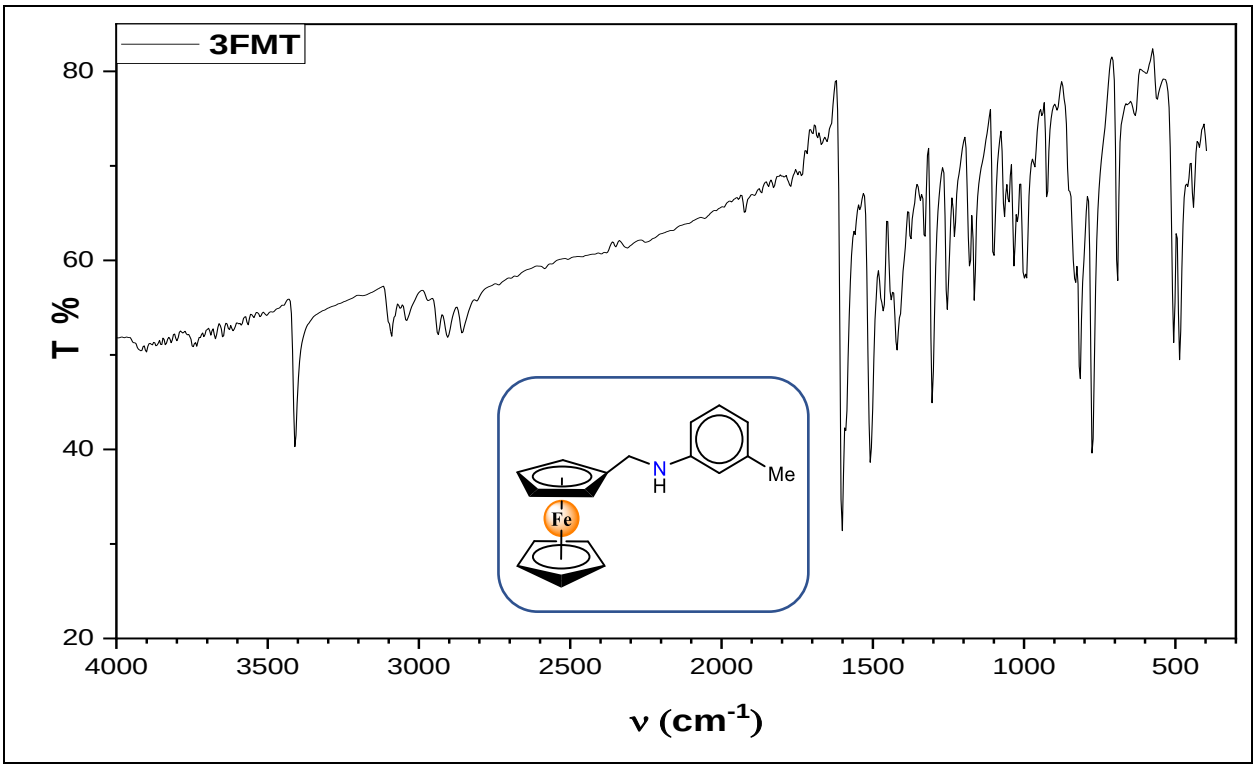

Figure S4. IR spectrum of 3FMT.

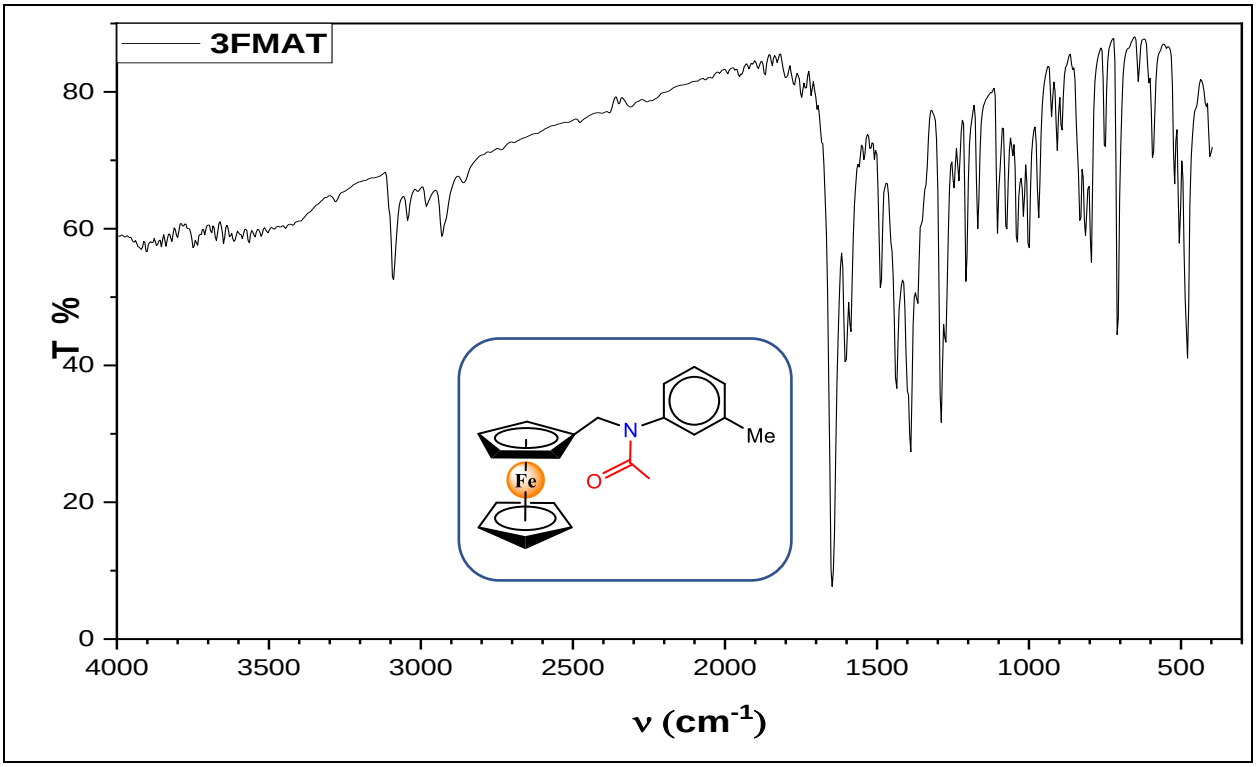

Figure S5. IR spectrum of 3FMAT.

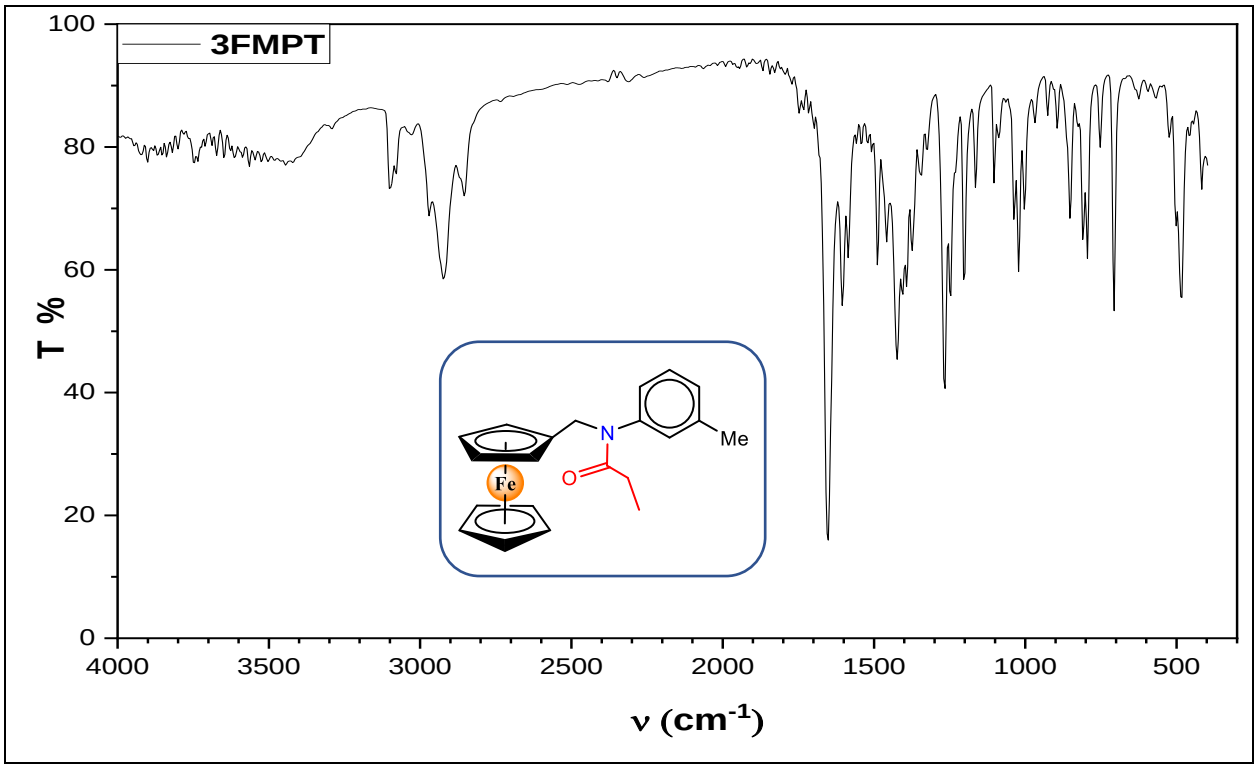

Figure S6. IR spectrum of 3FMPT.

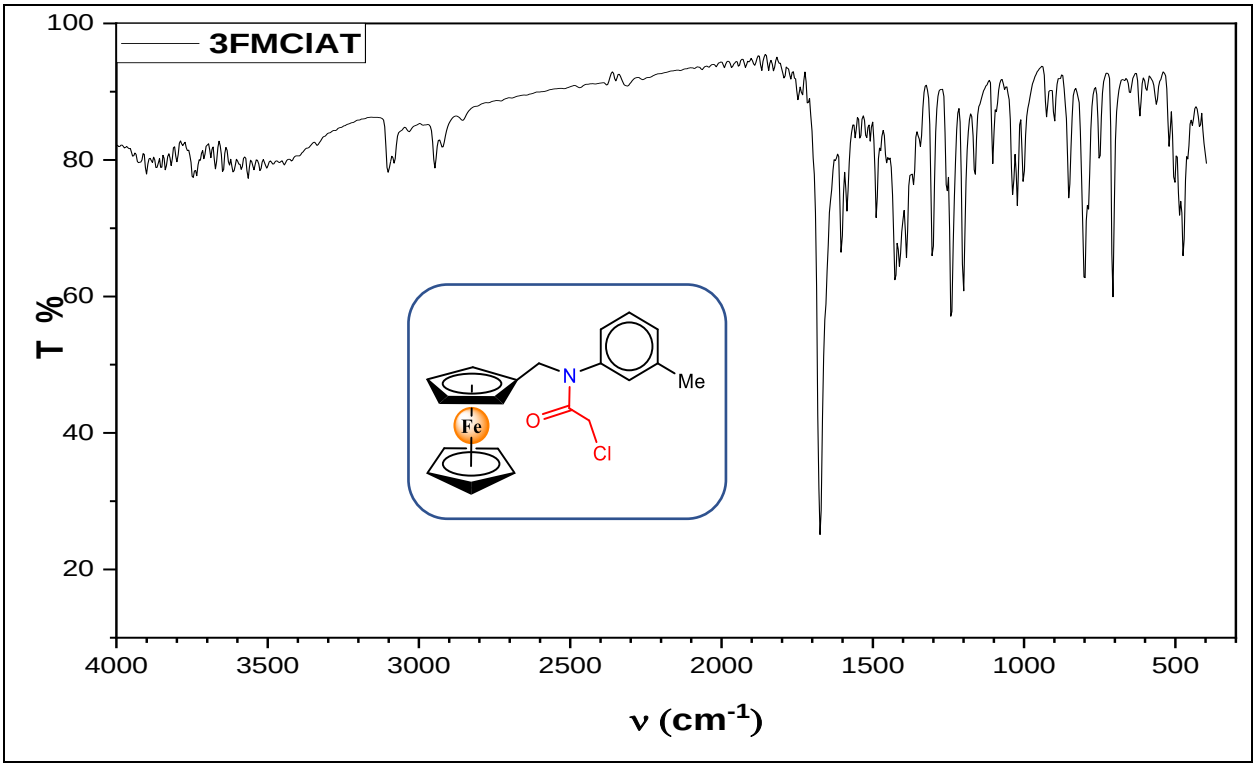

Figure S7. IR spectrum of 3FMClAT.

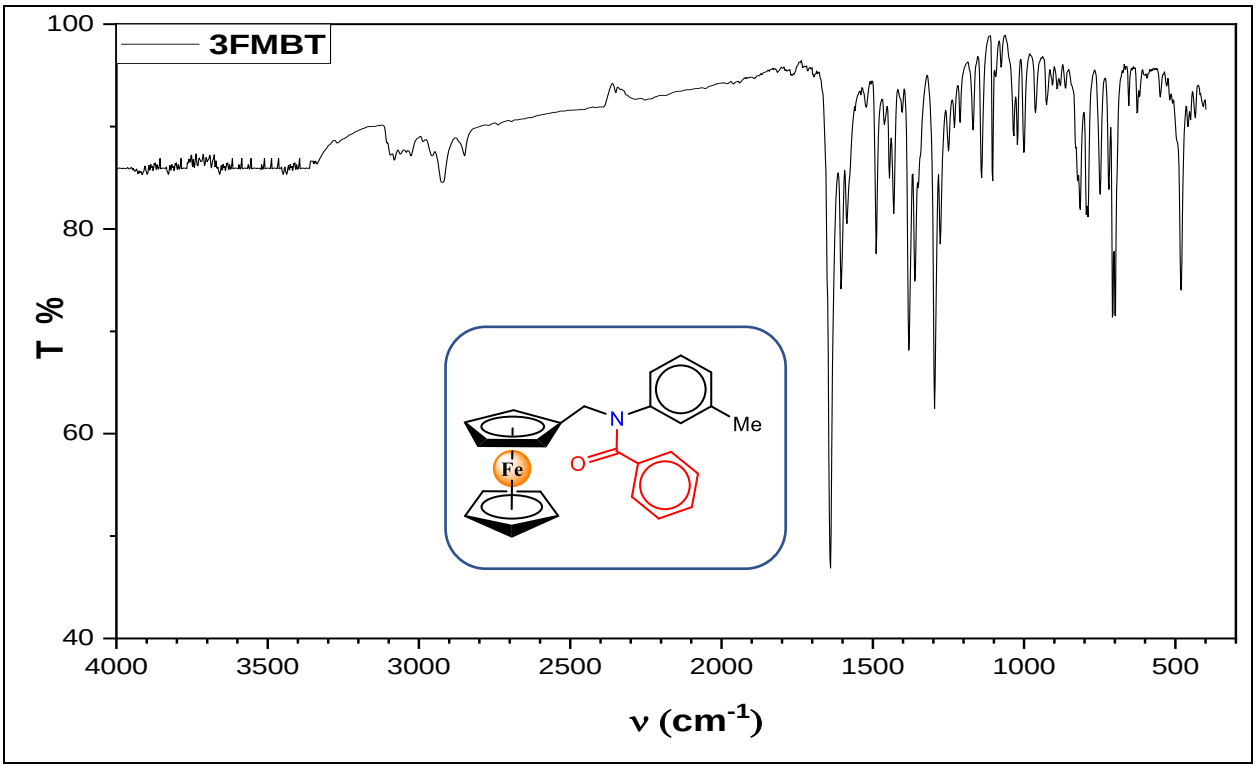

Figure S8. IR spectrum of 3FMBT.

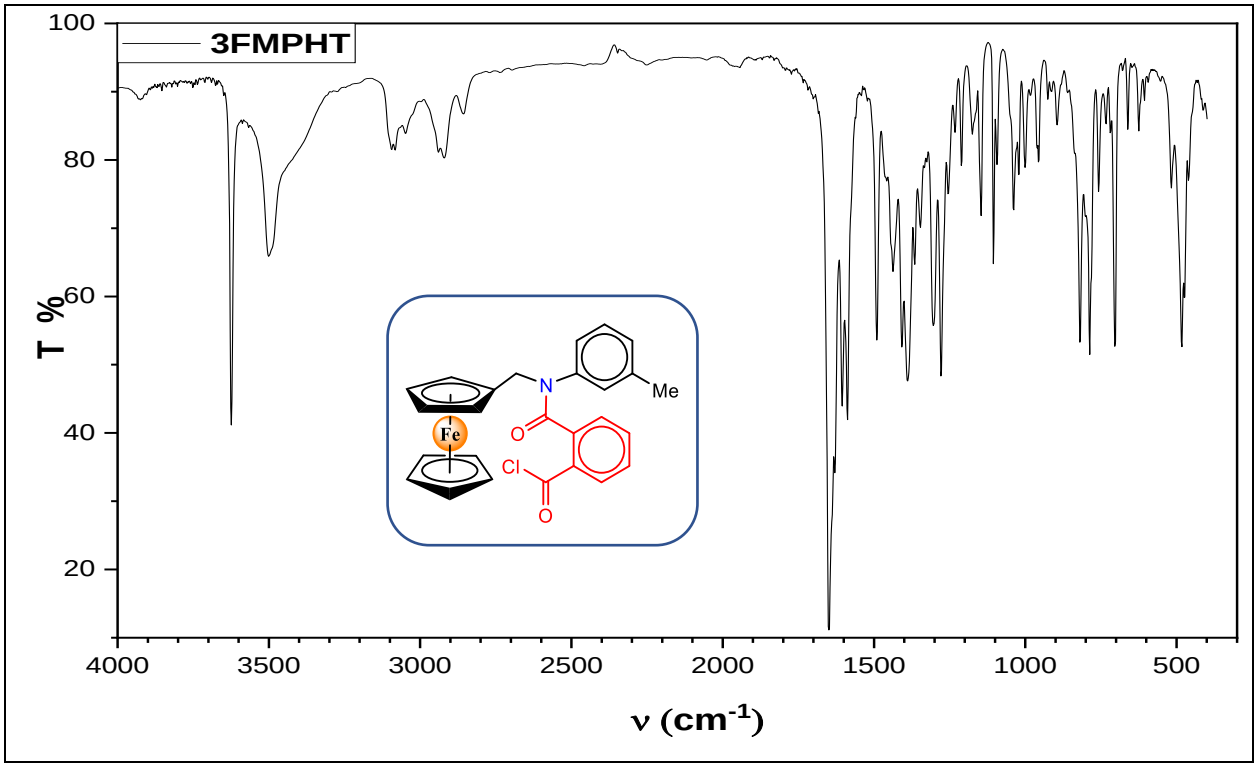

Figure S9. IR spectrum of 3FMPHT.

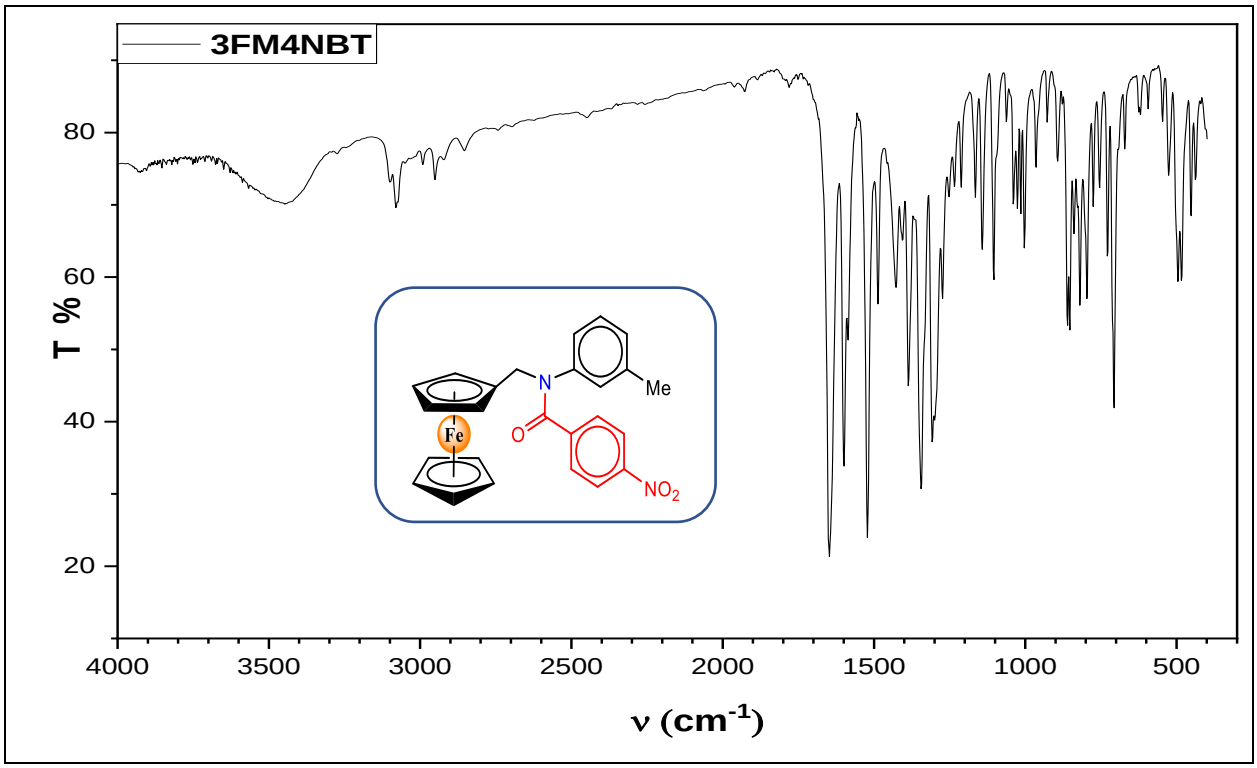

Figure S10. IR spectrum of 3FM4NBT.

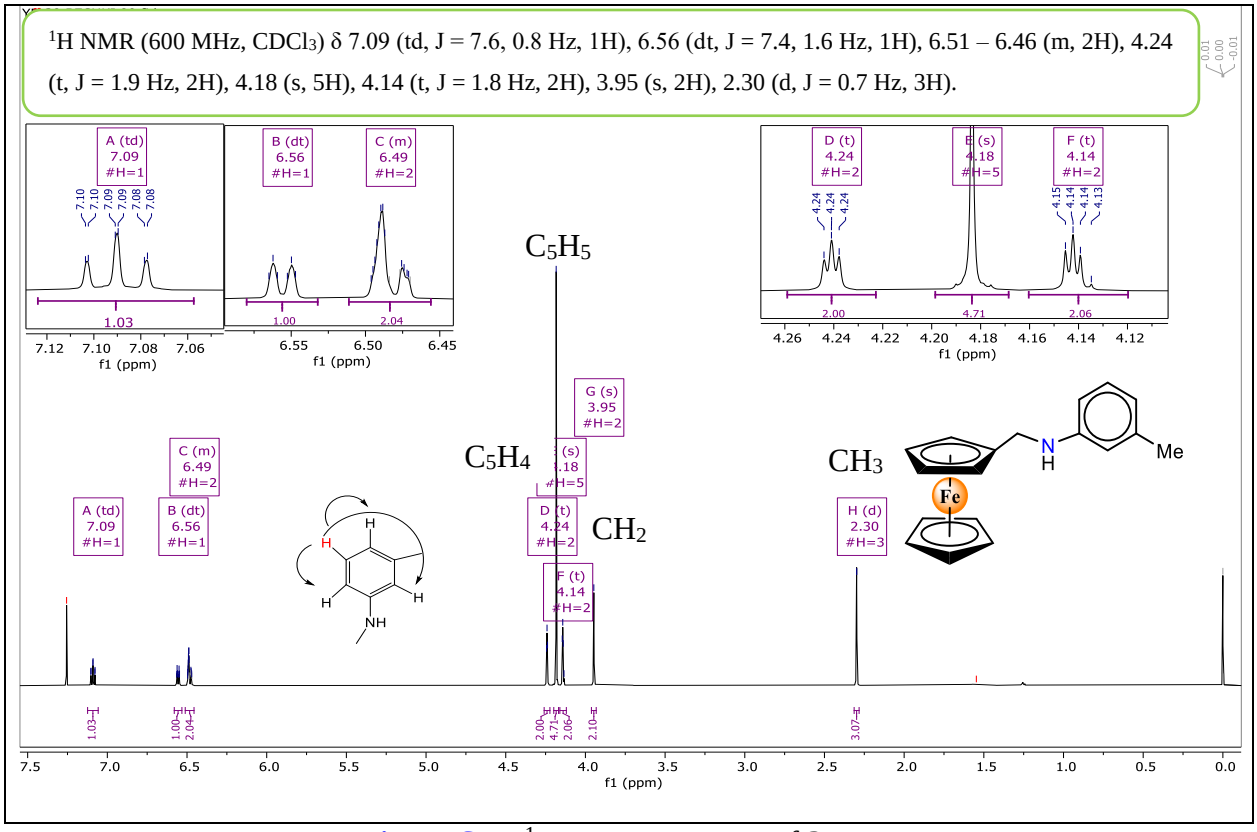

Figure S11. ^{1}H NMR spectrum of 3FMT.

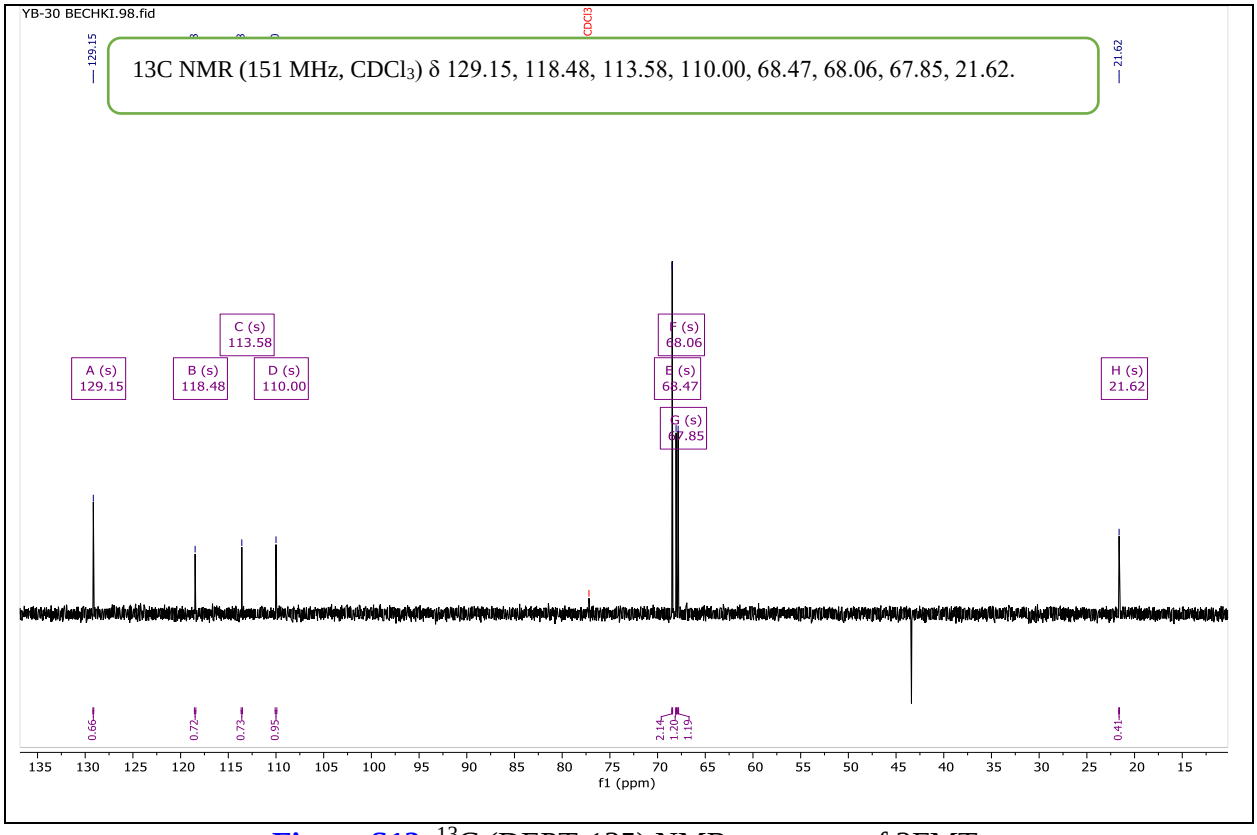

Figure S12. ^{13}C (DEPT-135) NMR spectrum of 3FMT.

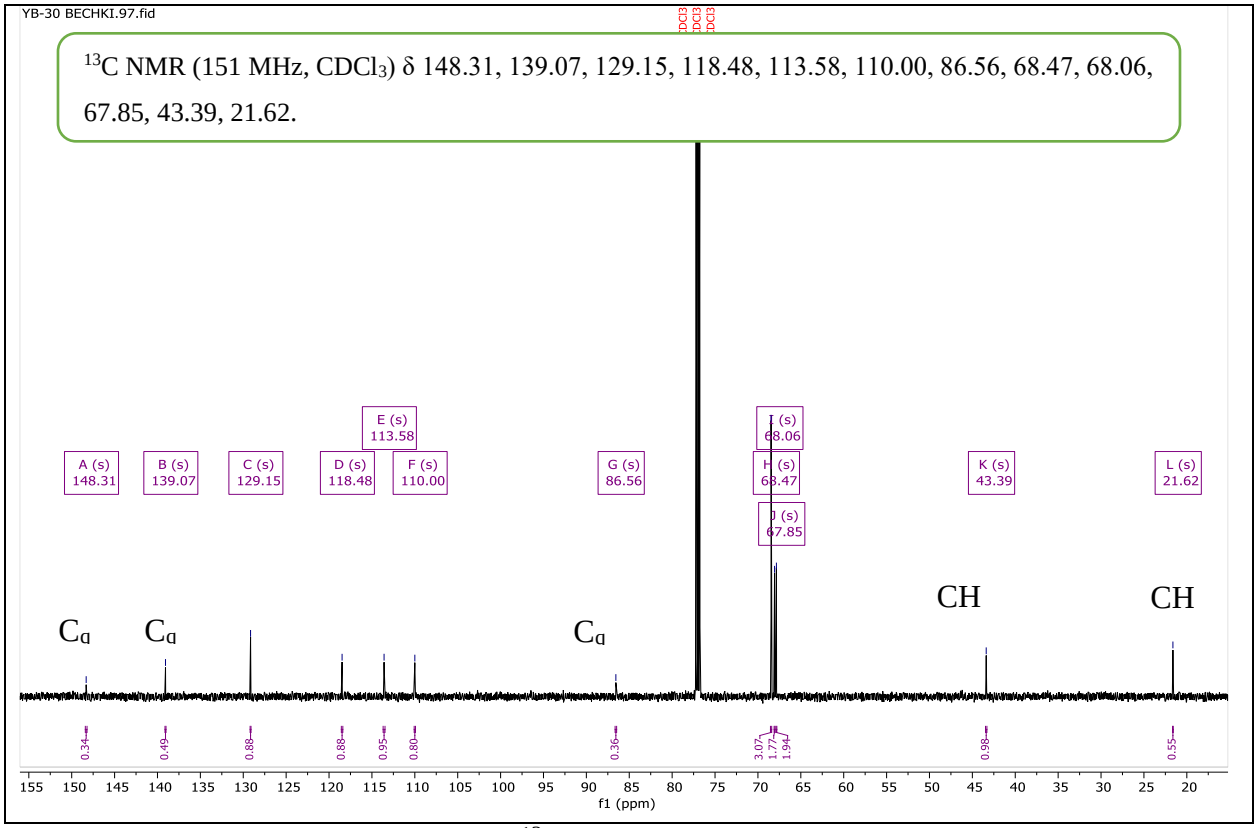

Figure S13. ^{13}C NMR spectrum of 3FMT.

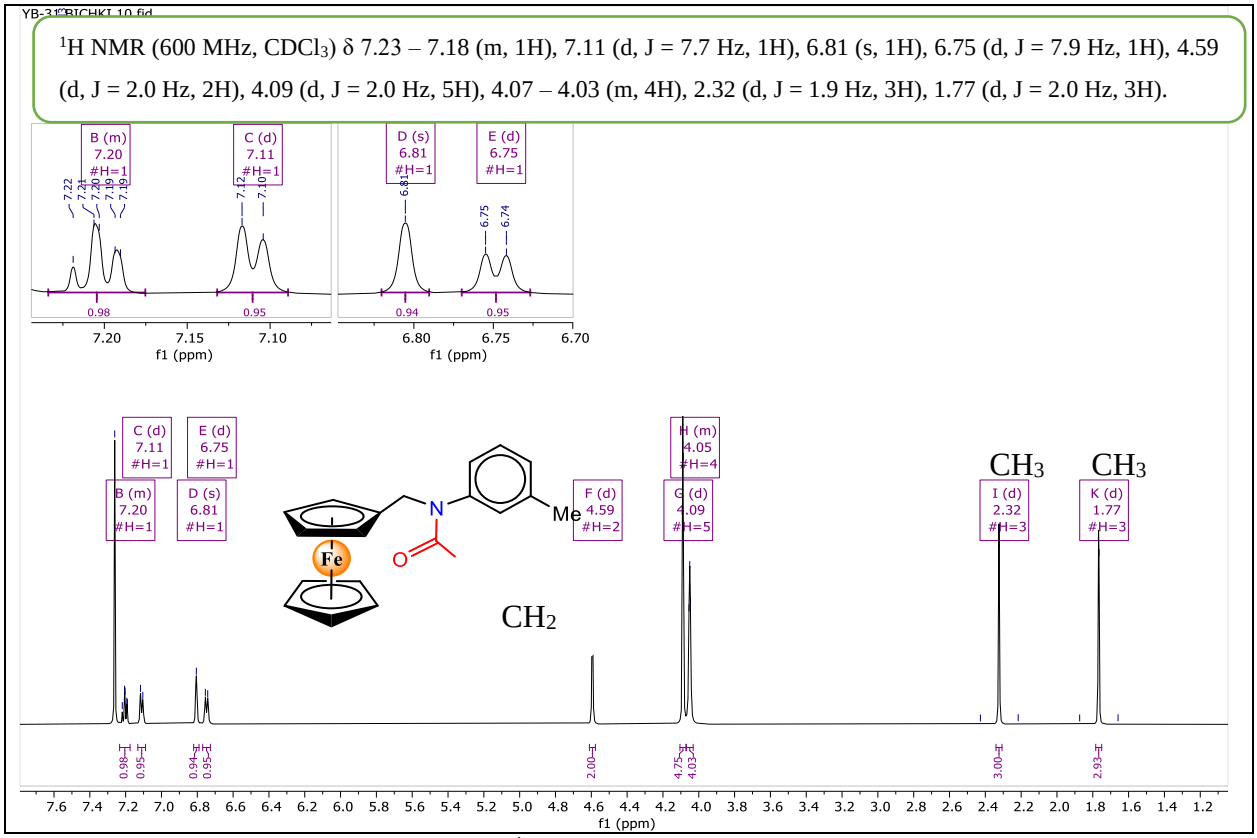

Figure S14. ^{1}H NMR spectrum of 3FMAT.

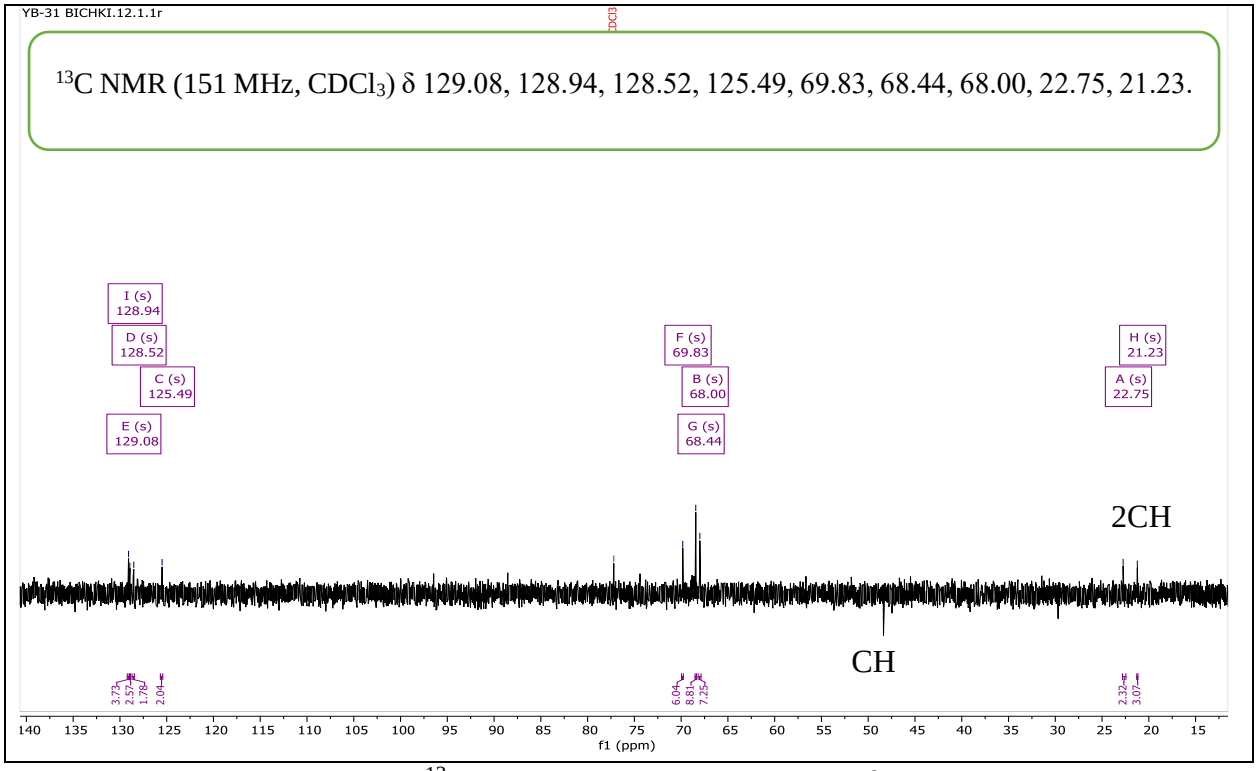

Figure S15. ^{13}C NMR (DEPT-135) spectrum of 3FMAT.

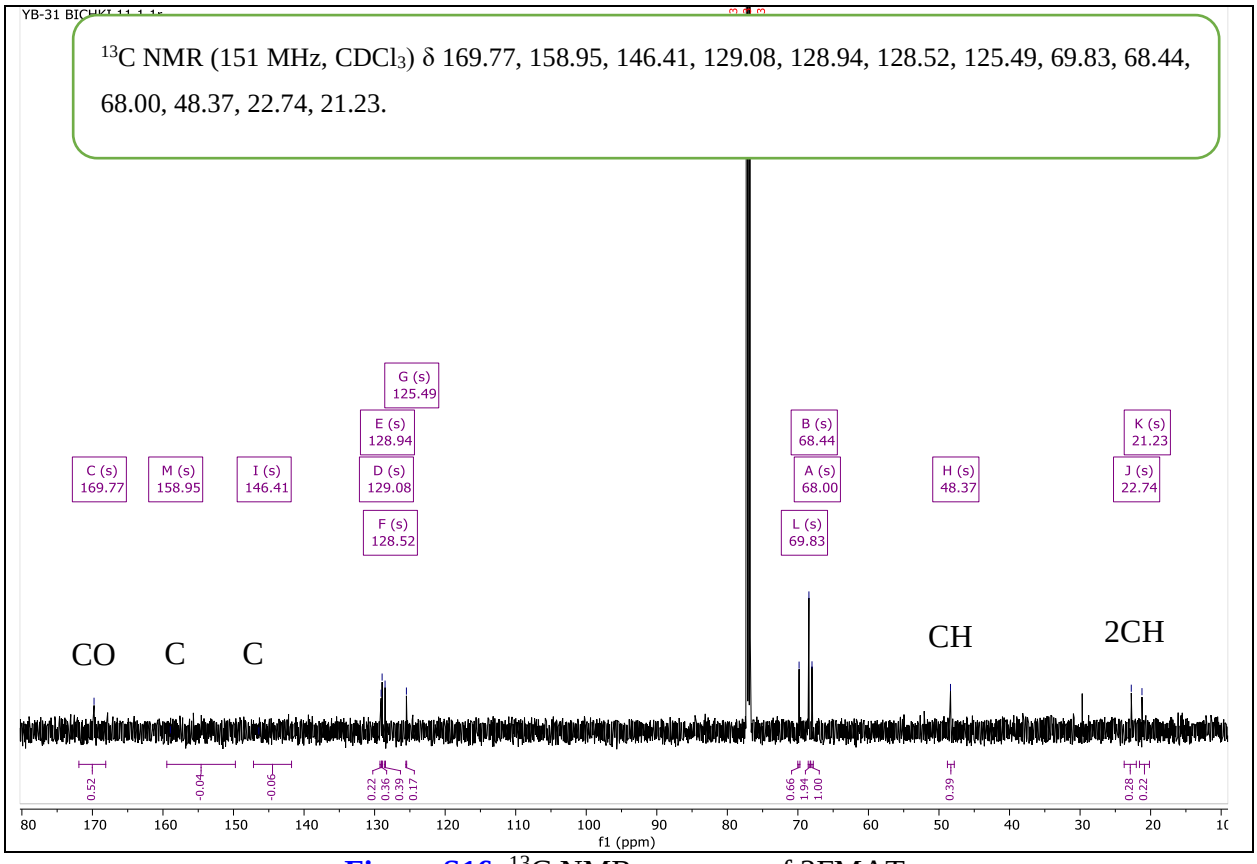

Figure S16. ^{13}C NMR spectrum of 3FMAT.

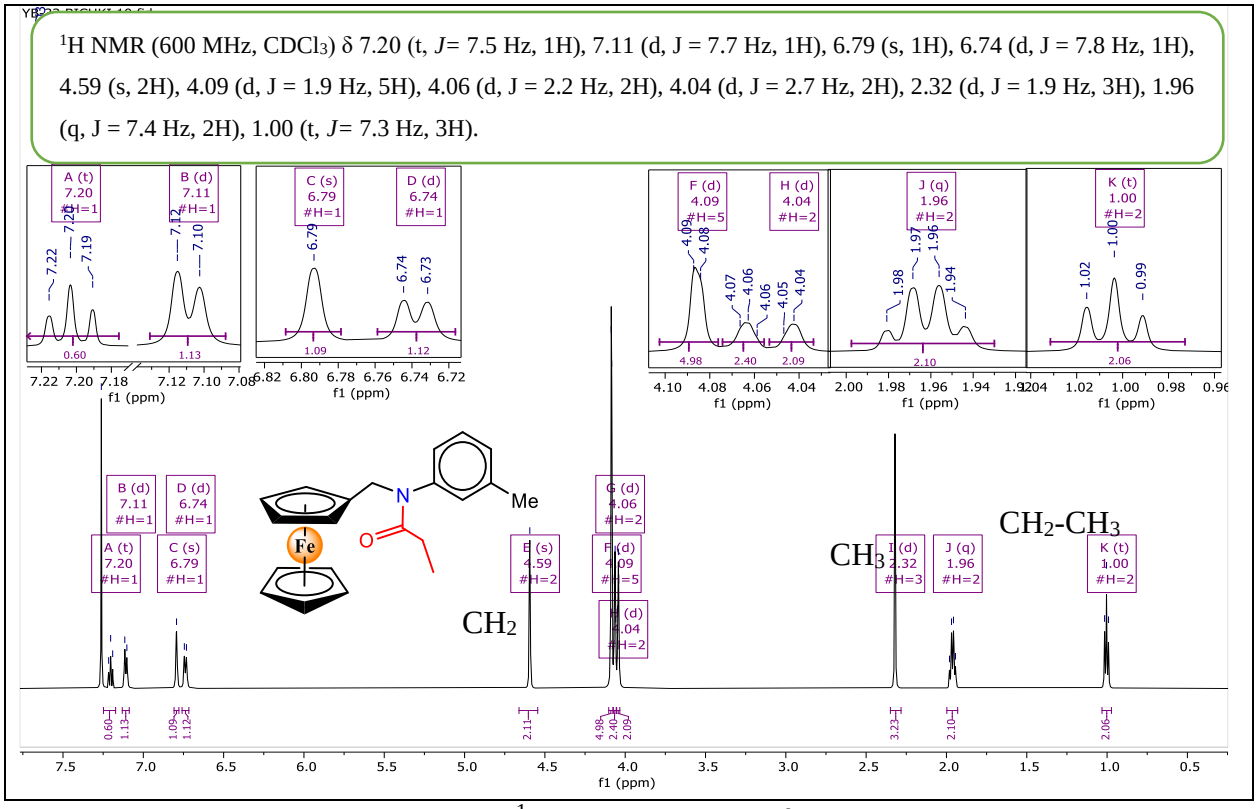

Figure S17. ^{1}H NMR spectrum of 3FMPT.

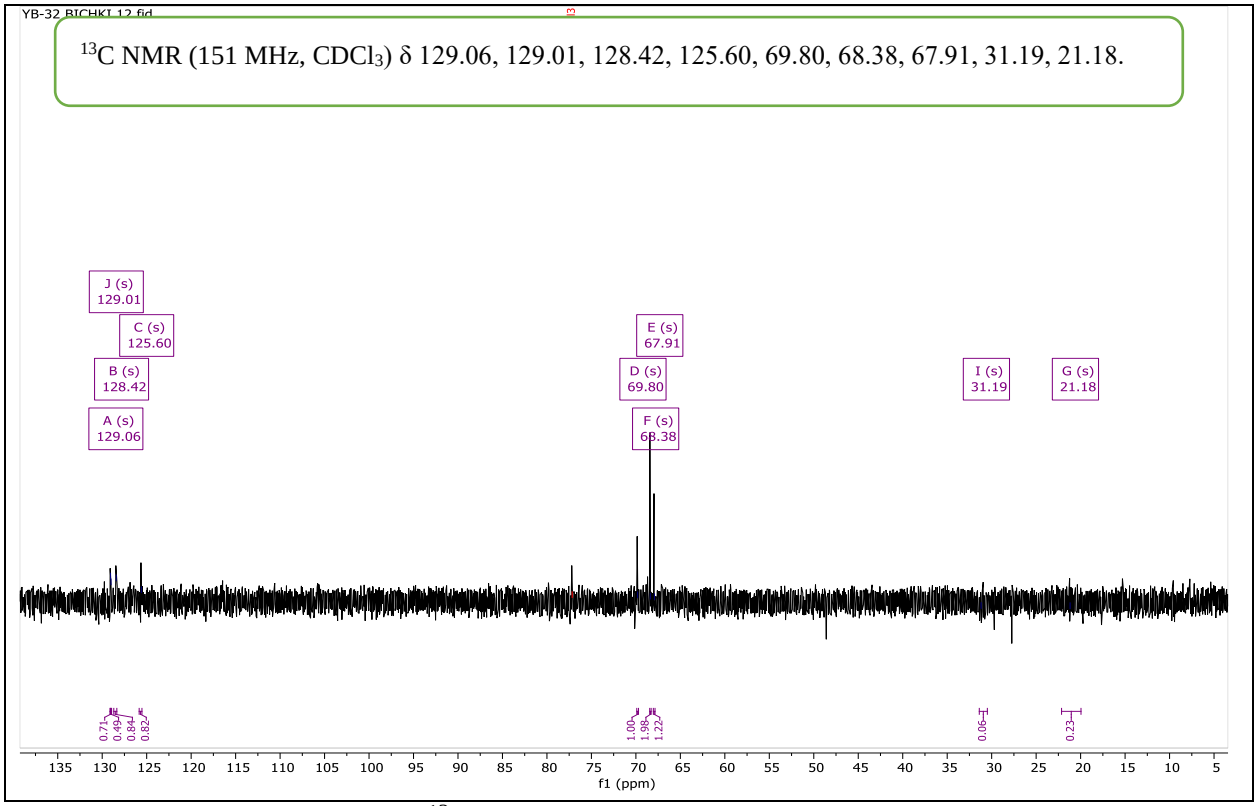

Figure S18. ^{13}C NMR (DEPT-135) spectrum of 3FMPT.

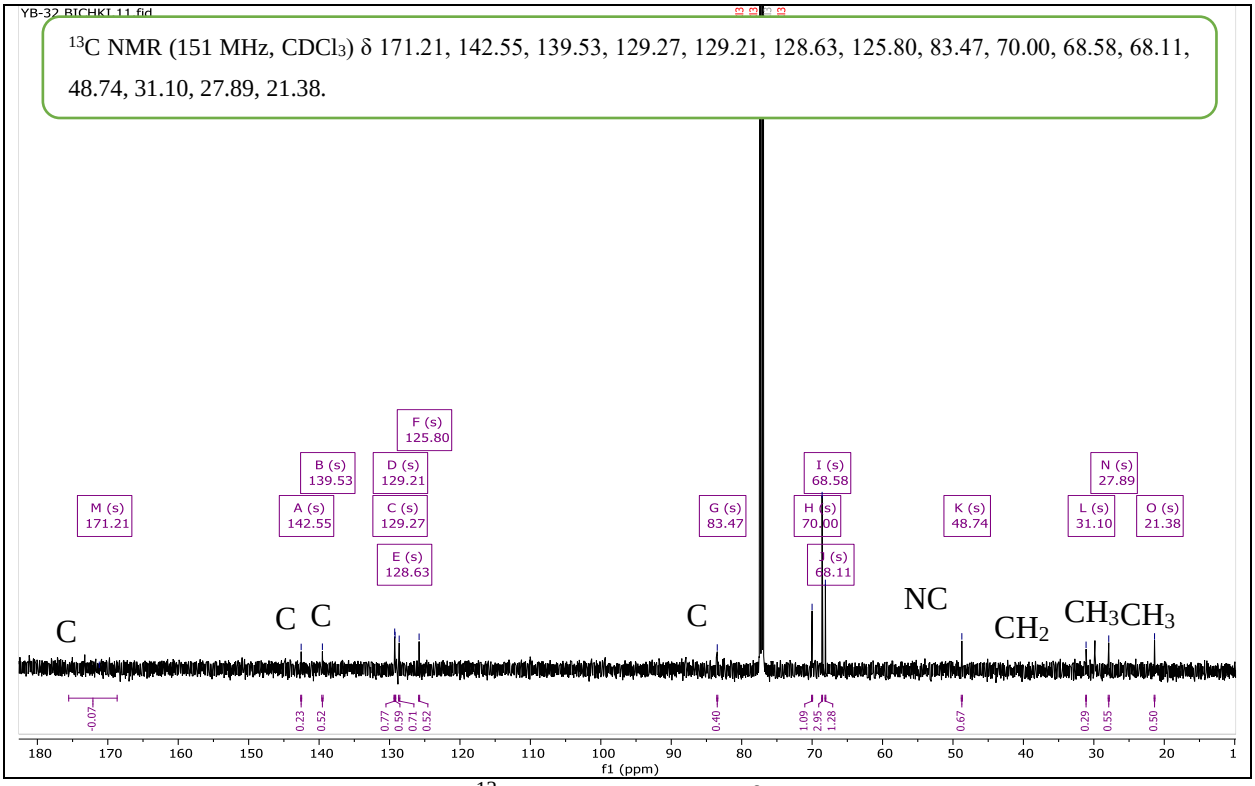

Figure S19. ^{13}C NMR spectrum of 3FMPT.

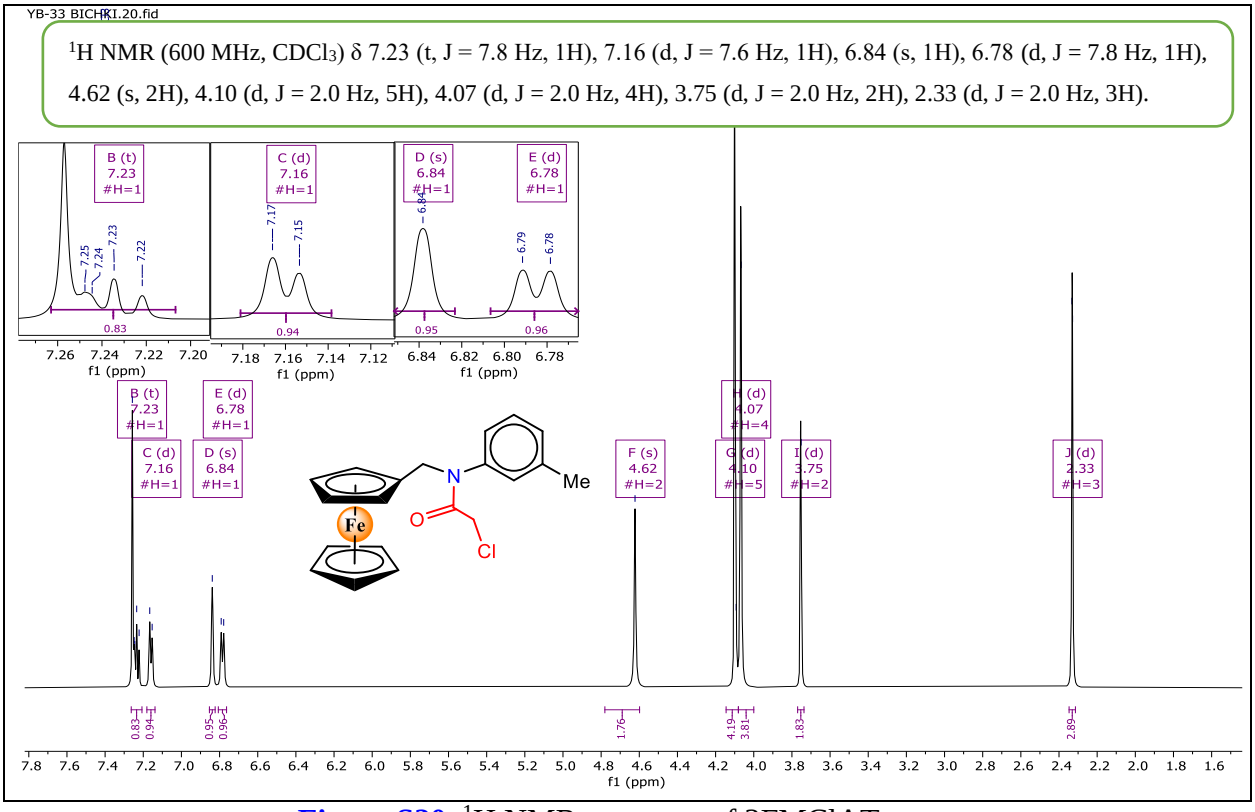

Figure S20. ^{1}H NMR spectrum of 3FMClAT.

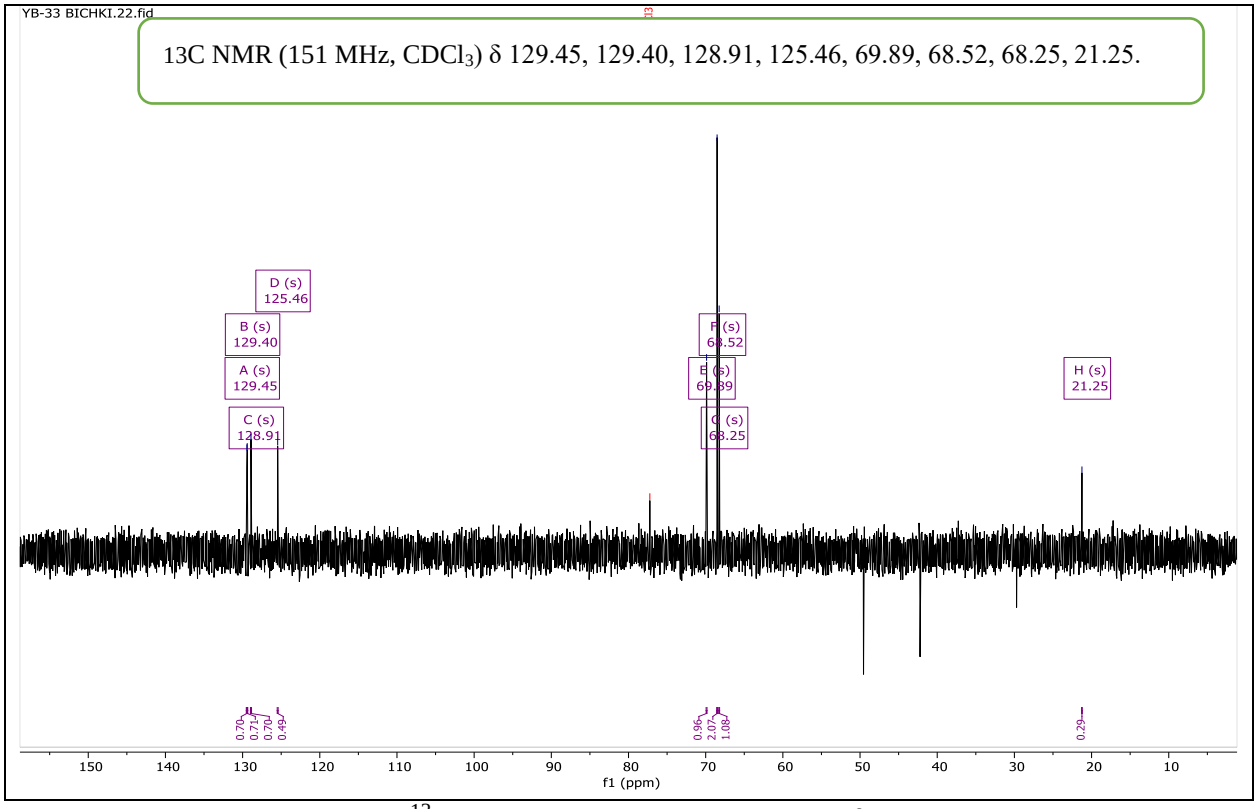

Figure S21. ^{13}C NMR (DEPT-135) spectrum of 3FMClAT.

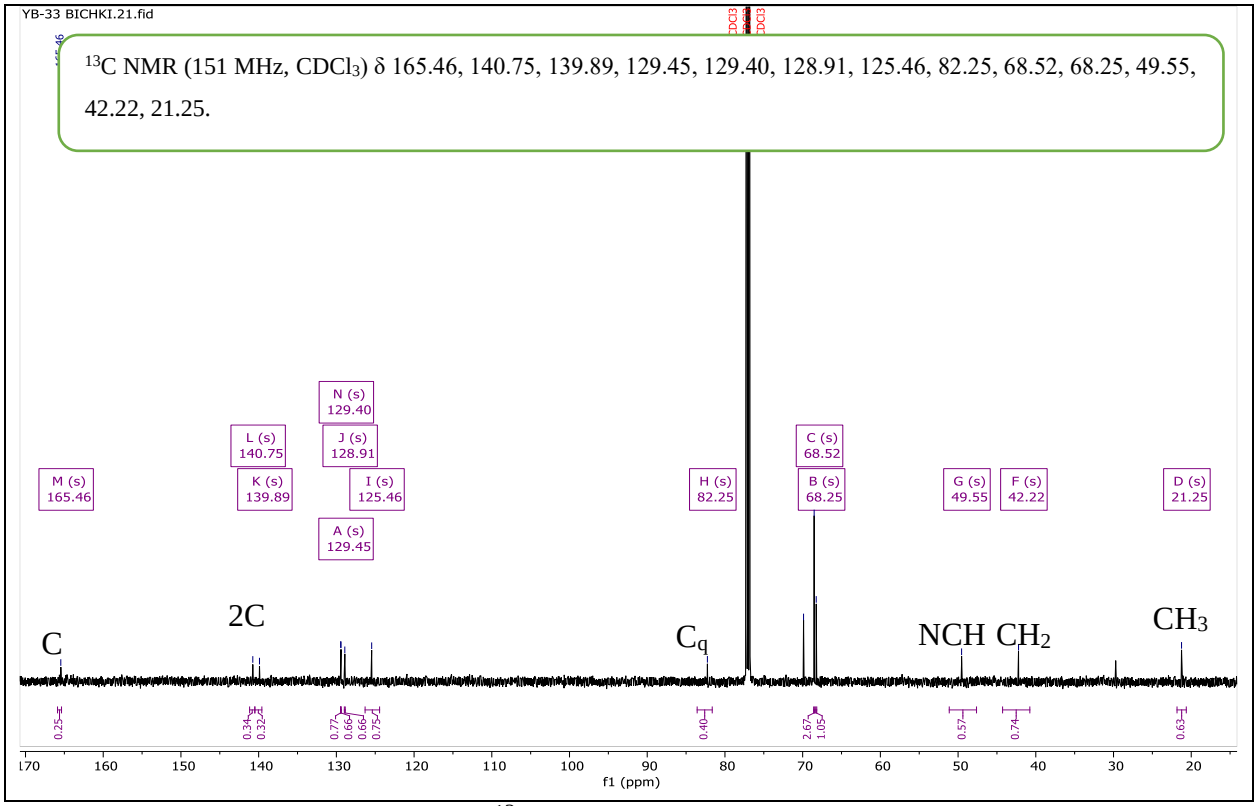

Figure S22. ^{13}C NMR spectrum of 3FMClAT.

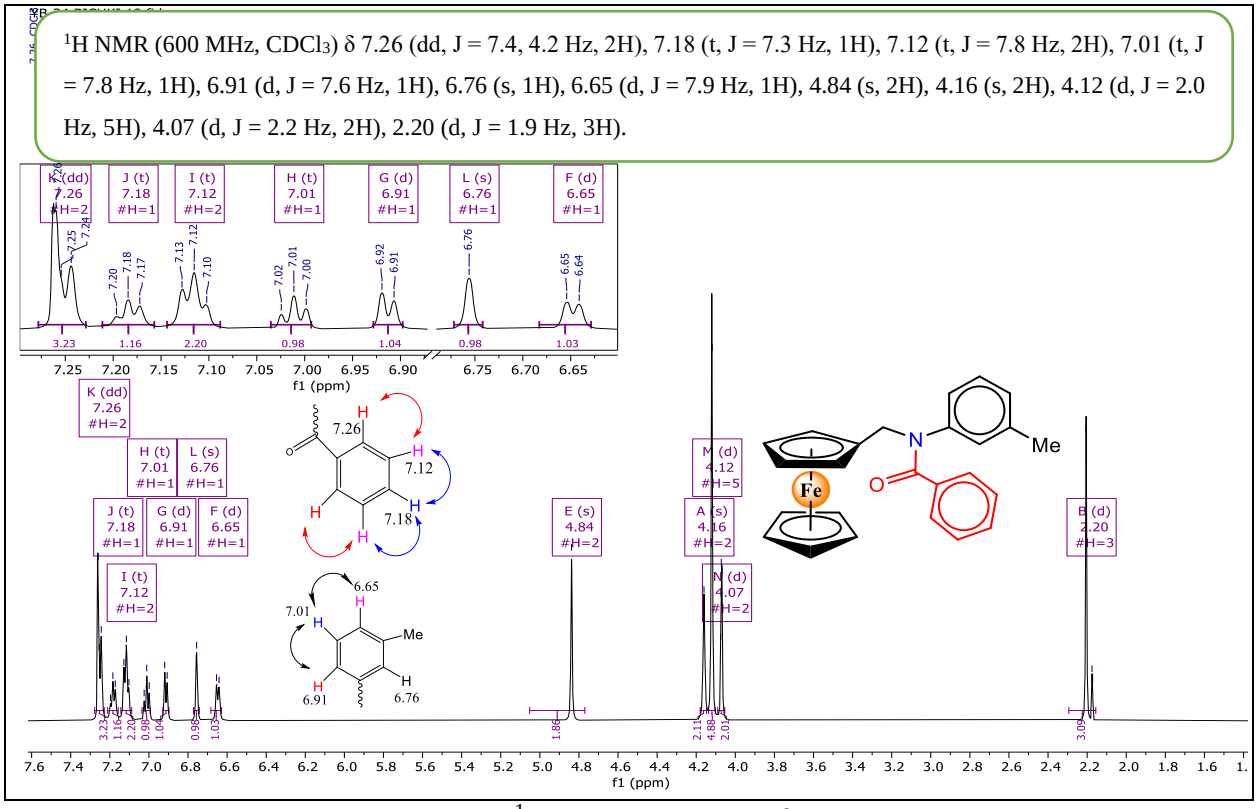

Figure S23. ^{1}H NMR spectrum of 3FMBT.

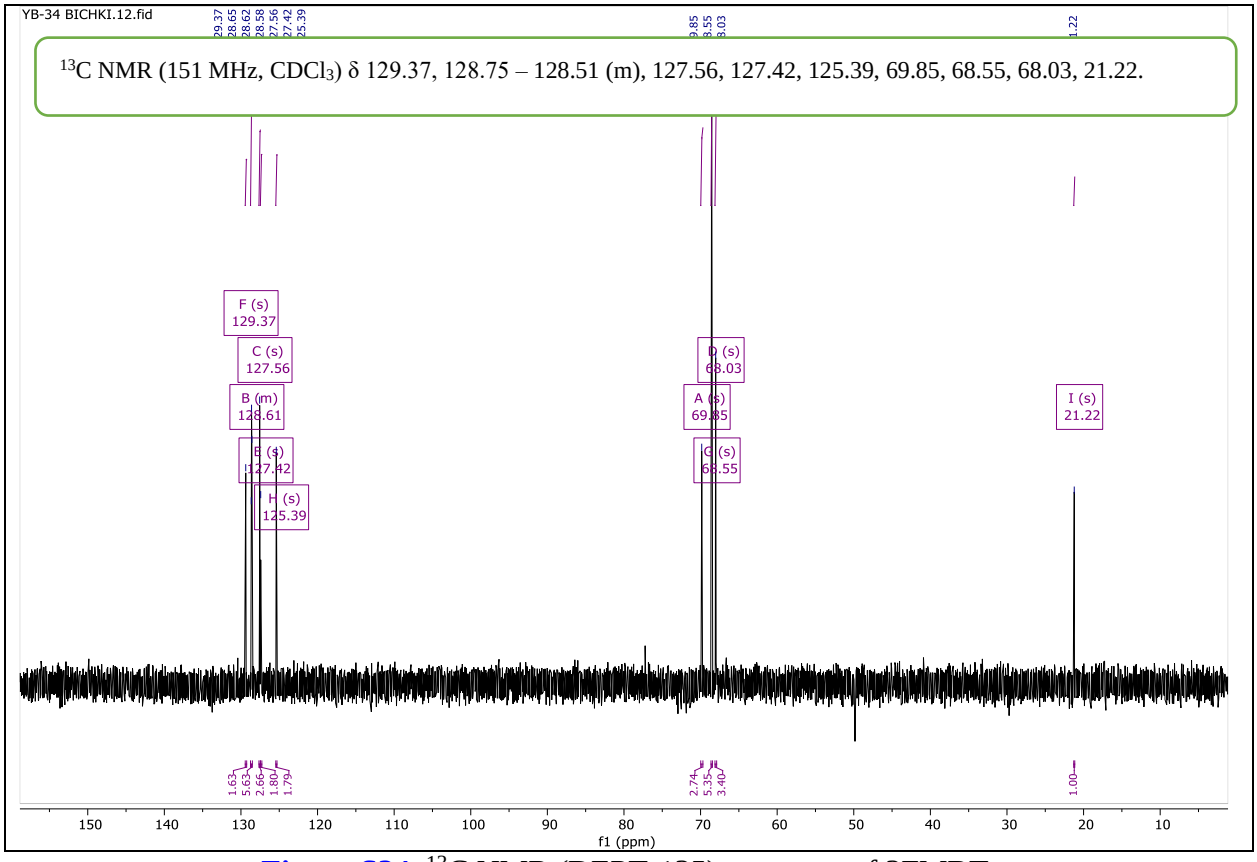

Figure S24. ^{13}C NMR (DEPT-135) spectrum of 3FMBT.

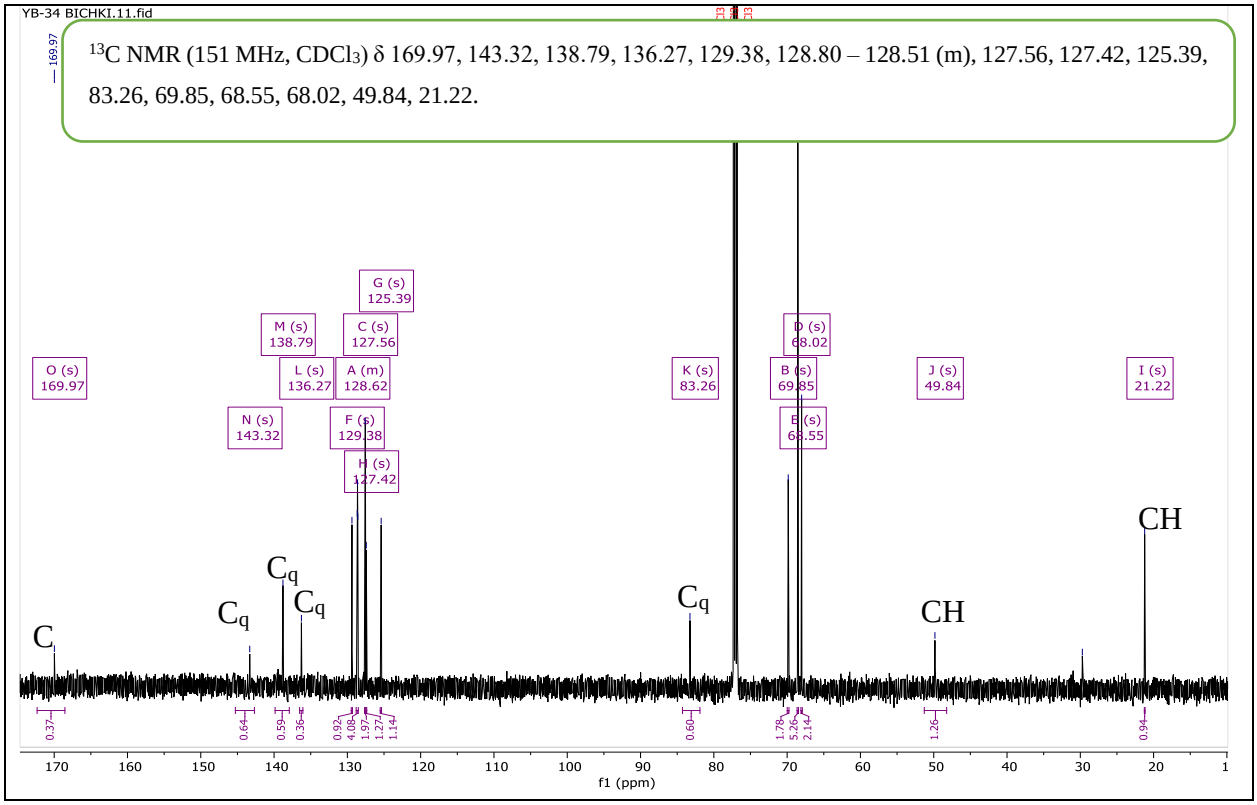

Figure S25. 13C NMR spectrum of 3FMBT.

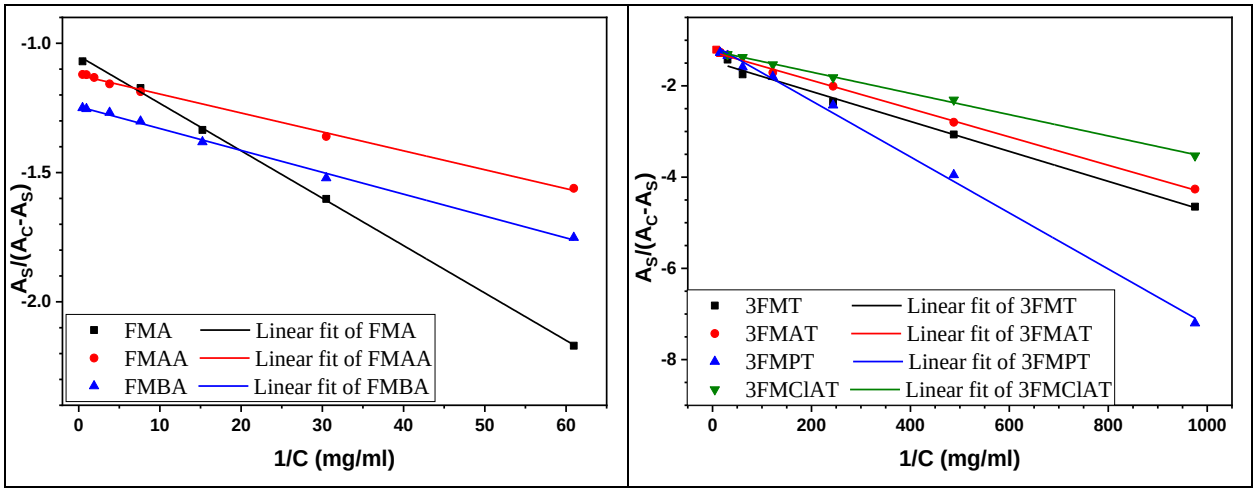

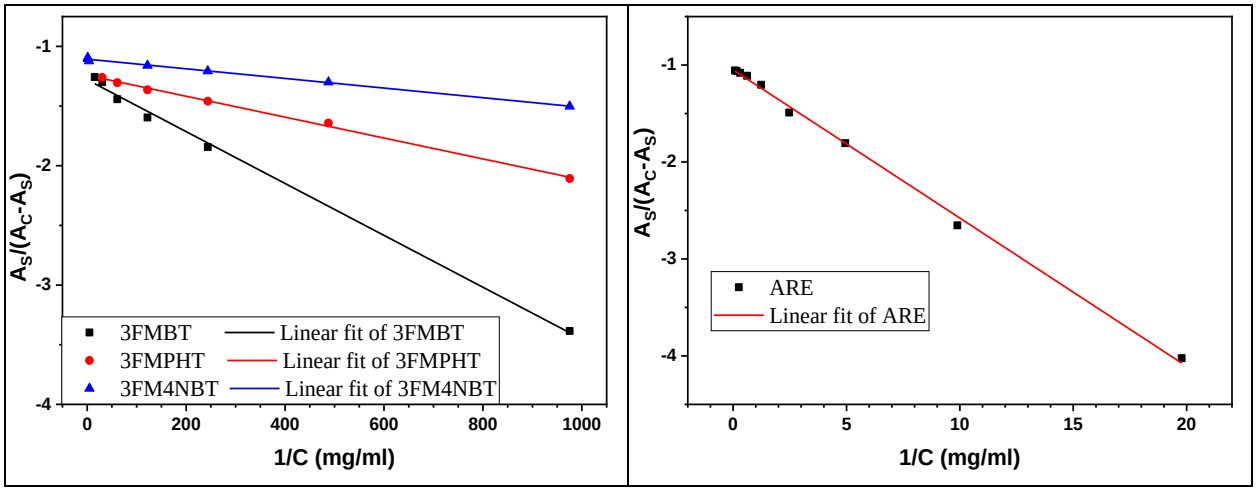

Figure S26. Typical plots of $A_S/(A_C-A_S)$ as a function of 1/ [C] used for calculation of the binding constants of acarbose (ARE), FMA, 3FMT, and their derivatives with α-amylase.

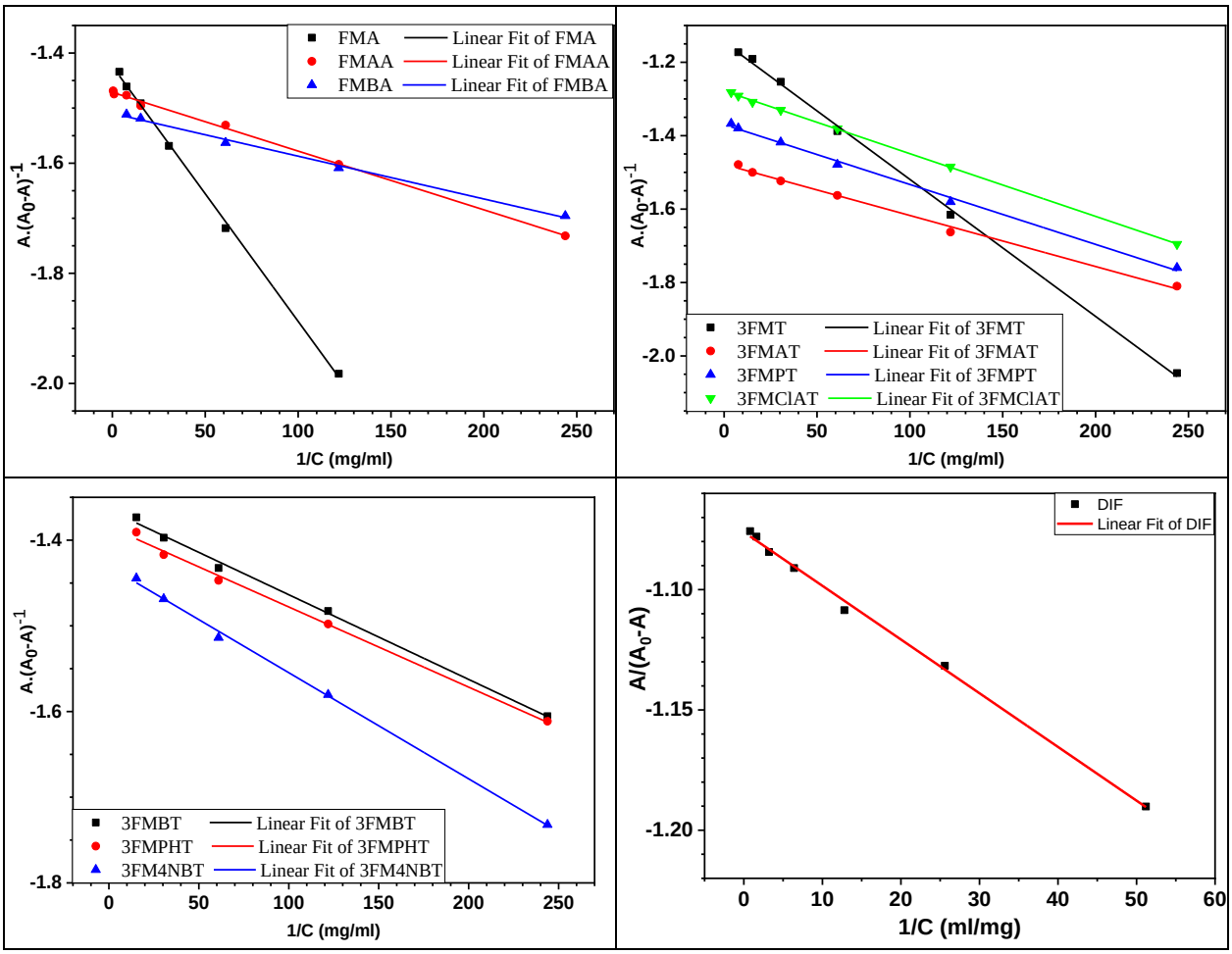

Figure S27. Typical plots of $A_S/(A_C-A_S)$ as a function of 1/ [C] used for calculation of the binding constants of Diclofenac (DIF), FMA, 3FMT, and their derivatives with BSA.

Table S.1. Inhibition Zone (mm) of synthesized compounds against *E. coli*.

	1.00	5.00	10.00	20.00	30.00	40.00	50.00	60.00

FMA	6.5	6.5	6.5	7	9	9	10	6
FMAA	6	6.5	6.5	7	7	8	8	6
FMBA	6.5	7	7	10	10	11	11	11
3FMT	6.5	6.5	6.5	7	8.5	9	9	6
3FMAT	6	7	7	7.5	7.5	7.5	8	8
3FMPT	7	7.5	8	8	8	8	9	9
3FMClAT	7	7.5	7.8	8	8.5	8.5	8.8	9.5
3FMBT	6	6.5	7	7.5	7.5	8	8.5	9
3FMPHT	7	7	7	7	7	8	11	11.5
3FM4NBT	6.5	7	7	7	7	8	11	12

Table S.2. Inhibition Zone (mm) of synthesized compounds against *K. pneumoniae*.

	1.00	5.00	10.00	20.00	30.00	40.00	50.00	60.00
FMA	6.5	6.5	6.5	7	7	8	8	9
FMAA	6.5	7	7	7	7	8	8	6
FMBA	6.5	7	7	7	7.5	8	9	10
3FMT	6	6	6	6.5	6.5	7	8	9
3FMAT	6	6	6	6	6.5	7	8	9
3FMPT	6.5	6.5	6.5	7	7	8	8	8.5
3FMClAT	6.5	6.5	7	8	8	8	8	10
3FMBT	7	7	7	8	8.5	9	9.5	11
3FMPHT	7	7	7	7	8	8.5	10	12
3FM4NBT	6	6.5	6.5	7	8	9	10.5	11

Table S.3. Inhibition Zone (mm) of synthesized compounds against *P. aeruginosa*.

	1.00	5.00	10.00	20.00	30.00	40.00	50.00	60.00
FMA	6.5	6.5	7	7.5	8	9	10.5	11.5
FMAA	6.5	6.5	6.5	6.5	7	7	8	10.5
FMBA	6.5	7	7	8	9.5	10	11	6
3FMT	6.5	6.5	7.5	8	9	10.5	11	6
3FMAT	6	6.5	7	7.5	9	11	11.5	12
3FMPT	6.5	6.5	6.5	7	7	7	8	11
3FMClAT	6.5	6.5	7	7.5	8	9	9	11
3FMBT	6	6.5	6.5	7	8	8.5	9	9
3FMPHT	6.5	7	7	7	7	7	7	7
3FM4NBT	6	6.5	6.5	7	7.5	9	9	9.5

Table S.4. Inhibition Zone (mm) of synthesized compounds against *S. aureus*.

	1.00	5.00	10.00	20.00	30.00	40.00	50.00	60.00
FMA	6	6	6	6.5	7	7.5	7.5	8
FMAA	6	6.5	7	7	7	9	9	9
FMBA	6	6	7	8	8	8	9	10
3FMT	6	6	6	6	6.5	6.5	6.5	7
3FMAT	6.5	7	7	8	8	8	9	9
3FMPT	6.5	7	7.5	7.5	8	8	8.5	9
3FMClAT	7	7	7.5	8	8.5	8.7	9	9
3FMBT	6.5	7	7	8	8	8	9	10

3FMPHT	6	6	6.5	6.5	10	11	11	14
3FM4NBT	6	6.5	10	11	11	12	13	14

Table S.5. Binding energy values (kcal/mol) of docked ligands with bacterial strain proteins.

	1KZN	1BSK	4OR7	5EIX	5OE3	1LRY	6I1E	2ZCQ	3SRW	3TTZ	5M18	3U74
Co-crystal	-8.24	-7.92	-8.80	-4.94	-10.45	-8.78	-4.74	-7.19	-8.80	-7.99	-4.17	-8.77
AXL	-6.76	-7.95	-7.77	-3.85	-8.85	-7.32	-6.97	-7.77	-7.33	-7.33	-6.85	-7.54
FMA	-6.19	-6.99	-6.00	-4.08	-7.54	-7.18	-5.96	-6.48	-6.56	-6.09	-6.61	-6.38
FMAA	-6.96	-8.15	-6.54	-4.70	-8.64	-7.91	-6.89	-7.64	-7.40	-6.02	-6.72	-6.83
FMBA	-6.99	-8.76	-7.04	-5.58	-11.36	-8.55	-7.99	-8.99	-8.80	-7.43	-7.37	-7.78
3FMT	-6.54	-7.16	-6.31	-4.43	-8.31	-7.50	-6.31	-6.88	-6.70	-6.46	-6.25	-6.78
3FMAT	-6.49	-8.32	-6.30	-4.64	-8.81	-8.14	-7.30	-7.32	-7.52	-6.22	-6.42	-7.33
3FMPT	-6.08	-7.85	-6.34	-4.53	-8.79	-7.48	-6.80	-7.35	-7.60	-6.36	-6.61	-7.27
3FMClAT	-6.56	-8.12	-6.66	-4.99	-8.91	-7.75	-7.30	-7.64	-7.80	-6.52	-6.66	-7.53
3FMBT	-6.93	-7.96	-7.02	-5.46	-11.97	-8.50	-7.60	-8.79	-8.25	-7.52	-7.44	-7.42
3FMPHT	-6.03	-8.36	-8.12	-5.77	-13.01	-8.91	-7.90	-8.50	-8.84	-7.12	-7.81	-8.27
3FM4NBT	-8.04	-8.28	-8.10	-4.93	-12.82	-7.97	-6.01	-8.48	-7.88	-8.31	-6.75	-8.30

Table S.6. Interaction type, and Binding interaction of ligands with α-amylase protein.

Ligand	Type	Residues	Distance
QV4	Conventional H-Bond	TYR A:62, GLN A:63, ASN A:105, ALA A:106, VAL A:107, THR A:163, ARG A:195, GLU A:233, HIS A:299, ASP A:300	1.72-3.30
	Carbon H-Bond	GLY A:164, ALA A:198	3.23-3.70
	Pi-Donor H-Bond	TYR A:62, HIS A:305	3.25-4.087
ARE	Conventional H-Bond	TRP A:59, THR A:163, LYS A:200, HIS A:201, GLU A:233, ILE A:235, HIS A:305	1.73-2.76
	Unfavorable D-D	HIS A:201	2.93
	Alkyl	LEU A:165	3.77
FMA	Conventional H-Bond	TRP A:59	1.95
	Pi-Pi T-Shaped	TRP A:59	5.53
	Alkyl	LEU A:162, LEU A:165	5.12-5.27
	Pi-Alkyl	TYR A:62, HIS A:101, LEU A:165	4.45-4.79
FMAA	Conventional H-Bond	HIS A:305	2.25
	Pi-Pi T-Shaped	TRP A:59	4.95-5.23
	Alkyl	LEU A:162, LEU A:165	5.24-5.30

	Pi-Alkyl	TYR A:62, HIS A:101, LEU A:165, HIS A:299	4.06-5.36
FMBA	Conventional H-Bond	HIS A:101	3.02
	Pi-Pi Stacked	TYR A:62	3.95
	Pi-Pi T-Shaped	TRP A:59	5.62
	Alkyl	LEU A:162	4.08-4.46
	Pi-Alkyl	LEU A:165, HIS A:305	4.53-4.62
3FMT	Conventional H-Bond	TRP A:59	1.97
	Pi-Pi T-Shaped	TRP A:59	4.76-5.49
	Alkyl	LEU A:162, LEU A:165	4.90-5.40
	Pi-Alkyl	TYR A:62, HIS A:101, LEU A:165	4.44-4.86
3FMAT	Conventional H-Bond	HIS A:300	1.71
	Pi-Anion	ASP A:300	3.48
	Alkyl	LEU A:165, ALA A:198	4.21-5.33
	Pi-Alkyl	TRP A:59	4.19-5.35
3FMPT	Conventional H-Bond	HIS A:305	2.24
	Pi-Sigma	TRP A:59	3.54
	Pi-Pi T-Shaped	TRP A:59	4.95-5.23
	Alkyl	LEU A:162, LEU A:165	4.68-5.27
	Pi-Alkyl	TRP A:59, TYR A:62, HIS A:101, LEU A:165, HIS A:299, HIS A:305	4.25-5.41
3FMClT	Conventional H-Bond	HIS A:305	2.22
	Pi-Pi T-Shaped	TRP A:59	4.97-5.24
	Alkyl	LEU A:162, LEU A:165	4.66-5.24
	Pi-Alkyl	TYR A:62, HIS A:101, LEU A:165, HIS A:299	4.05-5.42
3FMBT	Conventional H-Bond	HIS A:101	2.80
	Pi-Anion	ASP A:197	3.32
	Pi-Sigma	TRP A:59	3.79-3.81
	Pi-Pi Stacked	TRP A:59	5.11-5.12
	Alkyl	LEU A:162	4.43

	Pi-Alkyl	TRP A:59, LEU A:165, ALA A:198, HIS A:305	4.15-5.29
3FM4NBT	Conventional H-Bond	HIS A:101	2.07
	Pi-Sigma	TRP A:59	4.00
	Pi-Pi Stacked	TRP A:59, TYR A:62	3.92-4.69
	Alkyl	LEU A:162	5.33
	Pi-Alkyl	TRP A:59, HIS A:305	4.09-4.98
3FMPHT	Conventional H-Bond	LYS A:200	2.24
	Pi-Sigma	TYR A:62, LEU A:162	3.72-3.92
	Alkyl	LEU A:162, LEU A:165, ALA A:198	3.56-5.08
	Pi-Alkyl	TYR A:62, HIS A:101	4.84-5.22

Table S.7. Interaction type, and Binding interaction of ligands with BSA protein.

Ligand	Type	Residues	Distance
JGE	Attractive charge	HIS A:241, ARG A:256	3.78-4.04
	Conventional H-Bond	TYR A:149, ARG A:256	1.68-2.48
	Pi-Sigma	LEU A:259	3.75
	Alkyl	LEU A:237	4.87
	Pi-Alkyl	LEU A:218, LEU A:237, HIS A:241, ARG A:256, ALA A:260, ILE A:289, ALA A:290	4.15-5.46
DIF	Conventional H-Bond	TYR A:149, ARG A:256	1.70-1.92
	Pi-Sigma	LEU A:218, ILE A:289	3.67-3.94
	Pi-Alkyl	LEU A:259, ALA A:260, ILE A:263	4.65-547
FMA	Alkyl	ARG A:256, LEU A:259, ALA A:260, ILE A:263, ILE A:289, ALA A:290	3.44-5.18
	Pi-Alkyl	LEU A:218, LYS A:221	4.90-5.08
FMAA	Pi-Sigma	LEU A:218	3.89
	Alkyl	ARG A:256, LEU A:259, ALA A:260, ILE A:263, ILE A:289, ALA A:290	3.36-4.90
	Pi-Alkyl	LYS A:221	5.38
FMBA	Conventional H-Bond	TYR A:149, ARG A:256	1.68-2.61

	Pi-Cation	HIS A:241	4.07
	Pi-Pi T-Shaped	HIS A:241	5.06
	Alkyl	LEU A:218, LYS A:221, LEU A:237, ILE A:289, ALA A:290, VAL A:292	3.48-5.48
	Pi-Alkyl	PHE A:222, LEU A:237, ARG A:256, LEU A:259, ALA A:260, ILE A:289, ALA A:290	4.30-5.42
3FMT	Alkyl	LYS A:221, ARG A:256, LEU A:259, ALA A:260, ILE A:263, ILE A:289, ALA A:290	3.53-5.09
	Pi-Alkyl	LEU A:218, LYS A:221	4.78-5.18
3FMAT	Pi-Sigma	LEU A:218	3.84
	Alkyl	ARG A:217, LEU A:218, LYS A:221, ARG A:256, LEU A:259, ALA A:260, ILE A:263, ILE A:289,	3.33-5.45
	Pi-Alkyl	LYS A:221	5.32
3FMPT	Conventional H-Bond	TYR A:149, ARG A:256	1.78-2.72
	Pi-Cation	ARG A:198, ARG A:217	4.59-4.87
	Pi-Sigma	LEU A:237	3.93
	Alkyl	LYS A:221, LEU A:237, ARG A:256, LEU A:259, ALA A:260, ILE A:263, ILE A:289, ALA A:290	3.68-5.27
	Pi-Alkyl	TYR A:149, ARG A:217, ALA A:290	4.80-5.42
3FMClT	Conventional H-Bond	TYR A:149, ARG A:256	1.70-2.79
	Alkyl	ARG A:217, LEU A:218, LYS A:221, LEU A:233, LEU A:237, LEU A:259, ALA A:290	3.65-5.05
	Pi-Alkyl	LEU A:218, LEU A:237, LEU A:259, ILE A:263	4.63-5.44
3FMBT	Conventional H-Bond	TYR A:149, ARG A:256	1.73-2.34
	Pi-Cation	HIS A:241	4.52
	Pi-Sigma	ALA A:290	3.81

	Pi-Pi T-Shaped	HIS A:241	5.43
	Alkyl	LEU A:218, LYS A:221, LEU A:237, ILE A:289, ALA A:290, VAL A:292	3.60-5.47
	Pi-Alkyl	TRP A:213, PHE A:222, ARG A:256, LEU A:259, ALA A:260, ILE A:289	4.41-5.03
3FM4NBT	Conventional H-Bond	TYR A:149, HIS A:241, ARG A:256	1.66-1.87
	Pi-Cation	ARG A:198, ARG A:256	3.91-4.82
	Pi-Sigma	ALA A:290	3.81
	Alkyl	LEU A:218, LYS A:221, LEU A:237, ALA A:260, ILE A:289	3.27-5.26
	Pi-Alkyl	PHE A:222, LEU A:237, ARG A:256, LEU A:259,	4.22-5.47
3FMPHT	Conventional H-Bond	ARG A:198, ARG A:217	1.80-2.78
	Pi-Cation	ARG A:217	4.17
	Pi-Sigma	ILE A:263	3.09
	Alkyl	ARG A:256, LEU A:259, ALA A:260, ILE A:263, LEU A:274, ILE A:289, ALA A:290	3.43-5.48
	Pi-Alkyl	LEU A:218, PHE A:222, LEU A:233, ALA A:290	4.02-4.64

Table S.8. Interaction type, and Binding interaction of ligands with COX-2 protein.

Ligand	Type	Residues	Distance
Co- DIF	Conventional H-Bond	SER A:530	1.92
	Carbon H-Bond	ALA A:527	3.38
	Pi-Sulfur	MET A:522	5.22
	Pi-Pi T-shaped	TRP A:387	5.10
	Pi-Alkyl	VLA A:349, VAL A:523, ALA A:527	4.49-5.07
DIF	Conventional H-Bond	TRY 385, SER 530	1.88-2.03
	Carbon H-Bond	ALA A:527	3.25
	Pi-Sigma	VLA A:349	3.95
	Pi-Sulfur	MET A:522	5.16

	Pi-Pi T-shaped	TRP A:387	5.16
	Pi-Alkyl	VAL A:523, ALA A:527	4.44-4.78
FMA	Pi-Lone Pair	SER A:530	2.85
	Pi-Pi T-shaped	PHE A:205	4.53
	Alkyl	LEU A:352, VAL A:523, ALA A:527	4.01-5.48
	Pi-Alkyl	VAL A: 344, PHE A: 381, TYR A:385, TRP 3 A:87, LEU A:534	4.71-5.33
FMAA	Conventional H-Bond	SER A:530	2.05
	Pi-Sulfur	MET A:522	5.16
	Pi-Pi T-shaped	TRP A:387	5.23
	Alkyl	VAL A: 349, VAL A:523, ALA A:527, LEU A:531	3.78-4.86
	Pi-Alkyl	TYR A:355	4.82
FMBA	Pi-Sigma	VAL A: 349, SER A:353, VAL A:523	3.08-3.45
	Alkyl	VAL A: 349, LEU A:352, MET 522, VAL A:523, ALA A:527	4.40-5.31
	Pi-Alkyl	PHE A:381, TYR A:385, TRP 387, ALA A:527, PHE A:518	4.09-5.34
3FMT	Pi-Sigma	HIS A:90, VAL A:523	3.14-3.64
	Alkyl	VAL A:349, LEU A:352, MET A:522, VAL A:523, ALA 5 A:27	3.93-5.48
	Pi-Alkyl	TYR A:355, PHE A:381, TYR A:385, PHE A:518	4.35-5.29
3FMAT	Pi-Sigma	PHE A:518	3.77
	Pi-Sulfur	MET A:522	5.20
	Pi-Pi T-shaped	TRP A:387	5.34
	Alkyl	MET A:522, VAL A:349, VAL A:523, LEU A:531, ALA A:527	3.87-5.29
	Pi-Alkyl	TYR A:355	4.75
3FMPT	Conventional H-Bond	SER A:530	2.05
	Pi-Sigma	ALA A:527	3.94

	Alkyl	VAL 116, VAL 349, LEU A:352, LEU A:359, LEU A:384, VAL A:523, ALA A:527, LEU A:531, LEU A:534,	3.72-5.24
	Pi-Alkyl	VAL 349, TYR A:355, PHE A:381, TYR A:385, TRP A:387, PHE A:518	4.29-5.47
3FMClT	Alkyl	VAL 349, LEU A:352, LEU A:359, MET A:522, VAL A:523, ALA A:527	3.92-5.19
	Pi-Alkyl	VAL 349, TYR A:355, PHE A:381, TYR A:385, TRP A:387, PHE A:518, VAL A:523, ALA A:527	4.13-5.48
3FMBT	Unfavorable A-A	TYR A:355	2.88
	Pi-Sigma	VAL 349, SER 353, VAL A:523, ALA A:527	3.21-3.87
	Alkyl	VAL 349, LEU A:352, MET A:522, VAL A:523, ALA A:527	4.45-5.39
	Pi-Alkyl	TYR A:385, PHE A:518, LEU A:531	4.27-5.39
3FM4NBT	Pi-Sigma	VAL A:349, SER A:353, VAL A:523	3.06-3.74
	Alkyl	LEU A:352, MET A:522, VAL A:523, ALA A:527	4.51-5.15
	Pi-Alkyl	TYR A:385, TRP A:387, PHE A:518, ALA A:527, LEU A:531	4.16-5.46
3FMPHT	Carbon H-Bond	SER A:353	3.27
	Pi-Sigma	VAL A:349, SER A:353, VAL A:523, ALA A:527	3.18-3.89
	Alkyl	VAL A:349, LEU A:352, VAL A:523, ALA A:527,	4.59-5.03
	Pi-Alkyl	PHE A:381, TYR A:385 TRP A:387 PHE A:518, LEU A:531	4.15-5.34

Published Articles